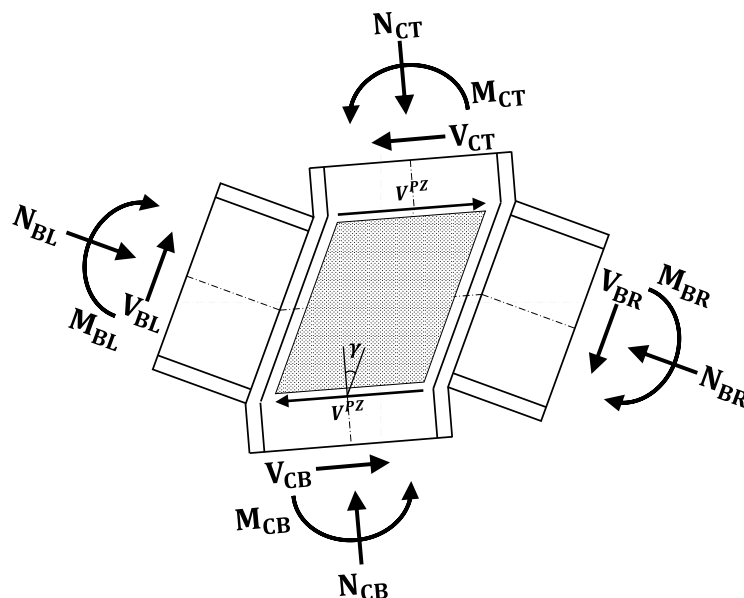# Characterization of the Full Non-Linear Behaviour up to Failure of the Sheared Panel Zone under Monotonic Loading Conditions

by

Adrien CORMAN

A thesis submitted in partial fulfilment of the requirements for the
degree of Doctor of Philosophy (Ph.D.) in Engineering Sciences

October 2022

Characterization of the Full Non-Linear Behaviour up to Failure of the Sheared Panel Zone under Monotonic Loading Conditions

A thesis submitted in partial fulfilment of the requirements
for the degree of Doctor of Philosophy (Ph.D.) in Engineering Sciences

by

Adrien CORMAN

Supervisor : Jean-Pierre JASPART

Co-supervisor : Jean-Fançois DEMONCEAU

Members of the Jury

President: Prof. Laurent Duchêne
                 University of Liège

Supervisor: Prof. Jean-Pierre Jaspart
                 University of Liège

Co-supervisor: Prof. Jean-François Demonceau
                 University of Liège

                 Dr. Ana Girão Coelho
                 *British Constructional Steelwork
                 Association*

                 Prof. Jean-Marc Franssen
                 University of Liège

                 Prof. Kim Rasmussen
                 University of Sydney

                 Prof. Luís Simões da Silva
                 University of Coimbra

Acknowledgments

First of all, I would like to acknowledge the international members of my jury, Dr. Ana Margarida Girão Coelho from the British Constructional Steelwork Association, Prof. Luís Simões da Silva from the University of Coimbra, and Prof. Kim Rasmussen from the University of Sydney, who have accepted to dedicate some of their precious time to read and evaluate my thesis.

« L'écriture d'une thèse est un marathon »

« Le sentiment que j'éprouve au moment de franchir la ligne d'arrivée est intense et difficile à décrire ; ce genre d'euphorie qui me fait oublier mon état de fatigue généralisé et mon corps, perfusé à la caféine, et endolori par de trop nombreuses journées, soirées, nuits… d'écriture ; un savoureux mélange de bonheur et de joie, une grande satisfaction personnelle, aussi, et puis beaucoup de soulagement… »

« Je me remémore alors, non sans émotion, le chemin parcouru : les moments de joie, les découvertes ; les difficultés, les moments de doute et les frustrations, aussi. Je pense, surtout, aux nombreuses personnes qui ont rendu cette aventure possible, que ce soit par leur présence, leur aide, leur soutien, leur compagnie, leurs conseils, ou leur bienveillance. Et je prends donc (enfin) le temps nécessaire pour leur adresser les remerciements qu'elles méritent »

« Je commencerai, comme il est coutume de le faire, par remercier mes sponsors, qui m'ont apporté une sérénité financière, me permettant de me focaliser à 100% sur ma recherche doctorale »

> *Durant ces 5 années de thèse, j'ai pu bénéficier du soutien financier de plusieurs organismes que je tiens ici à remercier : l'équipe CMM (Constructions Métalliques et Mixtes) du Professeur Jean-Pierre Jaspart, tout d'abord, pour le financement de ma première année de recherche, ainsi que les 3 derniers mois jusqu'à ma défense ; la Faculté des Sciences Appliquées, ensuite, pour le financement de ma seconde année de thèse et le FRIA (Fonds pour la Recherche dans l'Industrie et dans l'Agriculture), enfin, pour la bourse de recherche de 3 ans qu'il m'a accordée.*

« Ensuite, je tiens évidemment à remercier mes coaches qui ont cru en moi et qui ont, par leur expérience, leurs conseils et leurs encouragements, joué un rôle déterminant dans la finalisation de cette thèse »

> *Merci à mon promoteur, le Professeur Jean-Pierre Jaspart, et mon co-promoteur, le Professeur Jean-François Demonceau, pour la confiance qu'ils m'ont témoignée, pour leur gestion très humaine de l'équipe et pour la grande autonomie qu'ils m'ont accordée dans la gestion de mon travail au quotidien.*
> *Je remercie également les autres membres de mon comité de thèse, les Professeurs Laurent Duchêne et Jean-Marc Franssen, pour leur suivi au cours de ces 5 années.*

« Mes compagnons d'entraînement auront été, sans aucun doute, des personnes privilégiées, puisqu'ils auront partagé mon quotidien pendant 5 ans. Je les remercie chaleureusement pour la très chouette ambiance qu'ils ont participé à créer au niveau +1 du B52, et dans laquelle j'ai eu beaucoup de plaisir à évoluer quotidiennement »

> *Je voudrais remercier, en premier lieu, mes collègues au sein de l'équipe CMM : Aris, Loris, Marina, Maxime, Tudor et Zois. Merci, aussi, pour les chouettes moments que nous avons partagés à Aveiro. J'en garderai un très bon souvenir.*
> *Je remercie, aussi, les autres doctorants du couloir (côté robinet ET côté toilettes) pour les moments de détente, absolument nécessaires, que nous avons partagés lors de temps de midi, pauses café et autres.*

« Parmi ceux-ci, certains équipiers ont joué un rôle plus particulier que je souhaite souligner »

Marina, d'abord : merci pour ton accueil chaleureux au +1/537 et ta chouette compagnie pendant 2 ans et demi. Ton aide bienveillante et tes conseils précieux m'ont permis d'entamer sereinement le parcours doctoral.

Loris, ensuite : merci pour ta bonne humeur, ta complicité et ton soutien précieux dans la dernière ligne droite. Désolé pour mes nombreuses absences au bureau, pendant l'écriture. J'aurai l'occasion de me rattraper, maintenant que tu vis à Herve ! Je te souhaite bon courage pour la fin de ton assistanat.

Louis, Martin et Renaud, enfin : merci de m'avoir inspiré et encouragé à faire du vélotaf. Cette décision a réellement changé positivement mon quotidien. Merci aussi aux nombreux autres vélotafeurs qui m'ont accompagné, et en particulier à Gilles et Renaud pour les nombreuses heures passées « le cul sur la selle » à refaire le monde.

« Je pense également à tous mes supporters qui m'ont encouragé tout au long du parcours, et qui méritent eux aussi de chaleureux remerciements »

A mes amis de Blegny et de secondaire : je vous remercie pour votre amitié, votre présence et votre soutien, ainsi que pour votre simplicité qui fait que je me sens toujours à ma place avec vous. Je vous promets de me rattraper pour tous les événements que j'ai manqués au cours de l'année écoulée !

« Dans la dernière ligne droite, j'ai également pu compter sur le support technique précieux de plusieurs personnes, que je souhaite ici remercier »

Merci à Floriane et mon beau-père Jean-Marie pour leur relecture attentive de mon travail ; merci aussi à Tudor de m'avoir fourni les derniers résultats numériques qu'il me manquait pour conclure cette thèse.

« Avant de conclure, je voudrais évidemment remercier ma famille pour ses encouragements et sa présence à mes côtés tout au long du parcours »

A mes parents : merci pour votre amour et votre soutien inconditionnel depuis toujours.

A ma sœur : merci, Elise, d'être qui tu es, et d'apporter ton grain de « folie » à la famille.

A mon frère : merci, Gilles, d'être à mes côtés depuis ma naissance (+ 9 mois !). Je sais que je pourrai toujours compter sur toi. Bon courage pour ta fin de thèse !

A mon grand-père : merci pour ta simplicité et ta générosité naturelles. Tu es un exemple pour moi depuis mon plus jeune âge.

A ma belle-famille : merci pour votre soutien et vos encouragements.

« Enfin, on dit souvent que c'est dans les moments difficiles que l'on reconnait ses vrais supporters. Sophie, mes derniers mots te sont évidemment destinés, toi qui auras été ma plus fidèle supportrice tout au long de ce parcours. »

Merci pour ta patiente, ta compréhension, tes conseils et ton soutien inconditionnel, mais merci, surtout, pour les sacrifices que tu as consentis, au cours de l'année écoulée. Ta présence rassurante et bienveillante à mes côtés a constitué, sans aucun doute, le socle de ma réussite. Plus généralement, merci de partager ma vie et merci pour tout ce que tu m'apportes au quotidien. D'autres belles aventures nous attendent et je me réjouis de les vivre à tes côtés !

« Ça y est, je peux enfin le dire : I am a PhD finisher ! »

Adrien Corman, Octobre 2022

Abstract

Nowadays, modern building codes, such as the Eurocodes, require from the civil engineers to ensure an appropriate robustness to any structure. In steel and composite structures, this request for robustness mainly focuses on the joints between the members, which are seen as "weak" elements in the structure. To meet this request, it is recommended to provide sufficient ductility to the joints that would allow them to deform significantly without breaking in the case of an unforeseen exceptional event. However, the analytical method currently available in the part 1-8 of Eurocode 3 (EN 1993-1-8), i.e. the component method, does not allow to predict the rotation capacity of the joint under large deformations.

In this context, a large research project was launched at the University of Liège with the aim of extending the component method towards the large deformation field, and under complex loading conditions (impact, fire, explosion, earthquake…). The present thesis is the first outcome of this project and focuses on the behaviour of the panel zone (PZ), which is known to provide a significant reserve of ductility to the joint, when activated and appropriately designed. The main objective of the thesis thereby consists in providing a new sophisticated analytical model, which can predict the full non-linear behaviour of this component up to failure, under monotonic loading conditions.

To achieve this objective, an extensive literature review of existing scientific models was first conducted and set the theoretical background of the thesis. The performances of these models were assessed through comparisons with many experimental results carefully selected from the scientific literature. These comparisons revealed that none of them was able to accurately capture the complete non-linear behaviour of the PZ up to failure. Even for the prediction of the plastic resistance, all the investigated models also failed in providing consistent results. These observations validated the need to develop a more sophisticated constitutive model for the PZ.

The prediction of the plastic shear resistance was considered first, in the context of simple welded joints. The finite element (FE) approach was used to gain insight into the complex phenomena governing the PZ behaviour. This approach included the development and validation of a FE model and the use of this model to perform large parametric studies on various joint configurations. Based on the careful analysis of the FE results, the key geometric and mechanical parameters governing the resistance of the PZ could be identified and introduced in a new complex analytical model. After a validation step, this model proved to work well and to outperform existing analytical models.

Based on the knowledge acquired in the plastic field, the model could be further extended to the large deformation field. Again, the FE approach was used to identify the key parameters governing the deformability and the failure of the PZ. The resulting full-range model, encompassing those key parameters, was extensively validated against numerical and experimental results, where it proved to predict the PZ ultimate resistance and ultimate deformation capacity with reasonable accuracy.

The case of bolted joints was eventually tackled, considering the prediction of the plastic resistance first. Some adjustments in the new analytical expression as well as in the assembly procedure of the component method were suggested and validated through comparisons with experimental results. Secondly, the prediction of the deformation capacity was addressed, through preliminary comparisons with experimental results. From these comparisons, some limitations in the approach were highlighted and perspectives of improvement were discussed.

An additional outcome of the work consists of a set of new simplified design criteria for the prediction of the PZ initial stiffness, plastic resistance and deformation capacity. The first two expressions outperform the current EN 1993-1-8 criteria, which proved to be unsafe in many cases, while the third expression fills a gap in the EN 1993-1-8 norm where no criterion is currently available for the prediction of the PZ deformation capacity. This new set was proposed for integration in the forthcoming prEN 1993-1-8 pre-normative document.

Résumé

De nos jours, les normes de dimensionnement telles que l'Eurocode imposent aux ingénieurs de calcul de conférer une robustesse appropriée à toute structure. En construction métallique et mixte acier-béton, cette demande de robustesse se concentre principalement au niveau des assemblages entre les éléments structuraux, qui sont les éléments faibles de la structure. Pour rencontrer cette demande, il convient de conférer aux assemblages une ductilité suffisante qui leur permettrait de se déformer significativement sans casser en cas de chargement exceptionnel non-prévu. Cependant, la méthode disponible actuellement dans la partie 1-8 de l'Eurocode 3 (EN 1993-1-8), à savoir la méthode des composantes, ne permet pas de prédire la capacité de rotation des assemblages soumis à de grandes déformations.

Dans ce contexte, un projet de recherche a vu le jour à l'Université de Liège dans le but d'étendre la méthode des composantes vers le domaine des grandes déformations, sous chargement complexe (impact, incendie, explosion, séisme…). Cette thèse présente les premiers résultats de ce projet relatifs au comportement de la composante « zone de panneau » (PZ), qui confère en général une importante réserve de ductilité aux assemblages, lorsqu'elle est activée et conçue correctement. L'objectif principal de cette thèse vise donc à développer un nouveau modèle analytique sophistiqué, capable de prédire le comportement non-linéaire complet de cette composante jusqu'à la ruine, sous chargement statique.

Pour atteindre cet objectif, une revue de littérature des modèles existants a d'abord été menée et constitue le socle théorique de cette thèse. Les performances de ces modèles ont ensuite été évaluées au travers de comparaisons avec un très grand nombre de résultats expérimentaux, soigneusement sélectionnés dans la littérature scientifique. Ces comparaisons ont montré qu'aucun modèle n'était capable de capturer précisément le comportement de la PZ jusqu'à la ruine. Même pour la prédiction de la résistance plastique, tous les modèles investigués fournissent des résultats incohérents. Ces observations ont donc permis de valider le besoin de développer un nouveau modèle constitutif sophistiqué pour la PZ.

La résistance plastique de la PZ a d'abord été investiguée dans le cadre d'assemblages soudés. L'approche par éléments finis a été utilisée pour mieux comprendre les phénomènes complexes qui régissent le comportement de la PZ : un modèle aux éléments finis a été développé et validé, avant d'être utilisé pour effectuer un grand nombre d'études paramétriques sur diverses configurations d'assemblages. L'analyse minutieuse des résultats a permis d'identifier les principaux paramètres géométriques et mécaniques régissant la résistance de la PZ et de les introduire dans un nouveau modèle analytique complexe. Après une étape de validation, ce modèle s'est avéré efficace et plus performant que les modèles analytiques existants.

Sur la base de la connaissance acquise dans le domaine plastique, le modèle a pu être étendu au domaine des grandes déformations. Une fois encore, l'approche par éléments finis a été utilisée pour identifier les paramètres clés régissant la déformabilité et la ruine de la PZ. Le modèle constitutif complet résultant de cette étude a été largement validé sur des résultats numériques et expérimentaux, où il s'est avéré prédire correctement la résistance ultime et la capacité de déformation de la PZ.

Enfin, les modèles développés ont finalement été étendus au cas des assemblages boulonnés. Pour la prédiction de la résistance plastique, certains ajustements de la nouvelle formule analytique ainsi que de la procédure d'assemblage de la méthode des composants ont été proposés et validés au travers de comparaisons avec des résultats expérimentaux. Pour la prédiction de la capacité de déformation, les résultats préliminaires obtenus ont permis de mettre en évidence certaines limites de l'approche, et de proposer des pistes d'amélioration.

Dans le cadre de cette thèse, un ensemble de nouveaux critères de conception faciles à utiliser a également été proposé, pour la prédiction de la rigidité initiale, de la résistance plastique et de la capacité de déformation de la PZ. Les deux premières formules s'avèrent plus performantes que les critères actuels de la norme, insécuritaires dans de nombreux cas, tandis que la troisième formule comble une lacune de la norme actuelle où aucun critère n'est fourni pour prédire de la capacité de déformation de la PZ. Ce nouvel ensemble a été soumis au comité européen de normalisation pour être intégré dans la prochaine version de la norme EN 1993-1-8.

Table of content

Abbreviations

AIJ	:	Architectural Institute of Japan
AISC	:	American Institute of Steel Construction
BFC	:	Beam flange and web in compression
BT	:	Bolts in tension
BWT	:	Beam web in tension
CFB	:	Column flange in bending
CWC/CWC*	:	Column web in compression
CWP	:	Column web panel
CWS	:	Column web panel in shear
CWT	:	Column web in tension
ECCS	:	European Convention for Constructional Steelwork
EN 1990	:	Eurocode 0 - Basis of structural design
EN 1991-1-7	:	Eurocode 1 - Actions on structures - Part 1-7: General actions - Accidental actions
EN 1993-1-5	:	Eurocode 3: Design of steel structures - Part 1-5: Plated structural elements
EN 1993-1-8	:	Eurocode 3: Design of steel structures - Part 1-8: Design of joints
prEN 1993-1-8	:	Draft version of Eurocode 3: Design of steel structures - Part 1-8: Design of joints
EN 1993-1-14	:	Eurocode 3: Design of steel structures – Part 1-14: Design assisted by FE analysis
EPB	:	End-plate in bending
FE	:	Finite element
FCF	:	Flange contribution factor
GB_c	:	Global buckling of the column
HSS	:	High strength steel
LB_{BFC}	:	Local buckling of the BFC
LB_{CWC*}	:	Local buckling of the PZ
LB_{PZ}	:	Local buckling of the CWC*
MF	:	Fracture of the material
prEN 1993-1-8	:	Eurocode 3: Design of steel structures - Part 1-8: Design of joints
PZ	:	Panel zone
SE	:	Surrounding elements
WP	:	Work package

List of symbols

Lowercase Latin letters

a and b	: Parameters accounting for the type of joint configuration in the derivation of the β transformation parameter
b_b (resp. b_c)	: Width of the beam (resp. column) profile
d_b (resp. d_c)	: Clear depth of the beam (resp. column) profile
d_b^* (resp. d_c^*)	: Equivalent lever arm of the beam (resp. column) profile (= width (resp. depth) of the PZ)
f_y	: Yield strength of the steel material
$f_{y,fb}$ (resp. $f_{y,fc}$)	: Yield strength of the beam (resp. column) flanges
$f_{y,wb}$ (resp. $f_{y,wc}$)	: Yield strength of the beam (resp. column) web
f_u	: Ultimate strength of the steel material
$f_{u,fb}$ (resp. $f_{u,fc}$)	: Ultimate strength of the beam (resp. column) flanges
$f_{u,wb}$ (resp. $f_{u,wc}$)	: Ultimate strength of the beam (resp. column) web
h_b (resp. h_c)	: Height of the beam (resp. column) profile
h_{ic}	: Height of a built-up section
h_r	: Distance between the compression centre and the rth bolt-row in tension
k^c	: Axial stiffness of the "c" component
k_{ini}^c	: Initial axial stiffness of the "c" component associated to the bolt-row in compression (c = BFC, CWC, CWS, PZ)
$k_{ini,r}^c$	: Initial axial stiffness of the "c" component associated to the rth bolt-row in tension (c = CWT, CFB, EPB, BT, BWT)
$k_{ini,eq}^C$ (resp. $k_{ini,eq}^T$)	: Initial axial stiffness associated to the bolt-row in compression (resp. the equivalent bolt-row in tension)
$k_{ini,eff,r}^T$	: Initial axial stiffness associated to the rth bolt-row in tension
k_{pp}^c	: Strain-hardening (i.e. post-plastic) axial stiffness of the "c" component
k_τ	: Buckling coefficient related to the CWP
$k_{\tau,clamped}$ (resp. $k_{\tau,pinned}$)	: Buckling coefficient related to the CWP, assuming that the CWP is fully clamped (resp. simply supported)
m_c (resp. m_c')	: Level of bending moment in the column profile at yielding (resp. at ultimate)
n_c (resp. n_c')	: Level of axial load in the column profile at yielding (resp. at ultimate)
n_{fb} (resp. n_{fb}^*)	: Level of axial load in a rectangular beam flange at yielding, accounting for the contributions of N and M in the column (resp. accounting for the contribution of N only)
$n_{fb,T}$ (resp. $n_{fb,T}^*$)	: Level of axial load in a T-shaped beam flange at yielding, accounting for the contributions of N and M in the beam (resp. accounting for the contribution of

N only)

n_{fc} (resp. n_{fc}^*)   : Level of axial load in a rectangular column flange at yielding, accounting for the contributions of N and M in the column (resp. accounting for the contribution of N only)

$n_{fc,T}$ (resp. $n_{fc,T}^*$)   : Level of axial load in a T-shaped column flange at yielding, accounting for the contributions of N and M in the column (resp. accounting for the contribution of N only)

$\overline{n_{fc,T}}$: Average level of axial load in the T-shaped column flanges at yielding, accounting for the contributions of N and M in the column

n_{st} (resp. n_{st}^*)   : Level of axial load in a rectangular stiffener at yielding, accounting for the contributions of N and M in the beam (resp. accounting for the contribution of N only)

r : Weighted factor in the derivation of the buckling coefficient k_τ

r_b (resp. r_c)   : Radius of root fillet of the beam (resp. column) profile

t_{fb} (resp. t_{fc})   : Thickness of the beam (resp. column) flanges

t_{st} : Thickness of the stiffener

t_{wb} (resp. t_{wc})   : Thickness of the beam (resp. column) web

$\bar{u}_i^{pl}$: Equivalent plastic displacement

y_{CG} : Location of the centre of gravity of $A_{VC,2}^{compl}$

z_{eq} : Equivalent lever arm between the tension and compression centres

Uppercase Latin letters

A_b (resp. A_c)	: Cross-sectional area of the beam (resp. column) profile
A_{fc} (resp. $A_{fc,T}$)	: Cross-sectional area of a rectangular (resp. T-shaped) column flange
A_{VC}	: Effective shear area of the column profile
A_{VC}^{compl} (resp. A_{VC}^{simpl})	: Effective shear area of the column profile in the new complex (resp. simplified) model
$A_{VC,1}^{compl}$ (resp. $A_{VC,1}^{simpl}$)	: First part of the effective shear area of the column profile in the new complex (resp. simplified) model
$A_{VC,2}^{compl}$ (resp. $A_{VC,2}^{simpl}$)	: Second part of the effective shear area of the column profile in the new complex (resp. simplified) model
$A_{VC,fc}$ (resp. $A_{VC,fc,T}$)	: Effective shear area of a rectangular (resp. T-shaped) column flange
C_y^{CWP} (resp. C_u^{CWP})	: Reduction coefficient accounting for the non-uniform distribution of the shear stresses in the CWP at yielding (resp. at ultimate)
ΔC_y^{CWP}	: Post-plastic coefficient accounting for the initiation of strain-hardening in the CWP
C_y^{SE}	: Reduction coefficient accounting for the non-uniform distribution of the shear stresses in the SE at yielding
ΔC_y^{SE}	: Post-plastic coefficient accounting for the initiation of strain-hardening in the SE
C_r	: Constant accounting for the degree restraint of the equivalent beam at the centre of the CWP
C_s	: Constant to be determined (in the Krawinkler, Engelhardt and Schneider models)
C_1	: Material coefficient in the EN 1993-1-14 material model
D (or D_i)	: Damage variable
D_{cr}	: Critical damage variable
$(\Delta)E$	: (Increment of the) Young's modulus of the steel material
$(\Delta)E_{pp}$	: (Increment of the) strain-hardening (i.e. post-plastic) modulus of the steel material
F_{BL} (resp. F_{BR})	: Load-introduction force, coming from the <u>L</u>eft <u>B</u>eam (resp. the <u>R</u>ight <u>B</u>eam)
F^c	: Axial force applied to the "c" component
$F_{el,Rk}^c$ (resp. $F_{y,Rk}^c$)	: Elastic (resp. plastic) resistance of the "c" component associated to the bolt-row in compression (c = BFC, CWC, CWS, PZ)
$F_{el,Rk,r}^c$ (resp. $F_{y,Rk,r}^c$)	: Elastic (resp. plastic) resistance of the "c" component associated to the rth bolt-row in tension (c = CWT, CFB, EPB, BT, BWT)
$F_{u,Rk}^c$	: Ultimate resistance of the "c" component (c = BFC, CWC, CWS, PZ, CWT, CFB, EPB, BT, BWT)

$F_{y,Rk,r}$	: Plastic resistance of the rth bolt-row in tension
$F_{y,Rk,C}$	: Plastic resistance of the bolt-row in compression
G	: Shear modulus of the steel material
G_{pp}	: Strain-hardening (i.e. post-plastic) shear modulus of the steel material
I_c	: Second moment of area of the column profile
I_{fb} (resp. $I_{fb,T}$)	: Second moment of area of a rectangular (resp. T-shaped) beam flange
I_{fc} (resp. $I_{fc,T}$)	: Second moment of area of a rectangular (resp. T-shaped) column flange
I_{st}	: Second moment of area of a rectangular stiffener
K^c	: Axial stiffness of the "c" component
K^c_{ini}	: Initial axial stiffness of the "c" component
K^c_{pp}	: Strain-hardening (i.e. post-plastic) axial stiffness of the "c" component
K^{CWP}	: Shear stiffness of the CWP
$(\Delta)K^{CWP}_y$	: (Increment of the) elastic shear stiffness of the CWP
$K^{CWP}_{y,b}$ (resp. $K^{CWP}_{y,sh}$)	: Elastic shear stiffness of the CWP associated to the bending (resp. shear) deformation mode
$\Delta K^{CWP}_{y,mod}$	: Modified increment of the elastic shear stiffness of the CWP
$K^{CWP}_{y,2}$	: Post-elastic shear stiffness of the CWP (Engelhardt model)
$K^{CWP}_{y,b,2}$ (resp. $K^{CWP}_{y,sh,2}$)	: Post-elastic shear stiffness of the CWP associated to the bending (resp. shear) deformation mode (Engelhardt model)
$(\Delta)K^{CWP}_{pp}$	: (Increment of the) strain-hardening (i.e. post-plastic) shear stiffness of the CWP
K^{SE}	: Shear stiffness of the SE
K^{SE}_y	: Elastic shear stiffness of the SE
$K^{SE}_{y,b}$ (resp. $K^{SE}_{y,sh}$)	: Elastic shear stiffness of the SE associated to the bending (resp. shear) deformation mode
K^{SE}_{pp}	: Strain-hardening (i.e. post-plastic) shear stiffness of the SE
K^{PZ}	: Shear stiffness of the PZ
K^{PZ}_y	: Elastic shear stiffness of the PZ
$K^{PZ}_{y,exp}$	: Elastic shear stiffness of the PZ extracted from the $\left(M^j - \gamma\right)_{exp}$ experimental curve
$K^{PZ}_{y,simpl}$	: Elastic shear stiffness of the PZ computed with the simplified model
K_s	: Rotational stiffness of a rotational spring

L_b (resp. L_c)	: Length of the beam (resp. column)
L_E	: Characteristic length of the FE
$L_{h,fb,T}$ (resp. $L_{h,fc,T}$)	: Equivalent length of a plastic hinge forming in a T-shaped beam (resp. column) flange
$L_{h,st}$	: Equivalent length of a plastic hinge forming in a rectangular stiffener
M^c	: Bending moment applied to the joint, assuming that the "c" component is the governing component
$M^c_{y,Rk}$	: Plastic bending moment resistance of the joint, assuming that the "c" component is the governing component
$M^j_{(Ek)}$ (or M_B)	: Bending moment applied to the joint
$M^j_{el,Rk}$ (resp. $M^j_{y,Rk}$)	: Elastic (resp. plastic) bending moment resistance of the joint
$M^j_{y,Rk,exp}$	: Plastic bending moment resistance of the joint extracted from the $\left(M^j - \Phi\right)_{exp}$ experimental curve
$M^j_{y,Rk,compl}$ (resp. $M^j_{y,Rk,simpl}$)	: Plastic bending moment resistance of the joint computed with the new complex (resp. simplified) analytical model for the PZ component
$M^j_{y,Rk,EU}$ (resp. $M^j_{y,Rk,US}$)	: Plastic bending moment resistance of the joint computed with the EU (resp. US) model for the PZ component
M^j_{y,Rk,EU^*}	: Plastic bending moment resistance of the joint computed with the new proposed EU* model for the PZ component
$M^j_{u,Rk}$	: Ultimate bending moment resistance of the joint
$M^j_{u,Rk,exp}$ (resp. $M^j_{u,Rk,num}$)	: Ultimate bending moment resistance of the joint extracted from the $\left(M^j - \Phi\right)_{exp}$ experimental curve (resp. from the $\left(M^j - \Phi\right)_{num}$ numerical curve)
$M^{PZ}_{y,Rk}$	: Plastic bending moment resistance of the joint, assuming that the PZ is the governing component
M_{BL} (resp. M_{BR})	: Bending moment applied to the left (resp. right) side of the PZ, coming from the <u>L</u>eft <u>B</u>eam (resp. <u>R</u>ight <u>B</u>eam)
M_{CB} (resp. M_{CT})	: Bending moment applied to the bottom (resp. top) side of the PZ, coming from the <u>B</u>ottom of the <u>C</u>olumn (<u>T</u>op of the <u>C</u>olumn)
M_C	: Bending moment applied to the top side of the PZ
$M_{pl,c,(Rk)}$ (resp. $M_{u,c,(Rk)}$)	: Plastic (resp. ultimate) bending moment resistance of the column cross-section
$M_{pl,ep,(Rk)}$	: Plastic bending moment resistance of a rectangular endplate
$M_{pl,fc,(Rk)}$ (resp. $M_{pl,fc,T,(Rk)}$)	: Plastic bending moment resistance of a rectangular (resp. T-shaped) column flange, accounting for the M-N interaction
$\widehat{M}_{pl,fc,(Rk)}$ (resp. $\widehat{M}_{pl,fc,T,(Rk)}$)	: Characteristic plastic bending moment resistance of a rectangular (resp. T-shaped) column flange

$M_{pl,fb,(Rk)}$ (resp. $M_{pl,fb,T,(Rk)}$)	: Plastic bending moment resistance of a rectangular (resp. T-shaped) beam flange, accounting for the M-N interaction
$\widehat{M}_{pl,fb,(Rk)}$ (resp. $\widehat{M}_{pl,fb,T,(Rk)}$)	: Characteristic plastic bending moment resistance of a rectangular (resp. T-shaped) beam flange
$M_{pl,st,(Rk)}$	: Plastic bending moment resistance of a rectangular stiffener, accounting for the M-N interaction
$\widehat{M}_{pl,st,(Rk)}$	: Characteristic plastic bending moment resistance of a rectangular stiffener
N_B (or N_b)	: Axial force in the beam
N_{BL} (resp. N_{BR})	: Axial force applied to the left (resp. right) side of the PZ, coming from the <u>L</u>eft <u>B</u>eam (resp. <u>R</u>ight <u>B</u>eam)
N_C (or N_c)	: Axial force applied to the top side of the PZ
N_{CB} (resp. N_{CT})	: Axial force applied to the bottom (resp. top) side of the PZ, coming from the <u>B</u>ottom of the <u>C</u>olumn (resp. <u>T</u>op of the <u>C</u>olumn)
$N_{fc,Ek}^{(i)}$ (resp. $N_{fc,Ek}^{*}$)	: Vertical axial load in a column flange, computed at the ith corner of the PZ, accounting for the contributions of N and M in the column (resp. accounting for the contribution of N only)
$\overline{N_{fc,Ek}}$	: Average vertical axial load acting in the column flanges (accounting for the contributions of N and M in the column)
$N_{fb,Ek}$ (resp. $N_{fb,Ek}^{*}$)	: Horizontal axial load in a beam flange, accounting for the contributions of N and M in the beam (resp. accounting for the contribution of N only)
$N_{st,Ek}$ (resp. $N_{st,Ek}^{*}$)	: Horizontal axial load in a stiffener, accounting for the contributions of N and M in the beam (resp. accounting for the contribution of N only)
$N_{pl,c}$ (resp. $N_{u,c}$)	: Plastic (resp. ultimate) resistance of the column cross-section
$N_{pl,fc,(Rk)}$ (resp. $N_{pl,fc,T,(Rk)}$)	: Plastic resistance of a rectangular (resp. T-shaped) column flange
P	: Vertical load applied to the beam tip
R	: Horizontal reaction at the supports of the column
S^c	: Rotational stiffness of the joint assuming that the "c" component is the governing component
S_{ini}^{j}	: Initial rotational stiffness of the joint
$S_{ini,exp}^{j}$	: Initial rotational stiffness of the joint extracted from the $\left(M^j - \Phi\right)_{exp}$ experimental curve
$S_{ini,compl}^{j}$ (resp. $S_{ini,simpl}^{j}$)	: Initial rotational stiffness of the joint, computed using the new complex (resp. simplified) model for the PZ component
S_{pp}^{j}	: Strain-hardening (i.e. post-plastic) rotational stiffness of the joint
$S_{pp,exp}^{j}$	: Strain-hardening (i.e. post-plastic) rotational stiffness of the joint extracted from the $\left(M^j - \Phi\right)_{exp}$ experimental curve

V_{BL} (resp. V_{BR})	: Shear force applied to the left (resp. right) side of the PZ, coming from the <u>L</u>eft <u>B</u>eam (resp. <u>R</u>ight <u>B</u>eam)
V_{CB} (resp. V_{CT})	: Shear force applied to the bottom (resp. top) side of the PZ, coming from the <u>B</u>ottom of the <u>C</u>olumn (resp. <u>T</u>op of the <u>C</u>olumn)
$V_{(Ek)}^{CWP}$	: Equivalent shear force acting on the CWP
$(\Delta)V_{y,(CWP),Rk}^{CWP}$	: (Increment of the) plastic shear resistance of the CWP
$V_{y,Rk,num}^{CWP}$	: Plastic shear resistance of the CWP extracted from the $(V^{CWP} - \gamma^{CWP})_{num}$ numerical curve
$V_{y,Rk,compl}^{CWP(V1)}$ (resp. $V_{y,Rk,compl}^{CWP(V2)}$)	: Plastic shear resistance of the CWP computed with the 1ˢᵗ (resp. 2ⁿᵈ) version of the new complex model
$\hat{V}_{y,Rk,compl}^{CWP}$	: Plastic shear resistance of the CWP computed with the 2ⁿᵈ version of the new complex model, assuming no stress interaction
$V_{y,Rk,simpl}^{CWP}$ (resp. $\hat{V}_{y,Rk,simpl}^{CWP}$)	: Plastic shear resistance of the CWP computed with the new simplified model, accounting for the stress interaction (resp. assuming no stress interaction)
$V_{y,Rk,EU}^{CWP}$ (resp. $V_{y,Rk,US}^{CWP}$)	: Plastic shear resistance of the CWP computed with the EU (resp. US) model
V_{y,Rk,EU^*}^{CWP}	: Plastic shear resistance of the CWP computed with the new proposed EU* model
$V_{pp,(Rk)}^{CWP}$ (or $V_{y,PZ,(Rk)}^{CWP}$)	: Post-plastic shear resistance of the CWP
$V_{pp,Rk,compl}^{CWP}$	: Post-plastic shear resistance of the CWP computed with the new complex model
$(\Delta)V_{u,(PZ),Rk}^{CWP}$	: (Increment of the) ultimate shear resistance of the CWP
$V_{u,Rk,compl}^{CWP}$	: Ultimate shear resistance of the CWP computed with the new complex model
V_n^{CWP}	: Shear resistance of the CWP at necking
$V_{n,Rk,compl}^{CWP}$	: Shear resistance of the CWP at necking computed with the new complex model
$V_{f,Rk,compl}^{CWP}$	: Final shear resistance of the CWP computed with the new complex model
$\Delta V_{(Ek)}^{SE}$	: Equivalent shear force acting on the SE
$\Delta V_{y,CWP,(Rk)}^{SE}$	: Shear resistance of the SE at yielding of the CWP
$\Delta V_{y,(PZ),Rk}^{SE}$	: Plastic shear resistance of the SE at yielding of the whole PZ
$\Delta V_{y,Rk,num}^{SE}$	: Plastic shear resistance of the SE extracted from the $(\Delta V^{SE} - \gamma^{SE})_{num}$ numerical curve
$\Delta V_{y,Rk,compl}^{SE(V1)}$ (resp. $\Delta V_{y,Rk,compl}^{SE(V2)}$)	: Plastic shear resistance of the SE computed with the 1ˢᵗ (resp. 2ⁿᵈ) version of the new complex model

$\Delta V_{y,Rk,simpl}^{SE}$: Plastic shear resistance of the SE computed with the new simplified model

$\Delta V_{y,Rk,EU}^{SE}$ (resp. $\Delta V_{y,Rk,US}^{SE}$)   : Plastic shear resistance of the SE computed with the EU (resp. US) model

$\Delta V_{y,Rk,EU^*}^{SE}$: Plastic shear resistance of the SE computed with the new proposed EU* model

$\Delta V_{u,PZ,(Rk)}^{SE}$: Shear resistance of the SE at the ultimate shear deformation of the PZ

ΔV_n^{SE} : Shear resistance of the SE at necking

$\Delta V_{n,Rk,compl}^{SE}$: Plastic shear resistance of the SE at necking computed with the new complex model

$\Delta V_{f,Rk,compl}^{SE}$: Final shear resistance of the SE computed with the new complex model

$V_{(Ek)}^{PZ}$: Equivalent shear force acting on the PZ

$V_{y,CWP,(Rk)}^{PZ}$: Shear resistance of the PZ at yielding of the CWP

$V_{y,PZ,(Rk)}^{PZ}$ (or $V_{y,Rk}^{PZ}$)   : Plastic shear resistance of the PZ

$V_{y,Rk,exp}^{PZ}$ (resp. $V_{y,Rk,num}^{PZ}$)   : Plastic shear resistance of the PZ extracted from the $(V^{PZ} - \gamma^{PZ})_{exp}$ experimental curve (resp. the $(V^{PZ} - \gamma^{PZ})_{num}$ numerical curve)

$V_{y,Rk,compl}^{PZ}$ (resp. $V_{y,Rk,simpl}^{PZ}$)   : Plastic shear resistance of the PZ computed with the new complex (resp. simplified) model

$V_{y,Rk,EU}^{PZ}$ (resp. $V_{y,Rk,US}^{PZ}$)   : Plastic shear resistance of the PZ computed with the EU (resp. US) model

V_{y,Rk,EU^*}^{PZ} : Plastic shear resistance of the PZ computed with the new proposed EU* model

$V_{u,PZ,(Rk)}^{PZ}$ (or $V_{u,Rk}^{PZ}$)   : Ultimate shear resistance of the PZ

$V_{f,Rk,compl}^{PZ}$: Final shear resistance of the PZ computed with the new complex model

W : Weighting factor

Lowercase Greek letters

α	: Span-depth ratio of the column flange flexural member
$\beta_{(R)}$	: Transformation parameter of the (right exterior) joint
$\gamma^{(PZ)}$	: Shear deformation of the PZ
$\gamma_{el,b}^{CWP}$ (resp. $\gamma_{el,sh}^{CWP}$)	: Elastic shear deformation of the CWP associated to the bending (resp. shear) deformation mode
$\gamma_{el,tot}^{CWP}$	: Elastic shear deformation of the CWP associated to the bending and shear deformation modes
$\gamma_{el,b,2}^{CWP}$ (resp. $\gamma_{el,sh,2}^{CWP}$)	: Post-elastic shear deformation of the CWP associated to the bending (resp. shear) deformation mode (Engelhardt model)
$\gamma_{el,tot,2}^{CWP}$	: Post-elastic shear deformation of the CWP associated to the bending and shear deformation modes (Engelhardt model)
γ_y^{CWP}	: Yield shear deformation of the CWP
$\Delta\gamma_y^{CWP}$ (resp. $\Delta\gamma_{y,mod}^{CWP}$)	: (resp. Modified) increment of the yield shear deformation of the CWP
γ_{pp}^{CWP}	: Strain-hardening (i.e. post-plastic) shear deformation of the CWP
γ_u^{CWP} (resp. γ_u^{CWP})	: (resp. Modified) ultimate shear deformation of the CWP
$\Delta\gamma_u^{CWP}$ (resp. $\Delta\gamma_{u,mod}^{CWP}$)	: (resp. Modified) increment of the ultimate shear deformation of the CWP
γ_n^{CWP} (resp. $\gamma_{n,mod}^{CWP}$)	: (resp. Modified) yield shear deformation at necking of the CWP
γ_f^{CWP}	: Final shear deformation of the CWP
$\gamma_{el,b}^{SE}$ (resp. $\gamma_{el,sh}^{SE}$)	: Elastic shear deformation of the SE associated to the bending (resp. shear) deformation mode
$\gamma_{el,tot}^{SE}$	: Elastic shear deformation of the SE associated to the bending and shear deformation modes
γ_y^{SE} (resp. $\gamma_{y,mod}^{SE}$)	: (resp. Modified) yield shear deformation of the SE
γ_n^{SE} (resp. $\gamma_{n,mod}^{SE}$)	: (resp. Modified) shear deformation of the SE at necking
γ_f^{SE}	: Final shear deformation of the SE
γ_y^{PZ}	: Yield shear deformation of the PZ
γ_u^{PZ}	: Ultimate shear deformation of the PZ
$\gamma_{u,exp}^{PZ}$	: Ultimate shear deformation of the PZ extracted from the $\left(M^j - \Phi\right)_{exp}$ experimental curve
$\gamma_{f,compl}^{PZ}$ (resp. $\gamma_{f,simpl}^{PZ}$)	: Final shear deformation of the PZ computed with the new complex (resp. simplified) model
$\gamma_{f,exp}^{PZ}$	: Final shear deformation of the PZ extracted from the $\left(V^{PZ} - \gamma^{PZ}\right)_{num}$ numerical curve
ε	: Factor accounting for the effect of steel grade on the risk of shear buckling

of the PZ

ε_y (resp. ε_y^{eng})	: Yield strain of the steel material coming from the material true (resp. engineering) stress-strain curve
ε_{pp} (resp. ε_{pp}^{eng})	: Post-plastic strain of the steel material coming from the material true (resp. engineering) stress-strain curve
ε_u (resp. ε_u^{eng})	: Ultimate strain of the steel material coming from the material true (resp. engineering) stress-strain curve
ε_n (resp. ε_n^{eng})	: Strain of the steel material at the onset of necking, coming from the material true (resp. engineering) stress-strain curve
ε_r (resp. ε_r^{eng})	: Strain of the steel material at the onset of rupture, coming from the material true (resp. engineering) stress-strain curve
ε_f (resp. ε_f^{eng})	: Strain of the steel material at the onset of fracture, coming from the material true (engineering) stress-strain curve
$\Delta\varepsilon_y$ (resp. $\Delta\varepsilon_u$)	: Yield (resp. ultimate) strain increment
ε_n^{pl}	: Plastic strain of the steel material at the onset of necking, coming from the material true stress-strain curve
$\bar{\varepsilon}_0^{pl}$	: Equivalent plastic strain at the onset of necking
η :	: - Factor accounting for steel grades higher than S460 in the formula assessing the risk of shear buckling of the PZ - Stiffness modification factor in the new complex analytical model for the PZ
$\overline{\lambda_w}$	: Slenderness factor of the CWP
ν	: Poisson's ratio
ρ_y	: Reduction factor accounting for the possible shear buckling in the elastic range
$\rho_{pp}{}'$	: Reduction factor accounting for the possible shear buckling in the plastic range
$\rho_u{}'$	: Reduction factor accounting for the possible shear buckling in the post-plastic range
$\rho_n{}'$	: Reduction factor accounting for the possible shear buckling in the flowed range
σ_E	: Euler critical stress of the CWP
σ_i	: Horizontal normal stresses acting in the PZ, coming from the load-introduction forces
$\sigma_{n,(N)}$	: Vertical normal stresses acting in the PZ, coming from the axial load in the column
$\sigma_{n,M}$	: Vertical normal stresses acting in the PZ, coming from the bending moment in the column
$\sigma_{n,M-N}^{(i)}$	: Vertical normal stresses acting in the (i^{th} corner of the) PZ, coming from the axial load and the bending moment in the column

$\overline{\sigma_{n,M-N}}$	:	Average vertical normal stresses acting in the column flanges
$\Delta\sigma_y$ (resp. $\Delta\sigma_u$)	:	Yield (resp. ultimate) strength increment
σ_y (resp. σ_y^{eng})	:	Yield strength of the steel material coming from the material true (resp. engineering) stress-strain curve
σ_{pp} (resp. σ_{pp}^{eng})	:	Post-plastic strength of the steel material coming from the material true (resp. engineering) stress-strain curve
σ_u (resp. σ_u^{eng})	:	Ultimate strength of the steel material coming from the material true (resp. engineering) stress-strain curve
σ_n (resp. σ_n^{eng})	:	Strength of the steel material at the onset of necking, coming from the material true (resp. engineering) stress-strain curve
σ_{VM}	:	von Mises stresses
τ	:	Shear stresses acting in the PZ, coming from the equivalent shear force V_{Ek}^{PZ}
τ_{cr}	:	Shear critical strength of the CWP
τ_y (resp. τ_u)	:	Yield (resp. ultimate) shear strength of the steel material
τ_y^*	:	Yield shear strength of the material, computed at the onset of the root fillets in the column profile, and accounting for the $\tau - \sigma_{n,M-N}$ stress interaction
$\tau_{y,CG}^*$	:	Yield shear strength of the material, computed at the centre of gravity of $A_{VC,2}^{compl}$ in the column profile, and accounting for the $\tau - \sigma_{n,M-N}$ stress interaction
ϕ	:	Rotation of the connection
ϕ^c	:	Rotation of the "c" component
χ_i	:	Reduction factor accounting for the $\tau - \sigma_i$ stress interaction in the CWP
$\chi_{n,(N)}$ (resp. χ_n')	:	Reduction factor accounting for the $\tau - \sigma_n$ stress interaction in the CWP at yielding (resp. at ultimate)
$\chi_{n,M-N}$	:	Reduction factor accounting for the $\tau - \sigma_{n,M-N}$ stress interaction in the CWP at yielding
$\Delta\chi_{n,(N)}$	:	Reduction factor accounting for the $\tau - \sigma_n$ stress interaction in the SE
$\Delta\chi_{n,M-N}$	:	Reduction factor accounting for the $\tau - \sigma_{n,M-N}$ stress interaction in the SE

Uppercase Greek letters

Δ^c : Displacement (elongation or shortening) of the "c" component

Δ^c_{el} : Elastic displacement (elongation or shortening) of the "c" component

$\Delta^{CWP}_{el,b}$ (resp. $\Delta^{CWP}_{el,sh}$) : Elastic deformation of the CWP associated to the bending (resp. shear) deformation mode

$\Delta^{CWP}_{el,tot}$: Elastic deformation of the CWP associated to the bending and shear deformation modes

$\Delta^{CWP}_{el,b,2}$ (resp. $\Delta^{CWP}_{el,sh,2}$) : Post-elastic deformation of the CWP associated to the bending (resp. shear) deformation mode (Engelhardt model)

$\Delta^{CWP}_{el,tot,2}$: Post-elastic deformation of the CWP associated to the bending and shear deformation modes (Engelhardt model)

$\Delta^{SE}_{el,b}$ (resp. $\Delta^{SE}_{el,sh}$) : Elastic deformation of the SE associated to the bending (resp. shear) deformation mode

$\Delta^{SE}_{el,tot}$: Elastic deformation of the SE associated to the bending and shear deformation modes

Δ^c_{pl} (resp. Δ^c_u)   : Plastic (resp. ultimate) displacement (elongation or shortening) of the "c" component

Φ : Rotation of the joint

Φ_{el} : Elastic rotation of the joint

Φ_{pl} (resp. Φ_u)   : Plastic (resp. ultimate) rotation of the joint

$\Phi_{u,exp}$ (resp. $\Phi_{u,num}$)   : Ultimate rotation of the joint extracted from the $\left(M^j - \Phi\right)_{exp}$ experimental curve (resp. from the $\left(M^j - \Phi\right)_{num}$ numerical curve)

Ψ : Flange contribution factor

CHAPTER 1
Introduction

1.1 CONTEXT OF THE RESEARCH

1.1.1 Classical design approach for semi-rigid joints

In steel and steel-concrete composite frame structures, the joints are recognized as key elements which connect together the structural members (i.e. beams and columns) and transfer the internal forces (i.e. shear forces V, axial forces N and bending moments M) between them. Traditionally, they were considered as either fully rigid or pinned elements in the structural analysis; now it is widely accepted that most structural joints exhibit an actual semi-rigid behaviour. Accounting for this semi-rigidity implies a more complex structural analysis in which the joint behaviour influences not only the displacements but also the distribution and magnitude of the internal forces throughout the structure; the payback being the design of more economical structures.

Given the significant influence of the joints on the overall structural response, the accurate prediction of their behaviour remains an important task in order to achieve a safe and economic design of the structure. This behaviour is known to be highly non-linear and can be represented by a $\left(M^j - \Phi\right)$ moment-rotation curve, where M^j is the applied bending moment and Φ is the corresponding rotation between the members. When it comes to the prediction of this $\left(M^j - \Phi\right)$ curve, the reference normative document in Europe (but also in many other countries worldwide) is the Part 1-8 of Eurocode 3 (i.e. EN 1993-1-8, [1]) which recommends the use of a four-step procedure, namely:

1. The characterization of the main structural properties of the joint, namely the initial stiffness, the plastic resistance and the rotation capacity;
2. The classification of the joint, based on the so-obtained structural properties;
3. The modelling of the joint in view of its integration in the structural analysis;
4. The idealization of the joint behaviour, based on the analysis-verification process which has been selected.

This four-step procedure is schematically illustrated in Fig. 1-1 for the particular case of an exterior bolted joint with an extended end-plate connection. This joint has been extracted from a simple frame structure subjected to classical vertical and horizontal design loads.

The first step of the procedure consists in the characterization of the joint rotational response. To this aim, EN 1993-1-8 uses an analytical approach which is based on the component method. This method considers any joint as a set of individual basic components which have their own mechanical properties (i.e. stiffness, strength and ductility) either in tension, compression or shear, and which contribute to the overall resistance and stiffness characteristics of the joint. Practically speaking, the application of the component method follows a three-step procedure, as depicted in Fig. 1-1, namely: (i) identification of the active components in the joint being studied, (ii) characterization of each individual basic component in terms of its stiffness and resistance properties and (iii) assembly of all the active components through an hybrid analytical-mechanical approach in order to derive the stiffness and/or resistance characteristics of the whole joint. Currently, EN 1993-1-8 provides a large database of individual basic components for which analytical expressions are available to estimate the strength and stiffness under static loading conditions. The combination of these individual basic components allows covering a wide range of joint typologies.

The second step consists in the joint classification. Three classification criteria can be contemplated based on the so-obtained mechanical properties of the joint (i.e. rotational stiffness, flexural resistance and rotation capacity), as reported in Fig. 1-1. Based on the rotational stiffness, the joint can be

classified as: (i) nominally pinned, (ii) semi-rigid or (iii) fully-rigid. When referring to the strength of the joint, the latter can be classified as: (i) pinned, (ii) partial-strength or (iii) full-strength. Finally, the third classification criterion, based on the rotational capacity, also identifies three joint categories, namely: (i) ductile, (ii) semi-ductile and (iii) brittle. Practically speaking, EN 1993-1-8 defines stiffness and strength boundaries for the two first criteria, while it prescribes qualitative recommendations for the third one, which should ensure sufficient ductility to the joint.

Following the classification step, the joint can be modelled in view of its integration within the structural analysis. EN 1993-1-8 offers three main modelling approaches, namely: (i) the simple approach covering the case of pinned joints, (ii) the continuous approach covering the case of rigid/full-strength joints and (iii) the semi-continuous approach covering the intermediate cases, i.e. the rigid/partial-strength, semi-rigid/full-strength and semi-rigid/partial-strength cases; the most relevant approach to consider being function of the type of frame analysis performed by the designer, i.e. elastic, rigid-plastic or elasto-plastic analysis.

Finally, EN 1993-1-8 offers different possibilities for the idealization of the real non-linear $\left(M^j - \Phi\right)$ curve of the joint, namely: (i) the elastic, (ii) rigid-plastic, (iii) bilinear, (iv) trilinear and (v) non-linear representations. These different levels of idealization can all be used in the frame analysis without significant loss of accuracy, the most suitable level to consider depending again on the type of structural analysis performed by the designer.

The structural analysis can eventually be performed, accounting for the so-idealized joint behaviour. It should be reminded that the procedure described in the present Section 1.1.1 is valid under monotonic loading conditions only.

1.1.2 Limitation: robustness requirements

When a structure is exposed to an exceptional event, i.e. an event that is not explicitly accounted for in the design process due to its low probability of occurrence, Eurocode 0 (i.e. EN 1990, [2]) requests "*that the structure is not damaged to an extent disproportionate to the original cause, whether it is an explosion, an impact, a fire, or the consequences of human errors*". To this aim, the Part 1-7 of Eurocode 1 (i.e. EN 1991-1-7, [3]) provides some general guidelines and recommendations to achieve an appropriate structural robustness.

At the level of the joints, the main purpose of these recommendations is to ensure that they exhibit a sufficient reserve of ductility that would allow them to deform significantly without breaking, in the case of an unforeseen exceptional event. Indeed, the joints are often seen as "weak" elements in the structure: any premature failure in a brittle component (bolts, welds) could cause the separation of the connected members, leading to the risk of local or global progressive collapse of the structure. Therefore, in order to meet the robustness requirements, it is necessary to master and predict the complete behaviour of the joints under complex loading conditions, but the current procedure prescribed in EN 1993-1-8 (see previous Section 1.1.1 and Fig. 1-1) does not allow to do so.

A review of the scientific literature reveals that the capability of the component method to be extended to more complex loading conditions, either at room temperature [4] or under fire [5], dynamic [6] or cyclic ([7], [8]) loadings, has already been demonstrated through theoretical, experimental, and numerical approaches. The results have not been transposed yet within the normative document though. By contrast, the prediction of the joint ductility has gained interest only recently among the scientific community ([9]–[20]) and still requires substantial research efforts. This gap in knowledge stimulated the launching of a comprehensive research program at the University of Liège, which is briefly presented in the following Section 1.2.
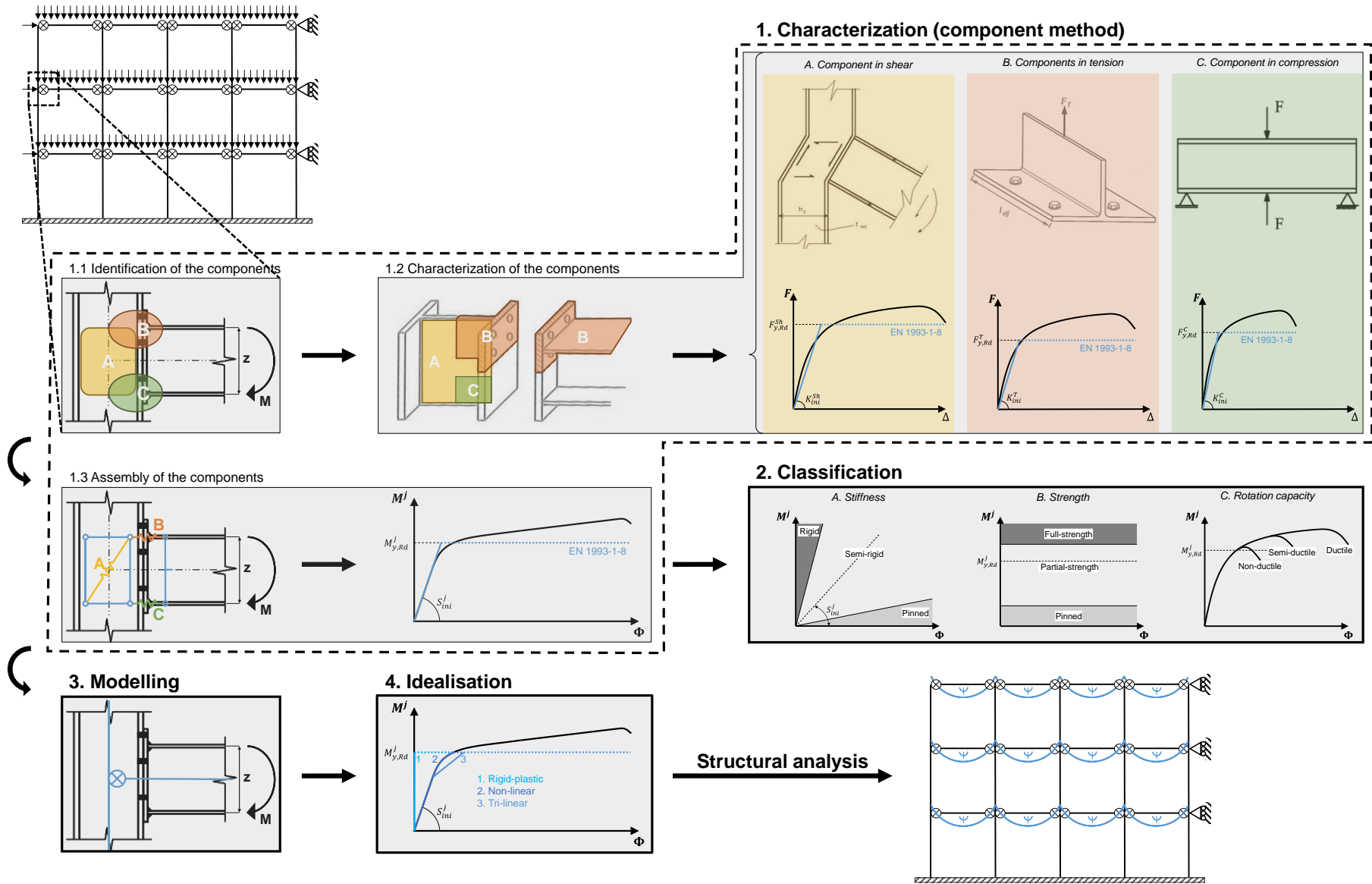
Fig. 1-1. Schematic representation of the design approach for semi-rigid joints under regular loading conditions.

1.2 SCOPE AND OBJECTIVES OF THE RESEARCH

1.2.1 Description of the research project

The objective of the research project carried out at the University of Liège can be summarized as follows:

> Extension of the component method:
>
> - towards the large deformation field;
> - under complex loading conditions (impact, fire, explosion, earthquake…).

Given the complexity of the phenomena to be dealt with, the scope of this research project has been purposely limited to a specific joint typology, namely the bolted joint with an extended end-plate connection, which is a typology commonly used in the design of steel frame structures. To achieve the objective stated hereabove, research efforts are required at four different levels in the component method, namely at the material level, at the component level, at the assembly level and at the level of the structure. For sake of clarity, the different research works to be performed have been reported in Fig. 1-2, which is an updated version of Fig. 1-1 and provides a schematic representation of the component method in the case of an exceptional event causing severe damage to the structure. Based on Fig. 1-2, one can identify five main work packages (WPs) which are briefly described here below:

- Material level

At the material level, reliable material models are required to predict the material laws of the individual basic components. This preliminary step is absolutely necessary in order to obtain an accurate characterization of these components. In the present research project, it is not intended to develop new material models. Instead, reference will be made to existing ones coming from the scientific literature. Consequently, this underlying level does not appear explicitly in Fig. 1-2.

- Component level (WP1)

At the component level, it is required to extend the existing models and/or to develop new sophisticated analytical models in order to predict the full non-linear behaviour of the different components up to failure, whatever is the applied load, i.e. static, dynamic, impact or fire. This research work constitutes the first work package of the project, named WP1. In the framework of the research project, it is not intended to study all the individual basic components available in EN 1993-1-8, but rather to concentrate on those showing a particular interest in the large deformation field. With this regard, the following components have been selected:

1. The component in shear, which designates the "column web panel in shear" (i.e. CWS). This component is known to be highly ductile when it is appropriately designed, which makes it particularly interesting in the large deformation field. This first part of WP1, named WP1A (see Fig. 1-2), is the topic of the present doctoral dissertation; its scope is presented in more details in the following Section 1.2.2, while the main outcome of this thesis is extensively described in the following Chapters.

2. Among the components in tension, particular attention will be paid to the "end-plate in bending" (i.e. EPB) and "column flange in bending" (i.e. CFB) which can be studied using the T-stub approach. Similarly to the CWS, these components are of particular interest since they provide a

significant reserve of ductility to the joint when they are activated and appropriately designed. A second PhD thesis has recently been initiated within the CMM research team with the aim of addressing this research question, and constitutes the second part of WP1, named WP1B (see Fig. 1-2).

3. The components in compression, by contrast with the components in shear and tension, usually exhibit a limited deformation capacity due to the occurrence of local buckling. Among them, it was decided to investigate the behaviour of the "Column Web in Compression" (i.e. CWC) since the failure of the latter is susceptible to limit the deformation capacity of the CWS. This research work constitutes the third part of WP1, named WP1C. It has been already partially addressed within the CMM research team. Preliminary results may be found in ([21], [22]).

- Assembly level (WP2)

At the assembly level, a new assembly procedure is required which is able to accommodate the new sophisticated models of components and to predict the full non-linear behaviour of the joint up to failure under various types of loading conditions. This research work constitutes the second work package of the global research project, named WP2 (see Fig. 1-2). It is currently being investigated within the CMM research team in the framework of a third PhD thesis dedicated to the robustness of structures. At the time of writing, this step is underway: a new generalised mechanical model has been developed and validated against analytical and experimental results for the prediction of the joint's plastic moment resistance. This innovative model overcomes two shortcomings of the current EN 1993-1-8 procedure, namely the consideration of the group effects on the one hand and of the actual distribution of the shear force along the height of the column web panel on the other hand. Preliminary results may be found in ([23], [24]). Future steps include the validation of this innovative joint model in the large deformation field once the new constitutive relationships at the component level become available, and its implementation in a finite element (FE) software as a macro-element which could be used in a frame analysis.

- Structure level (WP3)

The final step consists of a validation step: with the new macro-element developed in the framework of WP2, it will be possible to perform structural non-linear analysis of steel and steel-concrete composite structures subjected to an exceptional event, accounting for the complete rotational response of the joints up to failure. This will allow to study the performance of the joints in robustness applications and to propose guidelines for the design of safe and robust structures. This research work constitutes the third and last work package of the research project and is referred to as WP3 (see Fig. 1-2). It is being carried out together with WP2 in the framework of the PhD on structural robustness currently being held within the CMM research team.

To sum up, a comprehensive research project has been launched at the University of Liège with the aim of extending the component method towards the large deformation field and under complex loading conditions. This project is presented in Fig. 1-2 and focusses on a given joint typology, namely the bolted joint with an extended end-plate connection. Once the way is paved for this typology, the results can be easily extended to other typologies, relying on the "transposability" principle of the component method. To achieve this general objective, five main work packages have been identified, leading to the launching of three PhD theses within the CMM research team. The present thesis is the result of WP1 and focusses on the characterization of the CWS component. It is presented in more details in the following Section 1.2.2.
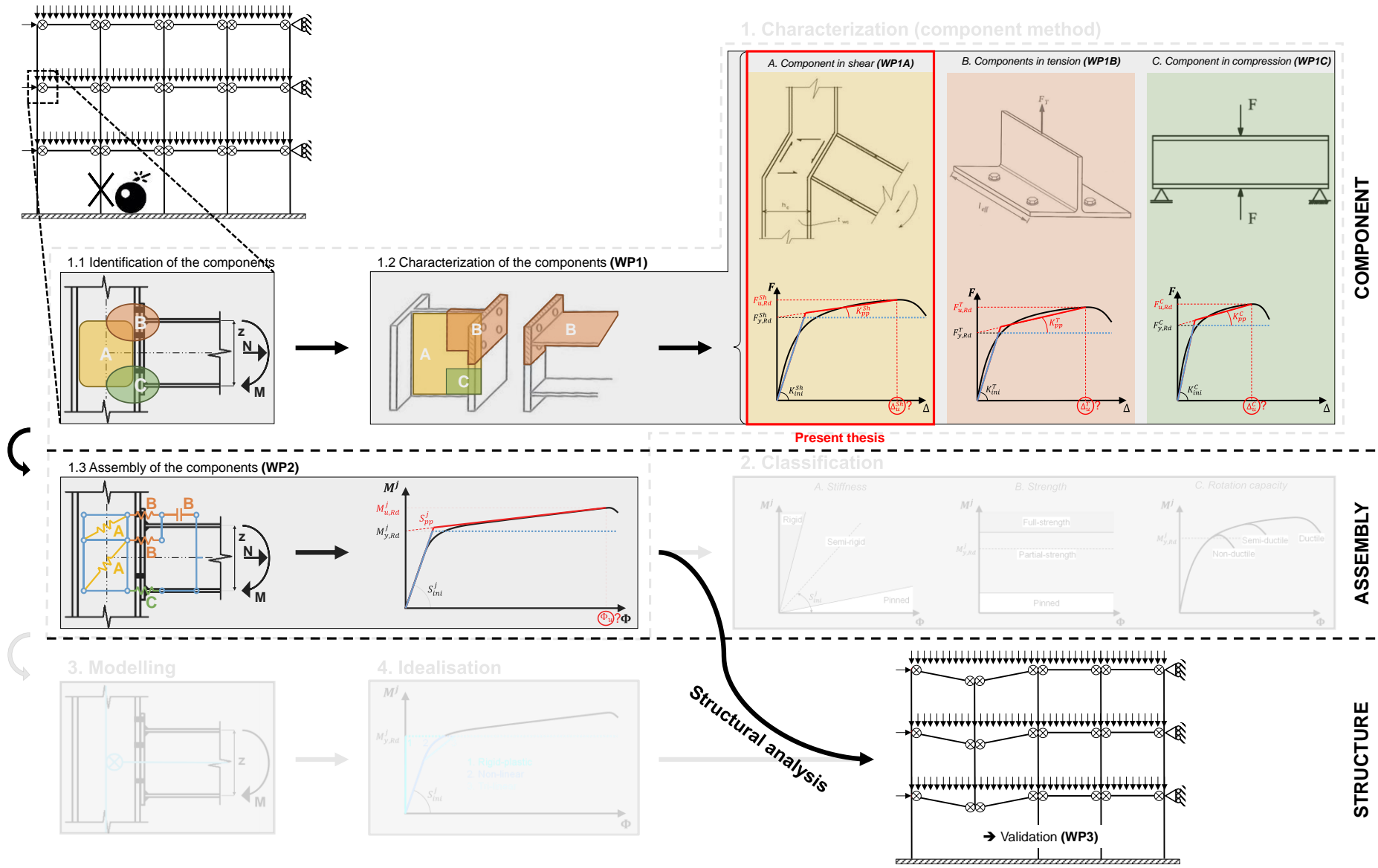
Fig. 1-2. Schematic representation of the design approach for semi-rigid joints under exceptional loading conditions (updated version of Fig. 1-1).

1.2.2 Contribution of the present thesis (WP1A)

The main objective of this doctoral thesis (see WP1A in Fig. 1-2) can be summarized as follows:

> Characterization of the full non-linear behaviour up to failure of the Column Web panel in Shear (CWS) under monotonic loading conditions.

The methodology which is employed to achieve this objective is depicted in Fig. 1-3 and combines experimental, numerical and analytical approaches.

For the experimental part, it is not intended to conduct additional experimental tests since a large number of well-documented experimental campaigns is already available in the scientific literature, covering various joint typologies and loading conditions. Instead, the objective of the experimental part is to carefully study those experimental results to select the most relevant ones for the present thesis, namely those displaying a significant deformation of the CWS. Based on this literature review, the selected experimental data can be used to get first insights of the behaviour of the CWS. The amount of information provided by the experimental results remains limited though, which justifies the use of the numerical approach. The experimental results are then mostly used for the validation of the models developed in the subsequent numerical and analytical parts.

The roles of the experimental and numerical parts are complementary in the present thesis: once validated against the experimental results, the numerical tool can be used as a "virtual laboratory" to perform extensive parametric studies. These parametric studies consist of sophisticated numerical simulations of welded beam-to-column sub-assemblies and allow investigating the influence of a large number of parameters on the behaviour of the CWS component up to failure. In addition, they provide a significant amount of information (distribution of stresses and strains, displacements, failure mode…), which is available at any location in the model and at any time step of the simulation. This is a great advantage of the numerical approach, compared to the experimental one. Based on the careful analysis of these numerical results, one can gain deep understanding of the physical phenomena governing the behaviour of the CWS up to failure. In this study, the commercial FE software Abaqus©[1] [25] has been chosen to perform the FE analyses.
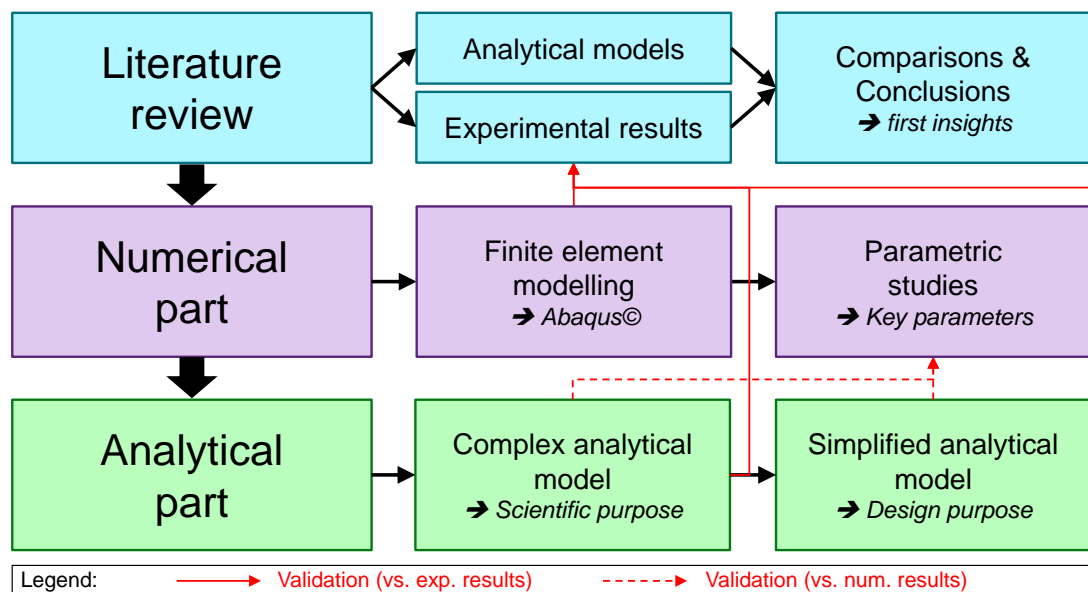
Fig. 1-3. Description of the methodology.

---

[1] Abaqus is a commercial FE software, developed by the Dassault Systèmes Simulia company, which is widely used in the automotive and aerospace industries. It is also very popular in the academic and scientific communities.

Based on the knowledge acquired in the parametric studies, the primary objective of the analytical part remains the development of a sophisticated constitutive model for the prediction of the monotonic behaviour of the CWS up to failure, which is able to account for the effect of the different key parameters highlighted in the parametric study. Along the way, some improvements of the current EN 1993-1-8 design standard will also be suggested, as regards the criteria for the prediction of the stiffness, strength and ductility properties of the CWS component. This constitutes a secondary objective of the analytical part. Both complex and simplified models developed in this thesis are validated through comparisons with experimental and numerical results.

Once the way is paved under monotonic loading conditions, perspectives of the present thesis include the extension of the model to more complex loading conditions. The ultimate goal being the integration of this new constitutive relationship for the CWS component in a macro-element capable of simulating the joint's non-linear behaviour up to failure in robustness application (see WP3 in Fig. 1-2).

1.3 STRUCTURE OF THE MANUSCRIPT

This doctoral thesis is divided into seven Chapters, as follows:

CHAPTER 1 ("Introduction") is the present introductory Chapter. It describes the context, motivations and objectives of the global research project in which the present thesis takes place. This research project, conducted at the University of Liège, aims at extending the component method towards the large deformation field and under complex loading conditions. The scope of the present thesis, which focuses only on the characterization of the full non-linear behaviour up to failure of the CWS, under monotonic loading, and the methodology to achieve this objective has also been highlighted.

CHAPTER 2 ("Literature review") sets the theoretical background of the present thesis. It provides a brief overview of the current component method and its main limitations. As regards the behaviour of the CWS, an extensive literature review of the existing scientific analytical models and simplified design criteria is conducted. From this survey, summary tables are built, using the same formalism for all the models in order to facilitate the comparisons between them.

In CHAPTER 3 ("Problem identification"), the performances of these complex and simplified analytical models are assessed through comparisons with experimental results carefully selected from the scientific literature. These comparisons raise the main problem addressed by the present thesis, namely the need to develop a more sophisticated analytical model capable of predicting the complete behaviour of the CWS up to failure.

CHAPTER 4 ("Characterization of the panel zone[2] plastic shear resistance") focuses first on the prediction of the plastic shear resistance of the CWS, in the case of welded joints only. It contains two main parts, namely a numerical part dedicated to the identification of the key parameters governing this level of resistance, and an analytical part dedicated to development and validation of a consistent analytical model.

CHAPTER 5 ("Characterization of the panel zone full-range behaviour up to failure") then focuses on the prediction of the complete behaviour up to failure of the CWS, again in the case of welded joints only. Similarly to CHAPTER 4, it is divided into two main parts, namely a numerical part dedicated to the study of the key parameters governing the deformability and the failure of the CWS, and an analytical part dedicated to the development and validation of a full-range constitutive model.

CHAPTER 6 ("Extension to bolted joints") extends the field of application of the models developed in CHAPTER 4 and CHAPTER 5, to column web panels in bolted joints. The prediction of the plastic shear resistance is first addressed, where some adjustments in the new analytical model and in the component method are suggested and validated through comparisons with experimental results. Secondly, the prediction of the deformation capacity is addressed, through preliminary comparisons with experimental results. From these comparisons, some limitations in the approach are highlighted and perspectives of improvement are discussed.

Finally, CHAPTER 7 ("Conclusions") provides some general conclusions, highlights the contribution of the research to the characterization of the behaviour of the CWS and gives an overview of the main limitations and perspectives of the present thesis.

---

[2] The term "panel zone (PZ)" will be introduced in Chapter 2. It refers to the same concept as the term "column web panel in shear (CWS)" but is more generic. From Chapter 2, the abbreviation "PZ" will be used instead of "CWS".

CHAPTER 2 Literature review

2.1 INTRODUCTION

2.1.1 Objectives of the Chapter

The objective of CHAPTER 2 is to set the theoretical background in which this doctoral thesis takes place, focussing on the behaviour of steel joints on the one hand and the behaviour of the CWS component on the other hand, which are the two main topics addressed in the present thesis.

2.1.2 Outline of the Chapter

Consequently, CHAPTER 2 has been divided into two main parts:

- The first part (see Section 1.1) deals with the behaviour of steel joints. General concepts are first introduced in Section 2.2.1 before the component method is briefly reviewed in Section 2.2.2, focussing on the application on two joint typologies, namely welded joints on the one hand and bolted joints with an extended end-plate connection on the other hand. The limitations of this method, when it comes to the prediction of the complete rotational response of the joint, are highlighted in Section 2.2.3. These limitations were already briefly introduced in CHAPTER 1 (see Section 1.1.2).
- The second part (see Section 2.3) addresses the behaviour of the CWS, which is the component of interest in the present thesis. A detailed review of past research works dedicated to the study of this component is conducted in Section 2.3.1. Particular attention is paid to the available analytical models to characterize the behaviour of the CWS. A non-exhaustive sample of some of these complex analytical models is provided in Section 2.3.2, while Section 2.3.3 reviews some simplified design criteria coming from various modern building codes. In the following CHAPTER 3, the performances of the so-identified complex and simplified models will be assessed through comparisons with available experimental results coming from the scientific literature. Based on of these comparisons, the strengths and weaknesses of each individual model will be highlighted, and conclusions will be drawn.

2.2 BEHAVIOUR OF STEEL JOINTS

2.2.1 Definitions

Typical steel frame structures include two types of major axis beam-to-column joints, namely interior joints (i.e. double-sided joints) and exterior joints (i.e. single-sided joints). These two joint configurations are depicted in Fig. 2-1 for a particular loading case which activates the column web panel in shear (subscripts B and C stand for <u>B</u>eam and <u>C</u>olumn respectively; subscripts T, R, B, L stand for <u>T</u>op, <u>R</u>ight, <u>B</u>ottom and <u>L</u>eft respectively). They can be divided into two main parts [26]:

- The <u>Panel Zone (PZ)</u> which consists of the Column Web Panel (CWP) and the so-called Surrounding Elements (SE), i.e. the column flanges, the root fillets and the possible transverse column web stiffeners, aligned with the beam flanges, if any.
- The left or (and) right <u>connection(s)</u>, concentrated at the beam-to-column interface(s), and which is (are) made of the connecting elements (e.g. bolts, endplates…) as well as the tensioned and compressed "load-introduction" parts of the column web.

These two parts both contribute to the overall joint deformability, as depicted in Fig. 2-2 for a particular right exterior joint in which the beam transfers bending moments and shear forces only (i.e. $N_{BR} = 0$ in Fig. 2-2) [26]:

- The PZ exhibits a shear deformation mode (see Fig. 2-2(b)) under the equivalent shear force V_{Ek}^{PZ} acting on the PZ. This force can be evaluated with Eq. (2-1) for a right exterior joint such as the one presented in Fig. 2-2, β_R being the transformation parameter and z_{eq} the equivalent lever arm between the tension and compression centres (assumed equal to $h_b - t_{fb}$ for welded joints and depending on the bolt-rows location for bolted joints, see Section 2.2.2). The resulting rotation γ between the beam and column axes makes possible the derivation of a first deformation curve $\left(V_{Ek}^{PZ} - \gamma\right)$ characterizing the rotational response of the PZ. In view of a simplified modelling of the joints for structural analysis, it is sometimes suggested to substitute the $\left(V_{Ek}^{PZ} - \gamma\right)$ curve for a $(M_{BR} - \gamma)$ curve, using the so-called transformation parameter β_R defined by Eq. (2-1) for the right connection, see [26].
- The connection exhibits two main sources of deformability, namely the deformation of the connecting elements (e.g. bolts, endplates…) and the transverse shortening and elongation of the column web, under the couple of tensile and compressive load-introduction F_{BR} forces, see Fig. 2-2. This couple of F_{BR} forces is statically equivalent to the beam moment M_{BR} and acts at mid-depth of the beam flanges. The so-obtained deformations result in a relative rotation ϕ between the beam and column axes, thus leading to a second deformation curve $(M_{BR} - \phi)$ characterizing the rotational response of the right connection.

$$V_{Ek}^{PZ} = \frac{M_{BR} - \overbrace{M_{BL}}^{=0}}{z_{eq}} - \frac{V_{CB} + V_{CT}}{2} = \frac{M_{BR}}{z_{eq}} \cdot \underbrace{\left[1 - \frac{z_{eq}}{2 \cdot M_{BR}} \cdot (V_{CB} + V_{CT})\right]}_{\beta_R} = \frac{M_{BR}}{z_{eq}} \cdot \beta_R = F_{BR} \cdot \beta_R \quad (2\text{-}1)$$
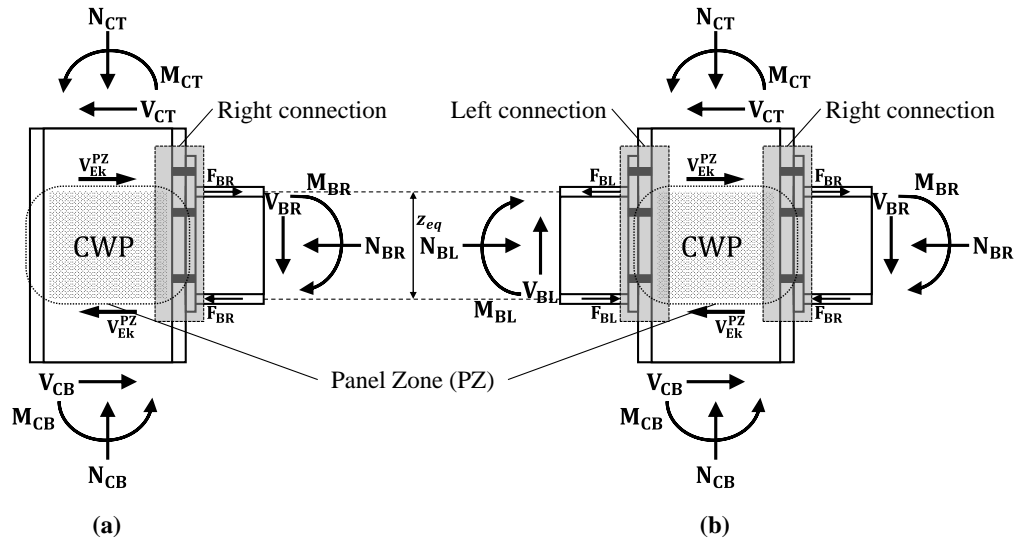
Fig. 2-1. Definition of the main parts of a beam-to-column joint (adapted from [26]): (a) exterior joint and (b) interior joint.
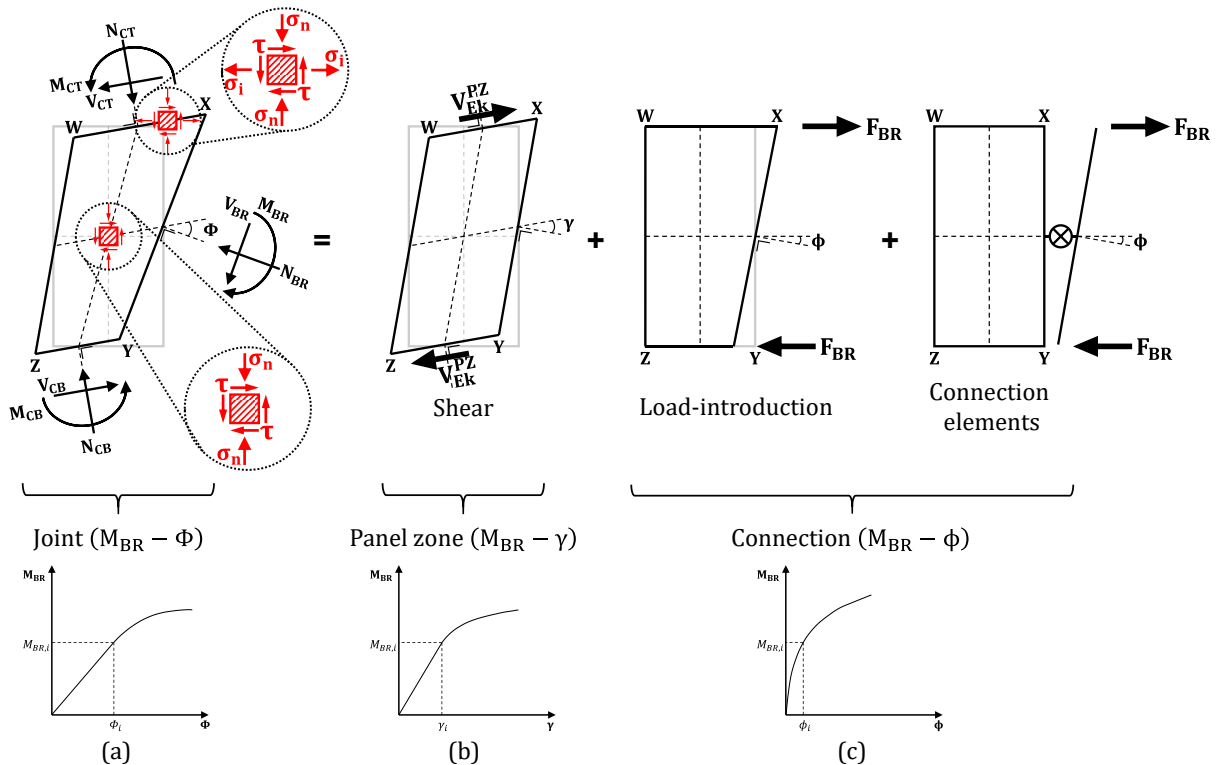
Fig. 2-2. Illustration of the joint deformability sources in an exterior joint (adapted from [27]): (a) resultant joint deformation, (b) shear deformation of the PZ and (c) load-introduction deformation of the connection.

The resulting $(M_{BR} - \Phi)$ curve (see Fig. 2-2(a)), representing the joint behaviour, is obtained as the sum of these two contributions of rotation γ and ϕ, coming from the PZ and the connection, respectively. For classical beam-to-column structural joints, such as the ones presented in Fig. 2-1, the $(M^j - \Phi)$ curve exhibits a bilinear-like shape, as illustrated in Fig. 2-3 (see the solid black lines), where M^j (or M_{Ek}^j) is the bending moment applied to the joint and is used indifferently from the bending moment M_{BR} (resp. M_{BL}) coming from the right (resp. left) beam. The elastic behaviour of the joint, characterized by an initial stiffness S_{ini}^j, develops until the elastic bending moment resistance $M_{el,Rk}^j$ of the joint is reached at the onset of yielding. It is followed by the progressive yielding of the joint (i.e. of one or more of its constituent components) until the plastic bending moment resistance $M_{y,Rk}^j$ of the joint is reached. During this process, the plasticity gradually spreads throughout the

components, leading to the progressive decrease of the joint stiffness and to the knee observed in the solid black curves in Fig. 2-3. The value $M_{el,Rk}^{j}$ of the elastic bending moment resistance can reasonably be estimated as 2/3 of $M_{y,Rk}^{j}$, see ([1], [26], [28]). The next stage features the development of a post-plastic behaviour (S_{pp}^{j}) which corresponds to the onset of strain-hardening, until the ultimate bending moment resistance $M_{u,Rk}^{j}$ of the joint is reached. When no instability or brittle failure occurs in the joint at ultimate state, $M_{u,Rk}^{j}$ differs significantly from $M_{y,Rk}^{j}$, and the bilinear shape of the $\left(M^{j} - \Phi\right)$ curve is well marked (see Fig. 2-3(a)). By contrast, in case of instability or brittle failure (e.g. local buckling of the column web in compression or failure of the bolts in tension), $M_{u,Rk}^{j}$ comes closer to $M_{y,Rk}^{j}$ and the bilinear character of the $\left(M^{j} - \Phi\right)$ curve may be difficult to detect (see Fig. 2-3(b)). Either way, the ultimate rotation capacity Φ_{u} of the joint is defined as the intersection between the $\left(M^{j} - \Phi\right)$ curve and the $M_{u,Rk}^{j}$ horizontal line.
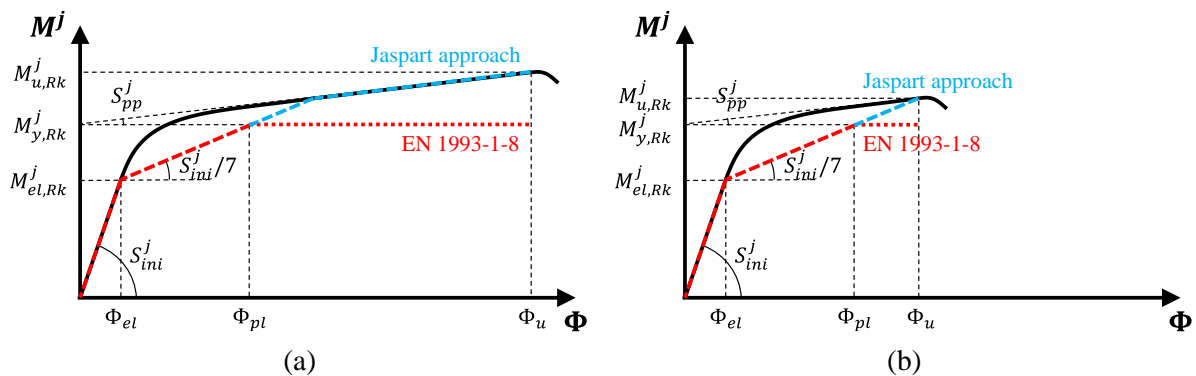
Fig. 2-3. Joint's typical $\left(M^{j} - \Phi\right)$ curve: (a) well-marked bilinear response and (b) less marked bilinear response.

2.2.2 Component method approach

2.2.2.1 Overview

Different approaches can be used to characterize the joint's $\left(M^{j} - \Phi\right)$ curve, ranging from experimental to numerical and analytical ones. This thesis primarily focuses on the component method approach, a hybrid analytical-mechanical approach, which is nowadays widely recognized as the reference method for the characterization and the design of steel and steel-concrete composite joints. The version of the component method presented in the present Section 2.2.2 is the one adopted in the Part 1-8 of Eurocode 3 (EN 1993-1-8, see [1]), which was briefly introduced in CHAPTER 1.

This method can be seen as a macroscopic application of the FE method. According to this method, any joint can be subdivided into a series of zones through which the forces are transferred. This is illustrated in Fig. 2-4 and Fig. 2-5 regarding the two types of joint configurations that will be extensively investigated in the present thesis, namely welded joints (see Fig. 2-4) and bolted joints with an extended end-plate connection (see Fig. 2-5), subjected to pure bending. For these two configurations, three main zones can be identified, namely the shear, tension and compression zones. These zones are then further discretised into a series of individual basic components which contribute to the overall response (strength and stiffness) of the joint. Table 2-1 summarizes the basic components which are active in the two joint configurations illustrated in Fig. 2-4(a) and Fig. 2-5(a). For sake of simplicity, the welds are assumed to be fully resistant and are therefore not reported in Table 2-1. The individual basic components given in Table 2-1 are named with two or three letters. Their behaviour is uniaxial and characterized by a non-linear $(F^{c} - \Delta^{c})$ deformation curve ("c" standing for "component"). Therefore, they can be modelled as extensional springs. These springs are then assembled using infinitely rigid pinned-end elements to form a mechanical model which can be

employed to simulate the joint's actual behaviour. This is depicted in Fig. 2-4(b) and Fig. 2-5(b) for the welded and bolted joints considered in the present study. For the bolted joint in Fig. 2-5, the 3rd bolt-row is considered as inactive since it is located very close to the compression centre. The estimated $\left(M^j - \Phi\right)_{an}$ curve provided by the mechanical model can eventually be assigned to rotational springs which are typically used to simulate the joints' behaviour in the structural analysis.

From a theoretical point of view, the component method approach could be applied to any joint configuration and any loading situation provided that the basic components are properly characterized. Practically speaking, the application of the component method requires the three following steps:

1) identification of the relevant (active) components for a given structural joint;
2) characterization of the $\left(F^c - \Delta^c\right)$ curve of each individual basic component;
3) assembly of the components in order to predict the joint's global $\left(M^j - \Phi\right)$ curve.

In the following Sections, these steps are reviewed in the framework of the EN 1993-1-8 approach.
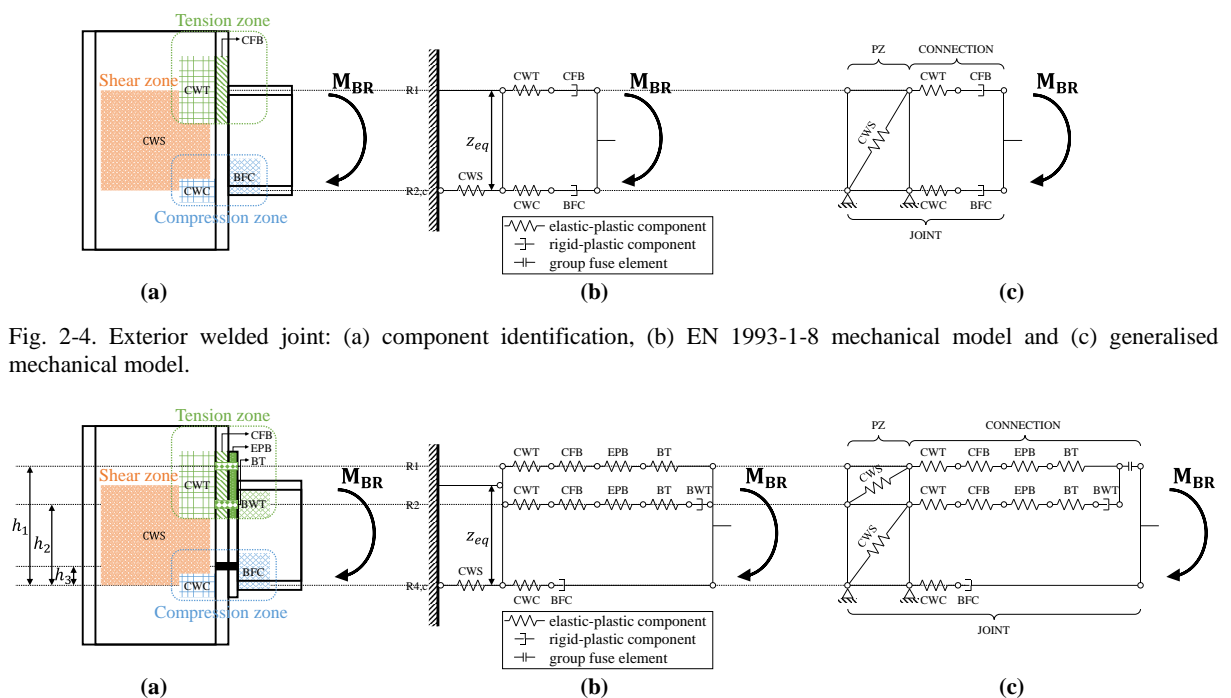
Fig. 2-4. Exterior welded joint: (a) component identification, (b) EN 1993-1-8 mechanical model and (c) generalised mechanical model.

Fig. 2-5. Exterior bolted joint: (a) component identification, (b) EN 1993-1-8 mechanical model and (c) generalised mechanical model.

Table 2-1. List of active components for the two joint configurations presented in Fig. 2-4 and Fig. 2-5.

Joint configuration			Welded		Bolted	
Zone	Component	Acronym	k_{ini}^c	$F_{y,Rk}^c$	k_{ini}^c	$F_{y,Rk}^c$
Shear	Column web panel in shear	CWS	✓	✓	✓	✓
Tension	Column web in tension	CWT	✓	✓	✓	✓
	Column flange in bending	CFB	*	✓	✓	✓
	End-plate in bending	EPB	/	/	✓	✓
	Bolts in tension	BT	/	/	✓	**
	Beam web in tension	BWT	/	/	*	✓
Compression	Column web in compression	CWC	✓	✓	✓	✓
	Beam flange and web in compression	BFC	*	✓	*	✓

Notes:
* The component is considered in the deformation of the beam
** The component is considered in the equivalent T-stub

2.2.2.2 Identification of the components

The identification of the active components depends on the joint typology and the loading conditions. In total, 20 individual basic components are covered by EN 1993-1-8, see [1]. For instance, the basic active components associated with the welded and bolted exterior joints presented in Fig. 2-4 and Fig. 2-5, are given in Table 2-1. This table shows that the welded joints represent the simplest case due to the reduced number of involved components. In the presence of transverse column web stiffeners, there are even fewer active components as the load-introduction components (i.e. CWC/CWT) do not contribute to the joint deformability anymore.

The behaviour of the bolted joints is influenced by the same components as the ones involved in welded joints, see Table 2-1. Moreover, additional sources of deformation related to the mechanically fastened elements can also be identified. This is the case of the column flange in bending (CFB) and the end-plate in bending (EPB).

2.2.2.3 Characterization of the components

Characterizing the behaviour of the active components is an important step as it is the input for the mechanical model used in the assembly procedure.

Each extensional spring (i.e. individual basic component) identified in Section 2.2.2.2 is characterized by a non-linear $(F^c - \Delta^c)$ curve (tension or compression) such as the ones presented in Fig. 2-6(a) and (b) (see the solid black curves), where F^c and Δ^c represent the force acting in the component "c" and the related displacement (i.e. elongation or shortening), respectively. These curves exhibit a globally bilinear shape, similarly to the joint's $(M^j - \Phi)$ curve (see Fig. 2-3). Therefore, they can be characterized by four key parameters:

- an initial elastic stiffness $K_{ini}^c = E \cdot k_{ini}^c$, where k_{ini}^c is called "stiffness coefficient";
- a plastic resistance $F_{y,Rk}^c$;
- a strain-hardening (more generally post-plastic) stiffness $K_{pp}^c = E \cdot k_{pp}^c$, where k_{pp}^c is called "post-plastic stiffness coefficient";
- an ultimate resistance $F_{u,Rk}^c$.

According to ([1], [26], [28]), the elastic resistance $F_{el,Rk}^c$ may be simply estimated as 2/3 of $F_{y,Rk}^c$.

When no instability or brittle failure occurs in the component at ultimate state, $F_{u,Rk}^c$ is associated to the material ultimate resistance and therefore significantly differs from $F_{y,Rk}^c$; in this case, the bilinear shape of the $(F^c - \Delta^c)$ curve is well marked (see Fig. 2-6(a)). When instability or brittle failure occurs, $F_{u,Rk}^c$ is closer (or even equal) to $F_{y,Rk}^c$, resulting in a more round final shape for the $(F^c - \Delta^c)$ curve (see Fig. 2-6(b)).
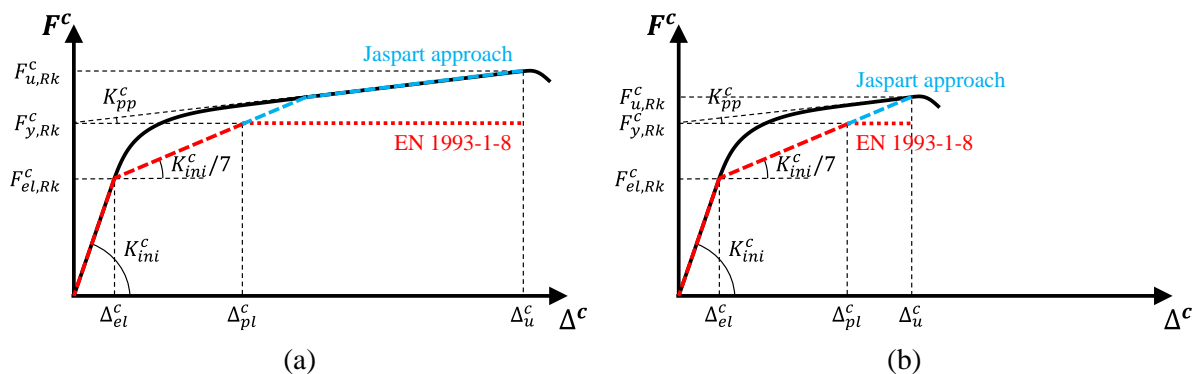

Fig. 2-6. Component's typical $(F^c - \Delta^c)$ curve: (a) well-marked bilinear behaviour and (b) less marked bilinear behaviour.

EN 1993-1-8 suggests a simplified trilinear modelling approach for the characterization of the components (see the trilinear red curves in Fig. 2-6(a) and (b)), which relies on the assumption of an elastic, perfectly-plastic behaviour of the components. Consequently, analytical expressions are provided in EN 1993-1-8 regarding the characterization of the basic components in terms of the initial stiffness coefficient k_{ini}^c and the plastic resistance $F_{y,Rk}^c$ only. No limitation to the yield plateau (i.e. ultimate deformation capacity Δ_u^c) is prescribed though. The analytical formulae (i.e. k_{ini}^c and $F_{y,Rk}^c$) associated to each basic component reported in Table 2-1 are briefly described in Table 2-2, while the key geometric parameters used in Table 2-2 are summarized in the following Table 2-3, Table 2-4 and Fig. 2-7. For more details about the application of these formulae, the reader is referred to the normative document [1]. It is noteworthy that for the BFC and the BWT, EN 1993-1-8 assumes a rigid-plastic behaviour, i.e. $k_{ini}^c = \infty$, see Table 2-2. The same applies to the CFB when it is active in a welded joint. This is because the deformability of these components is already accounted for in the deformation of the connected beam. As a consequence, these components only provide a limitation to the joint's plastic bending moment resistance.

2.2.2.4 Assembly of the components

Knowing the individual response of each active component, the assembly procedure can be contemplated. The joint components are combined into a spring model, as shown in previous Fig. 2-4(b) and Fig. 2-5(b). From these models, the mechanical properties of the joint (i.e. the rotational stiffness S_{ini}^j, the plastic bending moment resistance $M_{y,Rk}^j$ and the rotation capacity Φ_u) can be determined using analytical formulae. These formulae are briefly presented below, where they are particularised to the two joint configurations illustrated in Fig. 2-4(b) and Fig. 2-5(b), assuming for the latter that the 3rd bolt-row is inactive.

As regards the joint's initial rotational stiffness S_{ini}^j, it can be derived through Eq. (2-2):

$$S_{ini}^j = \frac{E \cdot z_{eq}^2}{\dfrac{1}{k_{ini,eq}^C} + \dfrac{1}{k_{ini,eq}^T}} \tag{2-2}$$

where $k_{ini,eq}^C$ and $k_{ini,eq}^T$ are the initial stiffnesses associated to the bolt-row in compression and the equivalent bolt-row in tension respectively, see Eqs. (2-3) and (2-4), and where z_{eq} is the equivalent lever arm between the latter, see Eq. (2-5):

$$k_{ini,eq}^C = \frac{1}{\dfrac{1}{k_{ini}^{CWC}} + \dfrac{1}{k_{ini}^{BFC}} + \dfrac{1}{k_{ini}^{CWS}}} \tag{2-3}$$

$$k_{ini,eq}^T = \begin{cases} k_{ini}^{CWT} & \text{welded joint (Fig. 2-4)} \\ \dfrac{\sum_{r=1}^2 k_{ini,eff,r}^T \cdot h_r}{z_{eq}} & \text{bolted joint (Fig. 2-5)} \end{cases} \tag{2-4}$$

$$z_{eq} = \begin{cases} h_b - t_{fb} & \text{welded joint (Fig. 2-4)} \\ \dfrac{\sum_{r=1}^2 k_{ini,eff,r}^T \cdot h_r^2}{\sum_{r=1}^2 k_{ini,eff,r}^T \cdot h_r} & \text{bolted joint (Fig. 2-5)} \end{cases} \tag{2-5}$$

with $k_{ini,eff,r}^T$ being the effective stiffness coefficient associated to the rth bolt-row in tension, see Eq. (2-6):

$$k_{ini,eff,r}^T = \frac{1}{\dfrac{1}{k_{ini,r}^{CWT}} + \dfrac{1}{k_{ini,r}^{CFB}} + \dfrac{1}{k_{ini,r}^{EPB}} + \dfrac{1}{k_{ini,r}^{BT}}} \tag{2-6}$$

As regards the joint's plastic bending moment resistance $M_{y,Rk}^j$, it can be evaluated through Eq. (2-7):

$$M_{y,Rk}^j = \begin{cases} F_{y,Rk,1} \cdot z_{eq} & \text{welded joint (Fig. 2-4)} \\ \sum_{r=1}^{2} F_{y,Rk,r} \cdot h_r & \text{bolted joint (Fig. 2-5)} \end{cases} \tag{2-7}$$

where $F_{y,Rk,1}$ and $F_{y,Rk,r}$ designate the plastic resistance of the tensile row in a welded joint and the plastic resistance of the rth bolt-row in tension in a bolted joint, respectively, and can be expressed through Eqs. (2-8) and (2-9):

$$F_{y,Rk,1} = \min\left(F_{y,Rk,1}^{CWT}; F_{y,Rk,1}^{CFB}; F_{y,Rk,C}\right) \tag{2-8}$$

$$F_{y,Rk,r} = \begin{cases} \min\left(F_{y,Rk,r}^{CWT}; F_{y,Rk,r}^{CFB}; F_{y,Rk,r}^{EPB}; F_{y,Rk,r}^{BT}; F_{y,Rk,C}\right) & r = 1 \\ \min\left(F_{y,Rk,r}^{CWT}; F_{y,Rk,r}^{CFB}; F_{y,Rk,r}^{EPB}; F_{y,Rk,r}^{BT}; F_{y,Rk,r}^{BWT}; F_{y,Rk,C} - F_{y,Rk,1}\right) & r = 2 \end{cases} \tag{2-9}$$

with $F_{y,Rk,C}$ the plastic resistance of the bolt-row in compression, see Eq. (2-10):

$$F_{y,Rk,C} = \min\left(F_{y,Rk}^{CWC}; F_{y,Rk}^{BFC}; F_{y,Rk}^{CWS}\right) \tag{2-10}$$

It is noteworthy that spring models such as the one presented in Fig. 2-5(b) do not account explicitly for the group effects, i.e. the possible plastic mechanisms which could develop around several adjacent bolt-rows in the plate components. Consequently, EN 1993-1-8 provides additional analytical formulae to check the distribution of forces among the bolt-rows with respect to their individual and group resistances. An example of such assembly formula is provided in Eq. (2-11) for the bolted joint considered in Fig. 2-5, where $F_{y,Rk,1-2}^{CWT}$, $F_{y,Rk,1-2}^{CFB}$ and $F_{y,Rk,1-2}^{BT}$ are the resistances of the group effects that can potentially occur between the two bolt-rows in tension:

$$F_{y,Rk,2,red} = \min\left(F_{y,Rk,2}; F_{y,Rk,1-2}^{CWT} - F_{y,Rk,1}; F_{y,Rk,1-2}^{CFB} - F_{y,Rk,1}; F_{y,Rk,1-2}^{BT} - F_{y,Rk,1}\right) \tag{2-11}$$

As regards the joint's rotation capacity Φ_u, unlike the two other properties, it cannot be derived from mechanical models, since no information is available at the component level in terms of deformation capacity Δ_u^c. Consequently, EN 1993-1-8 prescribes qualitative recommendations in order to ensure sufficient rotation capacity and ductility to the joints.

Based on the knowledge of S_{ini}^j, $M_{y,Rk}^j$ and Φ_u, EN 1993-1-8 suggests a simplified trilinear modelling approach for the idealization of the joint's $\left(M^j - \Phi\right)$ curve (see the trilinear red curves in Fig. 2-3(a) and (b)), similarly to what was done at the component level in Section 2.2.2.3 (see Fig. 2-6).

Table 2-2. Characterization of the individual basic components reported in Table 2-1, according to EN 1993-1-8 [1].

Component	k_{ini}^c	$F_{y,Rd}^c$	Parameters
CWS (unstiffened)	$\dfrac{0.38 \cdot A_{VC}}{\beta \cdot z_{eq}}$	$\dfrac{0.9 \cdot f_{y,wc} \cdot A_{VC}}{\sqrt{3} \cdot \beta \cdot \gamma_{M0}}$	$A_{VC} = A_c - 2 \cdot b_c \cdot t_{fc} + (t_{wc} + 2 \cdot r_c) \cdot t_{fc}$ $\beta = \begin{cases} 0 & \text{interior joint with balanced bending moments} \\ 1.0 & \text{exterior joint} \\ 2.0 & \text{interior joint with unbalanced bending moments} \end{cases}$ d_s: distance between the centrelines of the stiffeners $M_{pl,fc,Rd}$: design plastic moment resistance of a column flange $M_{pl,st,Rd}$: design plastic moment resistance of a stiffener
CWS (stiffened)	∞	$\dfrac{0.9 \cdot f_{y,wc} \cdot A_{VC}}{\sqrt{3} \cdot \beta \cdot \gamma_{M0}}$ $+ \min\left(4 \cdot \dfrac{M_{pl,fc,Rd}}{\beta \cdot d_s};\right.$ $\left. 2 \cdot \dfrac{M_{pl,fc,Rd} + M_{pl,st,Rd}}{\beta \cdot d_s}\right)$	
CWC	$\dfrac{0.7 \cdot b_{eff,cwc} \cdot t_{wc}}{d_c}$	$\min\left(\dfrac{\omega \cdot k_{wc} \cdot b_{eff,cwc} \cdot t_{wc} \cdot f_{y,wc}}{\gamma_{M0}};\right.$ $\left. \rho \cdot \dfrac{\omega \cdot k_{wc} \cdot b_{eff,cwc} \cdot t_{wc} \cdot f_{y,wc}}{\gamma_{M0}}\right)$	$b_{eff,cwc} = \begin{cases} t_{fb} + 2 \cdot \sqrt{2} \cdot a_{b,f} + 5 \cdot (t_{fc} + r_c) & \text{welded joint} \\ t_{fb} + 2 \cdot \sqrt{2} \cdot a_{p,f} + 5 \cdot (t_{fc} + r_c) + s_p & \text{bolted joint} \end{cases}$ $\omega = \begin{cases} 1.0 & 0 \leq \beta \leq 0.5 \\ \omega_1 + 2 \cdot (1-\beta) \cdot (1-\omega_1) & 0.5 < \beta \leq 1.0 \\ \omega_1 - (1-\beta) \cdot (\omega_2 - \omega_1) & 1.0 < \beta \leq 2.0 \end{cases}$ with $\begin{cases} \omega_1 = \dfrac{1}{\sqrt{1+1.3 \cdot \left(\frac{b_{eff,cwc} \cdot t_{wc}}{A_{VC}}\right)^2}} \\ \omega_2 = \dfrac{1}{\sqrt{1+5.2 \cdot \left(\frac{b_{eff,cwc} \cdot t_{wc}}{A_{VC}}\right)^2}} \end{cases}$ $k_{wc} = \begin{cases} 1.0 & \sigma_{n,N} \leq 0.7 \cdot f_{y,wc} \\ 1.7 - \dfrac{\sigma_{n,N}}{f_{y,wc}} & \sigma_{n,N} > 0.7 \cdot f_{y,wc} \end{cases}$ $\rho = \begin{cases} 1.0 & \bar{\lambda}_p \leq 0.72 \\ \dfrac{\bar{\lambda}_p - 0.2}{\bar{\lambda}_p^2} & \bar{\lambda}_p > 0.72 \end{cases}$ with $\bar{\lambda}_p = 0.932 \cdot \sqrt{\dfrac{b_{eff,cwc} \cdot d_c \cdot f_{y,wc}}{E \cdot t_{wc}^2}}$
CWT	$\dfrac{0.7 \cdot b_{eff,cwt} \cdot t_{wc}}{d_c}$	$\dfrac{\omega \cdot k_{wc} \cdot b_{eff,cwt} \cdot t_{wc} \cdot f_{y,wc}}{\gamma_{M0}}$	$b_{eff,cwt} = \begin{cases} t_{fb} + 2 \cdot \sqrt{2} \cdot a_{b,f} + 5 \cdot (t_{fc} + r_c) & \text{welded joint} \\ b_{eff,cfb} & \text{bolted joint} \end{cases}$
CFB (welded)	∞	$\dfrac{b_{eff,cfb} \cdot t_{fb} \cdot f_{y,fb}}{\gamma_{M0}}$	$b_{eff,cfb} = t_{wc} + 2 \cdot r_c + 7 \cdot k \cdot t_{fc}$ $k = \dfrac{f_{y,fc} \cdot t_{fc}}{f_{y,fb} \cdot t_{fb}}$
CFB (bolted)	$\dfrac{0.9 \cdot b_{eff,cfb} \cdot t_{fc}^3}{m_{fc}^3}$	$\min\left(F_{y,Rd,1}^{CFB}; F_{y,Rd,2}^{CFB}; F_{y,Rd,3}^{CFB}\right)$	$b_{eff,cfb} = \begin{cases} b_{eff,cfb,1} = \min\left(b_{eff,cfb}^{nc}; b_{eff,cfb}^{cp}\right) & \text{mode 1} \\ b_{eff,cfb,2} = b_{eff,cfb}^{nc} & \text{mode 2} \end{cases}$ $F_{y,Rd,1}^{CFB} = 4 \cdot \dfrac{M_{pl,fc,1,Rd}}{m_{fc}}$ with $M_{pl,fc,1,Rd} = \dfrac{b_{eff,cfb,1} \cdot t_{fc}^2}{4 \cdot \gamma_{M0}} \cdot f_{y,fc}$ $F_{y,Rd,2}^{CFB} = \dfrac{2 \cdot M_{pl,fc,2,Rd} + F_{y,Rd,3}^{CFB} \cdot n_{fc}}{m_{fc} + n_{fc}}$ with $M_{pl,fc,2,Rd} = \dfrac{b_{eff,cfb,2} \cdot t_{fc}^2}{4 \cdot \gamma_{M0}} \cdot f_{y,fc}$ $F_{y,Rd,3}^{CFB} = 2 \cdot F_{y,Rd}^{BT}$
EPB	$\dfrac{0.9 \cdot b_{eff,epb} \cdot t_p^3}{m_p^3}$	$\min\left(F_{y,Rd,1}^{EPB}; F_{y,Rd,2}^{EPB}; F_{y,Rd,3}^{EPB}\right)$	$b_{eff,epb} = \begin{cases} b_{eff,epb,1} = \min\left(b_{eff,epb}^{nc}; b_{eff,epb}^{cp}\right) & \text{mode 1} \\ b_{eff,epb,2} = b_{eff,epb}^{nc} & \text{mode 2} \end{cases}$ $F_{y,Rd,1}^{EPB} = 4 \cdot \dfrac{M_{pl,p,1,Rd}}{m_p}$ with $M_{pl,p,1,Rd} = \dfrac{b_{eff,epb,1} \cdot t_p^2}{4 \cdot \gamma_{M0}} \cdot f_{y,p}$ $F_{y,Rd,2}^{EPB} = \dfrac{2 \cdot M_{pl,p,2,Rd} + F_{y,Rd,3}^{EPB} \cdot n_p}{m_p + n_p}$ with $M_{pl,p,2,Rd} = \dfrac{b_{eff,epb,2} \cdot t_p^2}{4 \cdot \gamma_{M0}} \cdot f_{y,p}$ $F_{y,Rd,3}^{EPB} = 2 \cdot F_{y,Rd}^{BT}$
BFC	∞	$\dfrac{M_{b,Rd}}{h_b - t_{fb}}$	$M_{b,Rd}$: design plastic moment resistance of the beam cross-section
BWT	∞	$\dfrac{b_{eff,bwt} \cdot t_{wb} \cdot f_{y,wb}}{\gamma_{M0}}$	$b_{eff,bwt} = b_{eff,epb}$
BT	$\dfrac{1.6 \cdot A_s}{L_b}$	$\dfrac{0.9 \cdot f_{u,b} \cdot A_s}{\gamma_{M2}}$	A_s: bolt cross-section area L_b: bolt elongation length, see EN 1993-1-8

Notes :
- $E, f_{y,wc}, f_{y,fc}, f_{y,wb}, f_{y,fb}, f_{y,p}, f_{u,b}$: mechanical properties of the steel material
- $\gamma_{M0} = 1.0, \gamma_{M1} = 1.0, \gamma_{M2} = 1.25$: partial safety factors
- h_c (resp. h_b), b_c, t_{fc} (resp. t_{fb}), t_{wc} (resp. t_{fb}), r_c, d_c, A_c: geometric properties of the column (resp. beam) cross-section
- s_p: length obtained by dispersion at 45° through the end-plate, see EN 1993-1-8
- z_{eq}: equivalent lever arm, see forthcoming Eq. (2-5)
- $\sigma_{n,N}$: vertical normal stresses coming from the axial load in the column
- $b_{eff,cfb}^{cp}$ & $b_{eff,cfb}^{nc}$ ➔ see Table 2-3
- $b_{eff,epb}^{cp}$ & $b_{eff,epb}^{nc}$ ➔ see Table 2-3
- $a_{b,f}, a_{p,f}, t_p, m_{fc}, n_{fc}, m_p, n_p$: see Fig. 2-7

Table 2-3. Definition of the effective lengths $b_{eff,cfb}^{cp}$ and $b_{eff,cfb}^{nc}$ for a (un)stiffened CFB.

Bolt-row location	Bolt-row considered individually		Bolt-row considered as part of a group	
	Circular patterns $b_{eff,cfb}^{cp}$	Non-circ. patterns $b_{eff,cfb}^{nc}$	Circular patterns $b_{eff,cfb}^{cp}$	Non-circ. patterns $b_{eff,cfb}^{nc}$
End bolt-row adjacent to a stiffener	$\min(2\pi m_{fc}; \pi m_{fc} + 2e_1)$	$e_1 + \alpha m_{fc}$ $- (2m_{fc} + 0.625e_{fc})$	Not relevant	Not relevant
Inner bolt-row adjacent to a stiffener	$2\pi m_{fc}$	αm_{fc}	$\pi m_{fc} + p$	$0.5p + \alpha m_{fc}$ $- (2m_{fc} + 0.625e_{fc})$
Other inner bolt-row	$2\pi m_{fc}$	$4m_{fc} + 1.25e_{fc}$	$2p$	p
Other end bolt-row	$\min(2\pi m_{fc}; \pi m_{fc} + 2e_1)$	$\min(4m_{fc} + 1.25e_{fc};$ $2m_{fc} + 0.625e_{fc} + e_1)$	$\min(\pi m_{fc} + p; 2e_1 + p)$	$\min(2m_{fc} + 0.625e_{fc}$ $+ 0.5p; e_1 + 0.5p)$
Note: for the derivation of α, see EN 1993-1-8 [1]				

Table 2-4. Definition of the effective lengths $b_{eff,epb}^{cp}$ and $b_{eff,epb}^{nc}$ for an EPB.

Bolt-row location	Bolt-row considered individually		Bolt-row considered as part of a group	
	Circular patterns $b_{eff,epb}^{cp}$	Non-circ. patterns $b_{eff,epb}^{nc}$	Circular patterns $b_{eff,epb}^{cp}$	Non-circ. patterns $b_{eff,epb}^{nc}$
Bolt-row outside tension flange of beam	$\min(2\pi m_x; \pi m_x$ $+ w; \pi m_x + 2e_p)$	$\min(4m_x + 1.25e_x; e_p$ $+ 2m_x$ $+ 0.625e_x; 0.5b_p; 0.5w$ $+ 2m_x + 0.625e_x)$	Not relevant	Not relevant
1st bolt-row below tension flange of beam	$2\pi m_p$	αm_p	$\pi m_p + p$	$0.5p + \alpha m_p$ $- (2m_p + 0.625e_p)$
Other inner bolt-row	$2\pi m_p$	$4m_{ep} + 1.25e_p$	$2p$	p
Other end bolt-row	$2\pi m_p$	$4m_{ep} + 1.25e_p$	$\pi m_p + p$	$2m_p + 0.625e_p + 0.5p$
Note: for the derivation of α, see EN 1993-1-8 [1]				

$$m_{fc} = L_c - 0.8 \cdot r_c$$

$$n_{fc} = \min(e_{fc}; e_p; 1.25 \cdot m_{fc})$$

$$m_p = L_p - 0.8 \cdot \sqrt{2} \cdot a_{p,w}$$

$$n_p = \min(e_{fc}; e_p; 1.25 \cdot m_p)$$
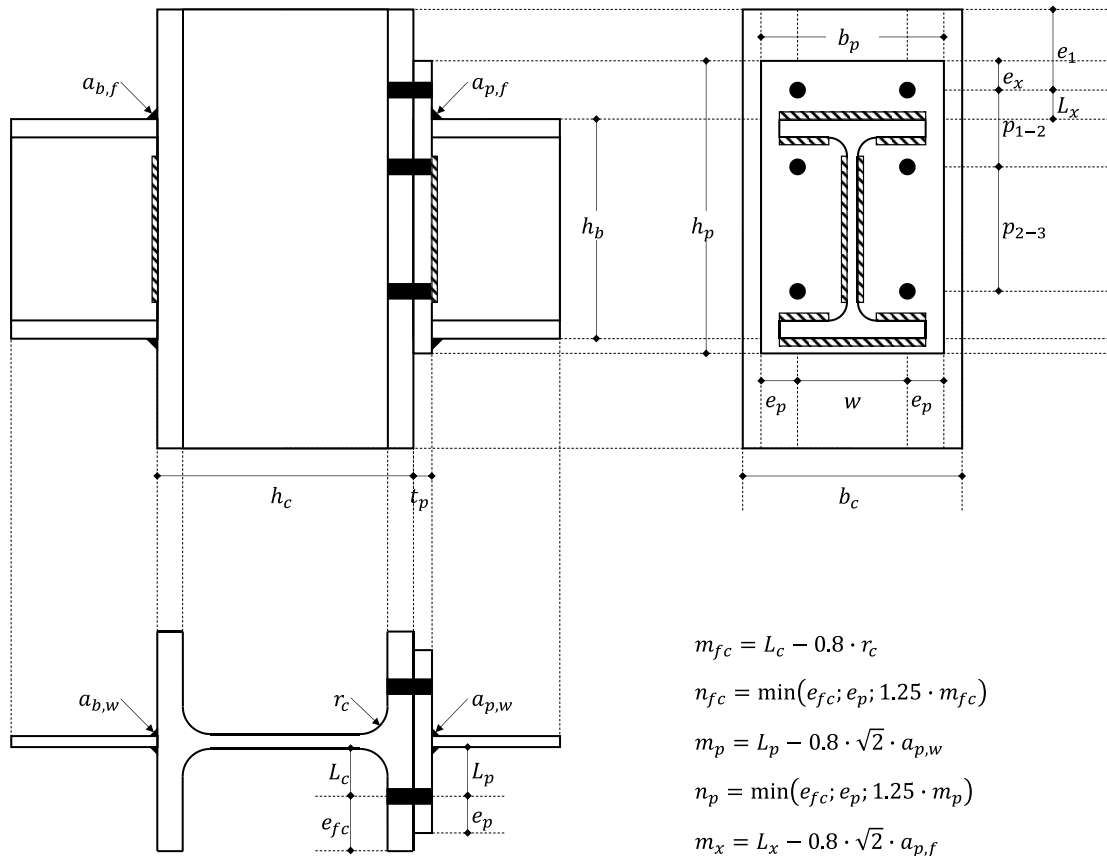
$$m_x = L_x - 0.8 \cdot \sqrt{2} \cdot a_{p,f}$$

Fig. 2-7. Definition of the main geometric parameters involved in Table 2-2, Table 2-3 and Table 2-4.

2.2.3 Limitations

The reliability of the method depends on both the quality of the characterization of the individual basic components (strength, stiffness and deformation capacity) and the ability of the mechanical model to combine these components correctly at the assembly level. These two aspects are addressed in the following Sections 2.2.3.1 and 2.2.3.2, respectively.

2.2.3.1 Characterization of the components

At the component level, EN 1993-1-8 provides analytical expressions for the characterization of two out of the four key properties of the components, i.e. the initial stiffness K_{ini}^c and the plastic resistance $F_{y,Rk}^c$, see Section 2.2.2.3. Based on these two parameters, a simplified elastic, perfectly-plastic $(F^c - \Delta^c)_{an}$ curve is built, as shown in Fig. 2-6. However, this model exhibits an infinite yield plateau since no information on the actual ductility of the individual components is provided in EN 1993-1-8. This model also neglects the influence of strain-hardening and consequently fails in predicting the components' ultimate resistance $F_{u,Rk}^c$ and deformation capacity Δ_u^c. For the characterization of the post-plastic behaviour of the components up to failure, it is referred to the scientific literature.

A preliminary study on the topic was conducted by Jaspart and his research team ([28]–[30]), which suggests implementing a simple methodology to account for strain-hardening. Each individual component is modelled by a trilinear relationship, as depicted by the blue dashed curves in Fig. 2-6(a). The first two branches are similar to the EN 1993-1-8 model. They can be described based on the expressions of the initial stiffness K_{ini}^c and the plastic resistance $F_{y,Rk}^c$. For the third branch, simple analytical expressions are provided for the strain-hardening (i.e. post-plastic) stiffness $K_{pp}^c = E \cdot k_{pp}^c$ of the components, based on the comparisons with numerous test results (see [28]). These expressions are illustrated in Eq. (2-12), where k_{pp}^c is the post-plastic stiffness coefficient, k_{ini}^c is the initial stiffness coefficient which is given in Table 2-2 for each basic component, E_{pp} is the strain-hardening modulus of the material (usually taken as $E/50$) and ν is the Poisson's ratio. Eq. (2-12) assumes that the components' post-plastic stiffness K_{pp}^c coincides with the one of the material constituting the components.

$$k_{pp}^c = \begin{cases} \dfrac{E_{pp}}{E} \cdot k_{ini}^c & c \sim \text{CWC, CWT, EPB or CFB} \\ \dfrac{2 \cdot (1 + \nu)}{3} \cdot \dfrac{E_{pp}}{E} \cdot k_{ini}^c & c \sim \text{CWS} \end{cases} \tag{2-12}$$

This preliminary study also suggests analytical expressions for the computation of the ultimate resistance $F_{u,Rk}^c$ and, consequently, the ultimate deformation capacity Δ_u^c. $F_{u,Rk}^c$ is easily obtained by substituting the material yield strength f_y by the material ultimate strength f_u in the formulae proposed in Table 2-2 for the characterization of the components' plastic resistance. Exception is made for the CWC and BFC components where the risk of local instability needs to be studied and could limit the development of strain-hardening, thus leading to a bilinear model, see Fig. 2-6(b). Knowing $F_{u,Rk}^c$, the ultimate deformation capacity Δ_u^c can be derived at the intersection between the post-plastic branch of the model and the $F_{u,Rk}^c$ horizontal line, as expressed through Eq. (2-13). Based on this new modelling of the components, Jaspart also proposed an extended version of the assembly procedure that is described in Section 2.2.2.4, in order to predict the joint's ultimate resistance $M_{u,Rk}^j$ and ultimate deformation capacity Φ_u (see the dashed blue curves in Fig. 2-3).

$$\Delta_u^c = max\left(\frac{F_{u,Rk}^c - F_{y,Rk}^c}{K_{pp}^c}; \frac{F_{el,Rk}^c}{K_{ini}^c} + \frac{F_{u,Rk}^c - F_{el,Rk}^c}{K_{ini}^c/7}\right) \tag{2-13}$$

Faella et al. proposed a similar approach in [31]. Other studies on the characterization of the components' post-plastic behaviour include the work of Kuhlmann and Kühnemund ([32], [33]) for the component associated to the compression zone (i.e. the CWC component) and the works of Piluso ([34], [35]), Girão Coelho [13], Faralli [36], Yan ([19], [20]) and Francavilla [37] for the components associated to the tension zone (i.e. the EPB, CFB and BT components, which are modelled using the T-stub approach). Beg and co-workers [14] also developed analytical expressions to predict the deformation capacity of the different individual basic components. These expressions were derived based on test results and numerical simulations. To date, no comprehensive study on the prediction of the full-range behaviour of the component associated with the shear zone (i.e. the CWS component) was found in the literature. This observation will be confirmed by the extensive literature review conducted in the forthcoming Section 2.3.1.

Despite these extensive research efforts spanning over the last 20 years, no consensus has been reached yet within the scientific community on the analytical expressions to be used to model the full behaviour up to failure of the different individual basic components. This demonstrates the need for additional research work before a thorough comprehension of the full $(F^c - \Delta^c)$ behaviour of each individual component is eventually achieved.

Based on this standpoint, several research projects were launched at the University of Liège on key components such as the CWC, CWS, CFB and EPB, as highlighted in CHAPTER 1 (see Section 1.2.1 and "WP1" in Fig. 1-2), the first results of which are already available. While the major outcomes of the CWS are extensively described within the present thesis (see "WP1A" in Fig. 1-2), the main conclusions related to the behaviour of the CWC (see "WP1C" in Fig. 1-2) can be found in ([21], [22]). In the latter, a new analytical approach, which was validated against numerous experimental results, is proposed for the prediction of the full $(F^c - \Delta^c)$ curve of the CWC. Through this study, possible improvements of the CWC plastic resistance have also been identified, potentially allowing a global increase of resistance of about 10% with a slight modification of the current formula given in Table 2-2. In the following, the acronym CWC* will be used when referring to this new analytical approach. Finally, the behaviour of the CFB and the EPB (see "WP1B" in Fig. 1-2) is currently being investigated within the CMM research team and preliminary results are expected soon.

These new full-range constitutive relationships for the different individual components can be introduced in mechanical models such as the ones illustrated in Fig. 2-4(b) and Fig. 2-5(b), thereby allowing the prediction of the joint's complete response when these components are activated at failure.

2.2.3.2 Assembly of the components

At the assembly level, EN 1993-1-8 applies an hybrid analytical-mechanical approach to derive the joint's overall $\left(M^j - \Phi\right)$ curve, as described in Section 2.2.2.4. For the derivation of the joint's stiffness S_{ini}^j, a mechanical model such as the ones presented in Fig. 2-4(b) and Fig. 2-5(b) is used and proves to work well. However, for the prediction of the bending moment resistance $M_{y,Rk}^j$, the use of such mechanical model is less appropriate as it disregards two key features which are likely to affect the joint's response, namely the group effects and the actual distribution of shear forces along the height of the CWP. As regards the group effects, EN 1993-1-8 provides the designer with additional analytical formulae (such as Eq. (2-11)) to verify the distribution of forces among the bolt-rows with respect to their individual and group resistances. For the definition of the shear force(s) acting on the PZ, EN 1993-1-8 suggests the use of an equivalent lever arm z_{eq}, which can be derived through a stiffness calculation (see Eq. (2-5)). This leads to the definition of a unique equivalent shear force V_{Ek}^{PZ} acting on the PZ, see Eq. (2-1). For welded joints with only two load-introduction rows such as the one depicted in Fig. 2-4, this definition seems relevant. On the contrary, for bolted joints with multiple load-introduction bolt-rows such as the one depicted in Fig. 2-5, this definition does not reflect

appropriately the actual distribution of the shear forces along the CWP height as, in reality, V_{Ek}^{PZ} varies along this height according to the loads introduced in the CWP by the connection rows.

In this context, a generalised innovative mechanical model has been developed within the CMM research team (see Section 1.2.1 and "WP2" in Fig. 1-2) and validated against experimental and analytical results. This model has been proven to overcome the limitations of the current EN 1993-1-8 mechanical model, thereby allowing to bypass the analytical procedure prescribed in EN 1993-1-8 for the characterization of the joint's plastic bending moment resistance $M_{y,Rk}^{j}$. Given the complexity of this model, its complete description turns out to be a rather tedious process. Therefore, it is purposely not reported here for sake of clarity of the present manuscript. The interested reader is referred to ([23], [24]) for more detailed information. Instead, to facilitate the reader's understanding, this new mechanical model is exemplified on the welded and bolted joint configurations considered in the present study, and the main features of the model are highlighted and discussed, see Fig. 2-4(c) and Fig. 2-5(c):

- As regards the group effects, they are simulated using fully rigid-plastic springs which can be seen as "fuse" elements with a plastic strength equal to the group resistance. This is illustrated in Fig. 2-5(c) for the group 1-2 (assuming that the 3rd bolt-row is not activated).
- As regards the modelling of the CWP, it is divided into a series of subpanels depending on the number of connecting rows. This modelling allows for the simulation of the actual deformation of the CWP while accounting for the variation of the shear force over the height of the CWP. This is illustrated in Fig. 2-5(c) for the exterior bolted joint. Assuming that the 3rd bolt-row is inactive, three load-introduction connection rows are contemplated on the height of the CWP, which is thus divided into two subpanels. By contrast, for the welded joint (see Fig. 2-4(c)), only two load-introduction rows are contemplated. Therefore, the equivalent lever arm z_{eq} is easily defined as the distance between the beam flanges centerlines, see Eq. (2-5), and the shear force is constant over the entire height of the CWP. For this specific case, there is no difference between the EN 1993-1-8 model (see Fig. 2-4(b)) and the new generalised mechanical model (see Fig. 2-4(c)).

2.3 BEHAVIOUR OF THE PANEL ZONE AS A JOINT COMPONENT

From now on, the acronym "CWS" referring to the "column web panel in shear" component will be replaced by the more generic "PZ" abbreviation, which designates the "sheared panel zone". As a reminder from Section 2.2.1, the PZ behaviour includes both contributions from the column web panel (CWP) and the surrounding elements (SE).

2.3.1 Literature review

Among the components described in Section 1.1, the sheared PZ is known to play a key role in the design of steel and steel-concrete composite joints as it can govern the joint resistance in a significant number of situations under static loads, but even more so under seismic loading conditions [38]. Moreover, when activated and appropriately designed, it is known to provide a reserve of ductility to the joint [39]. For all these reasons, a significant number of researchers have been studying its behaviour for more than 50 years.

Back to the '60s and early '70s, little attention was paid to the behaviour of the sheared PZ in the US, since the joints were usually modelled as rigid, full-strength elements in the structural analysis and designed as such. The philosophy behind this design approach was to force all plastic deformations (i.e. energy dissipation) to occur in the beams in case of an earthquake (strong PZ-weak beam philosophy). This design can only be achieved using welded connections rather than bolted ones, usually recognized as semi-rigid and partially resistant, and the heavy reinforcement of the PZ. This reinforcement mostly consisted in adding thick doubler plates, continuity plates (i.e. transverse column web stiffeners), possible diagonal stiffeners and heavy welding to the PZ, thus leading to rather uneconomical design solutions. Furthermore, in this solution, the welded connections, especially the weld detailing, required much more attention since the latter could undergo severe stress concentration under seismic loading conditions. Consequently, several experimental investigations were carried out at that time in the US (e.g. [40], [41]) on full-scale connection tests to determine the cyclic performances of different welded connection detailings.

From the '70s, extensive research effort spanning over 20 years was carried out in the US and in Japan to investigate the inelastic PZ behaviour under both monotonic and cyclic loading conditions. To this aim, numerous full-scale tests on beam-to-column sub-assemblies were conducted ([42]–[48], see also [41], [49] for a review of these experimental campaigns). Two major observations were made from these tests, which can be summarized as follows: (1) the significant strain-hardening which can be observed after the shear yielding of the CWP may be attributed not only to the material strain-hardening but also to the contribution of the SE, i.e. the column flanges, the root fillets and the possible transverse column web stiffeners; (2) the PZ may have a ductile and stable hysteretic behaviour that could enhance the energy dissipation capacity and also contribute to a reduction of the inelastic demands imposed on the beams. From these observations, new advanced analytical (i.e. Fielding [50], Krawinkler [51], [52], and Wang [53]) and semi-empirical (Kato [54], Matsuo [55]) models were developed for the characterization of the PZ elastic and inelastic shear behaviours. These models are usually presented in terms of a trilinear $(V^{PZ} - \gamma^{PZ})$ relationship, V^{PZ} and γ^{PZ} being the PZ shear strength and shear distortion. They exhibit an initial elastic behaviour up to the yielding of the CWP, followed by two plastic branches, the former accounting for the SE contribution, and the latter for the material strain-hardening. The accurate characterization of the PZ behaviour was a necessary preliminary step to reliably mobilize the PZ in the seismic energy dissipation. Among the models listed above, the Krawinkler model quickly became the most popular one, mainly due to its

ease of use and good performance, especially for the range of thin to medium column flanges. However, some studies ([52], [56]–[58]) pointed out that this model may not work well for cases with very thick column flanges, i.e. $t_{fc} > 30 - 40\ mm$. Therefore, this model was introduced in the US seismic design provisions with minor modifications to take into account the beneficial effects provided by the SE, thereby reducing the costs related to extensive joint welding. This change in the design philosophy, moving from a strong to a balanced PZ approach, resulted in a more significant influence from the PZ on the overall lateral stiffness and strength of the moment resisting frames ([54], [59]–[62]). The consideration of weaker PZs also imposed the need for more advanced joint models at the frame analysis stage to explicitly account for the PZ behaviour ([57], [62]–[66]).

However, the 1994 Northridge earthquake in California and the 1995 Kobe earthquake in Japan revealed the limitations of the new seismic design provisions. Although the moment-resisting frame structures and buildings were thought to be properly designed and met the seismic design requirements, extensive damage were observed in the aftermath of these earthquakes due to widespread unexpected brittle failures in the welded beam-to-column connections at the level of the tension flanges. Consequently, significant research efforts were carried out in the second part of the '90s with the aim of (1) understanding the causes of the observed damages, (2) assessing the main parameters affecting the cyclic behaviour of welded beam-to-column connections and (3) suggesting improvements to the connection configurations. To this aim, numerous full-scale tests on beam-to-column sub-assemblies were performed in the US ([67]–[74]), in Japan ([75]–[80]) and in Europe ([81]–[86]). An extensive review of these experimental campaigns is provided in [49].

From these research efforts, it was concluded that a number of factors weakened the welded connections, leaving them susceptible to brittle failure [87]. These factors include ([64], [84], [87]): (1) the welding type and procedure (potential welding defects), (2) the detailing (stress concentration in the welds due to PZ yielding), (3) the steel properties, (4) unusually high seismic input and (5) the beam size and geometry. Among them, the excessive inelastic PZ distortions allowed by the seismic design provisions resulted in local kinking of the column flanges, placing a high stress and strain demand on the welds at the beam-to-column interface. Without sufficient ductility and proper detailing, these welds were thus susceptible to fail by fracture. Numerical simulations confirmed this observation ([56], [80]). As a result of these research efforts, new configurations of beam-to-column connections were proposed in the US, together with repairment and upgrade strategies [87]. These research efforts also led to the formulation of new seismic design criteria for the PZ, prescribing a balanced design approach ([87], [88]). In this approach, the flexural yielding of the beam is targeted, directly followed by the limited yielding of the PZ. By contrast, the European seismic code [89] shifted from a potentially weak PZ approach to a more conservative strong PZ approach. The same method was prescribed by the Japanese and Chinese seismic codes ([90], [91]). As regards the European and American strategies, they were critically reviewed in ([64], [92]–[95]). The differences in the current seismic provisions between these two approaches reflect the uncertainty among the scientific community in estimating the actual contribution of the PZ to the inelastic response of the joint and whether the yielding of the PZ should be allowed ([64], [92]). The current European, American, Japanese and Chinese seismic design approaches for the PZ will be reviewed in more detail in the forthcoming Section 2.3.3.

The Northridge and Kobe earthquakes are also at the origin of a renewed interest in the development of more robust analytical models to simulate the inelastic PZ behaviour. In less than 20 years, several new analytical models were proposed (i.e. Schneider [62], Lin [70], Engelhardt [57], Namba [76], Castro [63], Kim [73], Mansouri [65]). Most of these models were built upon previously developed models and aimed to address the limitations of the Krawinkler model (see above), by introducing a number of new features and refinements. These refinements include for instance the consideration of both shear and bending deformation modes, or the use of distinct effective shear areas A_{VC}. The validation of these models was carried out through comparisons with experimental and numerical

results. However, the scientific community has not yet reached a consensus on an improved PZ model to be used in the seismic design of steel moment resisting frames [58]. An extensive review of the most referenced analytical models is performed in the forthcoming Section 2.3.2, where the assumptions and limitations of each model are highlighted and discussed.

In Europe, the use of bolted beam-to-column connections, either stiffened or not, is much more widespread than in the US, where the site-welded beam-to-column connection remains the common practice. Given the semi-rigid nature of the bolted joints, it was of primary importance to characterize the rotational response of the latter, first under monotonic loading [28], before extending the findings to cyclic loading conditions ([81], [84], [96]–[98]). These research efforts, which were carried out in the late 1980s and early 1990s, resulted in the proposition of a new method for the characterization of steel and steel-concrete composite joints, known as the component method. This method was introduced in EN 1993-1-8 and is nowadays recognised as the reference method in Europe for the design of joints under monotonic loading. Its popularity grew tremendously throughout the years due to its accuracy yet simplicity and its great flexibility for the designer compared to the prequalified joints approach recommended in the US. Its scope is now being extended to more complex loading conditions, either at room temperature [4], or under fire [5], dynamic [6] or cyclic ([7], [8]) loadings. The component method was extensively described in Section 2.2.2. As a reminder, this method allows predicting the $\left(M^j - \Phi\right)$ curve of a joint using a three-step procedure which relies on the identification, characterization, and assembly of the basic components active in the joint.

As regards the characterization of the PZ component, and more generally of all the components active in the CWP, including the CWC/CWT components, the first major contribution was made by Zoetemeijer [99], who defined the relevant stress interactions to be accounted for in the CWP, leading to the development of analytical models for the CWC/CWT components. Following this work, an extensive experimental programme on welded joints was launched at the University of Innsbruck ([100]–[103]) with the aim of separately characterizing the behaviour of the sheared component (i.e. the PZ) and that of the load-introduction ones (i.e. CWC/CWT). Some of these experimental results were later used by Atamaz and Frey [104] to perform some numerical studies. These results were exploited by Atamaz and Jaspart [105] and Jaspart ([28], [106], [107]) to derive multi-linear analytical models for the PZ, CWC and CWT components. These models were introduced in EN 1993-1-8 with some minor modifications [106]. Similarly to the Krawinkler model in the US design code, the PZ model proposed by Jaspart remains today the reference in the modern version of EN 1993-1-8.

Recent studies on the PZ behaviour mainly aim at extending the scope of the current PZ design provisions. A non-exhaustive survey of some of these research projects is suggested here below. For instance, Girão Coelho ([108]–[111]) investigated the sheared behaviour of PZs made of high strength steel (HSS) S690 and S960 relying on experimental and numerical studies. Results are also compared with the design provisions adopted in EN 1993-1-8 and conclusions are drawn. Jordao ([112], [113]) developed a new mechanical model for the characterisation of internal joints with beams of unequal depth, based on experimental and numerical studies. In this model, the PZ is divided into two sub-panels to account for the unequal beam depths. Jordao also investigated the applicability of this new modelling approach for internal joints made of HSS S690. Brandonisio [114] examined the shear buckling issue in the PZ by comparing the European and American code provisions to experimental and numerical results. Based on these comparisons, some possible improvements of the design criteria were suggested. Finally, Skiadopoulos [58] has recently developed a new PZ model for the seismic design of beam-to-column joints in steel moment resisting frames. This model was derived and calibrated based on the careful analysis of realistic shear stress distributions within the PZ, obtained from continuum FE analyses of representative PZ geometries. To assess the performance of the model, a comprehensive experimental data set of 100 tests was built [115], with an emphasis on those exhibiting inelastic PZ behaviour. Comparisons between analytical and experimental results showed a very good agreement.

2.3.2 Complex analytical models

2.3.2.1 General description

From Section 2.3.1, it can be seen that over the last 50 years, significant research efforts have been dedicated to the development of reliable multi-linear analytical models for characterizing the PZ sheared behaviour. As discussed in Section 2.2.2, such component models are required to predict as accurately as possible the actual joint behaviour, using mechanical models such as the ones presented in Fig. 2-4(c) and Fig. 2-5(c) for instance, so that the joint behaviour can be subsequently taken into account in the frame analysis.

Therefore, some of the most referenced scientific models introduced in Section 2.3.1 are reviewed in more detail in the present Section 2.3.2. This non-exhaustive sample includes the following ten analytical models, namely the Fielding (1971, [50]), Krawinkler (1971 [51] and 1978 [52]), Wang (1988, [53]), Jaspart (1991, [28]), Schneider (1998, [62]), Lin (2000, [70]), Engelhardt (2002, [57]), Kim (2015, [73]) and Skidaopoulos (2021, [58]) models. These models are presented in detail in Table 2-5, Table 2-6 and Table 2-7, where the same formalism has been used for all of them in order to facilitate their comparison.

From these tables, it can be observed that all the authors express the behaviour of the PZ (see the blue $(V^{PZ} - \gamma^{PZ})_{an}$ curves in Table 2-5 to Table 2-7) as the sum of two independent contributions. The first contribution accounts for the behaviour of the CWP (see the orange $(V^{CWP} - \gamma^{CWP})_{an}$ curves in Table 2-5 to Table 2-7). This contribution exhibits either a bilinear, trilinear or quad-linear shape. The second contribution accounts for the beneficial frame effect provided by the SE elements (see the green $(\Delta V^{SE} - \gamma^{SE})_{an}$ curves in Table 2-5 to Table 2-7). This contribution exhibits a bilinear shape in all the models. As a reminder, the SE consist of the column flanges, the root fillets and the transverse column web stiffeners, aligned with the beam(s) flanges, if any. Since these two contributions are assumed to behave independently, they can be studied separately and then superimposed through Eq. (2-14) and Eq. (2-15) to get the full non-linear model up to failure of the whole PZ.

$$V^{PZ} = V^{CWP} + \Delta V^{SE} \qquad (2\text{-}14)$$

$$K^{PZ} = K^{CWP} + K^{SE} \qquad (2\text{-}15)$$

The contributions of the CWP and the SE will be studied in detail in the following Sections 2.3.2.2 and 2.3.2.3 for each individual model, with a strong focus on the assumptions and limitations of each model. The capabilities of these scientific models will be assessed further below through comparisons with available experimental results, collected from the scientific literature (see CHAPTER 3). Based on these comparisons, the strengths and weaknesses of each individual model will be highlighted and discussed. The information presented in the following Sections 2.3.2.2 and 2.3.2.3 is not exhaustive. The interested reader is referred to the given references for more detailed information about the models.

Table 2-5. Description of the Fielding (1971), Krawinkler (1971), Krawinkler (1978) and Wang (1988) models.

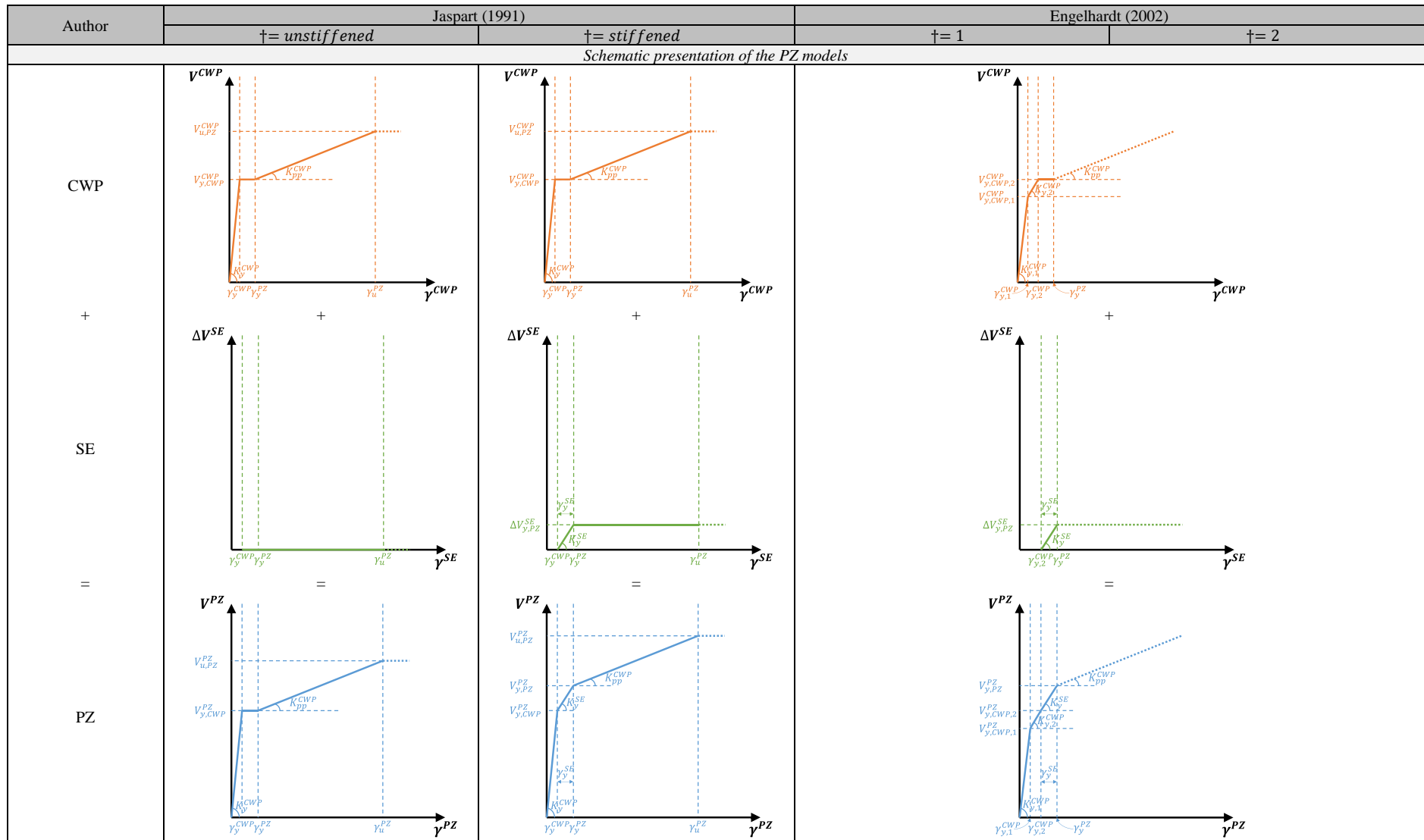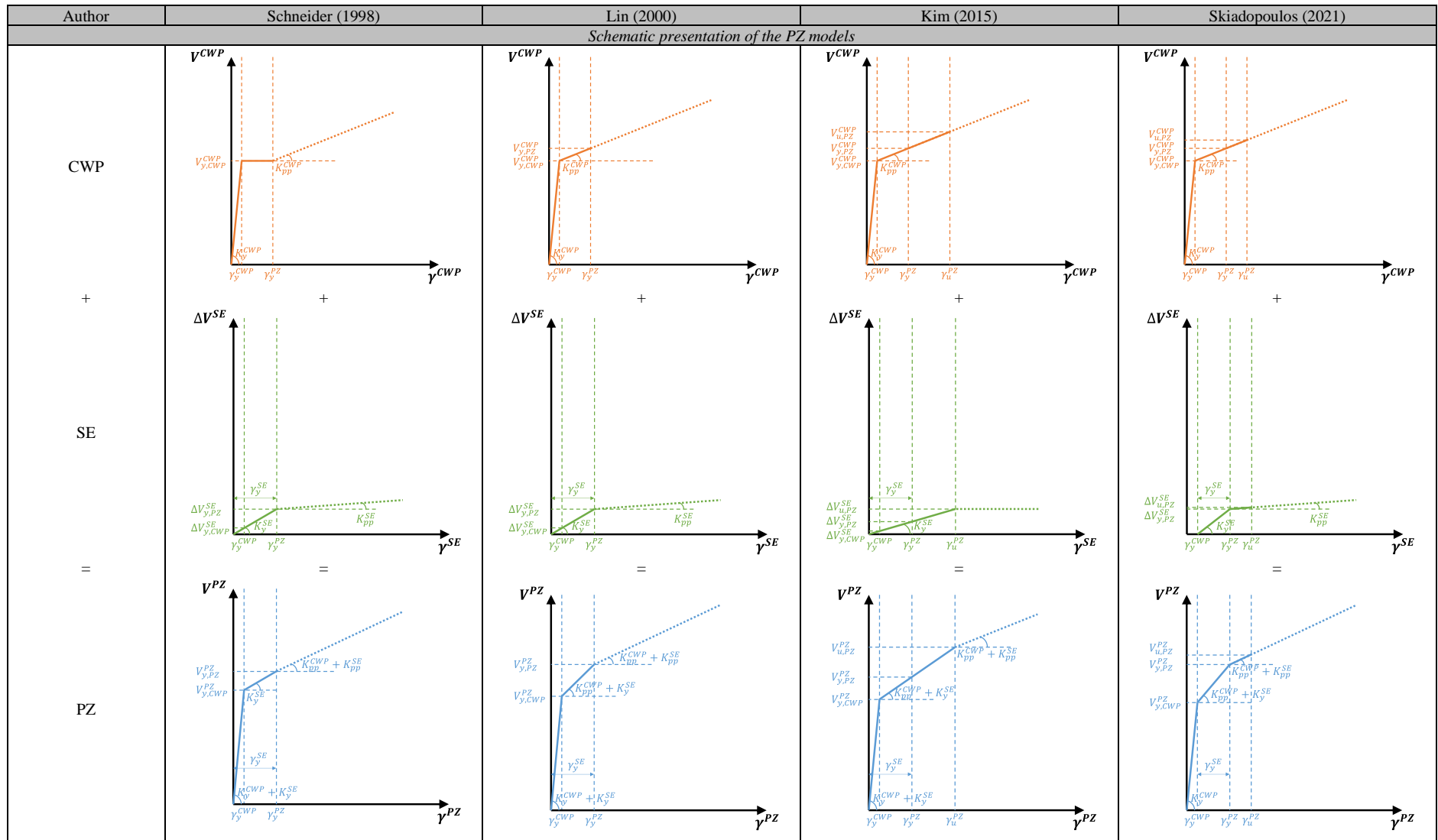| Description of the main parameters of the models				
K_y^{CWP}	$G \cdot A_{VC}$	$G \cdot A_{VC}$	$G \cdot A_{VC}$	$G \cdot A_{VC}$
K_{pp}^{CWP}	0	$G_{pp} \cdot A_{VC}$	$G_{pp} \cdot A_{VC}$	$G_{pp} \cdot A_{VC}$
K_y^{SE}	$24 \cdot \alpha \cdot \frac{E \cdot I_{fc}}{d_b^{*2}}$	$4.8 \cdot \alpha \cdot \frac{E \cdot I_{fc}}{d_b^{*2}}$	$4.8 \cdot \alpha \cdot \frac{E \cdot I_{fc}}{d_b^{*2}}$	$3.2 \cdot \alpha \cdot \frac{E \cdot I_{fc}}{d_b^{*2}}$
K_{pp}^{SE}	/	0	0	0
$V_{y,CWP}^{CWP}$	$C_y^{CWP} \cdot \chi_i \cdot \chi_n \cdot A_{VC} \cdot \tau_y$	$C_y^{CWP} \cdot \chi_i \cdot \chi_n \cdot A_{VC} \cdot \tau_y$	$C_y^{CWP} \cdot \chi_i \cdot \chi_n \cdot A_{VC} \cdot \tau_y$	$C_y^{CWP} \cdot \chi_i \cdot \chi_n \cdot A_{VC} \cdot \tau_y$
$V_{y,PZ}^{CWP}$	/	$\Delta C_y^{CWP} \cdot \chi_i \cdot \chi_n \cdot A_{VC} \cdot \tau_y$	$\Delta C_y^{CWP} \cdot \chi_i \cdot \chi_n \cdot A_{VC} \cdot \tau_y$	$\Delta C_y^{CWP} \cdot \chi_i \cdot \chi_n \cdot A_{VC} \cdot \tau_y$
$V_{u,PZ}^{CWP}$	/	/	/	/
$\Delta V_{y,CWP}^{SE}$	0	0	0	0
$\Delta V_{y,PZ}^{SE}$	/	$7.2 \cdot \frac{M_{pl,fc}}{d_b^*} \cdot \Delta \chi_n$	$7.2 \cdot \frac{M_{pl,fc}}{d_b^*} \cdot \Delta \chi_n$	$4 \cdot \frac{M_{pl,fc}}{d_b^*} \cdot \Delta \chi_n$
$\Delta V_{u,PZ}^{SE}$	/	/	/	/
γ_y^{CWP}	$\frac{V_{y,CWP}^{CWP}}{K_y^{CWP}}$	$\frac{V_{y,CWP}^{CWP}}{K_y^{CWP}}$	$\frac{V_{y,CWP}^{CWP}}{K_y^{CWP}}$	$\frac{V_{y,CWP}^{CWP}}{K_y^{CWP}}$
γ_y^{SE}	/	$\gamma_y^{PZ} - \gamma_y^{CWP}$	$\gamma_y^{PZ} - \gamma_y^{CWP}$	$\gamma_y^{PZ} - \gamma_y^{CWP}$
γ_y^{PZ}	/	$4 \cdot \gamma_y^{CWP}$	$4 \cdot \gamma_y^{CWP}$	$3.5 \cdot \gamma_y^{CWP}$
γ_u^{PZ}	/	/	/	/
Description of additional relevant parameters				
A_{VC}	$d_c^* \cdot t_{wc}$	$d_c^* \cdot t_{wc}$	$d_c^* \cdot t_{wc}$	$d_c^* \cdot t_{wc}$
d_c^*	$h_c - t_{fc}$	$h_c - t_{fc}$	$0.95 \cdot h_c$	$h_c - 2 \cdot t_{fc}$
d_b^*	$h_b - t_{fb}$	h_b	$0.95 \cdot h_b$	$h_b - t_{fb}$
C_y^{CWP}	1.0	1.0	1.0	1.0
ΔC_y^{CWP}	/	1.0	1.0	1.0
χ_i	1.0	1.0	1.0	1.0
χ_n	$\sqrt{1 - n_c^2}$	$\sqrt{1 - n_c^2}$	$\sqrt{1 - n_c^2}$	$\sqrt{1 - n_c^2}$
$\Delta \chi_n$	/	$\sqrt{1 - n_c^2}$	$\sqrt{1 - n_c^2}$	$\sqrt{1 - n_c^2}$
C_u^{CWP}	/	/	/	/
χ_n'	/	/	/	/
G_{pp}	/	$0.03 \cdot G$	$0.03 \cdot G$	$0.03 \cdot G$
α	1.0	d_b^*/t_{fc}	d_b^*/t_{fc}	d_b^*/t_{fc}

Notes :

- $n_c = N_c/N_{pl,c}$ where N_c is the resulting axial load applied at the top of the PZ and $N_{pl,c}$ is the plastic resistance of the column cross-section
- $I_{fc}, M_{pl,fc}$: second moment of area and plastic moment resistance of a rectangular column flange
- h_c (resp. h_b), t_{fc} (resp. t_{fb}), t_{wc}: geometric properties of the column (resp. beam) cross-section
- E, G, τ_y: mechanical properties of the steel material

Table 2-6. Description of the Jaspart (1991) and Engelhardt (2002) models.

Author	Jaspart (1991)		Engelhardt (2002)	
	†= unstiffened	†= stiffened	†= 1	†= 2
	Schematic presentation of the PZ models			
CWP				
+	+	+	+	
SE				
=	=	=	=	
PZ				

	Description of the main parameters of the models			
$K_{y,\dagger}^{CWP}$	$G \cdot A_{VC}$		$\frac{K_{y,sh,\dagger}^{CWP} \cdot K_{y,b,\dagger}^{CWP}}{K_{y,sh,\dagger}^{CWP}+K_{y,b,\dagger}^{CWP}}$	$2 \cdot \frac{K_{y,sh,\dagger}^{CWP} \cdot K_{y,b,\dagger}^{CWP}}{K_{y,sh,\dagger}^{CWP}+K_{y,b,\dagger}^{CWP}}$
$K_{pp,\dagger}^{CWP}$	$G_{pp} \cdot A_{VC}$		$G_{pp} \cdot A_{VC}$	
$K_{y,\dagger}^{SE}$	0	$24 \cdot \alpha \cdot \frac{E \cdot I_{fc}}{d_b^{*2}}$	$2.4 \cdot \alpha \cdot \frac{E \cdot I_{fc}}{d_b^{*2}}$	
$K_{pp,\dagger}^{SE}$	0		$/$	
$V_{y,CWP,\dagger}^{CWP}$	$C_y^{CWP} \cdot \chi_i \cdot \chi_n \cdot A_{VC} \cdot \tau_y$		$C_y^{CWP} \cdot \chi_i \cdot \chi_n \cdot A_{VC} \cdot \tau_y$	$\Delta C_y^{CWP} \cdot \chi_i \cdot \chi_n \cdot A_{VC} \cdot \tau_y$
$V_{y,PZ,\dagger}^{CWP}$	$\Delta C_y^{CWP} \cdot \chi_i \cdot \chi_n \cdot A_{VC} \cdot \tau_y$		$V_{y,CWP,2}^{CWP}$	
$V_{u,PZ,\dagger}^{CWP}$	$C_u^{CWP} \cdot \chi_i \cdot \chi_n' \cdot A_{VC} \cdot \tau_u$		$/$	
$\Delta V_{y,CWP,\dagger}^{SE}$	0		0	0
$\Delta V_{y,PZ,\dagger}^{SE}$	0	$4 \cdot \frac{M_{pl,fc}}{d_b^*} \cdot \Delta\chi_n$	$4 \cdot \frac{M_{pl,fc}}{d_b^*} \cdot \Delta\chi_n$	
$\Delta V_{u,PZ,\dagger}^{SE}$	$\Delta V_{y,PZ,\dagger}^{SE}$	$\Delta V_{y,PZ,\dagger}^{SE}$	$/$	
$\gamma_{y,\dagger}^{CWP}$	$\frac{V_{y,CWP,\dagger}^{CWP}}{K_{y,\dagger}^{CWP}}$		$\frac{V_{y,CWP,\dagger}^{CWP}}{K_{y,\dagger}^{CWP}}$	$\gamma_{y,1}^{CWP}+\frac{V_{y,CWP,\dagger}^{CWP}-V_{y,CWP,1}^{CWP}}{K_{y,\dagger}^{CWP}}$
$\gamma_{y,\dagger}^{SE}$	$\gamma_{y,\dagger}^{PZ}-\gamma_{y,\dagger}^{CWP}$	$\frac{\Delta V_{y,PZ,\dagger}^{SE}}{K_{y,\dagger}^{SE}}$	$\frac{\Delta V_{y,PZ,\dagger}^{SE}}{K_{y,\dagger}^{SE}}$	
$\gamma_{y,\dagger}^{PZ}$	$0.5 \cdot [\gamma_{y,\dagger}^{CWP}+\sqrt{3}\cdot(\varepsilon_{pp}-\varepsilon_y)]$	$\gamma_{y,\dagger}^{CWP}+\gamma_{y,\dagger}^{SE}$	$\gamma_{y,2}^{CWP}+\gamma_{y,\dagger}^{SE}$	
$\gamma_{u,\dagger}^{PZ}$	$\gamma_{y,\dagger}^{PZ}+\frac{V_{u,PZ,\dagger}^{CWP}-V_{y,PZ,\dagger}^{CWP}}{K_{pp,\dagger}^{CWP}}$	$\gamma_{y,\dagger}^{PZ}+\frac{V_{u,PZ,\dagger}^{CWP}-V_{y,PZ,\dagger}^{CWP}}{K_{pp,\dagger}^{CWP}}$	$/$	
	Description of additional relevant parameters			
A_{VC}	$\begin{cases} A_c - 2 \cdot b_c \cdot t_{fc} + (t_{wc} + 2 \cdot r_c) \cdot t_{fc} & \text{hot}-\text{rolled sections} \\ 1.2 \cdot h_{ic} \cdot t_{wc} & \text{built}-\text{up sections} \end{cases}$		$d_c^* \cdot t_{wc}$	
d_c^*	$h_c - t_{fc}$		h_c	
d_b^*	$h_b - t_{fb}$		$h_b - t_{fb}$	
C_y^{CWP}	1.0		$0.8 - 0.9$	
ΔC_y^{CWP}	1.0		1.0	
χ_i	1.0		1.0	
χ_n	$\sqrt{1-(m_c+n_c)^2}$		$\sqrt{1-n_c^2}$	
$\Delta\chi_n$	1.0		$1-n_c^2$	
C_u^{CWP}	1.0		$/$	
χ_n'	$\sqrt{1-(m_c'+n_c')^2}$		$/$	
G_{pp}	$\sim 0.02 \cdot G$		$0.03 \cdot G$	
α	1.0		d_b^*/t_{fc}	

Notes :
- $n_c = N_c/N_{pl,c}$, $m_c = M_c/M_{pl,c}$, $n_c' = N_c/N_{u,c}$, $m_c' = M_c/M_{u,c}$ where N_c and M_c are the resulting axial load and bending moment applied at the top of the PZ
- $K_{y,sh,1}^{CWP} = G \cdot A_{VC}$, $K_{y,b,1}^{CWP} = \frac{20 \cdot E \cdot I_c}{d_b^{*2}}$, $K_{y,sh,2}^{CWP} = G \cdot \left(\frac{h_c}{2} - \frac{d_c}{4}\right) \cdot t_{wc}$, $K_{y,b,2}^{CWP} = \frac{20 \cdot E \cdot I_{fc,T}}{d_b^{*2}}$ where $I_{fc,T}$ is the 2nd moment of area of a T-shaped column flange including ¼ of the column web depth
- $I_c, N_{pl,c}, N_{u,c}, M_{pl,c}, M_{u,c}$: 2nd moment of area, plastic resistance, ultimate resistance, plastic moment resistance and ultimate moment resistance of the column cross-section
- $I_{fc}, M_{pl,fc}$: 2nd moment of area and plastic moment resistance of a rectangular column flange
- h_c (resp. h_b), b_c, d_c, t_{fc} (resp. t_{fb}), t_{wc}, r_c, A_c, h_{ic}: geometric properties of the column (resp. beam) cross-section
- $E, G, \tau_y, \tau_u, \varepsilon_y, \varepsilon_{pp}$: mechanical properties of the steel material

Table 2-7. Description of the Schneider (1998), Lin (2000), Kim (2015) and Skiadopoulos (2021) models.

Author	Schneider (1998)	Lin (2000)	Kim (2015)	Skiadopoulos (2021)
	Schematic presentation of the PZ models			
CWP				
+	+	+	+	+
SE				
=	=	=	=	=
PZ				

	Description of the main parameters of the models			
K_y^{CWP}	$G \cdot A_{VC}$	$G \cdot A_{VC}$	$G \cdot A_{VC}$	K_e^{CWP}
K_{pp}^{CWP}	/	$G_{pp} \cdot A_{VC}$	$G_{pp} \cdot A_{VC}$	$\frac{V_u^{CWP} - V_y^{CWP}}{\gamma_u - \gamma_y}$
K_y^{SE}	$4 \cdot \alpha \cdot \frac{E \cdot I_{fc}}{d_b^{*2}}$	$24 \cdot \alpha \cdot \frac{E \cdot I_{fc}}{d_b^{*2}}$	$24 \cdot \frac{\alpha^2}{\alpha^2 + 3.45} \cdot \frac{E \cdot I_{fc}}{d_b^{*2}}$	$\frac{\Delta V_{y,PZ}^{SE}}{\gamma_y^{PZ} - \gamma_y}$
K_{pp}^{SE}	/	/	0	$\frac{\Delta V_u^{SE} - \Delta V_{y,PZ}^{SE}}{\gamma_u - \gamma_y^{PZ}}$
$V_{y,CWP}^{CWP}$	$C_y^{CWP} \cdot \chi_i \cdot \chi_n \cdot A_{VC} \cdot \tau_y$	$C_y^{CWP} \cdot \chi_i \cdot \chi_n \cdot A_{VC} \cdot \tau_y$	$C_y^{CWP} \cdot \chi_i \cdot \chi_n \cdot A_{VC} \cdot \tau_y$	$C_y^{CWP} \cdot \chi_i \cdot \chi_n \cdot A_{VC} \cdot \tau_y$
$V_{y,PZ}^{CWP}$	$\Delta C_y^{CWP} \cdot \chi_i \cdot \chi_n \cdot A_{VC} \cdot \tau_y$	$\Delta C_y^{CWP} \cdot \chi_i \cdot \chi_n \cdot A_{VC} \cdot \tau_y$	$\Delta C_y^{CWP} \cdot \chi_i \cdot \chi_n \cdot A_{VC} \cdot \tau_y$	$\Delta C_y^{CWP} \cdot \chi_i \cdot \chi_n \cdot A_{VC} \cdot \tau_y$
$V_{u,PZ}^{CWP}$	/	/	$C_u^{CWP} \cdot \chi_i \cdot \chi_n' \cdot A_{VC} \cdot \tau_y$	$C_u^{CWP} \cdot \chi_i \cdot \chi_n' \cdot A_{VC} \cdot \tau_y$
$\Delta V_{y,CWP}^{SE}$	$K_y^{SE} \cdot \gamma_y^{CWP}$	$K_y^{SE} \cdot \gamma_y^{CWP}$	$K_y^{SE} \cdot \gamma_y^{CWP}$	0
$\Delta V_{y,PZ}^{SE}$	$4 \cdot \frac{M_{pl,fc}}{d_b^*} \cdot \Delta \chi_n$	$K_y^{SE} \cdot \gamma_y^{PZ}$	$K_y^{SE} \cdot \gamma_y^{PZ}$	$2 \cdot \Delta C_y^{SE} \cdot \Delta \chi_n \cdot A_{fc}^* \cdot \tau_y$
$\Delta V_{u,PZ}^{SE}$	/	/	$4 \cdot \frac{M_{pl,fc}}{d_b^*} \cdot \Delta \chi_n$	$2 \cdot C_u^{SE} \cdot \Delta \chi_n \cdot A_{fc}^* \cdot \tau_y$
γ_y^{CWP}	$\frac{V_{y,CWP}^{CWP}}{K_y^{CWP}}$	$\frac{V_{y,CWP}^{CWP}}{K_y^{CWP}}$	$\frac{V_{y,CWP}^{CWP}}{K_y^{CWP}}$	$\frac{V_{y,CWP}^{CWP}}{K_y^{CWP}}$
γ_y^{SE}	$\frac{\Delta V_{y,PZ}^{SE}}{K_y^{SE}}$	$4 \cdot \frac{\gamma_y^{CWP}}{C_y^{CWP}}$	$4 \cdot \gamma_y^{CWP}$	$\gamma_y^{PZ} - \gamma_y^{CWP}$
γ_y^{PZ}	γ_y^{SE}	γ_y^{SE}	γ_y^{SE}	$4 \cdot \gamma_y^{CWP}$
γ_u^{PZ}	/	/	$\frac{\Delta V_{u,PZ}^{SE}}{K_y^{SE}}$	$6 \cdot \gamma_y^{CWP}$
	Description of additional relevant parameters			
A_{VC}	$d_c^* \cdot t_{wc}$	$d_c^* \cdot t_{wc}$	$d_c^* \cdot t_{wc}$	$d_c^* \cdot t_{wc}$
d_c^*	$h_c - t_{fc}$	$h_c - 2.3 \cdot t_{wc}$	$0.95 \cdot h_c$	$h_c - t_{fc}$
d_b^*	$h_b - t_{fb}$	$0.95 \cdot h_b$	$0.95 \cdot h_b$	h_b
C_y^{CWP}	1.0	1.25	1.0	$[0.58 \cdot (K_e^{SE}/K_e^{CWP}) + 0.88]/[1 - (K_e^{SE}/K_e^{CWP})]$
ΔC_y^{CWP}	1.0	~ 1.4	1.09	1.1
χ_i	1.0	1.0	1.0	1.0
χ_n	$\sqrt{1 - n_c^2}$	$\sqrt{1 - n_c^2}$	1.0	$\sqrt{1 - n_c^2}$
$\Delta \chi_n$	$\sqrt{1 - n_c^2}$	$\sqrt{1 - n_c^2}$	$1 - n_{fc}^2$	$\sqrt{1 - n_c^2}$
C_u^{CWP}	/	/	$0.97 + 0.009 \cdot (\alpha + 3.45/\alpha) \cdot \Delta \chi_n$	1.15
χ_n'	/	/	1.0	$\sqrt{1 - n_c^2}$
G_{pp}	/	$0.05 \cdot G$	$0.03 \cdot G$	/
α	$d_b^{*2}/[t_{fc} \cdot (d_b^* - 2 \cdot t_{fc})]$	1.0	d_b^*/t_{fc}	/

Notes :

- $n_c = N_c/N_{pl,c}$, $n_{fc} = 0.5 \cdot N_c/N_{pl,fc}$ where N_c is the resulting axial load applied at the top of the PZ
- $\Delta C_y^{SE} = 0.93 \cdot (K_e^{SE}/K_e^{CWP}) + 0.015$, $C_u^{SE} = 1.05 \cdot (K_e^{SE}/K_e^{CWP}) + 0.02$, $A_{fc}^* = (b_c - t_{wc}) \cdot t_{fc}$
- $K_e^{CWP} = \frac{K_{y,sh}^{CWP} \cdot K_{y,b}^{CWP}}{K_{y,sh}^{CWP} + K_{y,b}^{CWP}}$ and $K_e^{SE} = 2 \cdot \frac{K_{y,sh}^{SE} \cdot K_{y,b}^{SE}}{K_{y,sh}^{SE} + K_{y,b}^{SE}}$, with $K_{y,sh}^{CWP} = G \cdot A_{VC}$, $K_{y,b}^{CWP} = \frac{12 \cdot E \cdot I_c}{d_b^{*2}}$, $K_{y,sh}^{SE} = G \cdot (b_c \cdot t_{fc})$ and $\Delta K_{y,b}^{CWP} = \frac{12 \cdot E \cdot I_{fc}}{d_b^{*2}}$
- I_c, $N_{pl,c}$: 2nd moment of area and plastic resistance of the column cross-section
- I_{fc}, $N_{pl,fc}$, $M_{pl,fc}$: 2nd moment of area, plastic resistance and plastic moment resistance of a rectangular column flange
- h_c (resp. h_b), b_c, t_{fc} (resp. t_{fb}), t_{wc}: geometric properties of the column (resp. beam) cross-section
- E, G, τ_y: mechanical properties of the steel material

2.3.2.2 Contribution of the CWP

A. *Characterization of the CWP resistance*

The different analytical models presented in Table 2-5 to Table 2-7 (see the orange $(V^{CWP} - \gamma^{CWP})_{an}$ curves) exhibit three main values of resistance, namely:

- $V_{y,CWP}^{CWP}$ (i.e. $V^{CWP}(\gamma_y^{CWP})$ or $V_{y,CWP,Rk}^{CWP}$): the plastic shear resistance of the CWP;
- $V_{y,PZ}^{CWP}$ (i.e. $V^{CWP}(\gamma_y^{PZ})$ or $V_{y,PZ,Rk}^{CWP}$): the post-plastic shear resistance of the CWP at yielding of the whole PZ;
- $V_{u,PZ}^{CWP}$ (i.e. $V^{CWP}(\gamma_u^{PZ})$ or $V_{u,PZ,Rk}^{CWP}$): the shear resistance of the CWP at the ultimate shear deformation of the PZ.

The characterization of these different levels of resistance is based on the analysis of the complex stress state induced in the CWP by the forces acting at the boundaries of the latter. This stress state, which is depicted in Fig. 2-2(a) for the particular case of an exterior joint subjected to bending only, consists of the combination of three stress components ([26], [27], [50], [116]):

- shear stresses (τ), coming from the equivalent shear force V_{Ek}^{PZ} given by Eq. (2-1);
- vertical normal stresses ($\sigma_{n,M-N}$), coming from the N_{CT} (resp. N_{CB}) axial load ($\sigma_{n,N}$) and the M_{CT} (resp. M_{CB}) bending moment ($\sigma_{n,M}$) in the column;
- horizontal normal stresses (σ_i), coming from the couple of tensile and compressive load-introduction forces F_{BR}.

As regards the plastic shear resistance of the CWP (i.e. $V_{y,CWP,Rk}^{CWP}$, see Table 2-5 to Table 2-7), all the authors use the same formalism, see Eq. (2-16), which assumes a uniform shear stress distribution within the CWP:

$$V_{y,CWP,Rk}^{CWP} = C_y^{CWP} \cdot \chi_i \cdot \chi_n \cdot A_{VC} \cdot \tau_y \qquad (2\text{-}16)$$

Where:

- C_y^{CWP}: reduction factor which accounts for the fact that the actual shear stress distribution is not perfectly uniform over the CWP;
- χ_i: reduction factor which accounts for the $\tau - \sigma_i$ interaction;
- χ_n: reduction factor which accounts for the $\tau - \sigma_{n,M-N}$ interaction;
- A_{VC}: effective shear area;
- τ_y: material shear strength.

From Table 2-5 to Table 2-7, it can be observed that all the models neglect the $\tau - \sigma_i$ interaction (i.e. $\chi_i = 1.0$), the load-introduction phenomenon being assumed to be a localized phenomenon and hence not affecting $V_{y,CWP,Rk}^{CWP}$. However, they differ from each other according to the effective shear area A_{VC} which is considered. Some researchers (i.e. Engelhardt, Lin and Skiadopoulos) also account for the fact that the actual shear stress distribution is not perfectly uniform at yielding, by means of a reduction coefficient C_y^{CWP} different from 1.0. Regarding the effect of the axial load N_c which is applied to the column, it is taken into account in Eq. (2-16) by means of a reduction factor χ_n. In the models of Fielding, Krawinkler, Wang, Engelhardt, Schneider, Lin and Skiadopoulos, a uniform $\sigma_{n,N}$ stress distribution is assumed within the column cross-section. Therefore, χ_n is derived based on the application of the von Mises criterion. Kim assumes that the axial load N_c is carried by the column flanges only, thus using χ_n equal to 1.0. Finally, Jaspart accounts in his model for both $\sigma_{n,N}$ stresses coming from the N_c axial load in the column (see Fig. 2-1) and $\sigma_{n,M}$ stresses coming from the M_c bending moment in the column (see Fig. 2-1). The former is assumed to be uniformly distributed over

the column cross-section while the latter, which is neglected by all the other researchers, is assumed to be uniformly distributed over the column flanges only. The application of the von Mises criterion at the intersection between the CWP and the column flanges, where the $\sigma_{n,M-N}$ stresses are maximum, provides an estimation of χ_n. For sake of simplicity, this value was safely approximated to 0.9 by Jaspart.

Considering the derivation of the plastic shear resistance of the CWP at yielding of the whole PZ (i.e. $V_{y,PZ,Rk}^{CWP}$, see Table 2-5 to Table 2-7), it can be seen that the formalism used is similar to $V_{y,CWP,Rk}^{CWP}$ (see Eq. (2-16)), except that the reduction factor C_y^{CWP} has been replaced by a ΔC_y^{CWP} post-plastic coefficient which accounts for the initiation of strain-hardening in the CWP. Since most of the authors assume a plateau, $V_{y,PZ,Rk}^{CWP}$ does not differ from $V_{y,CWP,Rk}^{CWP}$ (i.e. $C_y^{CWP} = \Delta C_y^{CWP} = 1.0$). This is the case for Fielding, Krawinkler, Wang, Jaspart, Engelhardt and Schneider. However, the others (i.e. Lin, Kim and Skiadopoulos) account for the initiation of strain-hardening in the CWP, using a ΔC_y^{CWP} coefficient different from 1.0.

As regards the resistance of the CWP at the PZ ultimate shear deformation (i.e. $V_{u,PZ,Rk}^{CWP}$, see Table 2-5 to Table 2-6), only Jaspart, Kim and Skiadopoulos provide an estimation of this parameter. The value proposed by Jaspart corresponds to the actual failure of the CWP. It is obtained by substituting, in Eq. (2-16), τ_y by τ_u, C_y^{CWP} by C_u^{CWP} and χ_n by χ_n'. C_u^{CWP} can be taken equal to 1.0 while χ_n' can be derived similarly to χ_n but applying the von Mises criterion at ultimate state rather than yielding state. By contrast, the values of $V_{u,PZ,Rk}^{CWP}$ proposed by Kim and Skiadopoulos do not, strictly speaking, correspond to the actual failure of the CWP. The former is computed at the deformation level for which the plastic mechanism develops in the SE, while the latter is obtained for a deformation level equal to $6 \cdot \gamma_y^{CWP}$.

B. Characterization of the CWP deformation capacity

i. Elastic range

In the elastic range, before yielding initiates in the CWP, the latter undergoes shear and bending deformations. In order to derive the elastic stiffness K_y^{CWP}, the CWP can be modelled as two equivalent beams, which are symmetric with respect to the centre of the CWP (see Fig. 2-8). The boundary condition at the centre of the CWP can be considered as somewhere between free and fixed, while the boundary condition at the other end is fixed. The elastic deflection $\Delta_{el,tot}^{CWP}$ of the equivalent beam under the equivalent shear force V_{Ek}^{CWP} carried by the CWP can be expressed through Eq. (2-17). It is caused by the shear effect and the bending moment effect as shown in Fig. 2-8(a) and (b), respectively. The elastic deflections $\Delta_{el,sh}^{CWP}$ and $\Delta_{el,b}^{CWP}$ associated to these two deformation modes can be expressed through Eq. (2-18) and Eq. (2-19), using the elastic beam theory, where C_r is a constant which accounts for the degree of restraint of the equivalent beam at the centre of the CWP. The different geometric parameters used in Eq. (2-18) and Eq. (2-19) are presented in Fig. 2-8, and E and G are the Young's and shear moduli of the steel material.

$$\Delta_{el,tot}^{CWP} = \Delta_{el,sh}^{CWP} + \Delta_{el,b}^{CWP} \tag{2-17}$$

$$\Delta_{el,sh}^{CWP} = \frac{V_{Ek}^{CWP} \cdot (d_b^*/2)}{G \cdot A_{VC}} \tag{2-18}$$

$$\Delta_{el,b}^{CWP} = \frac{V_{Ek}^{CWP} \cdot (d_b^*/2)^3}{C_r \cdot E \cdot I_c} \tag{2-19}$$

Injecting Eq. (2-18) and Eq. (2-19) into Eq. (2-17) and dividing by $d_b^*/2$ gives the elastic shear deformation $\gamma_{el,tot}^{CWP}$ of the CWP under V_{Ek}^{CWP}, see Eq. (2-20), where $K_{y,sh}^{CWP}$ and $K_{y,b}^{CWP}$ are the shear and bending elastic stiffnesses of the CWP. Consequently, the elastic stiffness of the CWP can be expressed through Eq. (2-21).

$$\gamma_{el,tot}^{CWP} = \frac{\Delta_{el,sh}^{CWP}}{(d_b^*/2)} + \frac{\Delta_{el,b}^{CWP}}{(d_b^*/2)} = \frac{V_{Ek}^{CWP}}{G \cdot A_{VC}} + \frac{V_{Ek}^{CWP} \cdot (d_b^*/2)^2}{C_r \cdot E \cdot I_c} = V_{Ek}^{CWP} \cdot \left(\frac{1}{K_{y,sh}^{CWP}} + \frac{1}{K_{y,b}^{CWP}} \right) \tag{2-20}$$

$$K_y^{CWP} = \frac{V_{Ek}^{CWP}}{\gamma_{el,tot}^{CWP}} = \left(\frac{1}{K_{y,sh}^{CWP}} + \frac{1}{K_{y,b}^{CWP}} \right)^{-1} = \frac{K_{y,sh}^{CWP} \cdot K_{y,b}^{CWP}}{K_{y,sh}^{CWP} + K_{y,b}^{CWP}} \tag{2-21}$$
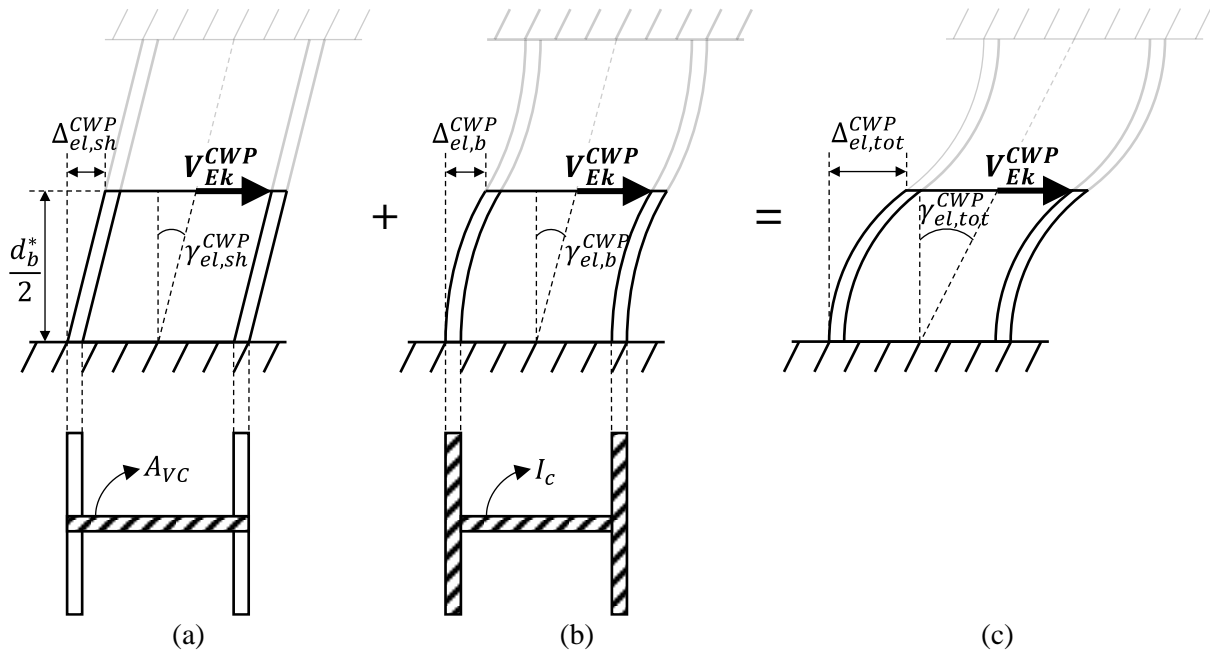
Fig. 2-8. Description of the CWP elastic deformation modes: (a) shear deformation mode, (b) bending deformation mode and (c) sum of the two.

Eq. (2-21) is the most general equation for the characterization of the elastic behaviour of the CWP. Most of the time, however, the deflection $\Delta_{el,b}^{CWP}$ associated to the bending deformation mode (see Fig. 2-8(b) and Eq. (2-19)) is significantly smaller than the deflection $\Delta_{el,sh}^{CWP}$ associated to the shear deformation mode (see Fig. 2-8(a) and Eq. (2-18)). Therefore, it can reasonably be neglected, resulting in a simplified expressions for K_y^{CWP}, see Eq. (2-22). For sake of simplicity, this assumption has been made by most of the authors (i.e. Fielding, Krawinkler, Wang, Jaspart, Schneider, Lin and Kim). Knowing the elastic stiffness K_y^{CWP}, the yield shear deformation γ_y^{CWP} of the CWP can be computed through Eq. (2-23):

$$K_y^{CWP} \backsim K_{y,sh}^{CWP} \tag{2-22}$$

$$\gamma_y^{CWP} = \frac{V_{y,CWP,Rk}^{CWP}}{K_y^{CWP}} \tag{2-23}$$

However, some researchers decided to keep the complex expression (see Eq. (2-21)) to describe the elastic behaviour of the CWP. This is the case of Skiadopoulos who assumed a value of C_r equal to 3.0 which corresponds to a free-end boundary condition at the centre of the CWP. Similarly, Engelhardt also used Eq. (2-21) to characterize the elastic behaviour of the CWP but up to the first yielding of the CWP only, assuming C_r equal to 5.0 based on calibration to test results. This first yielding is assumed to occur when the equivalent shear force V_{Ek}^{CWP} carried by the CWP reaches $80\% - 90\%$ of the plastic shear resistance $V_{y,CWP,Rk}^{CWP}$ of the CWP. To describe the behaviour of the CWP from first yielding up to the entire yielding of the CWP, Engelhardt assumed that the PZ is made of a yielded central part which can freely deform, surrounded by two fixed-ended column flanges, with a T-shaped cross-section. This is shown in Fig. 2-9. Each column flange exhibits a shear deformation mode (see Fig. 2-9(a)) and a bending deformation mode (see Fig. 2-9(b)), similarly to the whole CWP considered in Fig. 2-8. Therefore, the same approach consisting in modelling one half of the column flanges as cantilever beams can be used. Hence, the post-elastic stiffness $K_{y,2}^{CWP}$ of the system made of two T-shaped cantilever beams, whose lengths are one-half the CWP depth, and which are connected by a rigid link, can be expressed through Eq. (2-24), where $K_{y,sh,2}^{CWP}$ and $K_{y,b,2}^{CWP}$ are the post-elastic shear and bending stiffnesses of the CWP, see Eq. (2-25) and Eq. (2-26), respectively. The different geometric parameters used in Eq. (2-24) to Eq. (2-26) are presented in Fig. 2-9, while C_r is here again taken equal to 5.0 by Engelhardt.
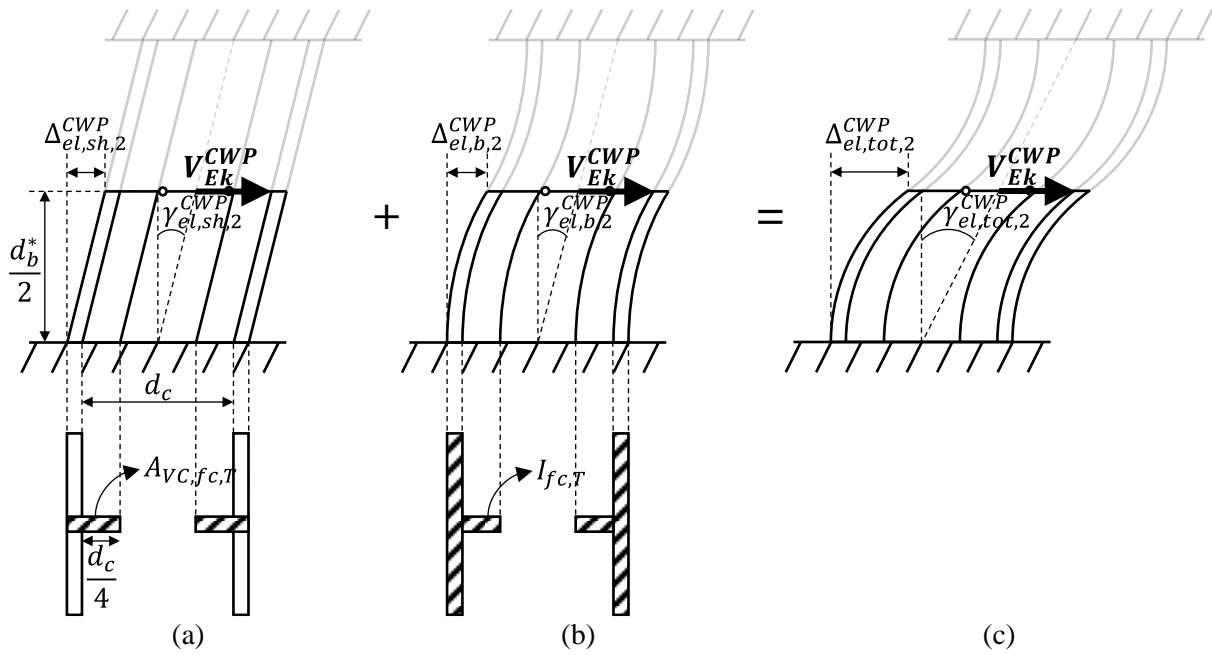
Fig. 2-9. Description of the CWP post-elastic deformation modes (in Engelhardt's model): (a) shear deformation mode, (b) bending deformation mode and (c) sum of the two.

$$K_{y,2}^{CWP} = 2 \cdot \left(\frac{1}{K_{y,sh,2}^{CWP}} + \frac{1}{K_{y,b,2}^{CWP}} \right)^{-1} = 2 \cdot \frac{K_{y,sh,2}^{CWP} \cdot K_{y,b,2}^{CWP}}{K_{y,sh,2}^{CWP} + K_{y,b,2}^{CWP}} \qquad (2\text{-}24)$$

$$K_{y,sh,2}^{CWP} = G \cdot A_{VC,fc,T} = G \cdot \left(\frac{h_c}{2} - \frac{d_c}{4} \right) \cdot t_{wc} \qquad (2\text{-}25)$$

$$K_{y,b,2}^{CWP} = \frac{C_r \cdot E \cdot I_{fc,T}}{(d_b^*/2)^2} \qquad (2\text{-}26)$$

ii. Post-elastic range(s)

The characterization of the post-elastic behaviour of the CWP is handled differently in the bilinear models on the one hand and the trilinear/quad-linear models on the other hand.

In the bilinear models (i.e. Lin, Kim and Skiadopoulos), strain-hardening is assumed to initiate in the CWP straight upon the entire shear yielding of the CWP. The strain-hardening (i.e. post-plastic) stiffness K_{pp}^{CWP} is usually taken as a percentage of K_y^{CWP}. Historically, a value of 3% was assumed in the literature [58]. This value has been taken by Kim. By contrast, Lin proposed a value of 5%. In his study [58], Skiadopoulos demonstrated, through FE analysis, that the commonly accepted post-plastic stiffness K_{pp}^{CWP} of $0.03 \cdot K_y^{CWP}$ was irrational. He did not provide any better estimate for K_{pp}^{CWP} but proposed analytical expressions of the CWP resistance at given levels of shear deformation (i.e. $4 \cdot \gamma_y^{CWP}$ and $6 \cdot \gamma_y^{CWP}$) to describe the CWP post-elastic behaviour.

In the trilinear (Fielding, Krawinkler, Wang, Jaspart, Schneider) and quad-linear (Engelhardt) models, the CWP is assumed to deform freely after it becomes fully yielded. This is materialized by a plateau in the analytical models. Strain-hardening initiates at a larger strain γ_y^{PZ}, when the SE become entirely yielded too. For this particular strain γ_y^{PZ}, which corresponds to the yielding of the entire PZ, Krawinkler and Wang proposed a value of $4 \cdot \gamma_y^{CWP}$ and $3.5 \cdot \gamma_y^{CWP}$, respectively. By contrast, Jaspart (stiffened), Engelhardt and Schneider computed γ_y^{PZ} as the sum of the yield shear deformation γ_y^{CWP} of the CWP (see Eq. (2-23)) and the yield shear deformation γ_y^{SE} of the SE (see the forthcoming Eq. (2-33)). Finally, Jaspart (unstiffened) provided an empirical expression for γ_y^{PZ} based on the mechanical properties of the steel material and Fielding did not provide any estimate for γ_y^{PZ}. As regards the strain-hardening branch of the models, Krawinkler, Wang and Engelhardt used the widely accepted value of $0.03 \cdot K_y^{CWP}$ for the strain-hardening (i.e. post-plastic) stiffness K_{pp}^{CWP} of the CWP, while Jaspart proposed a value of $0.02 \cdot K_y^{CWP}$. The strain-hardening effects have not been included in the models of Fielding and Schneider.

iii. Ultimate deformation capacity

Most of the models do not provide any estimate of the ultimate deformation capacity γ_u^{PZ} of the PZ. Indeed, the model of Fielding is valid up to γ_y^{CWP} only, while the models of Krawinkler, Wang, Engelhardt, Schneider and Lin are valid up to γ_y^{PZ} only. Jaspart proposed an analytical expression for γ_u^{PZ} in the case of both stiffened and unstiffened PZs. These expressions correspond to the actual ultimate deformation capacity of the CWP. By contrast, the γ_u^{PZ} values provided by Kim and Skiadopoulos can not be associated to the actual failure of the CWP, as discussed here above. They correspond to given levels of shear deformation of the PZ, associated to the formation of a plastic mechanism in the SE for the former, and equal to $6 \cdot \gamma_y^{CWP}$ for the latter.

2.3.2.3 Contribution of the SE

A. *Characterization of the SE resistance*

The different analytical models presented in Table 2-5 to Table 2-7 (see the green $(\Delta V^{SE} - \gamma^{SE})_{an}$ curves) exhibit three main values of resistance, namely:

- $\Delta V_{y,CWP}^{SE}$ (i.e. $\Delta V^{SE}(\gamma_y^{CWP})$ or $\Delta V_{y,CWP,Rk}^{SE}$): the shear resistance of the SE at yielding of the CWP;
- $\Delta V_{y,PZ}^{SE}$ (i.e. $\Delta V^{SE}(\gamma_y^{PZ})$ or $\Delta V_{y,PZ,Rk}^{SE}$): the plastic shear resistance of the SE at yielding of the whole PZ;
- $\Delta V_{u,PZ}^{SE}$ (i.e. $\Delta V^{SE}(\gamma_u^{PZ})$ or $\Delta V_{u,PZ,Rk}^{SE}$): the shear resistance of the SE at the ultimate shear deformation of the PZ.

As regards $\Delta V_{y,CWP,Rk}^{SE}$ (see Table 2-5 to Table 2-7), most of the researchers (i.e. Fielding, Krawinkler, Wang, Jaspart, Engelhardt and Skiadopoulos) assume that the SE only start withstanding shear forces upon the yielding of the CWP. Therefore, $\Delta V_{y,CWP,Rk}^{SE}$ is equal to 0. For the other ones (i.e. Schneider, Lin and Kim), $\Delta V_{y,CWP,Rk}^{SE}$ consists of a fraction of the actual plastic shear resistance $\Delta V_{y,PZ,Rk}^{SE}$ of the SE.

For the derivation of the plastic shear resistance of the SE (i.e. $\Delta V_{y,PZ,Rk}^{SE}$, see Table 2-5 to Table 2-7), Wang, Jaspart, Engelhardt, Schneider and Kim assume the formation of four plastic hinges in the column flanges, at the level of the beam flanges. However, Jaspart allows accounting for this beneficial frame action in the presence of transverse column web stiffeners only, while Kim assumes that the plastic shear resistance of the SE is reached before the formation of the four plastic hinges, for a shear deformation of $4 \cdot \gamma_y^{CWP}$. Krawinkler and Lin propose empirical formulae for $\Delta V_{y,PZ,Rk}^{SE}$ on the basis of experimental results and FE analysis. In the model of Skiadopoulos, the expression for $\Delta V_{y,PZ,Rk}^{SE}$ is based on the integration of the shear stress profile in the column flanges at a shear deformation of $4 \cdot \gamma_y^{CWP}$; and this formula was validated on FE results. Finally, Fielding does not propose any formula for $\Delta V_{y,PZ}^{SE}$. Regarding the effect of the axial load N_c which is applied to the column, it is taken into account in the different models using a reduction factor, namely $\Delta \chi_n$. In the models of Krawinkler, Wang, Schneider, Lin and Skiadopoulos, a uniform $\sigma_{n,N}$ stress distribution is assumed within the column cross-section. Therefore, $\Delta \chi_n$ is derived based on the application of the von Mises criterion, similarly to χ_n. The same assumption is made by Engelhardt regarding the $\sigma_{n,N}$ stress distribution, but $\Delta \chi_n$ is here derived based on the M-N interaction in a rectangular cross-section. Kim assumes that the axial load N_c is carried by the column flanges only; thus, he uses the same M-N interaction criterion as Engelhardt for the derivation of $\Delta \chi_n$. Finally, Jaspart kept $\Delta \chi_n$ equal to 1.0 in his model.

As regards the shear resistance of the SE at the PZ ultimate shear deformation (i.e. $\Delta V_{u,PZ,Rk}^{SE}$, see Table 2-5 to Table 2-7), most of the authors (i.e. Fielding, Krawinkler, Wang, Engelhardt, Schneider and Lin) do not provide any estimate for this parameter. Jaspart assumes that, after the development of a plastic collapse mechanism in the SE, the latter can freely deform until the failure of the CWP is reached. Therefore, $\Delta V_{u,PZ,Rk}^{SE}$ corresponds to $\Delta V_{y,PZ,Rk}^{SE}$. Kim does not allow such plastic deformations in the SE. According to him, the ultimate resistance $\Delta V_{u,PZ,Rk}^{SE}$ coincides with the formation of four plastic hinges in the column flanges, at the level of the beam flanges. Finally, Skiadopoulos proposes an expression for $\Delta V_{u,PZ,Rk}^{SE}$ that is based on the integration of the shear stress profile in the column flanges for a level of shear deformation equal to $6 \cdot \gamma_y^{CWP}$.

B. Characterization of the SE deformation capacity

i. Elastic range

Regarding the modelling of the elastic behaviour of the SE, the analytical models presented in Table 2-5 to Table 2-7 offer two main approaches, that are presented here below, and will be referred to as the Fielding's approach and the Krawinkler's approach.

The first approach was developed by Fielding and then re-used by Jaspart, Lin and Kim who introduced some minor modifications. This approach assumes that, after the yielding of the entire CWP, elastic stiffness is still available in the column flanges, which can bend around their weak axis until they are fully yielded too. This is shown in Fig. 2-10, where each column flange exhibits a shear deformation mode (see Fig. 2-10(a)) and a bending deformation mode (see Fig. 2-10(b)). To derive the elastic stiffness K_y^{SE} of the flanges, the system made of two equivalent beams - whose length is one half of the flanges and which are connected with a rigid link - can be considered (see Fig. 2-10). In the most general case, these equivalent beams are assumed to be somewhere between free and fixed at the centre of the column flanges, and fixed at the other end. The elastic deflection $\Delta_{el,tot}^{SE}$ of this system under the equivalent shear force ΔV_{Ek}^{SE} carried by the SE can be expressed through Eq. (2-27). It is caused by the bending moment effect and the shear effect as shown in Fig. 2-10(a) and (b), respectively. The elastic deflections $\Delta_{el,sh}^{SE}$ and $\Delta_{el,b}^{SE}$ associated to these two deformation modes can be expressed through Eq. (2-28) and Eq. (2-29), using the elastic beam theory, where C_r is a constant which accounts for the degree of restraint of the equivalent beams at the centre of the column flanges. The different geometric parameters used in Eq. (2-28) and Eq. (2-29) are presented in Fig. 2-10, and E and G are the Young's and shear moduli of the steel material.
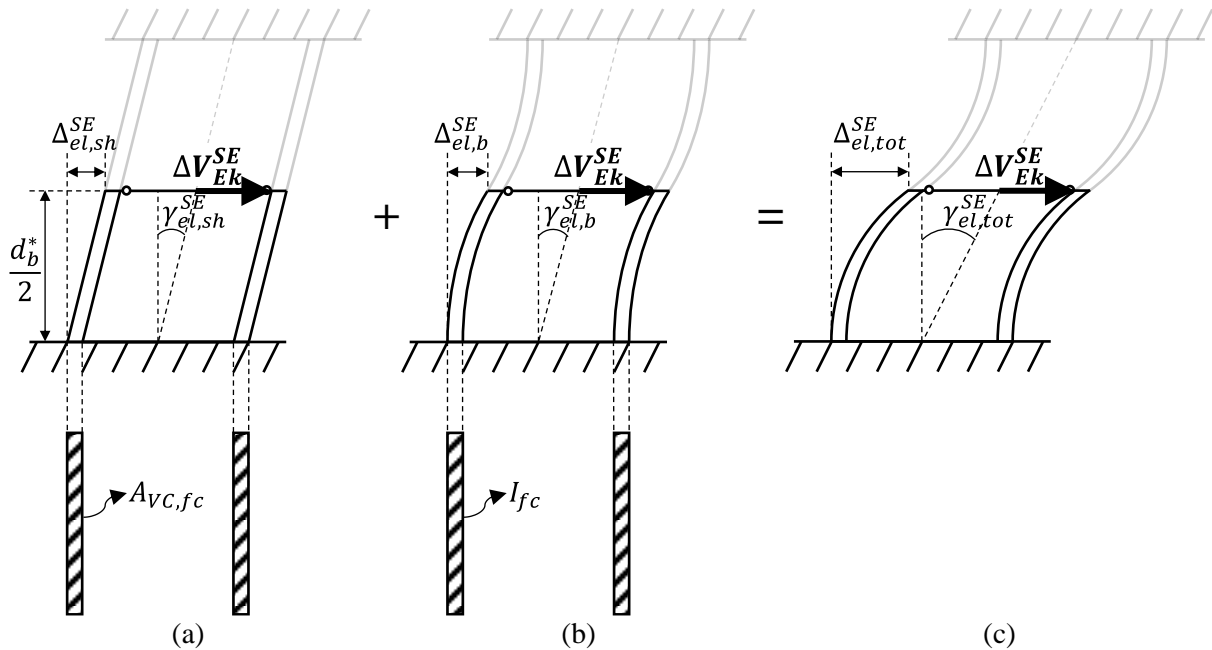
Fig. 2-10. Description of the SE elastic deformation modes: (a) shear deformation mode, (b) bending deformation mode and (c) sum of the two.

$$\Delta_{el,tot}^{SE} = \Delta_{el,b}^{SE} + \Delta_{el,sh}^{SE} \qquad (2\text{-}27)$$

$$\Delta_{el,b}^{SE} = \frac{\Delta V_{Ek}^{SE} \cdot (d_b^*/2)^3}{C_r \cdot E \cdot (2 \cdot I_{fc})} \qquad (2\text{-}28)$$

$$\Delta_{el,sh}^{SE} = \frac{\Delta V_{Ek}^{SE} \cdot (d_b^*/2)}{G \cdot A_{VC,fc}} \qquad (2\text{-}29)$$

Injecting Eq. (2-28) and Eq. (2-29) into Eq. (2-27) and dividing by $d_b^*/2$ gives the elastic shear deformation $\gamma_{el,tot}^{SE}$ of the SE under ΔV_{Ek}^{SE}, see Eq. (2-30), where $K_{y,sh}^{SE}$ and $K_{y,b}^{SE}$ are the shear and bending elastic stiffnesses of the SE. Consequently, the elastic stiffness of the SE can be expressed through Eq. (2-31).

$$\gamma_{el,tot}^{SE} = \frac{\Delta_{el,sh}^{SE}}{(d_b^*/2)} + \frac{\Delta_{el,b}^{SE}}{(d_b^*/2)} = \frac{\Delta V_{Ek}^{SE}}{G \cdot A_{VC,fc}} + \frac{\Delta V_{Ek}^{SE} \cdot (d_b^*/2)^2}{C_r \cdot E \cdot I_{fc}} = \Delta V_{Ek}^{SE} \cdot \left(\frac{1}{K_{y,sh}^{SE}} + \frac{1}{K_{y,b}^{SE}} \right) \tag{2-30}$$

$$K_y^{SE} = \frac{\Delta V_{Ek}^{SE}}{\gamma_{el,tot}^{SE}} = \left(\frac{1}{K_{y,sh}^{SE}} + \frac{1}{K_{y,b}^{SE}} \right)^{-1} = \frac{K_{y,sh}^{SE} \cdot K_{y,b}^{SE}}{K_{y,sh}^{SE} + K_{y,b}^{SE}} \tag{2-31}$$

Eq. (2-31) is the most general equation for the characterization of the elastic behaviour of the SE. However, the deflection $\Delta_{el,sh}^{CWP}$ associated to the shear deformation mode (see Fig. 2-10(a) and Eq. (2-29)) is usually significantly smaller than the deflection $\Delta_{el,b}^{CWP}$ associated to the bending deformation mode (see Fig. 2-10(b) and Eq. (2-28)). Therefore, it can reasonably be neglected, resulting in a simplified expression for K_y^{SE}, see Eq. (2-32). For sake of simplicity, this assumption was made by Fielding, Jaspart and Lin who all assumed a value of C_r equal to 3.0. This is the same as considering the equivalent beams as cantilevers. Lin also relaxed one of the main assumptions made by Fielding, which states that the SE contribute to both the stiffness and strength of the PZ solely after the entire yielding of the CWP. For Lin, the CWP and the SE work in parallel right since the beginning of the PZ loading. The same assumption was made by Kim who also went a step further by considering both shear and bending deformation modes for the derivation of the elastic stiffness of the SE (i.e. Eq. (2-31)). Kim also took C_r equal to 3.0. As a reminder, Jaspart allows accounting from the frame effect solely in the presence of transverse column web stiffeners. Knowing the elastic stiffness K_y^{SE} of the SE, the yield shear deformation γ_y^{SE} of the SE can be computed through Eq. (2-33):

$$K_y^{SE} \backsim K_{y,b}^{SE} \tag{2-32}$$

$$\gamma_y^{SE} = \frac{\Delta V_{y,PZ,Rk}^{SE}}{K_y^{SE}} \tag{2-33}$$

The second approach was developed by Krawinkler and then re-used by Engelhardt and Schneider. In this approach, the flanges and the stiffeners are modelled as rigid elements, assuming that any deformation of the latter is prevented by the presence of the beam(s) and column webs. The deformability of the SE is concentrated in very localized regions around the four corners of the PZ. Thus, four rotational springs are used in the four corners of the PZ to model the contribution of the SE. Each spring's rotational stiffness can be approximated by Eq. (2-34), where C_s is a constant to be determined. Subsequently, the initial elastic stiffness of the SE can be easily deduced from Eq. (2-34) and the application of the virtual work principle, see Eq. (2-35), where d_b^* is the PZ depth:

$$K_s = \frac{E \cdot b_c \cdot t_{fc}^2}{C_s} \tag{2-34}$$

$$K_y^{SE} = 4 \cdot \frac{K_s}{d_b^*} \tag{2-35}$$

For Krawinkler and Engelhardt, the SE contribute to the PZ stiffness and resistance after the shear yielding of the entire CWP only. Krawinkler assumed C_s equal to 10, based on FE analysis, while Engelhardt took C_s equal to 20, based on calibration to test results. By contrast, Schneider relaxed that main assumption, considering that the SE contribute to the PZ resistance and stiffness even when $\gamma < \gamma_y^{CWP}$. Schneider proposed a value of C_s equal to $12 \cdot d_b^*/(d_b^* - 2 \cdot t_{fc})$ based on a theoretical analysis of the mechanical behaviour of the column flanges.

Finally, Wang and Skiadopoulos assumed that the SE contribute to the PZ stiffness and resistance after the shear yielding of the entire CWP and up to a shear deformation level of $3.5 \cdot \gamma_y^{CWP}$ for the former and $4 \cdot \gamma_y^{CWP}$ for the latter. These values were calibrated on FE results. In order to characterize this elastic range, both of them assumed a PZ shear strength equilibrium instead of shear deformation compatibility. As already discussed above, Wang obtained the expression for the plastic shear resistance $\Delta V_{y,PZ,Rk}^{SE}$ of the SE from limit analysis, while the expression proposed by Skiadopoulos is based on the integration of the shear stress profile in the column flanges, and was calibrated on FE results.

ii. Post-elastic range

Most of the researchers assume an elastic, perfectly-plastic behaviour for the SE. Therefore, the post-elastic behaviour is characterized by a plateau, as this is the case for Krawinkler, Wang, Jaspart, Engelhardt and Kim. Schneider and Lin considered the possibility for the SE to strain-harden but did not provide any estimate for the strain-hardening (i.e. post-plastic) stiffness K_{pp}^{SE} of the SE. As regards Fielding model, the post-elastic behaviour of the SE has not been included.

Finally, Skiadopoulos described the post-plastic range following the same procedure as for the elastic range. The post-plastic range was assumed to extend from $4 \cdot \gamma_y^{CWP}$ up to $6 \cdot \gamma_y^{CWP}$ and the expressions of the shear resistance at these two deformation levels (i.e. $\Delta V_{y,PZ,Rk}^{SE}$ and $\Delta V_{u,PZ,Rk}^{SE}$) were derived and calibrated based on FE analyses, as previously described.

iii. Ultimate deformation capacity

As discussed here above for the CWP contribution, most of the researchers do not provide any estimate of the ultimate deformation capacity γ_u^{PZ} of the PZ. Fielding's model is valid up to γ_y^{CWP} only; the Krawinkler, Wang, Engelhardt, Schneider and Lin models up to γ_y^{PZ}. Only Jaspart, Kim and Skiadopoulos provide analytical expressions for γ_u^{PZ}, that correspond to various PZ shear distortion levels, i.e. at failure of the CWP for Jaspart, when a plastic collapse mechanism develops in the SE for Kim and equal to $6 \cdot \gamma_y^{CWP}$ for Skiadopoulos.

2.3.3 Simplified analytical models

2.3.3.1 Description

Some of the complex analytical models introduced in Section 2.3.2 were used as a basis for the derivation of design criteria to predict the plastic shear resistance of the PZ, providing some slight adjustments. According to these models, it is commonly accepted to express the plastic shear resistance of the PZ (i.e. $V_{y,PZ,Rk}^{PZ}$) through Eq. (2-36) as the sum of the plastic shear resistance of the CWP (i.e. $V_{y,PZ,Rk}^{CWP}$) and that of the SE (i.e. $\Delta V_{y,PZ,Rk}^{SE}$), where Ψ is the flange contribution factor (FCF).

N.B.: in Eq. (2-36) and in the rest of the present manuscript, the simpler $V_{y,Rk}^{PZ}$, $V_{y,Rk}^{CWP}$ and $\Delta V_{y,Rk}^{SE}$ notations will be used instead of $V_{y,PZ,Rk}^{PZ}$, $V_{y,PZ,Rk}^{CWP}$ and $\Delta V_{y,PZ,Rk}^{SE}$.

$$V_{y,Rk}^{PZ} = V_{y,Rk}^{CWP} + \Delta V_{y,Rk}^{SE} = V_{y,Rk}^{CWP} \cdot \underbrace{\left(1 + \frac{\Delta V_{y,Rk}^{SE}}{V_{y,Rk}^{CWP}}\right)}_{\Psi} = C_y^{CWP} \cdot \chi_i \cdot \chi_n \cdot A_{VC} \cdot \tau_y \cdot \Psi \tag{2-36}$$

In the present Section 2.3.3, the cases of the European, American, Japanese and Chinese design codes will be reviewed (see Sections 2.3.3.2 to 2.3.3.4 respectively). The main parameters involved in Eq. (2-36) are presented in Table 2-8 and Table 2-9 for each individual design criterion. These two tables use the same formalism for all the European, American, Japanese and Chinese provisions to facilitate their comparison.

The main difference between Table 2-8 and Table 2-9 is whether or not the contribution $\Delta V_{y,Rk}^{SE}$ of the SE can be taken into account. In the most general case, it is allowed to account for the beneficial frame action provided by the SE, see Table 2-8. However, in seismic design, it is usually recommended that the PZ moderately dissipates energy during an earthquake (i.e. intermediate to strong PZ design philosophy). This is to avoid any excessive inelastic PZ deformation which could lead to the premature brittle failure in the welds at the beam-to-column interface, as explained previously in Section 2.3.1. Consequently, it is recommended that the contribution of the SE is not anymore accounted for in Eq. (2-36), see Table 2-9.

The abilities of these design rules will be assessed later on in this manuscript through comparisons with available experimental results collected from the scientific literature. This will be reviewed in the forthcoming CHAPTER 3, where the strengths and weaknesses of each individual code will be highlighted and discussed. For this study, only the design rules presented in Table 2-8, which allow for the inelastic PZ deformation, will be considered.

Table 2-8. Description of the European, American, Japanese and Chinese design provisions for the PZ ($\Delta V_{y,Rk}^{SE}$ allowed).

Author	EN 1993-1-8 (2005) †$= EU$	AIJ (2012) †$= JPN$	AISC (2016) †$= US$	Chinese code (2018) †$= CHN$
	Description of the main parameters of the models			
$V_{y,Rk,†}^{CWP}$	$C_y^{CWP} \cdot \chi_i \cdot \chi_n \cdot A_{VC} \cdot \tau_y$		$C_y^{CWP} \cdot \chi_i \cdot \chi_n \cdot A_{VC} \cdot \tau_y$	
$\Delta V_{y,Rk,†}^{SE}$	$\min\left(4 \cdot \frac{M_{pl,fc,Rk}}{d_b^*} \cdot \Delta\chi_n ; 2 \cdot \frac{M_{pl,fc,Rk}+M_{pl,st,Rk}}{d_b^*} \cdot \Delta\chi_n\right)$	/	$7.2 \cdot \frac{M_{pl,fc,Rk}}{d_b^*} \cdot \Delta\chi_n$	/
	Description of additional relevant parameters			
A_{VC}	$\begin{cases} A_c - 2 \cdot b_c \cdot t_{fc} + (t_{wc} + 2 \cdot r_c) \cdot t_{fc} & hot-rolled\ sections \\ 1.2 \cdot h_{ic} \cdot t_{wc} & built-up\ sections \end{cases}$		$d_c^* \cdot t_{wc}$	
d_c^*	$h_c - t_{fc}$		h_c	
d_b^*	$h_b - t_{fb}$		h_b	
C_y^{CWP}	1.0	/	1.04	/
χ_i	1.0		1.0	
χ_n	0.9		$\begin{cases} 1.0 & n_c \le 0.75 \\ 1.9 - 1.2 \cdot n_c & n_c > 0.75 \end{cases}$	
$\Delta\chi_n$	1.0		$\begin{cases} 1.0 & n_c \le 0.75 \\ 1.9 - 1.2 \cdot n_c & n_c > 0.75 \end{cases}$	

Notes :
- $n_c = N_c/N_{pl,c}$ where N_c is the resulting axial load applied at the top of the PZ and $N_{pl,c}$ is the plastic resistance of the column cross-section
- $M_{pl,fc,Rk}$, $M_{pl,st,Rk}$: plastic moment resistance of a rectangular column flange and of a transverse column web stiffener
- h_c (resp. h_b), b_c, t_{fc} (resp. t_{fb}), t_{wc}, r_c, A_c, h_{ic}: geometric properties of the column (resp. beam) cross-section
- τ_y: shear strength of the steel material

Table 2-9. Description of the European, American, Japanese and Chinese design provisions for the PZ ($\Delta V_{y,Rk}^{SE}$ not allowed).

Author	EN 1998-1 (2005) †$= EU$	AIJ (2012) †$= JPN$	AISC (2016) †$= US$	Chinese code (2018) †$= CHN$
	Description of the main parameters of the models			
$V_{y,Rk,†}^{CWP}$	$C_y^{CWP} \cdot \chi_i \cdot \chi_n \cdot A_{VC} \cdot \tau_y$	$C_y^{CWP} \cdot \chi_i \cdot \chi_n \cdot A_{VC} \cdot \tau_y$	$C_y^{CWP} \cdot \chi_i \cdot \chi_n \cdot A_{VC} \cdot \tau_y$	$C_y^{CWP} \cdot \chi_i \cdot \chi_n \cdot A_{VC} \cdot \tau_y$
$\Delta V_{y,Rk,†}^{SE}$	0	0	0	0
	Description of additional relevant parameters			
A_{VC}	$\begin{cases} A_c - 2 \cdot b_c \cdot t_{fc} + (t_{wc} + 2 \cdot r_c) \cdot t_{fc} & hot-rolled\ sections \\ 1.2 \cdot h_{ic} \cdot t_{wc} & built-up\ sections \end{cases}$	$d_c^* \cdot t_{wc}$	$d_c^* \cdot t_{wc}$	$d_c^* \cdot t_{wc}$
d_c^*	$h_c - t_{fc}$	$h_c - t_{fc}$	h_c	$h_c - t_{fc}$
d_b^*	$h_b - t_{fb}$	$h_b - t_{fb}$	h_b	$h_b - t_{fb}$
C_y^{CWP}	1.0	1.0	1.04	1.0
χ_i	1.0	1.0	1.0	1.0
χ_n	1.0	$\sqrt{1 - n_c^2}$	$\begin{cases} 1.0 & n_c \le 0.4 \\ 1.4 - n_c & n_c > 0.4 \end{cases}$	$\begin{cases} 1.0 & n_c \le 0.4 \\ \sqrt{1 - n_c^2} & n_c > 0.4 \end{cases}$

Notes :
- $n_c = N_c/N_{pl,c}$ where N_c is the resulting axial load applied at the top of the PZ and $N_{pl,c}$ is the plastic resistance of the column cross-section
- h_c (resp. h_b), b_c, t_{fc} (resp. t_{fb}), t_{wc}, r_c, A_c, h_{ic}: geometric properties of the column (resp. beam) cross-section
- τ_y: shear strength of the steel material

2.3.3.2 European design codes

In EN 1993-1-8 [1], which is dedicated to the design of steel joints, the Jaspart model has been adopted to evaluate the plastic shear resistance $V_{y,Rk,Eu}^{PZ}$ of the PZ (see Table 2-8). Therefore, reference can be made to Eq. (2-36) and Table 2-6, leading to Eq. (2-37):

$$V_{y,Rk,EU}^{PZ} = V_{y,Rk,EU}^{CWP} + \Delta V_{y,Rk,EU}^{SE} = V_{y,Rk,EU}^{CWP} \cdot \Psi_{EU} = C_y^{CWP} \cdot \chi_i \cdot \chi_n \cdot A_{VC} \cdot \tau_y \cdot \Psi_{EU} \qquad (2\text{-}37)$$

with the following value for the FCF:

$$\Psi_{EU} = \begin{cases} 1 + \dfrac{\sqrt{3} \cdot b_c \cdot t_{fc}^2}{A_{VC} \cdot d_b^* \cdot C_y^{CWP} \cdot \chi_i} \cdot \dfrac{\Delta \chi_n}{\chi_n} & (EN\ 1993 - 1 - 8) \\ 1.0 & (EN\ 1998 - 1) \end{cases} \qquad (2\text{-}38)$$

All the parameters in Eqs. (2-37) and (2-38) are given in Table 2-8. They are similar to the ones defined in Table 2-6 for the Jaspart model. In particular, the suggested value of 0.9 was used for the χ_n reduction factor. The only difference is the limit set in EN 1993-1-8, to the contribution $\Delta V_{y,Rk,EU}^{SE}$ coming from the SE, see Table 2-8. As a reminder, in Eq. (2-37), the FCF can be accounted for in the presence of transverse column web stiffeners only. It is also noteworthy that the validity of Eq. (2-37) is limited to PZs which satisfy the Eq. (2-39) requirement in terms of CWP slenderness, where d_c is the clear depth of the column cross-section, t_{wc} is the column web thickness, $\eta = 1.2$ for steel grades lower than $S460$ and $\varepsilon = \sqrt{235/f_y}$. Eq. (2-39) ensures that the risk of shear buckling of the PZ is prevented.

$$\frac{d_c}{t_{wc}} \leq \frac{72}{\eta} \cdot \varepsilon \qquad (2\text{-}39)$$

By contrast, the design criteria for the PZ plastic resistance, as prescribed in Eurocode 8 (EN 1998-1, [89]) dedicated to seismic design, does not allow the contribution $\Delta V_{y,Rk,EU}^{SE}$ coming from the SE (see Table 2-9) to be accounted for. In addition, it is not required to account for the effect of the $\tau - \sigma_n$ stress interaction within the PZ, thus $\chi_n = 1.0$. All the other parameters in Table 2-9 are similar to the ones defined in Table 2-6 for the Jaspart model.

Finally, as regards the elastic stiffness, the expressions prescribed in EN 1993-1-8 and EN 1998-1 are similar to the one proposed by Jaspart, see K_y^{CWP} in Table 2-6.

2.3.3.3 American design code

By contrast with the European code, the model of Krawinkler has been adopted by the American Institute of Steel Construction (AISC, [88]) to evaluate the plastic shear resistance $V_{y,Rk,US}^{PZ}$ of the PZ. Therefore, reference can be made, here again, to Eq. (2-36) and Table 2-5, leading to Eq. (2-37):

$$V_{y,Rk,US}^{PZ} = V_{y,Rk,US}^{CWP} + \Delta V_{y,Rk,US}^{SE} = V_{y,Rk,US}^{CWP} \cdot \Psi_{US} = C_y^{CWP} \cdot \chi_i \cdot \chi_n \cdot A_{VC} \cdot \tau_y \cdot \Psi_{US} \qquad (2\text{-}40)$$

with the following value for the FCF:

$$\Psi_{US} = \begin{cases} 1 + \dfrac{3 \cdot b_c \cdot t_{fc}^2}{A_{VC} \cdot d_b^* \cdot C_y^{CWP} \cdot \chi_i} \cdot \dfrac{\Delta \chi_n}{\chi_n} & \left(\Delta V_{y,Rk,US}^{SE}\ allowed \right) \\ 1.0 & \left(\Delta V_{y,Rk,US}^{SE}\ not\ allowed \right) \end{cases} \qquad (2\text{-}41)$$

The parameters used in Eqs. (2-40) and (2-41) are given in Table 2-8 or Table 2-9, depending on whether the additional strength $\Delta V_{y,Rk,US}^{SE}$ provided by the SE may be accounted for in the design phase or not. From these tables, it can be seen that the reduction factor χ_n accounting for the $\tau - \sigma_{n,M-N}$

interaction is different from the one proposed by Krawinkler. In addition, for the derivation of the effective shear area A_{VC}, the AISC suggests to use $d_c^* = h_c$ instead of the value $d_c^* = 0.95 \cdot h_c$ recommended by Krawinkler. Finally, the AISC uses $0.6 \cdot f_y$ instead of $0.577 \cdot f_y$ as τ_y. This is taken into account in Eq. (2-40) by assuming $C_y^{CWP} = 1.04$ (see Table 2-8 and Table 2-9).

As regards the elastic stiffness, the formula suggested by the AISC is similar to the one proposed by Krawinkler, see K_y^{CWP} in Table 2-5.

2.3.3.4 Japanese and Chinese design codes

The plastic shear resistance $V_{y,Rk,JPN}^{PZ}$ of the PZ provided by the Architectural Institute of Japan (AIJ, [90]) can be expressed through Eq. (2-42):

$$V_{y,Rk,\dagger}^{PZ} = V_{y,Rk,\dagger}^{CWP} + \Delta V_{y,Rk,\dagger}^{SE} = V_{y,Rk,\dagger}^{CWP} \cdot \Psi_\dagger = C_y^{CWP} \cdot \chi_i \cdot \chi_n \cdot A_{VC} \cdot \tau_y \cdot \Psi_\dagger \quad (\dagger \sim JPN \ or \ CHN) \quad (2\text{-}42)$$

with the following value for the FCF:

$$\Psi_\dagger = 1.0 \quad (\dagger \sim JPN \ or \ CHN) \tag{2-43}$$

From Eqs. (2-42) and (2-43), it can be seen that the Japanese code does not allow the contribution $\Delta V_{y,Rk,JPN}^{SE}$ coming from the SE (see Table 2-9) to be accounted for. The same remark applies to the Chinese code [91]. The only difference between the Japanese and Chinese codes relies in the way how the axial load is accounted for in the models (i.e. see the parameter χ_n in Table 2-9).

2.4 CONCLUSIONS

In conclusion, the purpose of CHAPTER 2 was to set the theoretical background of the present thesis. With this respect, a brief description of the component method for the characterization of the steel joints' behaviour was first provided, emphasizing the main limitations of this method. Next, an extensive literature review of the main analytical models for the prediction of the PZ behaviour was conducted. The main observation was that all these models expressed the behaviour of the PZ as the sum of two independent contributions, namely that of the CWP and that of the SE, which can be modelled separately before being superimposed. However, different assumptions were made by the researchers for the modelling of these two contributions. Two sets of summary tables emerged from this review, and constitute the main outcome of the present CHAPTER 2: the first one (see Table 2-5 to Table 2-7) includes ten of the most referenced sophisticated analytical models coming from the scientific literature; the second one (see Table 2-8 to Table 2-9) includes four simplified design criteria coming from various international standards. These tables use the same formalism for all the models in order to facilitate their comparison. The following CHAPTER 3 will be dedicated to the comparisons of these models with experimental evidence in order to assess the performance of the different models, thereby highlighting their strengths and weaknesses.

CHAPTER 3 Problem identification

3.1 INTRODUCTION

3.1.1 Objectives of the Chapter

The objective of CHAPTER 3 is twofold: (i) collecting a large number of experimental results on welded and bolted joints from the scientific literature in order to build a database, and (ii) using these experimental results in comparisons with the analytical models introduced in CHAPTER 2, namely the complex analytical models coming from the scientific literature (see Section 2.3.2) and the simplified design criteria recommended in the building codes (see Section 2.3.3). Based on these comparisons, their strengths and weaknesses can be highlighted, and conclusions can be drawn.

In the following of the thesis, a performance indicator will be used to quantify the analytical models' ability to predict a given scalar parameter X, and to allow comparing the analytical models between them. In this thesis, the relative error E between the analytical prediction X_{an} and the observed (experimental or numerical) value X_{obs} has been chosen as the reference indicator, see Table 3-1. Based on the level of the relative error E, three main "accuracy categories" have been contemplated:

- The high accuracy category if $|E| \leq 5\%$ (see the light green box in Table 3-1);
- The moderate accuracy category if $5\% < |E| \leq 10\%$ (see the light orange box in Table 3-1);
- The low accuracy category if $|E| > 10\%$ (see the light red box in Table 3-1).

This performance indicator will be used extensively throughout the thesis, every time the performance of a model needs to be evaluated.

Table 3-1. Performance indicator and colour code for the assessment of the analytical models' performances.

Performance indicator	High accuracy class	Moderate accuracy class	Low accuracy class
$E = \frac{X_{an}-X_{obs}}{X_{obs}}$	$|E| \leq 5\%$	$5\% < |E| \leq 10\%$	$|E| > 10\%$

3.1.2 Scope of the Chapter

Theoretically, the above-mentioned comparisons between experimental and analytical results should be made against test results on isolated components, i.e. using specimens similar to the component to be characterized (e.g. tensile tests on T-stubs for the characterization of the CFB and EPB components, tests on web profiles subjected to local compression forces to characterize the CWC* component…). As regards the PZ, such tests (on isolated PZs) were not found in the scientific literature. This is easily understandable, as the PZ is a complex component whose behaviour depends on a large number of parameters (e.g. non-uniform shear stress distribution over the height of the PZ, stress interactions, influence of the connected beam(s), contribution from the SE...) which are actually difficult to reproduce experimentally (resp. numerically) in tests (resp. simulations) on isolated PZs. Thus, the validation of the analytical models must be conducted on full-scale tests of joints. The present thesis is not intended to perform such experimental tests, as it was shown in the literature review in Section 2.3.1 that a significant number of well documented experimental results were already available in the scientific literature. Consequently, particular attention will be paid to the selection of the most pertinent experimental data to evaluate the models' ability to predict accurately the behaviour of the sheared PZ under monotonic loading conditions. To be selected, an experimental result must exhibit the following two characteristics (or at least the first one):

1) a PZ plastic failure mode to evaluate how accurately the models can predict the plastic shear resistance $V_{y,Rk}^{PZ}$ of the PZ;

2) a PZ ultimate failure mode, or at least a significant PZ deformation, to evaluate the ability of the models to predict the PZ ultimate resistance $V_{u,Rk}^{PZ}$ and deformation capacity γ_u^{PZ}.

The selected experimental results will be divided into two categories based on the type of connection, i.e. either welded or bolted. This choice is deliberate, as these two types of experimental results will be used differently in this thesis, as explained here below:

1) <u>The welded joints</u>, whether stiffened, or unstiffened, are the simplest joints. They are characterized by a limited number of active components, as highlighted in the previous Section 2.2.2 (see Fig. 2-4 and Table 2-1). Moreover, they exhibit one single subpanel with a constant shear force over their entire height. Consequently, the equivalent lever arm z_{eq} can be accurately estimated as the distance between the beam flanges centrelines (see Eq. (2-5)), and so can the equivalent shear force V_{Ek}^{PZ}, through Eq. (2-1). These tests can thus be considered as the closest ones to isolated tests on PZs, giving them relevance in comparisons with analytical models predicting the PZ behaviour.

   For all these reasons, it will be made extensive use, throughout the whole thesis, of the experimental results on welded joints which are presented in the following Section 3.2.1.1:

   (i)   in CHAPTER 3, Section 1.1, to evaluate the performances of the complex and simplified analytical models coming from the scientific literature;

   (ii) in CHAPTER 4, Section 4.2.2, to validate the numerical tool that will be used for the development of new analytical models;

   (iii) in CHAPTER 4, Sections 4.3.1.3 and 4.3.2.3, to validate the new complex and simplified analytical expressions for the prediction of the PZ plastic shear resistance;

   (iv) in CHAPTER 5, Section 5.3.1.4, to validate the new complex analytical model for the prediction of the full PZ behaviour up to failure.

2) <u>The bolted joints</u>, on the other hand, are by far less simple than the welded ones, due to the higher number of active components involved, which significantly complicates the assembly procedure, as depicted in Fig. 2-5 (with respect to Fig. 2-4). In addition, the shear force varies along the height of the PZ according to the loads introduced by the connection rows. This makes it significantly more challenging to define an equivalent lever arm z_{eq}, and consequently an equivalent shear force V_{Ek}^{PZ} acting on the PZ, as reported in Section 2.2.3. Consequently, the experimental results on bolted joints appear less appropriate for the evaluation of the analytical models' performances.

   For all these reasons, the use of the experimental results on bolted joints reported in the following Section 3.2.1.2 will be limited to the following Sections:

   (i)   in CHAPTER 3, Section 3.3.2 to assess the validity of the simplified EN 1993-1-8 and AISC recommendations for the prediction of the PZ plastic shear resistance;

   (ii) in CHAPTER 4, Section 4.3.2.3, to assess the new proposed simplified expression for the evaluation of the plastic shear resistance of the PZ;

   (iii) in CHAPTER 6 to validate, in the case of bolted joints, the new complex and simplified models developed in CHAPTER 4 and CHAPTER 5 for welded joints.

3.1.3 Outline of the Chapter

In order to assess the performances of the analytical models introduced in CHAPTER 2, CHAPTER 3 has been organised as follows: (i) collection of relevant experimental results on welded and bolted joints and building of two distinct databases (see Section 3.2.1), (ii) processing of the data in order to extract the main properties of these test results, i.e. initial stiffness, plastic resistance, post-plastic stiffness, ultimate resistance and ultimate deformation capacity (see Section 3.2.2), (iii) evaluation of the complex and simplified analytical models' performances through comparisons with the selected experimental results (see Sections 3.3.1 and 3.3.2, respectively) and (iv) conclusions (see Section 3.4).

3.2 DATA COLLECTION

3.2.1 Relevant experimental campaigns

3.2.1.1 Welded joint configurations

Table 3-2 provides an overview of the database of the relevant experimental tests on welded joints which was built within the framework of the present thesis. This database contains 12 experimental results coming from seven different experimental campaigns ([50], [82], [84], [85], [100], [113], [117]). All the selected experimental results exhibit a PZ plastic failure mode and a significant PZ shear deformation. However, they differ in the type of joint being tested, either exterior (i.e. single-sided, "s") or interior (i.e. double-sided, "d"), the presence (" ∨ ") or otherwise (" − ") of transverse column web stiffeners, the presence (" ∨ ") or otherwise (" − ") of an axial load in the column, and the loading protocol, either monotonic ("m") or cyclic ("c"), see Table 3-2.

In addition, it can be observed from Table 3-2 that all the beam and column members exhibit traditional European hot-rolled steel sections except the ones in test B1, which exhibit American cross-sections, and the ones in test No. 3, which exhibit thin-walled built-up sections. Strictly speaking, test No. 3 does not fall within the scope of the present study since the column profile does not satisfy the CWP slenderness requirements, see Eq. (2-39). However, it was kept in the database as it is one of the few tests with a well-documented PZ deformation curve up to failure. As regards the members sections, it can also be noticed that some tests display the same beam/column combination. This is the case for the tests E1.1 and E1.2 on the one hand, and for the tests CP-R-M, XU-W1 and XU-CWP1 on the other hand. In the former case, the specimen E1.1 differs from the specimen E1.2 in the type of connection, i.e. welded flanges connection in test E1.1 and welded web, welded flanges connection in test E1.2. The same applies to the tests CP-R-M, XU-W1 and XU-CWP1, where the first and second tests exhibit a welded web, welded flanges connection while the test XU-CWP1 displays a welded cover plates, bolted web cleat connection. The test CP-R-M also differs from the test XU-W1 due to the absence of transverse column web stiffeners. Another observation from Table 3-2 is the presence of two cyclic tests, namely test XU-W1 and test XU-CWP1. Theoretically, they also fall out of the scope of the present study. Yet, they were integrated within the database since the envelope curves were made available, which makes possible the forthcoming comparisons with analytical models.

For sake of clarity of the present manuscript, the detailed data associated to each experimental result presented in Table 3-2 are not reported here. They can be found in Appendix A.1. These data include: (i) the test setup (see Fig. A-1(a) to Fig. A-12(a)); (ii) the available moment-rotation curve(s) (see Fig. A-1(b) to Fig. A-12(b)); the moment M_B being taken at the beam-to-column interface, and the rotation being either the shear distortion γ of the PZ or the total rotation Φ of the joint when the former is not available, (iii) the actual geometric properties, when available – if not, the nominal ones are reported (see Fig. A-1(c) to Fig. A-12(c), respectively); (iv) the actual material properties, when available (see Fig. A-1(d) to Fig. A-12(d), respectively).

As a reminder from Section 3.1.2 (see the boxed text), these 12 test results on welded joints reported in Table 3-2 will be extensively used throughout the thesis: (i) in CHAPTER 3, Section 1.1, to evaluate the performances of the complex and simplified analytical models coming from the scientific literature; (ii) in CHAPTER 4, Section 4.2.2, to validate the numerical tool that will be used for the development of the new analytical models; (iii) in CHAPTER 4, Sections 4.3.1.3 and 4.3.2.3, to validate the new complex and simplified analytical expressions for the prediction of the plastic shear resistance of the PZ; (iv) in CHAPTER 5, Section 5.3.1.4, to validate the new complex analytical model for the prediction of the PZ behaviour up to failure.

3.2.1.2 Bolted joint configurations

Table 3-3 provides an overview of the database of relevant experimental tests on bolted joints which was built within the framework of the present thesis. This database contains 14 experimental results coming from three different experimental campaigns ([28], [86], [98]). All the selected experimental results exhibit a PZ plastic failure mode and a significant PZ shear deformation. However, they differ in the type of joint being tested, either exterior (i.e. single-sided, "s") or interior (i.e. double-sided, "d"), the presence ("∨") or otherwise ("−") of transverse column web stiffeners, the presence ("∨") or otherwise ("−") of an axial load in the column, and the loading protocol, either monotonic ("m") or cyclic ("c"), see Table 3-3.

In addition, it is noteworthy that four cyclic tests are reported in Table 3-3, namely tests E1-XW-P-C1, E2-XW-P-C2, E3-XW-P-C2 and E3-TB-P-C2. The first three tests were performed on double-sided joints while the last one was performed on a single-sided joint with six bolt-rows. In theory, they all fall outside the scope of the present study, which focusses solely on monotonic tests. Yet, they were included within the database since the envelope curves were made available. They also exhibit joint typologies that were not yet available in the database, thereby allowing to widen the scope of the joint typologies investigated within the present thesis.

For sake of clarity of the present document, the detailed data associated to each experimental result presented in Table 3-3 are not reported here. They can be found in Appendix A.2. These data include: (i) the test setup (see Fig. A-13(a) to Fig. A-26(a)); (ii) the available moment-rotation curve(s) (see Fig. A-13(b) to Fig. A-26(b)), the moment M_B being taken at the beam-to-column interface, and the rotation being either the shear distortion γ of the PZ or the total rotation Φ of the joint when the former is not available; (iii) the actual geometrical properties, when available – if not, the nominal ones are reported (see Fig. A-13(c) to Fig. A-26(c), respectively); (iv) the actual material properties (see Fig. A-13(d) to Fig. A-26(d), respectively).

As a reminder from Section 3.1.2 (see the boxed text), these 14 test results on bolted joints reported in Table 3-3 will be used from time to time in the present thesis (i) to assess the validity of the simplified EN 1993-1-8 and AISC recommendations for the prediction of the plastic shear resistance of the PZ (see CHAPTER 3, Section 3.3.2); (ii) to evaluate the new proposed simplified expression for the evaluation of the plastic shear resistance of the PZ (see CHAPTER 4, Section 4.3.2.3) and, (iii) to evaluate the performance of the new complex and simplified analytical models when applied to bolted joints (see CHAPTER 6).

Table 3-2. Database of test results on welded joints.

No.	Authors	Specimen	Column section	Beam section	Test setup Single-sided = "s" Double-sided = "d"	Stiffeners Yes = "v" No = "-"	Axial load Yes = "v" No = "-"	Loading protocol Monotonic = "m" Cyclic = "c"	University, Country	Year
1	Fielding et al. [50]	B1	W14x184	W24x160	s	v	v	m	Lehigh, USA	1971
2	Klein [100]	NR2	HEB140	IPE220	s	-	-	m	Innsbruck, Austria	1985
3	Klein [100]	NR3	HEB140	IPE300	s	-	-	m	Innsbruck, Austria	1985
4	Klein [100]	NR4	HEB160	IPE330	s	-	-	m	Innsbruck, Austria	1985
5	Klein [100]	NR7	HEB180	IPE400	s	-	-	m	Innsbruck, Austria	1985
6	Calado et al. [82]	BCC5-E	HEB160	IPE300	s	v	-	m	Lisbon, Portugal	1999
7	Dubina et al. [84]	XU-W1	HEB300	IPE360	d	v	-	c	Timisoara, Romania	2000
8	Dubina et al. [84]	XU-CWP1	HEB300	IPE360	d	v	-	c	Timisoara, Romania	2000
9	Jordão [113]	E1.1	HEB240	IPE400	s	-	-	m	Coimbra, Portugal	2008
10	Jordão [113]	E1.2	HEB240	IPE400	s	-	-	m	Coimbra, Portugal	2008
11	Ciutina et al. [85]	CP-R-M	HEB300	IPE360	d	-	-	m	Timisoara, Romania	2008
12	Fasoulakis et al. [117]	No. 3	220x3x150x10	320x3x180x10	s	v	-	m	Athens, Greece	2021

Table 3-3. Database of test results on bolted joints.

No.	Authors	Specimen	Column section	Beam section	Test setup Single-sided = "s" Double-sided = "d"	Stiffeners Yes = "v" No = "-"	Axial load Yes = "v" No = "-"	Loading protocol Monotonic = "m" Cyclic = "c"	University, Country	Year
1	Jaspart [28]	01	HEB160	IPE200	s	v	v	m	Liège, Belgium	1991
2	Jaspart [28]	04	HEB160	IPE200	s	v	v	m	Liège, Belgium	1991
3	Jaspart [28]	07	HEB160	IPE200	s	-	-	m	Liège, Belgium	1991
4	Jaspart [28]	010	HEB160	IPE300	s	-	-	m	Liège, Belgium	1991
5	Nogueiro [86]	J1.1	HEA320	IPE360	s	-	-	m	Coimbra, Portugal	2009
6	Nogueiro [86]	J2.1	HEA320	IPE360	s	v	v	m	Coimbra, Portugal	2009
7	Nogueiro [86]	J3.1	HEB320	IPE360	s	v	-	m	Coimbra, Portugal	2009
8	Nogueiro [86]	J4.1	HEA320	HEA280	s	v	-	m	Coimbra, Portugal	2009
9	Equaljoints+ [98]	E1-TB-E-M	HEB280	IPE360	s	v	-	m	Naples, Italy	2018
10	Equaljoints+ [98]	E1-XW-P-C1	HEB340	IPE360	d	v	-	c	Naples, Italy	2018
11	Equaljoints+ [98]	E2-TB-E-M	HEB340	IPE450	s	v	-	m	Liège, Belgium	2018
12	Equaljoints+ [98]	E2-XW-P-C2	HEB500	IPE450	d	v	-	c	Liège, Belgium	2018
13	Equaljoints+ [98]	E3-TB-E-C2	HEB500	IPE600	s	v	-	c	Liège, Belgium	2018
14	Equaljoints+ [98]	E3-XW-P-C2	HEB650	IPE600	d	v	-	c	Liège, Belgium	2018

3.2.2 Data processing

The so-selected experimental results on welded and bolted joints were then processed to extract the main performance parameters from the experimental $\left(M^j - \Phi\right)_{exp}$ moment-rotation curves. These key parameters were introduced in Section 2.2.1 (see Fig. 2-3) and consist of: (i) the initial stiffness S^j_{ini}, (ii) the plastic bending moment resistance $M^j_{y,Rk}$, (iii) the post-plastic stiffness S^j_{pp}, (iv) the ultimate bending moment resistance $M^j_{u,Rk}$ and the associated ultimate rotation capacity Φ_u. They are summarized in Table 3-4 and Table 3-5 for the welded and bolted test results that are considered in the present thesis. They will be used in the following Section 1.1 in relevant comparisons to assess the performances of the analytical models introduced in Section 2.3.

3.2.2.1 Description of the elasto-plastic behaviour up to yielding

A. Elastic stiffness $S^j_{ini,exp}$

As regards the initial elastic stiffness $S^j_{ini,exp}$, it may be determined by adjusting a straight line $\boxed{A}$ to the initial elastic branch of the experimental curves, which ranges from the point of zero loading up to the onset yielding. This is schematically depicted in Fig. 3-1, see the graphical constructions in light blue. This procedure has been applied to the 12 welded and 14 bolted experimental results reported in Appendix A (see the graphical constructions in light blue in Fig. A-1(b) to Fig. A-26(b)). In addition, Table 3-4 and Table 3-5 give an overview of the values of $S^j_{ini,exp}$ that were obtained graphically.

However, it is noteworthy that the initial slope of the experimental curve is highly sensitive to the initial flexibility of the test setup, which may arise from the gaps and slips between the bolted components at the level of the connection or at the supports of the test setup. Therefore, it is usually recommended to fit the elastic stiffness to the unloading branch of an unloading-reloading cycle, when such a cycle has been contemplated in the experimental protocol.
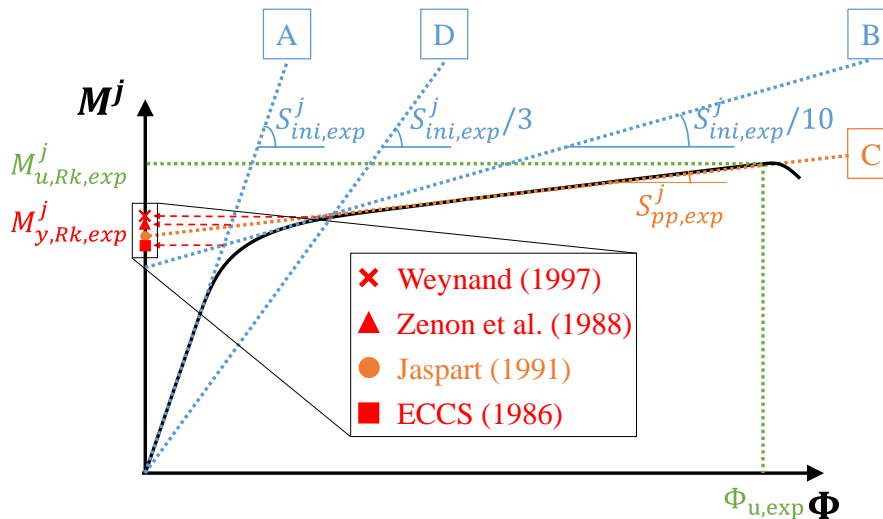

Fig. 3-1. Schematic definition of the main performance parameters of a joint's typical $\left(M^j - \Phi\right)_{exp}$ curve.

B. Plastic bending moment resistance $M_{y,Rk,exp}^{j}$

Theoretically, the plastic bending moment resistance $M_{y,Rk,exp}^{j}$ of the joint corresponds to the yielding (or the failure) of the joint's weakest component. However, for ductile components, this phenomenon does not appear suddenly; instead, plasticity gradually spreads throughout the component. This leads to the progressive decrease of the joint stiffness and to the knee observed in the experimental $\left(M^{j} - \Phi\right)_{exp}$ curve, see Fig. 3-1. Consequently, it is difficult to define a precise experimental value for $M_{y,Rk,exp}^{j}$ and several methods can be found in the scientific literature (summarized in [118]), which are schematically illustrated in Fig. 3-1:

- The European Convention for Constructional Steelwork (ECCS, [119], 1986) defines $M_{y,Rk,exp}^{j}$ as the intersection between two straight lines $\boxed{A}$ and $\boxed{B}$ corresponding to the initial stiffness $S_{ini,exp}^{j}$ and a given post-plastic stiffness. The latter is defined as the tangent to the experimental $\left(M^{j} - \Phi\right)_{exp}$ curve, with a slope given by $S_{ini,exp}^{j}/h$, where h is set at 10 (see the red square in Fig. 3-1). This procedure was originally developed to assess the behaviour of joints under cyclic loads.
- Zenon et al. ([120], 1988) use the same definition for $M_{y,Rk,exp}^{j}$ as the one recommended by the ECCS but they adjust the value of h on a case-by-case basis in such a way that the second (orange) straight line $\boxed{C}$ becomes tangent to the post-plastic branch following the knee of the joint response. The so-obtained $M_{y,Rk,exp}^{j}$ value is highlighted with a red triangle in Fig. 3-1.
- Jaspart ([28], 1991) defines $M_{y,Rk,exp}^{j}$ as the intersection between the y-axis and a second (orange) straight line $\boxed{C}$ corresponding to the experimental post-plastic stiffness $S_{pp,exp}^{j}$ of the joint. The so-obtained $M_{y,Rk,exp}^{j}$ value is highlighted with an orange dot in Fig. 3-1.
- Weynand ([121], 1997) defines $M_{y,Rk,exp}^{j}$ as the intersection between the experimental curve and a secant stiffness equal to one-third of the initial elastic stiffness $S_{ini,exp}^{j}$ (line $\boxed{D}$). This definition, which is highlighted with a red cross in Fig. 3-1, has been adopted by EN 1993-1-8.

The author is aware that these methods are highly dependent on the points chosen on the experimental curve to determine $S_{ini,exp}^{j}$ and $S_{pp,exp}^{j}$. Their accuracy is thus questionable, especially in the absence of a well-marked bilinear behaviour of the tested joints. Nevertheless, the procedures of Zenon et al., Jaspart and Weynand (the ECCS procedure is more relevant for cyclic tests) were applied to the 26 welded and bolted experimental results presented in Appendix A (see the graphical constructions in Fig. A-1(b) to Fig. A-26(b)). The Zenon et al. and Jaspart procedures produce very similar results in terms of $M_{y,Rk,exp}^{j}$ for all experimental results, which gives confidence in the so-obtained $M_{y,Rk,exp}^{j}$ values. By contrast, the values obtained with the Weynand procedure are a bit more erratic.

The Jaspart definition is perfectly in line with the modelling approaches defined in Fig. 2-3 and therefore appears as the most suitable one to evaluate the performances of the analytical models introduced in Section 2.3. Consequently, this definition has been adopted by the author for the rest of the present thesis. Table 3-4 and Table 3-5 provide an overview of the $M_{y,Rk,exp}^{j}$ values obtained for the welded and bolted test results with the Jaspart procedure only.

3.2.2.2 Description of the post-plastic behaviour up to failure

A. Post-plastic stiffness $S_{pp,exp}^{j}$

As regards the strain-hardening (i.e. post-plastic) stiffness $S_{pp,exp}^{j}$, it may be determined by adjusting a (orange) straight line $\boxed{C}$ to the post-plastic branch of the experimental curves, following the knee of the curves. This is schematically depicted in Fig. 3-1 (see the graphical constructions in light orange). This procedure has been applied to the 26 welded and bolted experimental results reported in Appendix A (see the graphical constructions in light orange in Fig. A-1(b) to Fig. A-26(b)). In addition, Table 3-4 and Table 3-5 summarize the graphically obtained $S_{pp,exp}^{j}$ values for the welded and bolted test results, respectively. Again, it is noteworthy that the accuracy of the approach is strongly dependent on the well-marked bilinear shape of the curve.

B. Ultimate bending moment resistance $M_{u,Rk,exp}^{j}$ and deformation capacity $\Phi_{u,exp}$

As regards the joint's ultimate performance parameters (i.e. $M_{u,Rk,exp}^{j}$ and $\Phi_{u,exp}$), they depend on the type of ultimate failure mode actually developing in the joint. In typical joints, several failure modes could theoretically be contemplated and cause the test to stop, namely:

- The <u>global instability</u> of the column (i.e. global column buckling, "GB_c") when the column withstands a significant axial load;
- The <u>local instability</u> of the sheared PZ (i.e. the shear buckling of the PZ, "LB_{PZ}"), or of one of the compressed components (i.e. either the local buckling of the CWC*, "LB_{CWC^*}", or the local buckling of the BFC, "LB_{BFC}"). However, these failure modes do not, strictly speaking, correspond to the actual failure of the joint. In fact, due to their high ductility, they allow additional rotation of the joint under almost zero bending moment. Consequently, the loading procedure can be carried on until the fracture of a brittle component occurs.
- The <u>fracture of the material</u> (i.e. material fracture, "MF") which usually occurs in a brittle element (e.g. bolts or welds) and is caused by the excessive deformation of one of the active components. This failure mode is known to be brittle and causes a sudden drop in the joint resistance which may be seen as the end of the experimental test.

Based on this discussion, the test results reported in previous Table 3-2 and Table 3-3 can be classified into three main categories as follows:

- Category I (failure mode: "Testing setup"): these tests were not designed nor performed with the aim of investigating the ultimate deformation capacity of the joint. Consequently, they were stopped before reaching the ultimate failure of the joint, due to the limitation of the measurement devices or the capacity of the loading cell. This is the case for the welded test results NR2, NR3, NR4, NR7 and CP-R-M and for the bolted test results J3.1, E1-TB-E-M and E1-XW-P-C1.
- Category II (failure mode: "LB_{PZ}", "LB_{CWC^*}" or "LB_{BFC}"): these tests were stopped after the initiation of local buckling in the PZ, the CWC* or the BFC, but before reaching any fracture of the material. This is the case for the welded tests No. 3 (initiation of LB_{PZ}), B1 and BCC5-E (initiation of LB_{BFC}), E1.1 and E1.2 (initiation of LB_{CWC^*}) and the bolted tests 01, 04, 07, 010 (initiation of LB_{CWC^*}).
- Category III (failure mode: "MF"): for these tests, the fracture of the material was reached in one of the active components, namely in the fillet welds at the beam-to-column interface for the welded test results XU-W1 and XU-CWP1, and in the EPB component for the bolted test results J1.1, J2.1, J4.1, E2-TB-E-M, E2-XW-P-C2, E3-TB-P-C2 and E3-XW-P-C2.

The observed failure modes associated to each welded (resp. bolted) test result are so reported in the last column of Table 3-4 (resp. Table 3-5), together with the ultimate bending moment resistance $M_{u,Rk,exp}^{j}$ and rotation capacity $\Phi_{u,exp}/\gamma_{u,exp}^{PZ}$. The latter ones correspond to the maximum bending moment recorded during the testing procedure and the associated rotation, respectively (see the graphical constructions in light green in Fig. A-1(b) to Fig. A-26(b)). From the discussion above, it is clear that these ultimate performance parameters (i.e. $M_{u,Rk,exp}^{j}$ and $\Phi_{u,exp}$) only define the actual failure of the joint for those belonging to category III.

Table 3-4. Key behavioural parameters associated to the test results on welded joints.

No.	Specimen	$S_{ini,exp}^{j}$ (kNm/rad)	$M_{y,Rk,exp}^{j}$ (kNm)	$S_{pp,exp}^{j}$ (kNm/rad)	$M_{u,Rk,exp}^{j}$ (kNm)	$\Phi_{u,exp}/\gamma_{u,exp}^{PZ}$ (rad)	Ultimate failure mode
1	B1	363,636.4	868.4	8,446.5	1,671.8	0.107	LB_{BFC}
2	NR2	8,790.5	58.8	336.9	85.5	0.133	Testing setup
3	NR3	15,383.3	81.8	437.6	122.3	0.133	Testing setup
4	NR4	10,255.6	118.2	215.4	141.0	0.115	Testing setup
5	NR7	16,365.2	158.1	678.0	210.7	0.130	Testing setup
6	BCC5-E	23,325.0	133.3	655.8	192.3	0.182	LB_{BFC}
7	XU-W1	59,429.0	190.9	1,141.0	242.7	0.052	MF
8	XU-CWP1	62,939.0	198.2	1,779.1	282.7	0.052	MF
9	E1.1	60,318.6	334.4	1,203.4	415.4	0.133	LB_{CWC*}
10	E1.2	63,054.0	328.2	1,504.3	440.0	0.125	LB_{CWC*}
11	CP-R-M	51,166.7	141.8	848.7	222.8	0.145	Testing setup
12	No. 3	7,068.2	53.5	182.9	79.0	0.169	LB_{PZ}

Table 3-5. Key behavioural parameters associated to the test results on bolted joints.

No.	Specimen	$S_{ini,exp}^{j}$ (kNm/rad)	$M_{y,Rk,exp}^{j}$ (kNm)	$S_{pp,exp}^{j}$ (kNm/rad)	$M_{u,Rk,exp}^{j}$ (kNm)	$\Phi_{u,exp}/\gamma_{u,exp}^{PZ}$ (rad)	Ultimate failure mode
1	01	20,488.9	58.8	200.6	79.0	0.103	LB_{CWC*}
2	04	16,612.6	55.9	241.6	74.9	0.088	LB_{CWC*}
3	07	16,612.6	59.0	249.6	81.2	0.096	LB_{CWC*}
4	010	36,640.0	86.2	863.7	124.6	0.052	LB_{CWC*}
5	J1.1	69,450.0	333.8	1,300.9	422.1	0.069	MF
6	J2.1	47,793.1	325.3	1,300.9	391.9	0.096	MF
7	J3.1	111,878.8	381.5	2,042.1	471.8	0.044	Testing setup
8	J4.1	37,849.3	266.2	1,375.7	388.5	0.100	MF
9	E1-TB-E-M	92,100.0	338.1	1,065.0	424.5	0.079	Testing setup
10	E1-XW-P-C1	34,666.7	295.8	790.4	347.9	0.074	Testing setup
11	E2-TB-E-M	148,848.5	530.6	3,364.4	707.0	0.055	MF
12	E2-XW-P-C2	130,793.7	533.3	2,155.7	661.8	0.070	MF
13	E3-TB-E-C2	343,333.3	1,230.3	7,262.7	1,460.6	0.033	MF
14	E3-XW-P-C2	166,612.9	919.9	4,004.3	1,137.5	0.067	MF

3.3 EVALUATION OF THE MODELS PERFORMANCES

3.3.1 Complex analytical models

3.3.1.1 Characterization of the elasto-plastic behaviour up to yielding

A. Elastic stiffness S_{ini}^j

Among the 12 experimental results on welded joints reported in Table 3-2, five are stiffened, namely the tests B1, BCC5-E, XU-W1, XU-CWP1 and No. 3. For the latter, the PZ turns out to be the only active component contributing to the joint deformability (since the deformations of the two other active components, namely the BFC and the CFB, are considered in the deformation of the connected beam). Therefore, these experimental results are particularly relevant for assessing how accurately the analytical models introduced in Section 2.3.2 can predict the PZ initial stiffness $K_{y,exp}^{PZ}$. The test CP-R-M was also considered, as the $\left(M^j - \gamma\right)_{exp}$ deformation curve of the PZ was recorded during the test.

For each of these six welded experimental results, the PZ initial stiffness K_y^{PZ} was first assessed analytically with the nine analytical models introduced in Section 2.3.2. These analytical estimations were obtained through Eq. (2-15), using the analytical expressions provided in Table 2-5 to Table 2-7, and the actual geometric and mechanical properties shown in Appendix A (see Fig. A-1(c),(d) to Fig. A-12(c),(d)) for the six relevant welded experimental results.

As a second step, these values were assembled through Eq. (2-2) to obtain an analytical estimation S_{ini}^j of the initial rotational stiffness for the different welded joints considered in the present study. Since the PZ is the only component contributing to the joint stiffness, Eq. (2-2) can be simplified as follows, see Eq. (3-1), where k_{ini}^{PZ} is the stiffness coefficient associated to the PZ and can be expressed through Eq. (3-2):

$$S_{ini}^j = \frac{E \cdot z_{eq}^2}{\dfrac{1}{k_{ini}^{PZ}}} = E \cdot k_{ini}^{PZ} \cdot z_{eq}^2 \tag{3-1}$$

$$E \cdot k_{ini}^{PZ} = \frac{K_y^{PZ}}{\beta \cdot z_{eq}} \tag{3-2}$$

In Eq. (3-1) and Eq. (3-2), E is the Young's modulus, z_{eq} can be obtained from Eq. (2-5) for welded joints and β is the transformation parameter, which was introduced in Section 2.2.1 (see Eq. (2-1)) and which depends on the loading and support conditions. For the joints considered in the present thesis, β can be computed through Eq. (3-3), where a and b are two parameters accounting for the type of joint configuration, either exterior ($a = 1.0$) or interior ($a = 2.0$), and the type of support conditions, either hinged ($b = 0$) or fixed ($b = 0.25$). For the values of the other geometric parameters involved in Eq. (3-3), the reader is referred to the description of the different experimental results in Appendix A (see Fig. A-1(a),(c) to Fig. A-12(a),(c)).

$$\beta = a \cdot \left[1 - \frac{\left(L_b + \dfrac{h_c}{2}\right) \cdot z_{eq} \cdot (1 + 2 \cdot b)}{L_b \cdot L_c}\right] \tag{3-3}$$

The S_{ini}^{j} values obtained with Eq. (3-1) are reported in Table 3-6 for each analytical model, where they are compared to the experimental $S_{ini,exp}^{j}$ values coming from Table 3-4. These comparisons are conducted on the basis of the performance indicator and the colour code defined in Table 3-1.

Table 3-6. Comparisons between S_{ini}^{j} and $S_{ini,exp}^{j}$ for six of the test results on welded joints coming from Table 3-2.

Authors	Test B1		Test BCC5-E		Test XU-W1	
	S_{ini}^{j} (kNm/rad)	E (%)	S_{ini}^{j} (kNm/rad)	E (%)	S_{ini}^{j} (kNm/rad)	E (%)
Exp. results	363,636.4	-	23,325.0	-	59,429.0	-
Fielding (1971)	500,028.3	37.51	37,208.6	59.52	55,444.6	-6.70
Krawinkler (1978)	521,075.4	43.30	38,474.2	64.95	56,202.7	-5.43
Wang (1988)	451,556.1	24.18	33,918.0	45.41	51,728.4	-12.96
Jaspart (1991)	576,252.0	58.47	55,659.1	138.62	83,464.6	40.44
Schneider (1998)	548,847.2	50.93	40,024.6	71.60	60,509.7	1.82
Lin (2000)	491,151.3	35.07	36,553.8	56.71	55,362.3	-6.84
Engelhardt (2002)	515,699.1	41.82	37,406.7	60.37	57,297.3	-3.59
Kim (2015)	536,064.4	47.42	39,181.6	67.98	57,692.5	-2.92
Skiadopoulos (2021)	452,068.1	24.32	32,750.3	40.41	52,578.5	-11.53
Authors	Test XU-CWP1		Test CP-R-M		Test No. 3	
	S_{ini}^{j} (kNm/rad)	E (%)	S_{ini}^{j} (kNm/rad)	E (%)	S_{ini}^{j} (kNm/rad)	E (%)
Exp. results	62,939.0	-	51,166.7	-	7,068.2	-
Fielding (1971)	63,409.3	0.75	51,198.9	0.06	19,575.7	176.95
Krawinkler (1978)	64,272.1	2.12	51,927.7	1.49	19,196.8	171.59
Wang (1988)	59,163.9	-6.00	47,737.0	-6.70	18,944.2	168.02
Jaspart (1991)	94,353.1	49.91	78,558.7	53.53	22,733.1	221.62
Schneider (1998)	64,018.5	1.72	56,225.3	9.89	21,303.9	201.41
Lin (2000)	62,788.2	-0.24	51,566.3	0.78	20,222.5	186.11
Engelhardt (2002)	65,084.5	3.41	53,047.2	3.68	20,032.6	183.42
Kim (2015)	65,658.8	4.32	53,428.5	4.42	19,644.7	177.93
Skiadopoulos (2021)	59,447.1	-5.55	48,713.5	-4.79	19,278.0	172.74

The following conclusions can be drawn from Table 3-6:

- For the three single-sided tests, i.e. B1, BCC5-E and No. 3, the initial stiffness of the PZ is significantly much overestimated by all the analytical models. For the tests B1 and BCC5-E, this scatter is certainly due to the assumption of perfectly-fixed support conditions regarding the derivation of β, whereas it is likely that these supports actually had some flexibility arising from the gaps and slips between the bolted components at the supports. For the test No. 3, it can be noticed from the $M_B - \Phi$ curve in Appendix A (see Fig. A-12(b)) that there were some issues with the initial recordings of the test data, which may explain the high discrepancy observed between the experimental and analytical stiffnesses.
- By contrast, for the three double-sided tests, i.e. XU-W1, XU-CWP1 and CP-R-M, a fairly good agreement is observed between the analytical predictions and experimental observations, except with the Jaspart (resp. Wang) model, which significantly overestimates (resp. moderately underestimates) the initial stiffness due to the over-estimation (resp. under-estimation) of the effective shear area A_{VC}, as suggested in ([39], [94]) (resp. [57], [122]).

These results show that the prediction of the PZ initial stiffness mostly relies on an accurate estimation of the effective shear area A_{VC}, while the consideration of the bending mode has very low influence on the results.

B. Plastic bending moment resistance $M_{y,Rk}^{j}$

The plastic shear resistance $V_{y,Rk}^{PZ}$ of the PZ can first be assessed analytically for the 12 experimental results on welded joints reported in Table 3-2, using the nine analytical models introduced in Section 2.3.2. This is done through Eq. (2-14), using the analytical expressions provided in Table 2-5 to Table 2-7 for $V_{y,Rk}^{CWP}$ and $\Delta V_{y,Rk}^{SE}$ (used as simpler expressions instead of $V_{y,PZ,Rk}^{CWP}$ and $\Delta V_{y,PZ,Rk}^{SE}$) and the actual geometric and mechanical properties given in Appendix A (see Fig. A-1(a)-(d) to Fig. A-12(a)-(d)) for the 12 relevant welded experimental results.

These $V_{y,Rk}^{PZ}$ values can subsequently be transformed into load-introduction connection forces $F_{y,Rk}^{PZ}$ and assembled through Eq. (2-7) to obtain an analytical estimation of the plastic bending moment resistance $M_{y,Rk}^{j}$ for the different welded joints considered in the present study. Since all the test results exhibit a PZ plastic failure mode, Eq. (2-7) can be simplified as follows, see Eq. (3-4), where β can be derived through Eq. (3-3) according to the type of joint configuration and boundary conditions and z_{eq} is given in Eq. (2-5):

$$M_{y,Rk}^{j} = M_{y,Rk}^{PZ} = F_{y,Rk}^{PZ} \cdot z_{eq} = \frac{V_{y,Rk}^{PZ}}{\beta} \cdot z_{eq} \qquad (3\text{-}4)$$

These $M_{y,Rk}^{j}$ values (the notation $M_{y,Rk}^{PZ}$ could also be used since the PZ is the failing component) are reported in Table 3-7 for each analytical model, where they are compared to the experimental $M_{y,Rk,exp}^{j}$ values. These comparisons are conducted using the performance indicator and the colour code defined in Table 3-1. Visual comparisons are also provided in Appendix A for each experimental result (see Fig. A-1(e) to Fig. A-12(e)). The following conclusions can be drawn from Table 3-7 and Fig. A-1(e) to Fig. A-12(e) regarding the performances of the different analytical models:

- The Krawinkler model performs well in the case of stiffened joints (tests B1, BCC5-E, XU-W1, XU-CWP1, No. 3), with a relative error ranging from −2.17% to 3.81% (high level of accuracy). However, for unstiffened interior and exterior joints (tests CR-R-M, NR2, NR4, NR7, E1.1 and E1.2), the model tends to overestimate $M_{y,Rk,exp}^{j}$, with a relative error varying from 4.60% up to 10.74% (high to low level of accuracy). The same applies in the presence of stocky columns with thick column flanges (i.e. $t_{fc} > 30 - 40\ mm$), as evidenced in the literature ([52], [56]–[58]).

- The Wang (resp. Lin) model significantly underestimates (resp. overestimates) $M_{y,Rk,exp}^{j}$ in most of the cases, with a relative error ranging from −6.38% to −23.20% (resp. 3.34% to 26.94%). This is mostly due to the underestimation (resp. overestimation) of the effective shear area A_{VC}, as suggested in ([57], [122]).

- The Jaspart model features a moderate to low level of accuracy as it tends to overestimate (sometimes significantly) $M_{y,Rk,exp}^{j}$ in all the cases, but one (i.e. the test No. 3 with built-up sections). This observation is in line with the main conclusion drawn in ([39], [122]), where the authors suggest the effective shear area A_{VC} to be re-evaluated.

- The Engelhardt model provides an accurate estimation of $M_{y,Rk,exp}^{j}$ (moderate to high level of accuracy) for unstiffened interior and exterior joints. However, in the presence of transverse column web stiffeners, the model tends to be more conservative, especially in the case of stiffened interior joints (low level of accuracy). These observations, which also apply to the Kim and Skiadopoulos models, suggest that the contribution of the SE should be re-evaluated.

- The Schneider model underestimates $M_{y,Rk,exp}^{j}$ in all the cases, but especially for stiffened interior and exterior joints where it displays a low level of accuracy.

- The Fielding model is not assessed here since it does not suggest any expression for the plastic shear resistance $V_{y,Rk}^{PZ}$ of the whole PZ.

These comparisons show that none of the complex analytical models introduced in Section 2.3.2 provides satisfactory results (i.e. highly accurate results) for all 12 investigated cases. This emphasizes the need for a better understanding of the physical phenomena governing the plastic shear resistance of the PZ.

Table 3-7. Comparisons between $M_{y,Rk}^{j}$ and $M_{y,Rk,exp}^{j}$ for the 12 experimental results on welded joints reported in Table 3-2.

Authors	Test B1		Test NR2		Test NR3		Test NR4	
	$M_{y,Rk}^{j}$ (kNm)	E (%)	$M_{y,Rk}^{j}$ (kNm)	E (%)	$M_{y,Rk}^{j}$ (kNm)	E (%)	$M_{y,Rk}^{j}$ (kNm)	E (%)
Exp. results	868.4	-	58.8	-	81.8	-	118.2	-
Krawinkler (1978)	892.5	2.77	62.9	7.00	85.6	4.68	123.7	4.62
Wang (1988)	713.1	-17.88	51.3	-12.69	70.2	-14.16	104.2	-11.83
Jaspart (1991)	925.0	6.52	62.7	6.71	87.9	7.51	137.2	16.11
Schneider (1998)	778.3	-10.38	55.9	-4.96	76.6	-6.40	112.8	-4.57
Lin (2000)	968.9	11.58	70.4	19.68	95.8	17.11	142.7	20.75
Engelhardt (2002)	829.4	-4.49	60.4	2.77	82.9	1.35	121.4	2.69
Kim (2015)	924.6	6.48	61.0	3.82	82.0	0.25	121.3	2.60
Skiadopoulos (2021)	824.9	-5.01	59.4	1.00	81.9	0.15	121.2	2.54
Authors	Test NR7		Test BCC5-E		Test XU-W1		Test XU-CWP1	
	$M_{y,Rk}^{j}$ (kNm)	E (%)	$M_{y,Rk}^{j}$ (kNm)	E (%)	$M_{y,Rk}^{j}$ (kNm)	E (%)	$M_{y,Rk}^{j}$ (kNm)	E (%)
Exp. results	158.1	-	133.3	-	190.9	-	198.2	-
Krawinkler (1978)	175.1	10.74	130.4	-2.17	174.3	-8.70	194.5	-1.88
Wang (1988)	148.0	-6.38	107.7	-19.18	146.6	-23.20	165.1	-16.71
Jaspart (1991)	183.6	16.10	153.5	15.13	203.7	6.73	228.0	15.04
Schneider (1998)	160.1	1.26	117.0	-12.20	155.7	-18.45	164.4	-17.06
Lin (2000)	200.1	26.56	148.7	11.53	197.3	3.34	221.8	11.90
Engelhardt (2002)	172.2	8.89	126.3	-5.22	164.8	-13.69	185.8	-6.24
Kim (2015)	170.9	8.08	126.6	-5.04	164.2	-13.97	184.7	-6.80
Skiadopoulos (2021)	172.2	8.89	125.3	-6.00	165.3	-13.43	186.4	-5.98
Authors	Test E1.1		Test E1.2		Test CP-R-M		Test No. 3	
	$M_{y,Rk}^{j}$ (kNm)	E (%)	$M_{y,Rk}^{j}$ (kNm)	E (%)	$M_{y,Rk}^{j}$ (kNm)	E (%)	$M_{y,Rk}^{j}$ (kNm)	E (%)
Exp. results	334.4	-	328.2	-	141.8	-	53.5	-
Krawinkler (1978)	358.9	7.31	358.9	9.34	142.5	0.49	55.5	3.81
Wang (1988)	302.7	-9.48	302.7	-7.77	119.6	-15.64	49.0	-8.43
Jaspart (1991)	391.7	17.13	391.7	19.34	152.5	7.55	52.3	-2.22
Schneider (1998)	325.0	-2.82	325.0	-0.98	127.1	-10.37	50.4	-5.84
Lin (2000)	416.6	24.58	416.6	26.94	162.9	-14.86	64.2	19.93
Engelhardt (2002)	347.2	3.84	347.2	5.80	134.6	-5.11	51.8	-3.25
Kim (2015)	347.6	3.95	347.6	5.92	135.0	-4.77	49.8	-6.82
Skiadopoulos (2021)	348.2	4.13	348.2	6.10	135.3	-4.56	53.4	-0.26

3.3.1.2 Characterization of the post-plastic behaviour up to failure

Among the nine analytical models presented in Table 2-5 to Table 2-7, only three of them go beyond the yielding of the PZ, being the ones of Jaspart, Kim and Skiadopoulos. The Kim model assumes that the PZ deformation capacity is exhausted as soon as four plastic hinges form in the column flanges. In reality, the PZ exhibits a significant reserve of ductility and can go far beyond the yielding of the SE. The same observation was made with the Skiadopoulos model which limits the PZ shear distortion to $6 \cdot \gamma_y^{CWP}$ to avoid the development of brittle failure in the welds at the beam-to-column interface, γ_y^{CWP} being the yield shear distortion of the PZ. Therefore, these criteria are not relevant as soon as the prediction of the ultimate deformation capacity of the PZ is concerned.

The Kim and Skiadopoulos models will thus be excluded from the present study which will focus solely on the Jaspart model and assess its capacity to predict the PZ post-plastic behaviour up to failure. This will be done through comparisons with the 12 test results on welded joints reported in Table 3-2.

Among these tests, four were excluded from the comparisons, namely the tests NR2, NR3, NR4 and NR7, since the strain-hardening and ultimate material properties were not available, thus preventing any computation of the post-plastic behaviour of the PZ. As regards the eight remaining test results, it is noteworthy that only one, namely test No. 3, actually exhibits a PZ ultimate failure mode (LB_{PZ}). For all the others, despite exhibiting significant PZ shear deformations, the ultimate failure of the PZ is bypassed by other failure modes, being the LB_{CWC^*} for the tests E1.1 and E1.2, the LB_{BFC} for the tests B1 and BCC5-E, the MF for the tests XU-W1 and XU-CWP1 and the limitation of the testing setup for the test CP-R-M. Consequently, only qualitative visual comparisons may be contemplated between experimental results and analytical predictions. This is a clear limitation of the present study which aims at assessing the ability of the Jaspart model in accurately predicting the PZ post-plastic behaviour up to failure.

To compare the eight selected welded experimental results, it is required to derive the $\left(M^j - \Phi\right)_{an}$ analytical curves of the joints. These curves can be obtained from the assembly of the active individual components' deformation curves.

As regards the PZ behaviour, it was assessed with the Jaspart model, first in terms of $(V^{PZ} - \gamma)_{an}$ curves. These analytical curves were obtained using: (i) the analytical expressions provided in Table 2-6 and (ii) the actual geometric and mechanical properties given in Appendix A (see Fig. A-1(c),(d) to Fig. A-12(c),(d)) for the eight relevant experimental results. The Jaspart model being semi-empirical, the ECCS material model was used to derive the missing mechanical properties (i.e. the strain-hardening properties E_{pp} and ε_{pp}). This material model is presented in detail in the forthcoming Section 4.2.2. The so-obtained $(V^{PZ} - \gamma)_{an}$ curves were then substituted by $(M^{PZ} - \gamma)_{an}$ curves through the use of Eq. (3-5), where β and z_{eq} are given in Eq. (3-3) and Eq. (2-5), respectively. These $(M^{PZ} - \gamma)_{an}$ are depicted in Appendix A (see the blue solid curves in Fig. A-1(g) to Fig. A-12(g)) for the eight relevant experimental results.

$$M^c = F^c \cdot z_{eq} = \begin{cases} \dfrac{V^c}{\beta} \cdot z_{eq} = \overbrace{\left[\dfrac{K^c \cdot z_{eq}}{\beta}\right]}^{s^c} \cdot \gamma & c \sim \text{PZ} \\[2em] \underbrace{\left[E \cdot k^c \cdot z_{eq}^2\right]}_{s^c} \cdot \phi^c & c \sim \text{CWC}^*, \text{CWT}, \text{CFB or BFC} \end{cases} \tag{3-5}$$

Similarly, the $(F^c - \Delta^c)_{an}$ curves (subscript $"c"$ standing for "CWC*", "CWT", "CFB" or "BFC") were analytically derived for all the other components that are active at the level of the connection, i.e. the CFB and the BFC, plus the CWC*/CWT when the joint is unstiffened. These analytical $(F^c -$

$\Delta^c)_{an}$ curves were obtained using: (i) the analytical expressions given in Table 2-2 for the description of the elasto-plastic behaviour; (ii) the procedure suggested by Jaspart (see Section 2.2.3.1) for the description of the post-plastic behaviour up to failure; and (iii) the actual geometric and mechanical properties given in Appendix A (see Fig. A-1(c),(d) to Fig. A-12(c),(d)) for the eight relevant experimental results. These $(F^c - \Delta^c)_{an}$ curves were then substituted by $(M^c - \phi^c)_{an}$ curves, by applying Eq. (3-5), where E is the Young's modulus and z_{eq} can be obtained from Eq. (2-5) for welded joints. The so-obtained $(M^c - \phi^c)_{an}$ curves are depicted in Appendix A (see Fig. A-1(g) to Fig. A-12(g), where the green, pink, purple and blue solid curves are associated to the CWC*, CWT, CFB and BFC components, respectively).

For the characterization of the BFC component, the risk of local buckling needs to be considered. Depending on the beam flange slenderness, instability is known to occur either in the elastic range (slender flange) or in the post-plastic range (stocky flange). However, this kind of verification is not yet covered by EN 1993-1-8. For the flanges considered in the present study, it is reasonable to assume that they are rather stocky and thereby likely to buckle in the post-plastic range. Consequently, to account for this risk of local buckling, it was decided to limit the resistance of that component to the plastic resistance, knowing that this approach could yield conservative results when this component governs the joint resistance.

For the characterization of the CWC* component, the new procedure developed in [21] was prioritized over the EN 1993-1-8 expressions given in Table 2-2.

These component $(M^c - \phi^c)_{an}$ and $(M^{PZ} - \gamma)_{an}$ curves were eventually assembled to get the full $\left(M^j - \Phi\right)_{an}$ curves of the joints. These curves are depicted in Appendix A (see the bolded red solid curves in Fig. A-1(g) to Fig. A-12(g)) for the eight relevant experimental results, where they are compared to the experimental $\left(M^j - \Phi\right)_{exp}$ curves. The following conclusions can be drawn from these visual comparisons:

- For the tests B1, XU-W1 and XU-CWP1, the Jaspart model provides satisfactory results, both in terms of resistance and deformation capacity of the PZ;
- By contrast, for the test BCC5-E, the model significantly underestimates the deformation capacity of the PZ;
- The same observation was made for the tests E1.1 and E1.2. However, unlike the test BCC5-E, it is here impossible to conclude whether the PZ is the only cause for these observed discrepancies, since other components (i.e. CWC*/CWT) are active and contribute to the PZ deformability;
- For the test CP-R-M, the model provides satisfactory results in terms of resistance but underestimates the actual deformation capacity of the PZ;
- For the test No. 3, the model correctly predicts the first part of the curve, but fails in predicting the actual deformation capacity as well as the buckling of the PZ.

These graphical comparisons show that the Jaspart model predicts the PZ post-plastic behaviour inconsistently; depending on the test result, it may either perform well or dramatically mispredict the actual ultimate resistance or deformation capacity. From the author's point of view, these discrepancies arise from various causes which sometimes add up and sometimes compensate each other. Among them, the overestimation of the effective shear area A_{VC}, affecting both the PZ resistance and deformability, may be pointed out as the main cause, but the model also underestimates the contribution of the SE (see forthcoming CHAPTER 4) and neglects the risk of shear buckling in the CWP and the effect of strain-hardening in the SE. These observations highlight the need for a more advanced analytical model, which would depict all the complex phenomena governing the behaviour of the PZ up to failure more coherently.

3.3.2 Simplified analytical models

The second step consisted in assessing the ability of the simplified analytical models introduced in Section 2.3.3 to predict the plastic shear resistance $V_{y,Rk}^{PZ}$ of the PZ, by comparing them with the 26 test results on welded and bolted joints coming from Table 3-2 and Table 3-3. In this study, only the analytical models presented in Table 2-8, which allow for the inelastic PZ deformation, will be considered.

Again, the $V_{y,Rk,EU}^{PZ}$ (resp. $V_{y,Rk,US}^{PZ}$) values first had to be transformed into $M_{y,Rk,EU,}^{j}$ (resp. $M_{y,Rk,US}^{j}$) values to allow comparisons with the $M_{y,Rk,exp}^{j}$ experimental observations extracted in Section 3.2.2. For welded joints, the $M_{y,Rk,EU}^{j}$ (resp. $M_{y,Rk,US}^{j}$) values can be easily derived through the simplified assembly formula given in Eq. (3-4), while, for bolted ones, the whole assembly procedure must be contemplated. This procedure was exemplified in Eqs. (2-7) to (2-11) for the simple case of an exterior bolted joint under bending with two bolt-rows in tension.

The $M_{y,Rk,EU}^{j}$ and $M_{y,Rk,US}^{j}$ analytical values associated to the European and American design standards are reported in Table 3-8 and Table 3-9, where they are compared to the experimental $M_{y,Rk,exp}^{j}$ values coming from the test results on welded and bolted joints respectively. These comparisons are conducted based on the performance indicator and the colour code defined in Table 3-1. Graphical comparisons are also provided in Appendix A (see, in Fig. A-1(f) to Fig. A-26(f), the EU blue broken curve and the US orange broken curve, respectively). The following conclusions can be drawn as regards the performances of the European and American design criteria:

- The EU (i.e. EN 1993-1-8) model is directly inspired from the Jaspart model. Consequently, the same conclusion can be drawn as for the Jaspart model, at least for the welded test results, being that the EU model significantly overestimates the $M_{y,Rk,exp}^{j}$ values. The overestimation of the effective shear area A_{VC} was reported as the primary reason. In some cases (i.e. for stiffened double-sided joints), the EU model tends to perform a little bit better though. This is due to the underestimation of the $\Delta V_{y,Rk,EU}^{SE}$ contribution by the model (as it will be shown in the forthcoming CHAPTER 4), which partially compensates for the overestimation of the $V_{y,Rk,EU}^{CWP}$ contribution. As regards the bolted joints, this conclusion remains valid. The relative error ranges from -1.76% to 27.10% and the model shows a rather good performance for stiffened double-sided joints (i.e. the tests E1-XW-P-C1, E2-XW-P-C2 and E3-XW-P-C2) due to the compensation of errors.
- The US (i.e. AISC) model is directly based on the Krawinkler model, albeit with some minor modifications that were discussed in Section 2.3.3.3. However, the latter tend to amplify the $M_{y,Rk,US}^{j}$ values with respect to the Krawinkler model, which already proved to be rather unsafe in the case of unstiffened joints. As a consequence, it can be observed that the US criterion overestimates (usually significantly) the $M_{y,Rk,exp}^{j}$ values for all the welded and bolted unstiffened test results. For stiffened joints, the model performs a little better, although it still provides unsafe results. This "improvement" comes from the underestimation of the $\Delta V_{y,Rk,US}^{SE}$ contribution, as for the EU model.
- The EU* (i.e. prEN 1993-1-8) model is one of the outcomes of the following CHAPTER 4 and CHAPTER 6. It describes the new model that will be proposed for inclusion in the forthcoming prEN 1993-1-8 pre-normative document. This model will be extensively described in those Chapters and is given here for information purposes only.

These comparisons clearly show that the EU and US design criteria systematically provide unsafe and inconsistent estimations of the actual plastic shear resistance $V^{PZ}_{y,Rk,exp}$ of the PZ.

Table 3-8. Comparisons between $M^j_{y,Rk,EU}$, $M^j_{y,Rk,US}$, M^j_{y,Rk,EU^*} and $M^j_{y,Rk,exp}$ for the 12 experimental results on welded joints reported in Table 3-2.

No.	Specimen	$M^j_{y,Rk,exp}$ (kNm)	$M^j_{y,Rk,EU}$ (kNm)	E (%)	$M^j_{y,Rk,US}$ (kNm)	E (%)	M^j_{y,Rk,EU^*} (kNm)	E (%)
1	B1	868.4	876.5	0.93	1,111.5	27.99	911.8	4.99
2	NR2	58.8	62.7	6.71	69.3	17.94	55.0	-6.43
3	NR3	81.8	87.9	7.51	92.7	13.28	75.4	-7.82
4	NR4	118.2	137.2	16.11	136.1	15.17	110.2	-6.77
5	NR7	158.1	183.6	16.10	189.7	20.01	156.2	-1.17
6	BCC5-E	133.3	152.6	14.47	144.1	8.14	118.1	-11.41
7	XU-W1	190.9	199.3	4.41	188.6	-1.22	155.7	-18.44
8	XU-CWP1	198.2	223.4	12.73	213.8	7.88	174.4	-12.00
9	E1.1	334.4	391.7	17.13	409.3	22.40	328.6	-1.75
10	E1.2	328.2	391.7	19.34	409.3	24.71	328.6	0.11
11	CP-R-M	141.8	152.5	7.55	156.0	10.04	122.8	-13.42
12	No. 3	53.5	52.3	-2.22	57.9	8.16	50.4	-5.76

Table 3-9. Comparisons between $M^j_{y,Rk,EU}$, $M^j_{y,Rk,US}$, M^j_{y,Rk,EU^*} and $M^j_{y,Rk,exp}$ for the 14 experimental results on bolted joints reported in Table 3-3.

No.	Specimen	$M^j_{y,Rk,exp}$ (kNm)	$M^j_{y,Rk,EU}$ (kNm)	E (%)	$M^j_{y,Rk,US}$ (kNm)	E (%)	M^j_{y,Rk,EU^*} (kNm)	E (%)
1	01	58.8	60.3	2.51	65.0	10.62	56.4	-4.09
2	04	55.9	60.2	7.67	64.8	15.86	56.2	0.54
3	07	59.0	60.2	2.04	64.8	9.87	56.2	-4.68
4	010	94.4	101.3	7.26	102.9	9.03	85.9	-8.99
5	J1.1	333.8	392.1	17.47	359.6	7.73	316.6	-5.14
6	J2.1	325.3	392.1	20.54	359.6	10.55	316.6	-2.66
7	J3.1	381.5	CWC*	CWC*	CWC*	CWC*	374.0	-1.95
8	J4.1	266.2	290.3	9.05	273.9	2.88	246.2	-7.52
9	E1-TB-E-M	338.1	364.5	7.82	342.6	1.34	318.0	-5.96
10	E1-XW-P-C1	282.4	364.5	7.82	274.1	-2.93	254.6	-9.85
11	E2-TB-E-M	530.6	674.4	27.10	640.8	20.77	579.1	9.15
12	E2-XW-P-C2	533.3	523.9	-1.76	539.4	1.15	483.3	-9.38
13	E3-TB-E-C2	1,230.3	1,294.1	5.18	1,297.8	5.49	1,202.6	-2.25
14	E3-XW-P-C2	938.1	942.9	0.51	988.1	5.33	872.9	-6.95

3.4 CONCLUSIONS

The present CHAPTER 3 aimed at assessing the performances of the complex and simplified analytical models introduced in CHAPTER 2 (see Sections 2.3.2 and 2.3.3, respectively) through comparisons with experimental evidence, to highlight their strengths and weaknesses. To this aim, two databases have been compiled, including respectively 12 experimental results on welded joints and 14 experimental results on bolted joints, carefully selected from the scientific literature. These test results all display a PZ plastic failure and a significant PZ shear deformation. They were processed in order to extract the main performance parameters (i.e. initial stiffness, plastic resistance, post-plastic stiffness, ultimate resistance and deformation capacity), thereby allowing comparisons with the analytical models. The main outcomes from these comparisons are summarized here below:

- As regards the prediction of the PZ initial stiffness K_y^{PZ}, it was observed that the consideration, in the analytical formulae, of the bending deformation mode, in addition to the principal shear one, has very little impact on the results. By contrast, the effective shear area A_{VC} is a key parameter which significantly influences the results. With this respect, a reasonable estimation of the experimental stiffness was obtained with all the models, but the Jaspart and Wang ones, for which significant discrepancies were observed resulting from the misprediction of the effective shear area A_{VC}.
- As regards the prediction of the PZ plastic shear resistance $V_{y,Rk}^{PZ}$, the main observation was that none of the complex analytical models introduced in CHAPTER 2 was able to provide a consistent estimation of this parameter. Several causes have been identified which can explain these discrepancies. In all cases, they arise from a poor understanding and subsequent modelling of the key parameters governing the plastic shear resistance of the PZ. The so-drawn conclusions also apply to the simplified EU and US design criteria since they are directly derived from the Jaspart and Krawinkler models, respectively. Furthermore, these criteria have been demonstrated to overestimate the plastic shear resistance of the PZ in many cases, what is rather concerning from a safety point of view.
- As regards the prediction of the PZ post-plastic behaviour up to failure, two main observations were made: (i) on the one hand, it was observed very few experimental results which exhibit an actual PZ ultimate failure mode, what was pointed out as a clear limitation of the study; (ii) on the other hand, solely the Jaspart model provides analytical expressions to capture the end of the curve. Notwithstanding that, qualitative graphical comparisons were performed showing that the Jaspart model was rather inconsistent in predicting the actual deformability of the PZ. These observed discrepancies are believed to arise from various causes which sometimes add up and sometimes compensate each other.

The conclusions from this comparative study clearly highlight the need for a more sophisticated analytical model, built upon the deep understanding of the complex phenomena governing the behaviour of the PZ up to failure. To achieve this objective, a reliable estimation of the plastic shear resistance of the PZ is first required. This topic is covered in the following CHAPTER 4. Based on this knowledge, the model can be subsequently extended to the prediction of the complete behaviour of the PZ up to failure, topic addressed in the subsequent CHAPTER 5. It is noteworthy that this new sophisticated model will be developed in the context of welded joints only. This is because the welded joints are significantly simpler than the bolted ones, as discussed in the present CHAPTER 3 (see the boxed text in Section 3.1.2), making them more suitable for the validation of the analytical models that will be developed in CHAPTER 4 and CHAPTER 5. The extension of the models to PZs in bolted joints will be addressed in CHAPTER 6.

CHAPTER 4 Characterization of the panel zone plastic shear resistance

4.1 INTRODUCTION

4.1.1 Objectives of the Chapter

CHAPTER 4 addresses _the problem of prediction of the plastic shear resistance of the PZ_, identified in CHAPTER 3. More precisely, it focuses on the development and validation of a new analytical expression for the prediction of this resistance level. This step is of primary importance to predict the ductility and the deformation capacity of this component in a subsequent stage (see CHAPTER 5).

4.1.2 Scope of the Chapter

The scope of this study was limited to welded joints under monotonic loading only, for two main reasons: (i) to facilitate the derivation of the shear force V_{Ek}^{PZ} acting on the PZ, which can be assumed constant over the whole depth d_b^* of the PZ for welded joints, and (ii) to avoid the occurrence of any other failure mode in the connecting elements (i.e. bolts in tension, endplates in bending…). In addition, fillet welds were assumed to be sufficiently resistant (i.e. there is no premature failure of the welds) and the PZ dimensions were chosen to prevent the occurrence of any premature local yielding within the compressed and tensile zones of the CWP, prior to the shear yielding of the PZ. The risk of shear buckling of the PZ has also been prevented by choosing PZ dimensions which satisfy EN 1993-1-8 requirements in terms of CWP slenderness (see Eq. (2-39)).

Two types of joint configurations have been considered in the present study, namely exterior joints and interior joints with beams of equal depth, see Fig. 4-1 and Fig. 4-2, respectively. These joints are loaded in such a way that the PZ becomes the governing component of the joint response. This particular loading is illustrated in Fig. 4-1(a) and Fig. 4-2(a) for exterior and interior joints, respectively. Columns are subjected to an axial force N_c coming from the gravity loads and which is limited to $0.5 \cdot N_{pl,c}$ in the present study, $N_{pl,c}$ being the axial capacity of the column profile. They are also subjected to shear forces and bending moments resulting from the horizontal reactions R. Beams transfer bending moments and shear forces only, coming from the applied external load P. For interior joints, the unbalanced bending moments are assumed to be equal (i.e. $|M_{BL}| = |M_{BR}|$). No horizontal axial force N_b is transferred by the beams. This kind of anti-symmetrical loading could be caused by either wind or earthquake (or even gravity loads in the case of exterior joints) and generates a particular distribution of bending moments M, shear forces V and axial forces N acting on the PZ. This system of internal forces, depicted with blue arrows in Fig. 4-1 and Fig. 4-2 (subscripts B and C stand for <u>B</u>eam and <u>C</u>olumn, respectively; subscripts T, R, B, L stand for <u>T</u>op, <u>R</u>ight, <u>B</u>ottom and <u>L</u>eft respectively), causes significant shear in the PZ, as shown in the M-N-V diagrams in Fig. 4-1(b) and Fig. 4-2(b).

In particular, the shear distribution over the PZ depth, shown in Fig. 4-1(b) and Fig. 4-2(b), is assumed to be uniform. This is equivalent to saying that the beam moment M_{BR} (resp. M_{BL}) is transferred to the PZ by the couple of equal but opposite forces F_{BR} (resp. F_{BL}), acting at mid-depth of the beam flanges and statically equivalent to the beam moment M_{BR} (resp. M_{BL}), see Fig. 2-1. This assumption seems reasonable for welded joints as most of the beam moment is carried by the flanges in typical I-shaped beams [50]. Regarding the support conditions, both joint configurations are simply supported, which is similar to assuming that the point of contraflexure of the bending moment diagram occurs at the column mid-height [122].
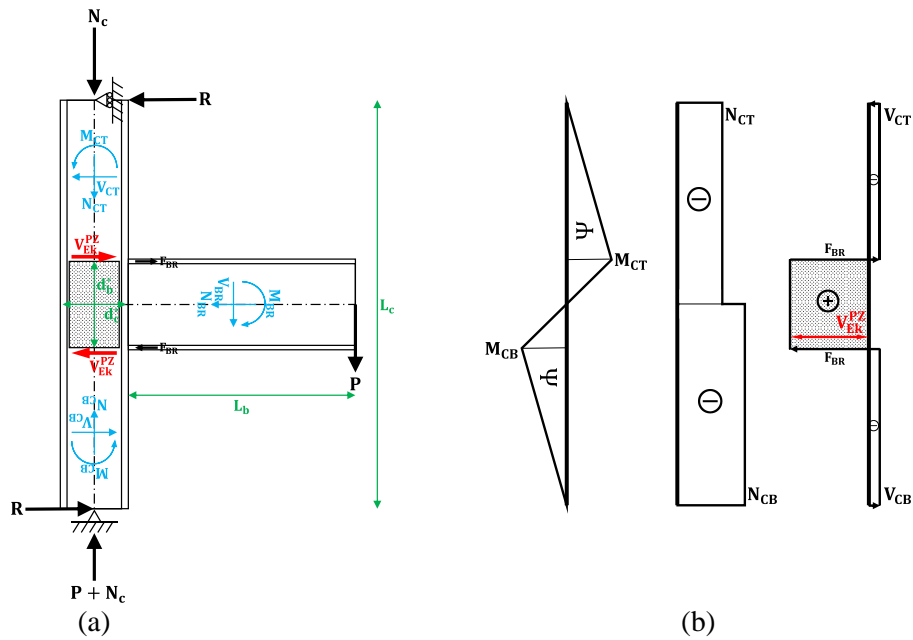
Fig. 4-1. Exterior welded joint: (a) loading conditions maximizing shear in the PZ and (b) resulting M-N-V diagrams in the column.
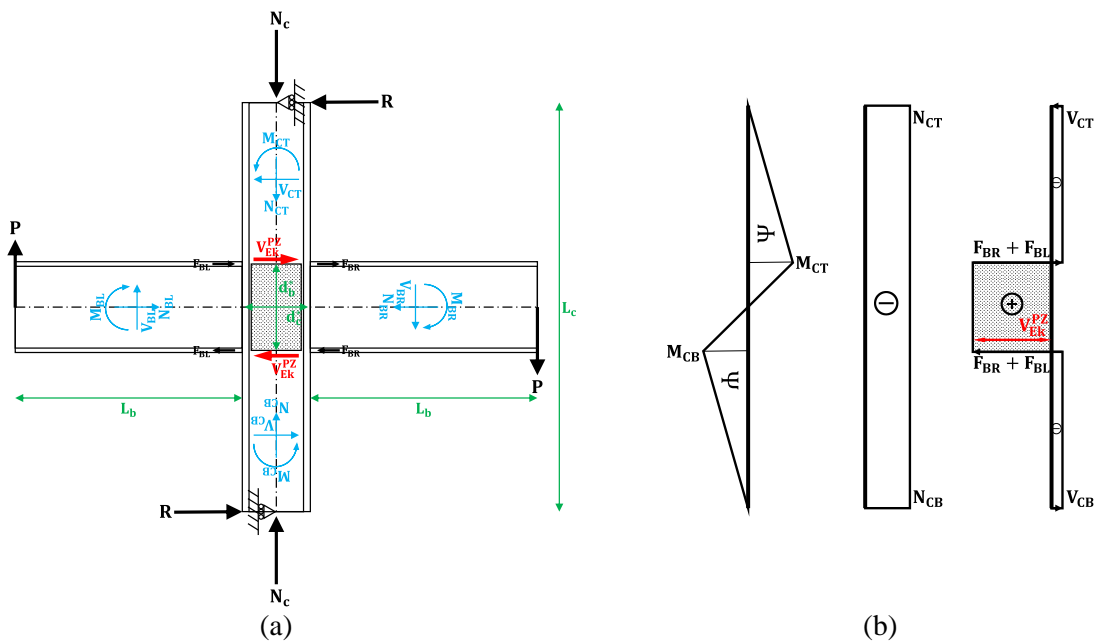

Fig. 4-2. Interior welded joint: (a) loading conditions maximizing shear in the PZ and (b) resulting M-N-V diagrams in the column.

4.1.3 Outline of the Chapter

To derive a new analytical expression for the prediction of the PZ plastic shear resistance, a scientifically-based methodology has been used, consisting of (i) the development and validation of a sophisticated finite element model (see Section 4.2.2); (ii) the development of an extensive parametric study to highlight the key parameters governing the plastic shear resistance of the PZ (see Sections 4.2.3-4.2.4); (iii) the development and validation of a new complex analytical formulation for scientific purposes, which encompasses all the so-identified key parameters (see Section 4.3.1); and (iv) the simplification of this complex model in view of its possible integration in design codes (see Section 4.3.2).

4.2 NUMERICAL PART

4.2.1 Introduction

The conclusions drawn in CHAPTER 3 were investigated using the finite element (FE) approach. The role of the FE analysis in the present study is twofold: (i) developing an extensive parametric study to highlight the key parameters governing the plastic shear resistance of the PZ and (ii) using the so-obtained FE results to validate the new complex and simplified analytical models developed in Section 4.3.1 and Section 4.3.2, respectively. In this thesis, the commercial FE software Abaqus© [25] was chosen to conduct the FE analyses, as already mentioned in CHAPTER 1.

4.2.2 FE modelling

4.2.2.1 Development of an FE model

As a preliminary step, the numerical tool had to be validated. To this aim, two pushover tests, namely tests NR4 (already presented in Table 3-2) and NR16, taken from [100], were numerically modelled within the Abaqus© environment. These two specimens consist of an IPE330 beam welded to an HEB160 column and of an HEB500 beam welded to an HEB300 column, respectively. All actual geometric properties may be found in ([100], [104]) and are recalled in Table 4-1. Fillet welds were not modelled explicitly and an initial imperfection was taken into account. The magnitude of the latter was fixed to "$d_c/200$", as suggested in Part 1-14 of Eurocode 3 (EN 1993-1-14, [123]), where d_c is the clear depth of the column cross-section. The Young's modulus and the Poisson's ratio were taken equal to $210,000\ MPa$ and 0.3, respectively. The available mechanical properties (i.e. the material yield strength f_y given in [100] and the material ultimate strength f_u given in [104]) are reported in Table 4-2 for each specimen's web and flanges. Based on them, it was possible to reconstruct the full material law of each specimen's web and flanges, using the quad-linear model developed by Yun et al. [124] and recently integrated in EN 1993-1-14 [123]. The main parameters of this model, named EN 1993-1-14 model in the rest of the thesis, are defined in Table 4-3 and the reconstructed engineering stress-strain curves ("$eng.$") are presented in Fig. 4-3 (see the black and grey solid curves).

Table 4-1. Actual geometric properties for specimens NR4 and NR16.

Specimen	C…column B…beam	h (mm)	b (mm)	t_w (mm)	t_f (mm)	r (mm)	A (cm^2)	L (mm)
NR4	C…HEB160	159	160	8.0	12.2	15	51.7	1350
	B…IPE330	329	162	8.0	11.4	18	64.2	698
NR16	C…HEB300	298	300	10.6	18.0	27	142.0	1600
	B…HEB500	500	301	14.7	27.6	27	237.8	580

Table 4-2. Available mechanical properties for specimens NR4 and NR16.

Specimen	C…column B…beam		E (MPa)	f_y (MPa)	f_u (MPa)
NR4	C…HEB160	Web		355	485
		Flange		295	408
	B…IPE330	Web		317	436
		Flange		286	395
NR16	C…HEB300	Web	210,000	284	440
		Flange		271	420
	B…HEB500	Web		299	440
		Flange		271	400

Table 4-3. Definition of the parameters used in the EN 1993-1-14 material model (engineering stress-strain curve).

| Parameters		Formula	Units
E	(Young's modulus)	$= 210,000$	(MPa)
σ_y	(yield strength)	$= f_y$	(MPa)
ε_y	(yield strain)	$= \dfrac{\sigma_y}{E}$	$(-)$
σ_{pp}	(post-plastic strength)	$= f_y$	(MPa)
ε_{pp}	(post-plastic strain)	$= 0.1 \cdot \dfrac{f_y}{f_u} - 0.055 \quad \text{but} \quad 0.015 \leq \varepsilon_{pp} \leq 0.03$	$(-)$
E_{pp}	(post-plastic modulus)	$= \dfrac{f_u - f_y}{0.4 \cdot (\varepsilon_n - \varepsilon_{pp})}$	(MPa)
σ_u	(ultimate strength)	$= \sigma_{pp} + E_{pp} \cdot (\varepsilon_u - \varepsilon_{pp})$	(MPa)
ε_u	(ultimate strain)	$= C_1 \cdot \varepsilon_n$	$(-)$
ΔE_{pp}	(post-plastic modulus increment)	$= \dfrac{\sigma_n - \sigma_u}{\varepsilon_n - \varepsilon_u}$	(MPa)
σ_n	(strength at the onset of necking)	$= f_u$	(MPa)
ε_n	(strain at the onset of necking)	$= 0.6 \cdot \left(1 - \dfrac{f_y}{f_u}\right) \quad \text{but} \quad 0.06 \leq \varepsilon_n$	$(-)$
C_1	(material coefficient)	$= \dfrac{\varepsilon_{pp} + 0.25 \cdot (\varepsilon_n - \varepsilon_{pp})}{\varepsilon_n}$	$(-)$
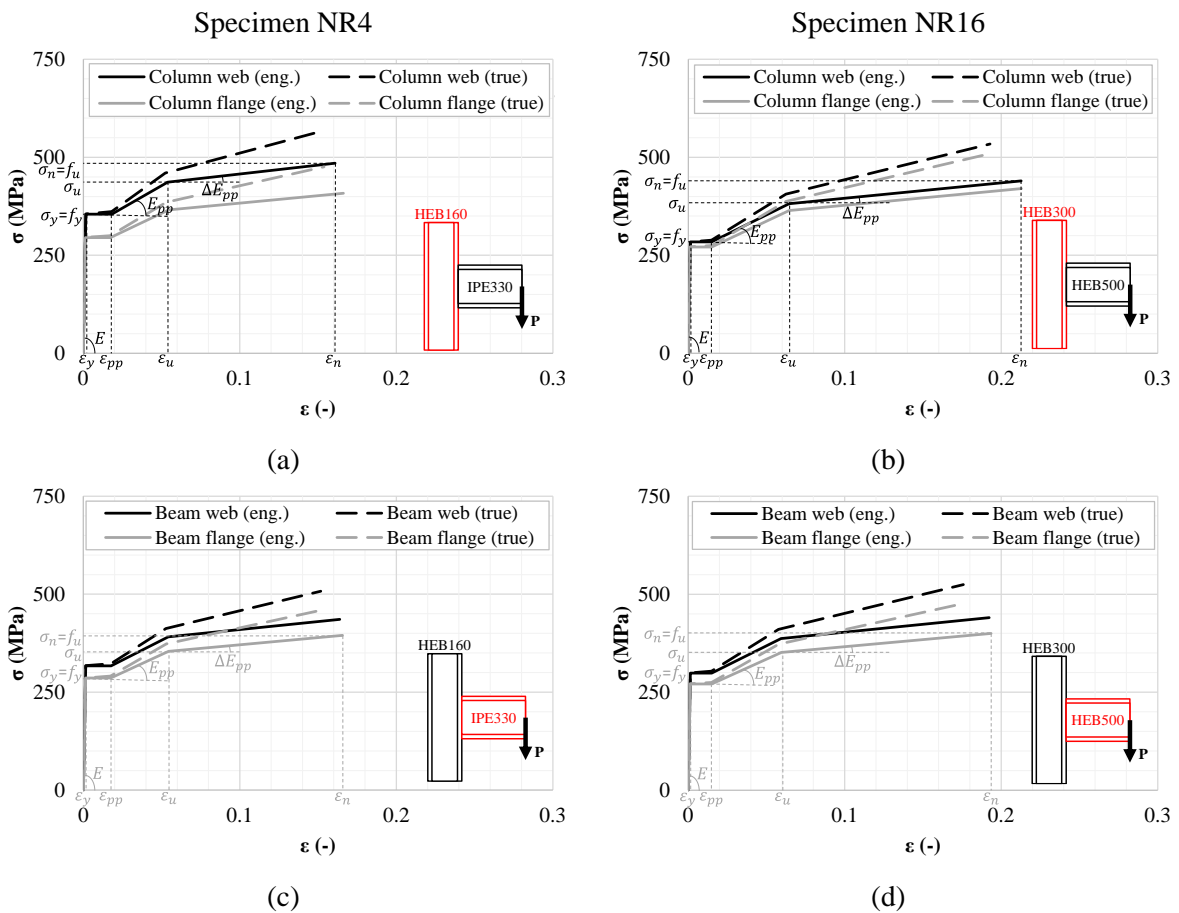
Fig. 4-3. Reconstructed material laws (EN 1993-1-14 material model) used in the numerical simulations: (a) NR4 column profile, (b) NR16 column profile, (c) NR4 beam profile and (d) NR16 beam profile.

The reconstructed engineering stress-strain curves were translated into true stress-strain curves ("*true*", see the black and grey dashed curves in Fig. 4-3) to comply with the Abaqus© formalism, using Eq. (4-1) and Eq. (4-2), σ and ε being the true stress and strain respectively, and σ^{eng} and ε^{eng} being the engineering stress and strain, respectively.

$$\sigma = \sigma^{eng} \cdot (1 + \varepsilon^{eng}) \tag{4-1}$$

$$\varepsilon = \ln(1 + \varepsilon^{eng}) \tag{4-2}$$

Both mesh density and FE type were selected based on a preliminary mesh sensitivity analysis. A coarse mesh made of eight-node brick elements with reduced integration (C3D8R) was adopted in almost all the model except for the PZ region and the column supports which were more densely meshed using fully-integrated eight-node brick elements (C3D8). The root fillets were modelled using six-node triangular prisms with full integration (C3D6). Four finite elements were placed throughout the webs and flanges thicknesses. Fig. 4-4(a) and Fig. 4-4(b) give a general overview of the final mesh used for the specimens NR4 and NR16, respectively.

Simply-supported boundary conditions were applied to the column ends similarly to the experimental tests. A monotonic displacement history was imposed on the beam tip in order to mimic the real loading conditions. Furthermore, the beam end section was properly restrained against out-of-plane displacement. Numerical simulations were performed using a general static analysis and they were stopped before failure, since the failures of the specimens were not captured during the experimental campaign due to the limits of the testing machine.
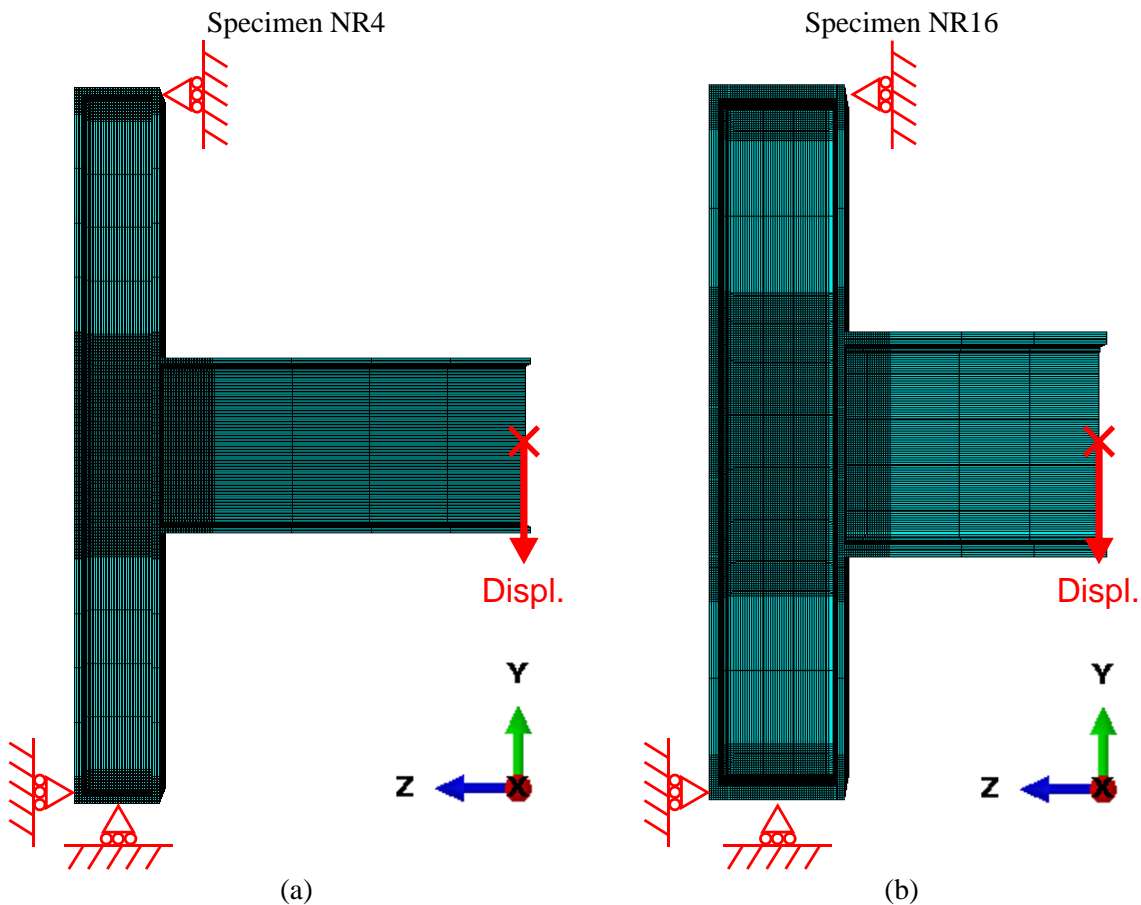

Fig. 4-4. Description of the FE models: (a) specimen NR4 and (b) specimen NR16.

4.2.2.2 Validation

The FE models were validated through comparisons between experimental (solid lines) and numerical (dashed lines) results in terms of load-deflection curves at the beam tip (see Fig. 4-5(a) and (b)), load-introduction force vs. column web shortening/elongation curves (see Fig. 4-5(c) and (d)) and load-introduction force vs. column lateral deflection curves (see Fig. 4-5(e) and (f)). Comparisons show a rather good agreement between experimental and numerical curves for both specimens NR4 and NR16, especially in the elasto-plastic range of the curves being investigated in this CHAPTER 4. In the post-plastic range of the curves, some discrepancies can be observed. This is due to the fact that strain-hardening and ultimate properties given in Table 4-2 had to be assumed, as they were not made available in [100].
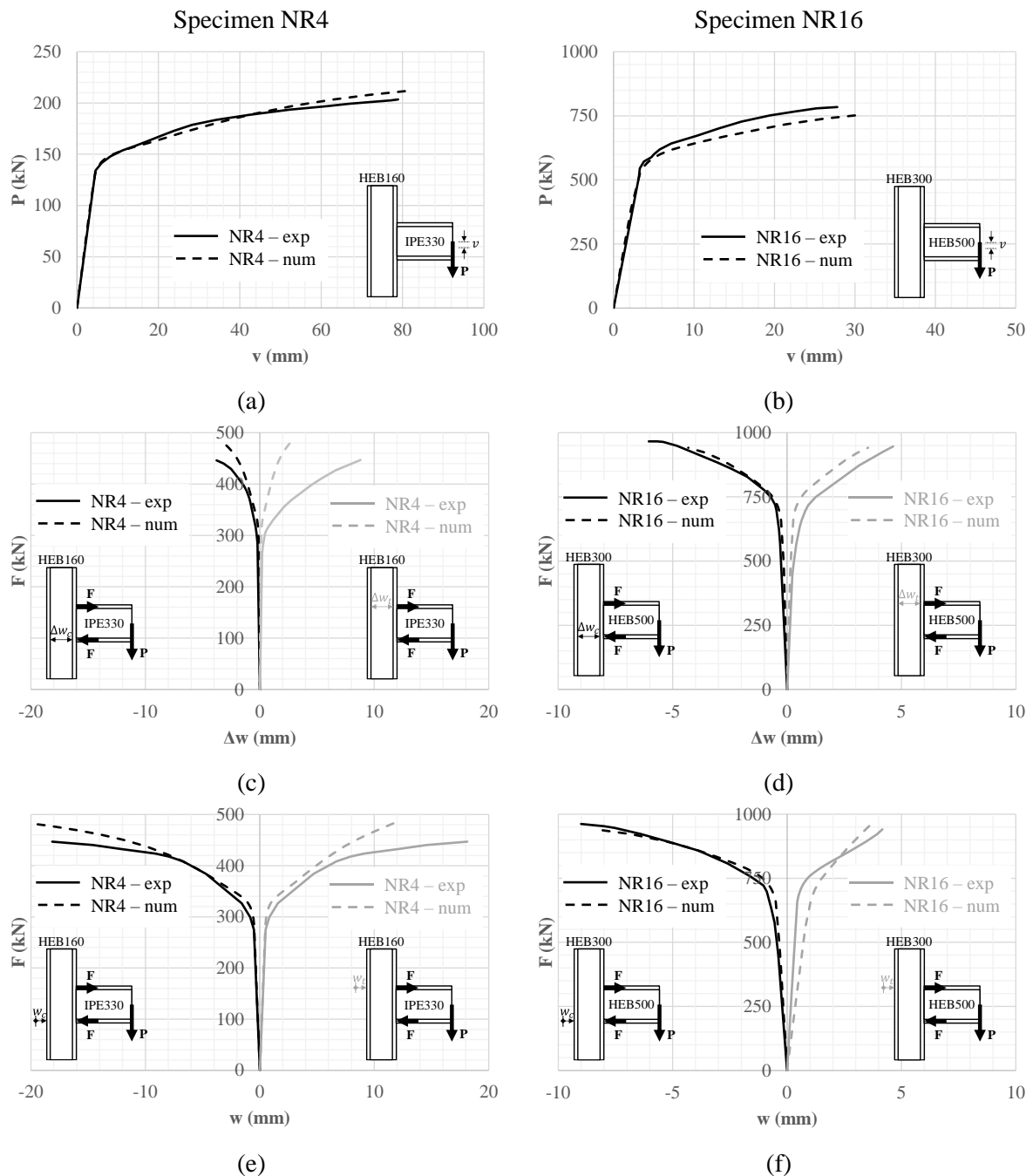
Fig. 4-5. Validation of the numerical models: (a)-(b) $(P - v)$ curves, (c)-(d) $(F - \Delta_w)$ curves and (e)-(f) $(F - w)$ curves.

4.2.3 Parametric study

The so-validated numerical models were then used to perform a parametric study with the aim of appraising, one by one, the influence of four parameters on the plastic shear resistance of the PZ. These parameters are: (i) the spread of yielding across the PZ, (ii) the type of plastic collapse mechanism actually developing in the SE, (iii) the $\tau - \sigma_i$ interaction within the PZ and (iv) the $\tau - \sigma_{n,M-N}$ interaction within the PZ. As a preliminary step, some slight changes were made to the original NR4 and NR16 numerical models regarding their geometric and material properties. These changes were designed to make the parametric study as general as possible and are listed below:

- the column supports were moved towards the column centreline;
- the column length L_c was increased to $4\ m$ to reduce the influence of the support reactions;
- the beam length L_b was increased in such a way that the distance between the column centreline and the beam end is $1.5\ m$;
- actual geometric properties of the steel profiles were replaced by nominal ones;
- actual material laws were replaced by a fictitious elastic, perfectly-plastic one (i.e. strain-hardening neglected) for all members to facilitate the derivation of the plastic shear resistance of the PZ (see the engineering and true stress-strain curves illustrated in Fig. 4-6(a) and Fig. 4-6(b), respectively);
- $S355$ steel grade with nominal yield strength f_y was considered for all members (Table 4-4).
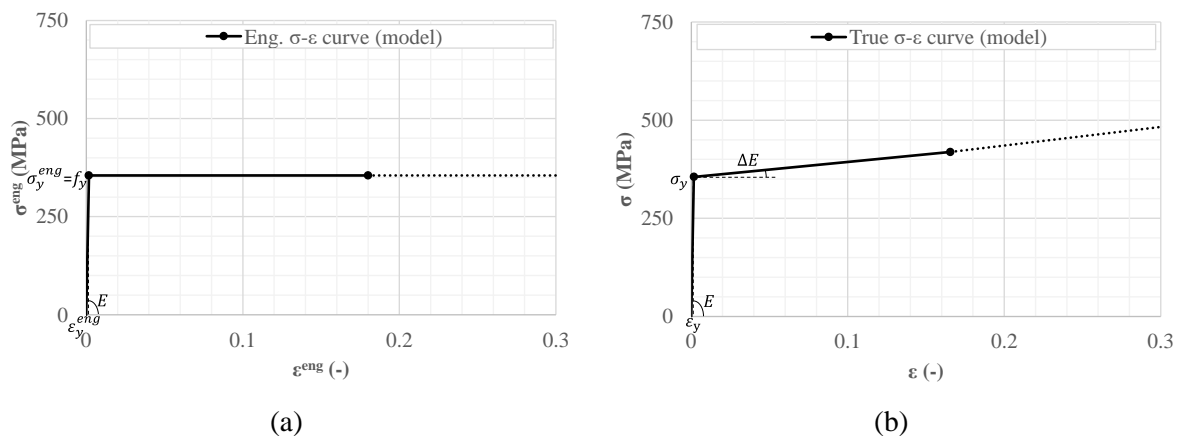

| (a) | (b) |

Fig. 4-6. Fictitious elastic, perfectly-plastic material model: (a) engineering stress-strain curve and (b) true stress-strain curve.

Table 4-4. Definition of the parameters used in the fictitious material law defined in Fig. 4-6.

Parameters	Engineering stress-strain curve		True stress-strain curve		Units
E (Young's modulus)	=	210,000	=	210,000	(MPa)
σ_y (yield strength)	=	$f_y = 355$	=	355	(MPa)
ε_y (yield strain)	=	$\dfrac{\sigma_y}{E} = 0.00169$	=	0.00169	$(-)$
ΔE (initial modulus increment)	=	0	=	358	(MPa)

In order to broaden the parametric study, two additional models, named A and B, were added to the study. These models are characterized by an IPE200 beam welded to an HEB160 column and by an IPE300 beam welded to an HEB340 column, respectively. A summary of the four beam-to-column assemblies considered in the present study is provided in Table 4-5. These numerical models were then used to perform the parametric study, which covers the following eight joint configurations:

- (non-)axially loaded (un-)stiffened exterior joints;
- (non-)axially loaded (un-)stiffened interior joints.

The thickness t_{st} of the transverse column web stiffeners, if any, is given in Table 4-5. The magnitude of the axial load N_c in the column, if any, was set to $0.5 \cdot N_{pl,c}$, $N_{pl,c}$ being the axial strength of the column cross-section. This load level is assumed to be representative of the maximum axial load that a column may encounter in a typical steel frame structure. These values are summarized in Table 4-5 as well. Finally, Table 4-5 also shows the column web-to-flange thickness ratio t_{wc}/t_{fc}. This parameter oscillates between 0.55 and 0.62 which is the range of validity for all the developments presented in this study.

Table 4-5. Details of the numerical models used in the parametric study.

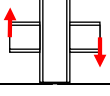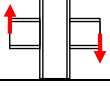| Model	Column profile	Beam profile	t_{st} (mm)	N_c (kN)	t_{wc}/t_{fc} (−)
NR4	HEB160	IPE330	12	1000	0.615
NR16	HEB300	HEB500	30	2500	0.579
A	HEB160	IPE200	10	1000	0.615
B	HEB340	IPE300	12	3000	0.558
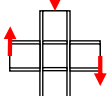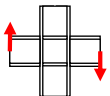
In total, 32 numerical simulations were performed within the framework of the parametric study. A general overview of these simulations is given in Table 4-7. To identify the different simulations, a specific nomenclature has been adopted: for instance, the numerical simulation performed on the unstiffened (i.e. "0") exterior (i.e. single-sided, "s") NR4 joint configuration without any axial load in the column (i.e. "/") is named "NR4-0-s-/". By contrast, the numerical simulation performed on the stiffened (i.e. "1") interior (i.e. double-sided, "d") NR16 joint configuration with an axial load in the column (i.e. "$0.5N_{pl}$") is named "NR16-1-d-0.5N$_{pl}$".

The component method was applied to each of them, in accordance with EN 1993-1-8, following the procedure described in Section 2.2.2. The detailed results are reported in APPENDIX C for each individual numerical simulation (see Table C-1 to Table C-32). However, for sake of clarity, the expected plastic failure mode associated to each numerical simulation is recalled in Table 4-6, together with the plastic bending moment resistance $M_{y,Rk}^j$. From Table 4-6, it can be seen that 18 numerical simulations are characterized by a PZ plastic failure mode, while the 14 remaining simulations are characterized by another plastic failure mode (either CWC*/CWT or CFB). Among the latter, only the results associated to the four exterior joints in the B series, highlighted in light blue in Table 4-6, feature a low level of plastic deformation of the PZ, as shown by the $(V^{PZ} - \gamma)_{num}$ curves in APPENDIX C (see the blue continuous curves in Fig. C-25(c), Fig. C-27(c), Fig. C-29(c) and Fig. C-31(c)). Therefore, these numerical results will not be accounted for in the following sections.

Table 4-6. Description of the expected plastic failure mode and expected plastic bending moment resistance associated to each individual numerical simulation of the parametric study, according to EN 1993-1-8.

Configuration	Category I (X="d", Y="/") $M_{y,Rk}^j$ (kNm)	Pl. failure mode	Category II (X="s", Y="/") $M_{y,Rk}^j$ (kNm)	Pl. failure mode	Category III (X="d", Y="0.5N$_{pl}$") $M_{y,Rk}^j$ (kNm)	Pl. failure mode	Category IV (X="s", Y="0.5N$_{pl}$") $M_{y,Rk}^j$ (kNm)	Pl. failure mode
NR4-0-X-Y	56.40	PZ	112.67	CWC*/CWT	56.40	PZ	112.67	CWC*/CWT
NR4-1-X-Y	61.25	PZ	122.50	PZ	61.25	PZ	122.50	PZ
NR16-0-X-Y	237.37	PZ	414.36	CWC*/CWT	237.37	PZ	414.36	CWC*/CWT
NR16-1-X-Y	259.47	PZ	518.95	PZ	259.47	PZ	518.95	PZ
A-0-X-Y	32.72	PZ	57.79	CFB	32.72	PZ	57.79	CFB
A-1-X-Y	36.74	PZ	57.79	CFB	36.74	PZ	57.79	CFB
B-0-X-Y	162.83	PZ	164.84	CFB	162.83	PZ	164.84	CFB
B-1-X-Y	164.84	CFB	164.84	CFB	164.84	CFB	164.84	CFB

Table 4-7. General overview of the parametric study.

Configuration	Transverse column web stiffener	Type of joint	Axial load	Test numbers	Loading situation
X stands for NR4, NR16, A or B	Yes…………………...1 No……....................0	Single-sided…………s Double-sided………..d	Yes…………….0.5N_{pl} No……………… /		
X	1	s	0.5N_{pl}	X-1-s-0.5N_{pl}	
			/	X-1-s-/	
		d	0.5N_{pl}	X-1-d-0.5N_{pl}	
			/	X-1-d-/	
	0	s	0.5N_{pl}	X-0-s-0.5N_{pl}	
			/	X-0-s-/	
		d	0.5N_{pl}	X-0-d-0.5N_{pl}	
			/	X-0-d-/	

4.2.4 FE results and discussions

For sake of clarity, the FE results obtained from the parametric study are not presented in the present Section 4.2.4. They can be found in APPENDIX C, where they are extensively described in terms of $(P - v)_{num}$ curves (see Fig. C-1(a) to Fig. C-32(a)), $(V - \gamma)_{num}$ curves (see Fig. C-1(c) to Fig. C-32(c)) and $(M_B - \Phi)_{num}$ curves (see Fig. C-1(e) to Fig. C-32(e)) for each individual numerical simulation. The $(P - v)_{num}$ curves were obtained as direct output from the numerical simulations. The $(M_B - \Phi)_{num}$ curves can be easily derived from the $(P - v)_{num}$ curves, following the procedure described in APPENDIX B.2.

Regarding the $(V - \gamma)_{num}$ curves, a distinction is made between the $(V^{PZ} - \gamma)_{num}$ curve of the PZ, the $(V^{CWP} - \gamma)_{num}$ curve of the CWP and the $(\Delta V^{SE} - \gamma)_{num}$ curve of the SE. The former can be extracted from the numerical results by expressing the equilibrium equations of the PZ in deformed shape. The procedure is described in APPENDIX B.1.2. The $(V^{CWP} - \gamma)_{num}$ curve of the CWP can be extracted from the numerical results using a numerical integration procedure. This latter is described in APPENDIX B.1.3. Finally, the $(\Delta V^{SE} - \gamma)_{num}$ curve of the SE can be obtained by subtracting the CWP $(V^{CWP} - \gamma)_{num}$ curve from the PZ $(V^{PZ} - \gamma)_{num}$ curve. This is explained in APPENDIX B.1.4.

In total, four main conclusions were drawn from the careful analysis of the FE results. These conclusions concern: (i) the spread of yielding across the PZ, (ii) the type of collapse mechanism actually developing in the SE, (iii) the influence of the $\tau - \sigma_i$ interaction on the plastic shear resistance of the PZ and (iv) the influence of the $\tau - \sigma_{n,M-N}$ interaction on the plastic shear resistance of the PZ. They are described in details in the following Sections 4.2.4.1 to 4.2.4.4 and will serve as a basis for the development of the complex analytical model in Section 4.3.1.

To illustrate the different conclusions, 24 relevant σ_{VM}, τ, $\sigma_{n,M-N}$ and σ_i states of stress, coming from Abaqus©, are reported in Table 4-8 to Table 4-11. They belong to the eight numerical simulations performed with the model NR4 (see Table 4-7), i.e. 3 states of stress per simulation; these ones are identified in the $(V - \gamma)_{num}$ curves which are given in Fig. 4-7 to Fig. 4-10, respectively (see the numbers "1" to "24"). These $(V - \gamma)_{num}$ curves were extracted following the procedures provided in APPENDIX B.1.

4.2.4.1 Study of the spread of yielding across the PZ

Regarding the spread of yielding across the PZ, the following observations were made:

- Yielding initiates in the centre of the CWP and is not affected by the SE, as depicted by the states of stress No. 1, 4, 7 and 10 in Table 4-8 and Table 4-9, the black parts on the pictures being the parts yielding in pure shear. This is due to the fact that the shear stiffness of the CWP is significantly larger than that of the SE, and so the CWP first "attracts" most of the forces.
- Yielding very quickly spreads across the entire panel, as depicted by the states of stress No. 2, 5, 8 and 11 in Table 4-8 and Table 4-9, the plastic shear resistance of the CWP being reached for a $V^{CWP}_{y,Rk,compl}$ value. This contribution is highlighted in red in Fig. 4-7 to Fig. 4-10. For this shear level, it can be seen that, strictly speaking, only the clear depth of the CWP yields. Therefore, it is suggested to account for the actual shear stress distribution in the derivation of $V^{CWP}_{y,Rk,compl}$.
- Extra shear forces are then transferred to the SE, which contribute to the resistance of the PZ with a $\Delta V^{SE}_{y,Rk,compl}$ value before large plastic rotations develop (see the states of stress No. 3, 6, 9 and 12 in Table 4-8 and Table 4-9). This second contribution is highlighted in red in Fig. 4-7 to Fig. 4-10.

4.2.4.2 Study of the actual collapse mechanism in the SE

Regarding the collapse mechanism which develops in the SE, the following observations were made:

- In the absence of transverse column web stiffeners, four plastic hinges form in the column flanges at the level of the beam flanges (see the states of stress No. 3, 6, 15 and 18 in Table 4-8 and Table 4-10, where the locations of the plastic hinges have been highlighted with yellow circles).
- In the presence of transverse column web stiffeners, additional plastic hinges form either in the beam(s) flanges or in the transverse column web stiffeners (see the states of stress No. 9, 12, 21 and 24 in Table 4-9 and Table 4-11, the locations of the plastic hinges being indicated with yellow circles). These additional plastic hinges have to be explicitly accounted for in the derivation of the contribution $\Delta V_{y,Rk,compl}^{SE}$. A similar observation was shared with other authors ([76], [80]).
- N.B.: The difference in the number of required additional plastic hinges is a first reason explaining the difference in strength observed between the interior and exterior joints in Fig. 4-7 to Fig. 4-10. Another reason comes from the influence of the $\tau - \sigma_i$ interaction and is discussed hereafter in Section 4.2.4.3.

4.2.4.3 Influence of the $\tau - \sigma_i$ interaction

Regarding the influence of the $\tau - \sigma_i$ interaction, the following observations were made:

- This interaction was neglected by all the authors in the models introduced in Section 2.3.2, the load-introduction phenomenon being assumed to be a localized phenomenon and hence not affecting the plastic shear resistance of the PZ.
- For interior joints, this assumption seems reasonable as half of the "load-introduction" force is introduced on each side of the column profile. Consequently, no significant σ_i stress is observed within the CWP (see the σ_i stresses in the states of stress No. 4-6, No. 10-12, No. 16-18 and No. 22-24 in Table 4-8 to Table 4-11).
- For exterior joints, this assumption is much more questionable, as it is shown in Table 4-8 to Table 4-11 (see the σ_i stresses in the states of stress No. 1-3, No. 7-9, No. 13-15 and No. 19-21) that significant σ_i stresses develop in the CWP at the level of the beam flanges, where loads are introduced in the PZ. This leads to an overall decrease in the level of shear strength for the exterior joints, with respect to the interior joints. This observation can be made in Fig. 4-7 to Fig. 4-10, where the $(V^{PZ} - \gamma)_{num}$ curves of the exterior joints (see the blue curves in Fig. 4-7(a) to Fig. 4-10(a) are lower than those of the corresponding interior joints (see the blue curves in Fig. 4-7(b) to Fig. 4-10(b), respectively).
- This decrease mainly affects the contribution of the CWP. Therefore, it is suggested to explicitly account for the $\tau - \sigma_i$ interaction in the assessment of the contribution $V_{y,Rk,compl}^{CWP}$ of the CWP, for the exterior joints only.

4.2.4.4 Influence of the $\tau - \sigma_{n,M-N}$ interaction

Finally, regarding the influence of the $\tau - \sigma_{n,M-N}$ interaction, the following observations were made:

- The comparisons between the blue $(V^{PZ} - \gamma)_{num}$ curves for the non-axially loaded joints (see Fig. 4-7 and Fig. 4-8) with respect to their corresponding $(V^{PZ} - \gamma)_{num}$ curves for the axially loaded joints (see Fig. 4-9 and Fig. 4-10) show that the axial force applied to the column reduces the resistance of the PZ. Therefore, its effect has to be taken into account in both contributions $V_{y,Rk,compl}^{CWP}$ and $\Delta V_{y,Rk,compl}^{SE}$.

- The $\sigma_{n,M-N}$ stresses feature a uniform distribution across the column cross-section at the beginning of the simulations, before shear is introduced into the PZ and therefore in the absence of any M_C moment in the column. This observation is shown in Table 4-10 and Table 4-11 (see the $\sigma_{n,M-N}$ stresses in the states of stress No. 13, 16, 19 and 22).
- Once shear is introduced into the PZ, redistribution of forces occurs. The CWP, whose shear stiffness is significantly larger than that of the SE, "attracts" most of the shear force. By contrast, the SE, whose axial stiffness is significantly larger than that of the CWP, "attract" most of the axial force. This observation is shown in Table 4-10 and Table 4-11 (see the $\sigma_{n,M-N}$ stresses in the states of stress No. 14-15, No. 17-18, No. 20-21 and No. 23-24). A similar observation was made by other authors ([28], [52], [54], [73]).

4.2.4.5 Conclusion of the parametric study

In conclusion, the parametric study clearly indicates that the resistance of the PZ can always be divided into the contributions of the CWP ($V_{y,Rk,compl}^{CWP}$) and the SE ($\Delta V_{y,Rk,compl}^{SE}$), as follows:

$$V_{y,Rk,compl}^{PZ} = V_{y,Rk,compl}^{CWP} + \Delta V_{y,Rk,compl}^{SE} \tag{4-3}$$

This formalism is in line with Eq. (2-14) (see Section 2.3.2). However, both contributions need to be re-evaluated, with respect to the expressions given in Table 2-5 to Table 2-7 for the different analytical models investigated in Section 2.3.2. The contribution $V_{y,Rk,compl}^{CWP}$ of the CWP has to more accurately account for the actual shear stress distribution at yielding, and for both $\tau - \sigma_i$ and $\tau - \sigma_{n,M-N}$ interactions. It is re-evaluated in Section 4.3.1.1. The contribution $\Delta V_{y,Rk,compl}^{SE}$ of the SE has to reflect more accurately the plastic collapse mechanism actually developing and has to account for the influence of the axial load in the column flanges. It is re-evaluated in Section 4.3.1.2.

(a)   (b)
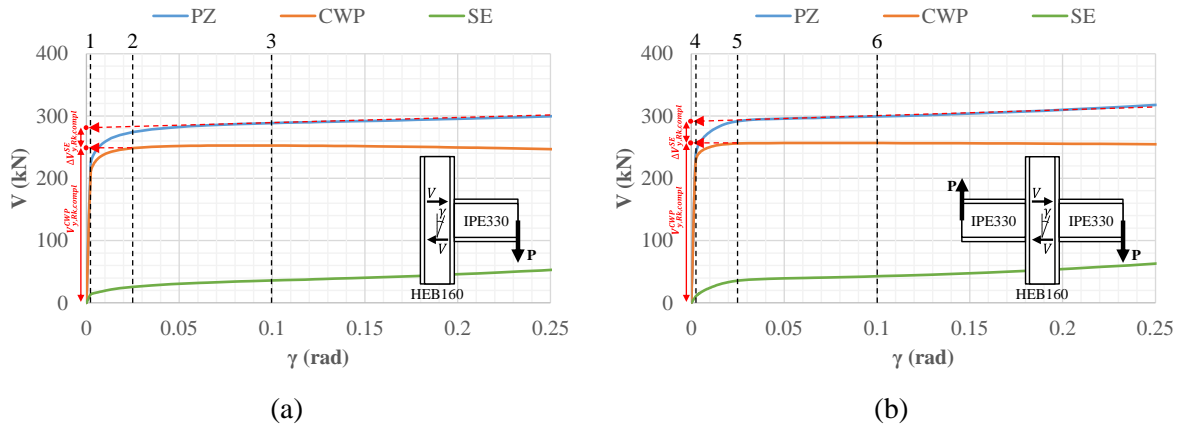
Fig. 4-7. Numerical results in terms of $(V - \gamma)_{num}$ curves: (a) simulation NR4-0-s-/ and (b) simulation NR4-0-d-/.

Table 4-8. Description of the 6 relevant states of stress introduced in Fig. 4-7(a) and (b) for the simulations NR4-0-s-/ and NR4-0-d-/ (in terms of σ_{VM}, τ, $\sigma_{n,M-N}$ and σ_i stresses).

(a)   (b)
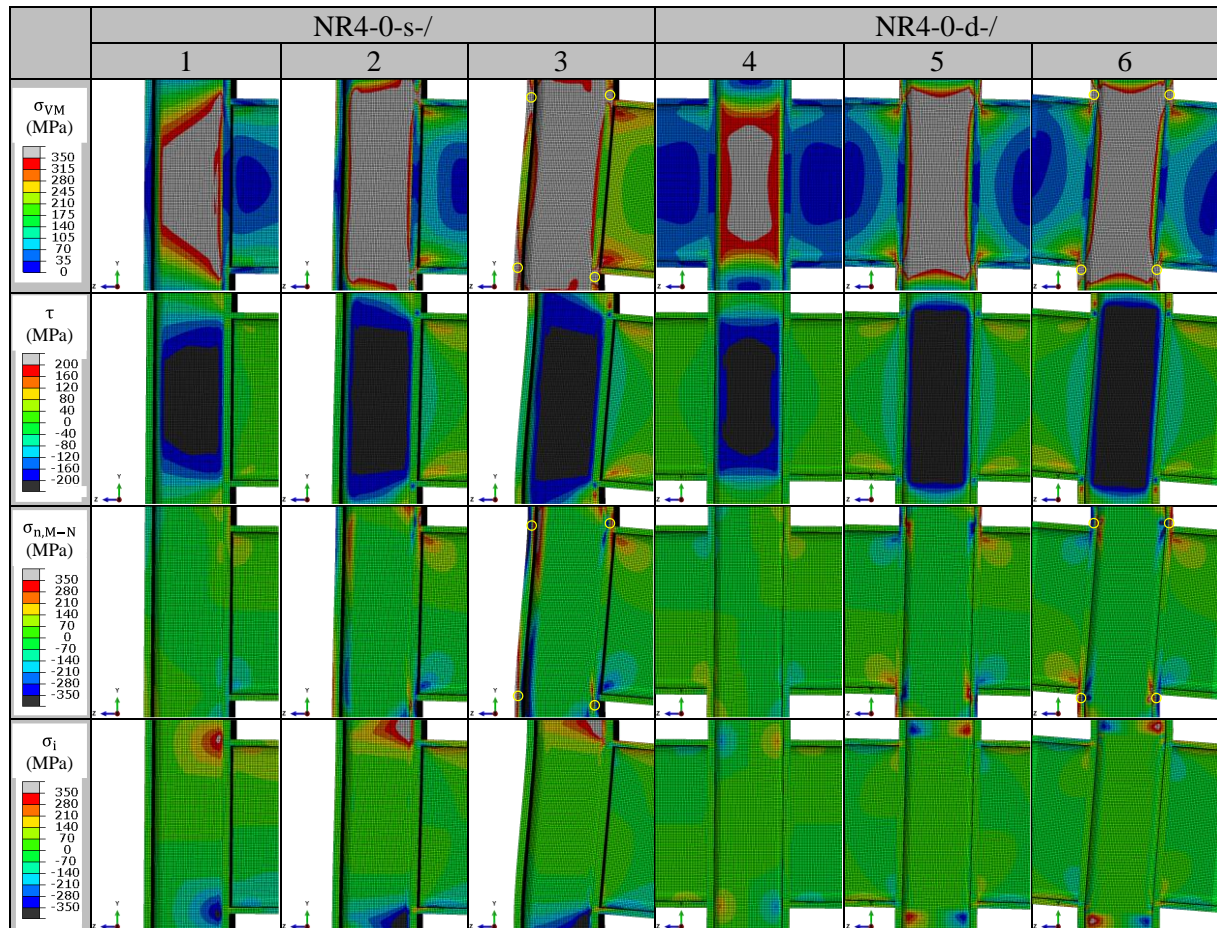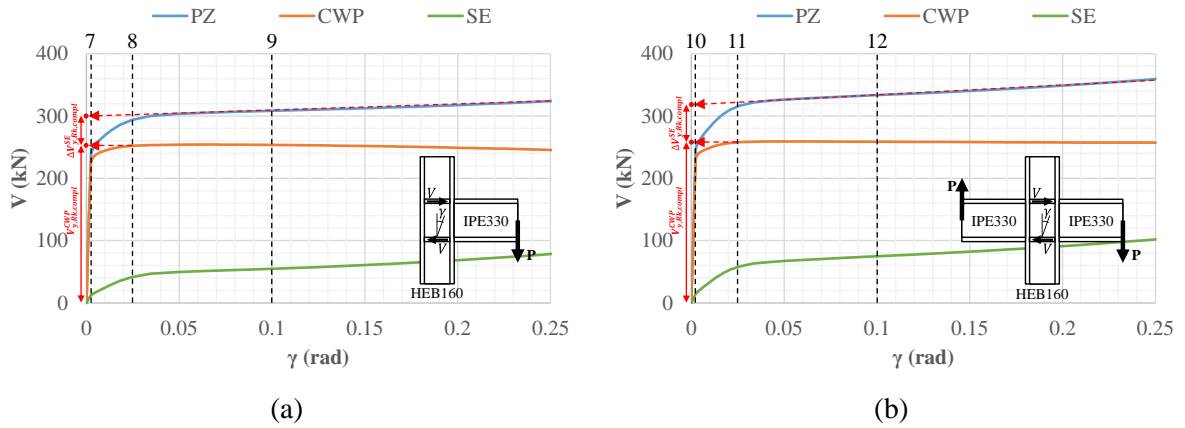
Fig. 4-8. Numerical results in terms of $(V - \gamma)_{num}$ curves: (a) simulation NR4-1-s-/ and (b) simulation NR4-1-d-/.

Table 4-9. Description of the 6 relevant states of stress introduced in Fig. 4-8(a) and (b) for the simulations NR4-1-s-/ and NR4-1-d-/ (in terms of σ_{VM}, τ, $\sigma_{n,M-N}$ and σ_i stresses).

(a) (b)
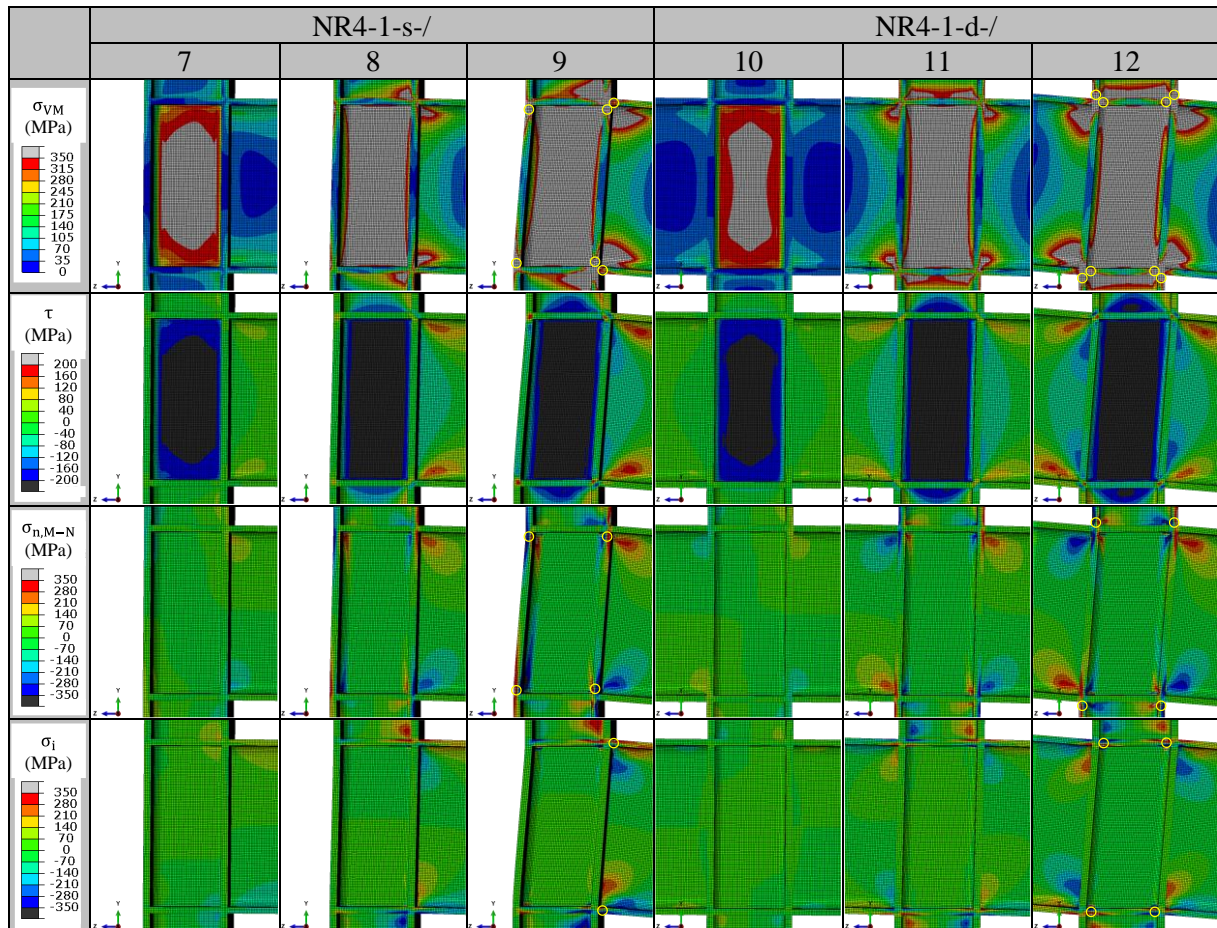
Fig. 4-9. Numerical results in terms of $(V - \gamma)_{num}$ curves: (a) simulation NR4-0-s-0.5N$_{pl}$ and (b) simulation NR4-0-d-0.5N$_{pl}$.

Table 4-10. Description of the 6 relevant states of stress introduced in Fig. 4-9(a) and (b) for the simulations NR4-0-s-0.5N$_{pl}$ and NR4-0-d-0.5N$_{pl}$ (in terms of σ_{VM}, τ, $\sigma_{n,M-N}$ and σ_i stresses).

(a)   (b)

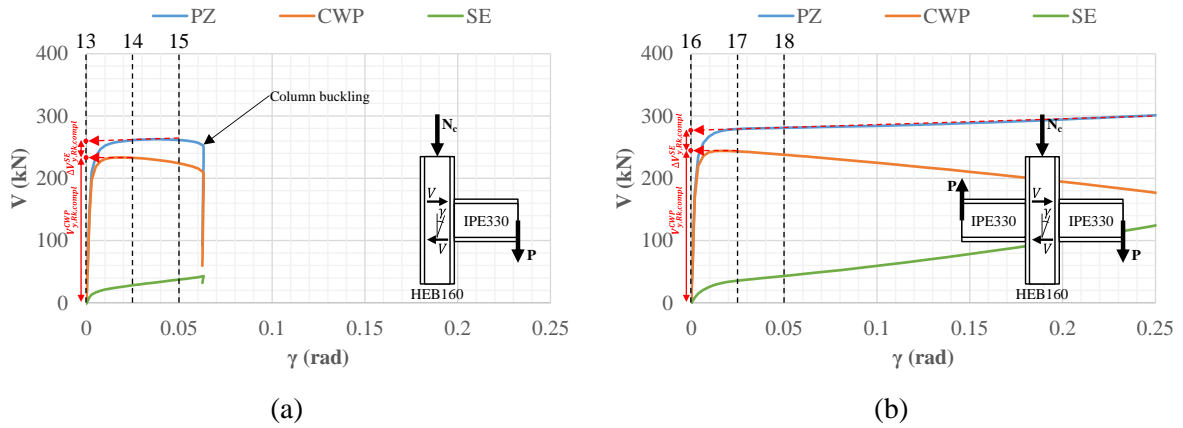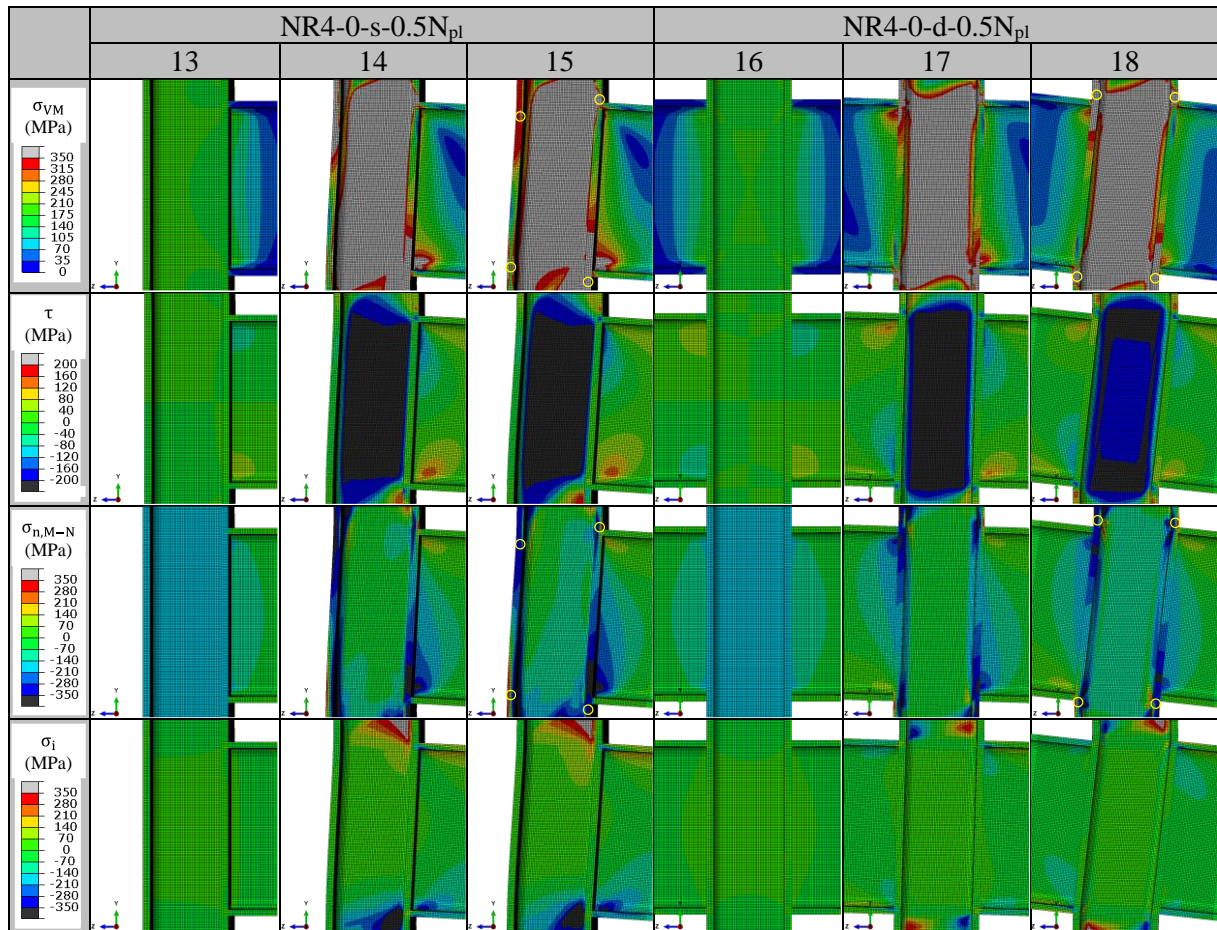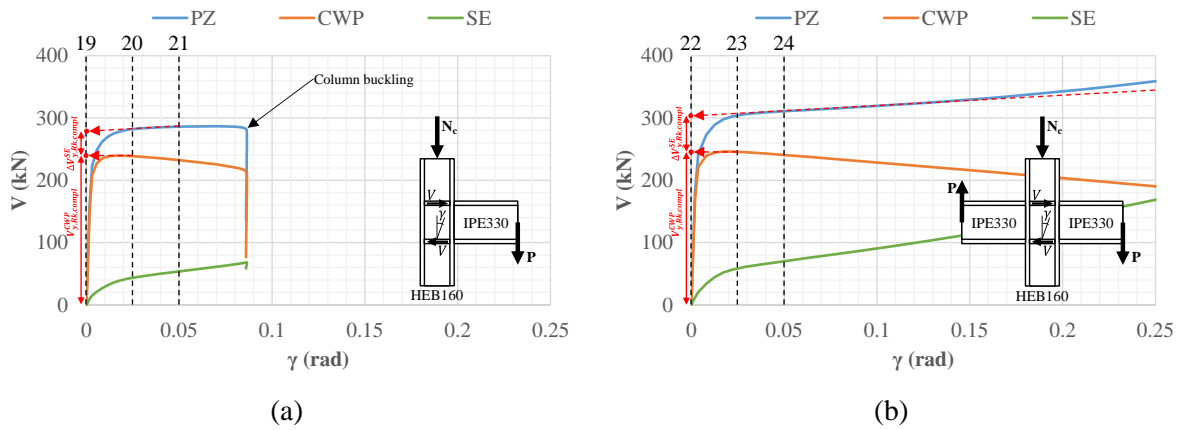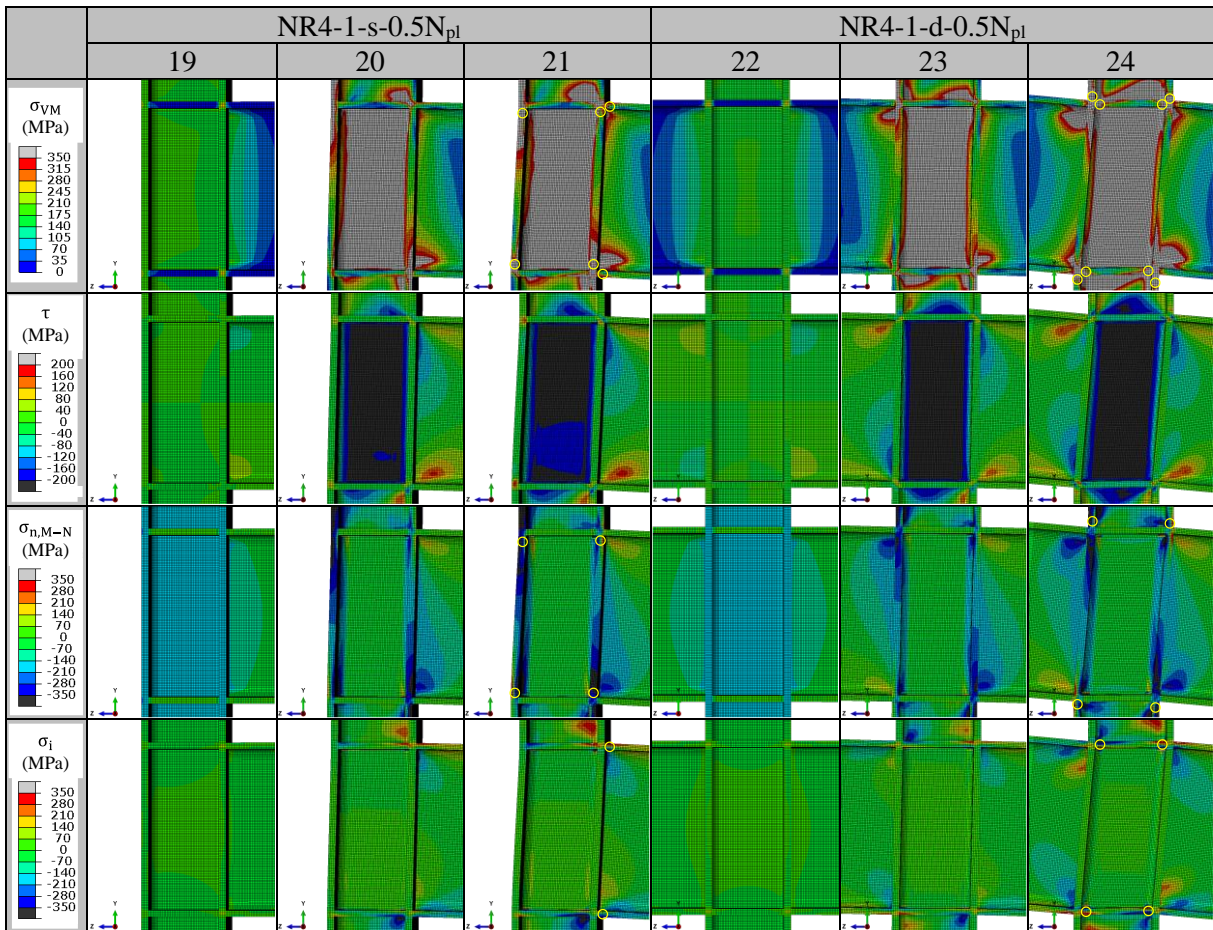Fig. 4-10. Numerical results in terms of $(V - \gamma)_{num}$ curves: (a) simulation NR4-1-s-0.5N_{pl} and (b) simulation NR4-1-d-0.5N_{pl}.

Table 4-11. Description of the 6 relevant states of stress introduced in Fig. 4-10(a) and (b) for the simulations NR4-1-s-0.5N_{pl} and NR4-1-d-0.5N_{pl} (in terms of σ_{VM}, τ, $\sigma_{n,M-N}$ and σ_i stresses).

4.3 ANALYTICAL PART

4.3.1 Complex analytical model

4.3.1.1 Contribution of the CWP

A. *Description of the model*

Based on the conclusions drawn from the parametric study, it has been decided to express the contribution $V_{y,Rk,compl}^{CWP}$ of the CWP through Eq. (4-4) as the product of the equivalent plastic shear resistance of the CWP with no stress interaction and assuming a simplified uniform shear stress distribution (i.e. $V_{y,Rk}^{CWP}$), multiplied by two reduction factors, i.e. χ_i and $\chi_{n,M-N}$. The latter account for the $\tau - \sigma_i$ and $\tau - \sigma_{n,M-N}$ interactions, and for the actual shear stress distribution within the CWP. The $\tau - \sigma_i - \sigma_{n,M-N}$ interaction, if any, is included in the two aforementioned coefficients.

The model proposed in Eq. (4-4) has been developed and validated based on the FE results. The latter consist of the numerical estimations $V_{y,Rk,num}^{CWP}$ of the plastic shear resistance of the CWP. They were extracted from the numerical $(V^{CWP} - \gamma)_{num}$ curves presented in APPENDIX C (see the orange continuous curves in Fig. C-1(c) to Fig. C-32(c)), using Eq. (4-5), for each numerical simulation. The so-obtained values are reported in Table 4-12, where they are sorted into four main categories:

- Category I includes the results of the numerical simulations performed on the non-axially loaded (un-)stiffened interior joints (i.e. eight in total). In these simulations, both $\tau - \sigma_i$ and $\tau - \sigma_{n,M-N}$ interactions are minimum.
- Category II includes the results of the numerical simulations performed on the non-axially loaded (un-)stiffened exterior joints (i.e. six in total). In these simulations, the $\tau - \sigma_i$ interaction is maximum while the $\tau - \sigma_{n,M-N}$ interaction is minimum.
- Category III includes the results of the numerical simulations performed on the axially loaded (un-)stiffened interior joints (i.e. eight in total). In these simulations, the $\tau - \sigma_{n,M-N}$ interaction is maximum while the $\tau - \sigma_i$ interaction can be neglected.
- Category IV includes the results of the numerical simulations performed on the axially loaded (un-)stiffened exterior joints (i.e. six in total). In these simulations, both $\tau - \sigma_i$ and $\tau - \sigma_{n,M-N}$ interactions are maximum.

$$V_{y,Rk,compl}^{CWP} = \chi_i \cdot \chi_{n,M-N} \cdot V_{y,Rk}^{CWP} \tag{4-4}$$

$$V_{y,Rk,num}^{CWP} = \max_t \left(V_{Ek,num}^{CWP,t} \right) \tag{4-5}$$

Table 4-12. Numerical estimation $V_{y,Rk,num}^{CWP}$ of the plastic shear resistance of the CWP for each individual numerical simulation (in kN).

Configuration	Category I (X="d", Y="/")	Category II (X="s", Y="/")	Category III (X="d", Y="0.5N$_{pl}$")	Category IV (X="s", Y="0.5N$_{pl}$")
NR4-0-X-Y	256.3	251.9	244.1	233.4
NR4-1-X-Y	258.8	253.7	245.9	239.4
NR16-0-X-Y	684.4	657.1	657.5	619.6
NR16-1-X-Y	701.9	668.6	672.6	638.1
A-0-X-Y	268.6	255.2	252.8	238.0
A-1-X-Y	270.1	261.1	254.4	245.7
B-0-X-Y	851.2	/	804.0	/
B-1-X-Y	851.6	/	811.6	/

i. Estimation of χ_i

In Eq. (4-4), the local effect of the $\tau - \sigma_i$ interaction in the CWP has been taken into account using a global reduction factor χ_i. This latter was assessed based on the comparisons between the FE results from the categories II and IV (i.e. exterior joints where the $\tau - \sigma_i$ interaction is maximum) and their corresponding FE results from the categories I and III (i.e. interior joints where the $\tau - \sigma_i$ interaction is minimum). This is done in Table 4-13. As the ratio between the two oscillates a bit above 0.95, the value of χ_i has been set at 0.95 for exterior joints while it remains equal to 1.0 in the case of interior joints, as expressed through Eq. (4-6).

N.B.: In the case of stiffened exterior joints, this value may seem slightly conservative as the stiffeners attract part of the "load-introduction" forces, thereby reducing the $\tau - \sigma_i$ interaction in the CWP. However, given the low influence of this parameter on the plastic shear resistance of the CWP, χ_i was set equal to 0.95 for both (un-)stiffened exterior joints, for the simplicity of the analytical model.

$$\chi_i = \begin{cases} 0.95 & for\ exterior\ joints \\ 1.0 & for\ interior\ joints \end{cases} \tag{4-6}$$

Table 4-13. Determination of the reduction factor χ_i.

Configuration	Exterior joints (X="s") $V_{y,Rk,num}^{CWP}(s)\ (kN)$	Interior joints (X="d") $V_{y,Rk,num}^{CWP}(d)\ (kN)$	Ratio $\chi_{i,num} = \dfrac{V_{y,Rk,num}^{CWP}(s)}{V_{y,Rk,num}^{CWP}(d)}\ (-)$
NR4-0-X-/	251.9	256.3	0.983
NR4-1-X-/	253.7	258.8	0.980
NR4-0-X-0.5N$_{pl}$	233.4	244.1	0.956
NR4-1-X-0.5N$_{pl}$	239.4	245.9	0.974
NR16-0-X-/	657.1	684.4	0.960
NR16-1-X-/	668.6	701.9	0.953
NR16-0-X-0.5N$_{pl}$	619.6	657.5	0.942
NR16-1-X-0.5N$_{pl}$	638.1	672.6	0.949
A-0-X-/	255.2	268.6	0.950
A-1-X-/	261.1	270.1	0.967
A-0-X-0.5N$_{pl}$	238.0	252.8	0.941
A-1-X-0.5N$_{pl}$	245.7	254.4	0.966
Mean value			0.960

ii. Estimation of $V_{y,Rk}^{CWP}$ and $\chi_{n,M-N}$

The other two parameters, i.e. $V_{y,Rk}^{CWP}$ and $\chi_{n,M-N}$, both depend on the shear stress (τ) and vertical normal stress ($\sigma_{n,M-N}$) distributions within the PZ and their interaction. Consequently, they were assessed together.

Regarding the $\sigma_{n,M-N}$ stress distribution, it was observed in the parametric study (see Section 4.2.4.4) that, at yielding, these latter are mostly transferred by the column flanges (including the root fillet region). They arise from the equivalent vertical axial load $N_{fc,Ek}$ acting in the column flanges. This latter can be computed at each corner of the PZ using the equivalent truss models provided in APPENDIX B.1.2 (see Fig. B-5 and B-11). This is expressed through Eq. (4-7), where "*TL*", "*TR*", "*BL*" and "*BR*" stand for "Top-Left", "Top-Right", "Bottom-Left" and "Bottom-Right", respectively, and where the expressions of M_{CT} (resp. M_{CB}) and N_{CT} (resp. N_{CB}) are given in APPENDIX B.1.2 (see Table B-1 and Table B-4). Therefore, the $\sigma_{n,M-N}$ stress distribution in the column flanges can be expressed through Eq. (4-8) as the sum of the $\sigma_{n,M}$ stress coming from the M_{CT} (resp. M_{CB}) bending moment in the column and the $\sigma_{n,N}$ stress coming from the N_{CT} (resp. N_{CB}) axial load in the column, if

any. The $\sigma_{n,M-N}$ stress distribution is presented in Fig. 4-11(a) for the central row of FE in the simulation NR4-1-d-0.5N$_{pl}$. Although the $\sigma_{n,M-N}$ stress distribution is not truly uniform over the whole depth d_b^* of the PZ, it was assumed so to facilitate the derivation of the parameters $V_{y,Rk}^{CWP}$ and $\chi_{n,M-N}$. The adopted uniform distribution is reported in Fig. 4-11(b), where $\overline{\sigma_{n,M-N}}$ may be computed through Eq. (4-9) as the average of the four vertical normal stresses $\sigma_{n,M-N}^i$ computed at each corner of the PZ through Eq. (4-8).

$$N_{fc,Ek} = \begin{cases} -\dfrac{M_{CT}}{d_b^*} - \dfrac{N_{CT}}{2} & TL\ corner \\[2mm] \dfrac{M_{CT}}{d_b^*} - \dfrac{N_{CT}}{2} & TR\ corner \\[2mm] \dfrac{M_{CB}}{d_b^*} - \dfrac{N_{CB}}{2} & BL\ corner \\[2mm] -\dfrac{M_{CB}}{d_b^*} - \dfrac{N_{CB}}{2} & BR\ corner \end{cases} \quad \rightarrow \quad n_{fc,T} = \dfrac{N_{fc,Ek}}{N_{pl,fc,T,Rk}} \tag{4-7}$$

$$\sigma_{n,M-N}^i = \frac{N_{fc,Ek}^i}{A_{fc,T}} = \sigma_{n,M}^i + \sigma_{n,N}^i \quad i = TL, TR, BL, BR \tag{4-8}$$

$$\overline{\sigma_{n,M-N}} = \frac{1}{4} \cdot \sum_i \left| \sigma_{n,M-N}^i \right| \quad i = TL, TR, BL, BR \tag{4-9}$$
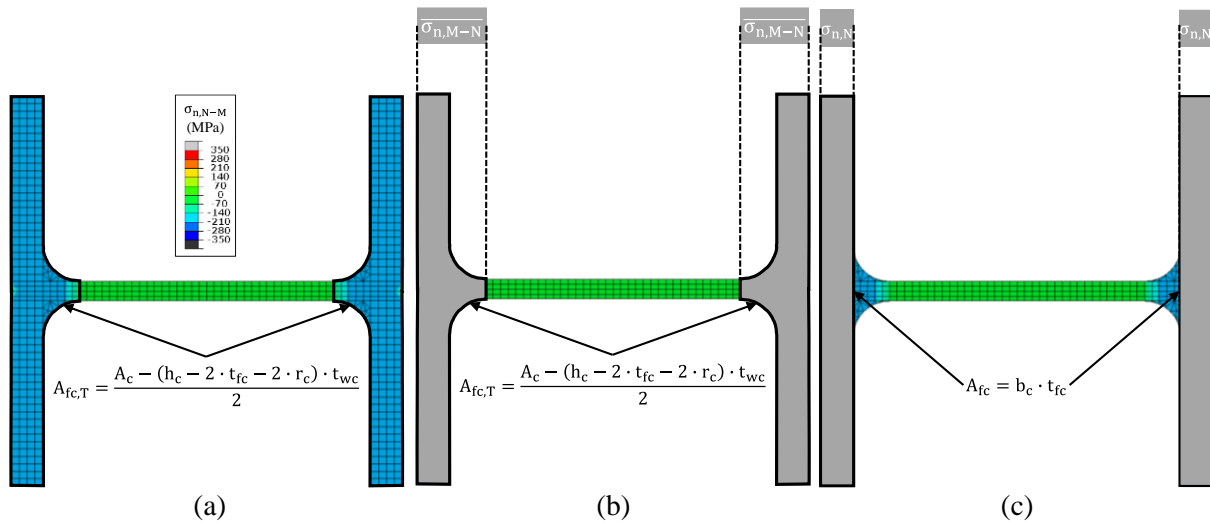
Fig. 4-11. $\sigma_{n,M-N}$ stress distribution at yielding: (a) FE results, (b) complex and (c) simplified analytical models.

Regarding the τ stress distribution, it was observed a uniform distribution at yielding over the whole depth d_b^* of the PZ for all the numerical simulations performed in the parametric study. Therefore, the ith row of FE can be arbitrarily extracted from the PZ. This is done in Fig. 4-12(a) for the central row of FE of the simulation NR4-1-d-0.5N$_{pl}$. From Fig. 4-12(a), the τ stress distribution has been studied and an analytical estimation of the plastic shear resistance $V_{y,Rk,compl}^{CWP}$ of the CWP has been derived (see Fig. 4-12(b)), following a five-step procedure:

- Firstly, it can be seen from Fig. 4-12(a) that, strictly speaking, only the clear depth of the column cross-section yields. Therefore, a uniform τ stress distribution was considered over the area $A_{VC,1}^{compl}$, as depicted by the black rectangles in Fig. 4-12(b).

- It was secondly observed that, when the flow of shear stress reaches the root fillets and the flanges of the column cross-section, it spreads over a larger area $A_{VC,2}^{compl}$, which coincides with a general decrease in the shear stress level. Therefore, a linearly decreasing shear stress distribution can be assumed over $A_{VC,2}^{compl}$, varying from τ_y^* at the onset of the root fillets to 0 at the extremity of the column flanges, as shown in Fig. 4-12(b).

- τ_y^* is the reduced material shear strength accounting for the $\tau - \sigma_{n,M-N}$ interaction in the column flanges. It can be expressed through Eq. (4-10) based on the use of the von Mises criterion and on the above-mentioned assumption of a uniform $\overline{\sigma_{n,M-N}}$ stress distribution in the column flanges (see Fig. 4-11(a) and (b)). In Eq. (4-10), $\overline{n_{fc,T}}$ is the average level of axial load in the column flanges and can be derived through Eq. (4-11), where $\overline{N_{fc,Ek}}$ is the average axial load in the column flanges.

- The integration of the triangular shear stress profile over $A_{VC,2}^{compl}$ is not easy. Therefore, a simplified procedure is proposed, consisting in: (i) computing the location y_{CG} of the centre of gravity of $A_{VC,2}^{compl}$ (see the formula in Fig. 4-12(b)); (ii) deriving the shear stress level $\tau_{y,CG}^*$ at the centre of gravity of $A_{VC,2}^{compl}$ (based on the aforementioned assumption of a triangular shear stress distribution over $A_{VC,2}^{compl}$, see Fig. 4-12(b)); and (iii) using $\tau_{y,CG}^*$ as the mean shear stress over the whole area $A_{VC,2}^{compl}$, as depicted by the grey rectangles in Fig. 4-12(b).

- Therefore, the analytical estimation of the plastic shear resistance $V_{y,Rk,compl}^{CWP}$ of the CWP can be expressed through Eq. (4-12) as the sum of the black and grey contributions presented in Fig. 4-12(b). This Eq. (4-12) can be further developed to make the parameters $V_{y,Rk}^{CWP}$ and $\chi_{n,M-N}$ appear explicitly (see Eq. (4-13)).

$$\overline{\sigma_{n,M-N}}^2 + 3 \cdot \tau_y^{*2} = f_y^2 \quad \blacktriangleright \quad \tau_y^* = \tau_y \cdot \sqrt{1 - \left(\overline{n_{fc,T}}\right)^2} \tag{4-10}$$

$$\overline{N_{fc,Ek}} = \frac{1}{4} \cdot \sum_i \left|N_{fc,Ek}^i\right| \quad i = TL, TR, BL, BR \quad \blacktriangleright \quad \overline{n_{fc,T}} = \frac{\overline{N_{fc,Ek}}}{N_{pl,fc,T,Rk}} = \frac{\overline{\sigma_{n,M-N}}}{f_y} \tag{4-11}$$
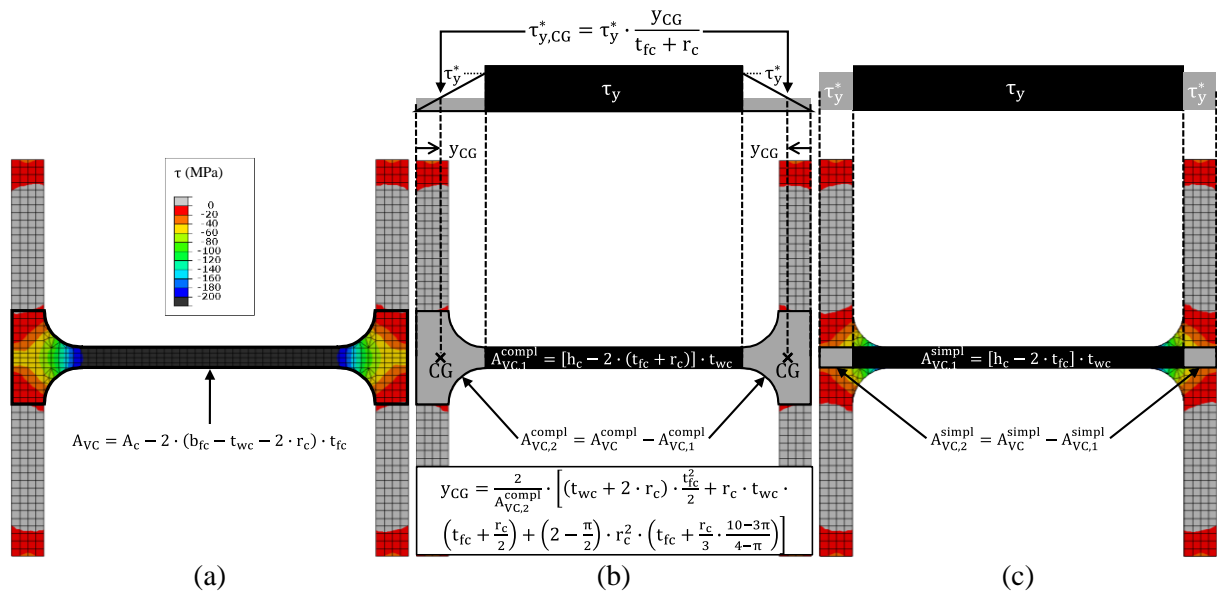

Fig. 4-12. τ stress distribution at yielding: (a) FE results, (b) complex analytical model and (c) simplified analytical model.

$$V_{y,Rk,compl}^{CWP} = \chi_i \cdot \left(A_{VC,1}^{compl} \cdot \tau_y + 0.95 \cdot A_{VC,2}^{compl} \cdot \tau_{y,CG}^* \right) \tag{4-12}$$

$$= \chi_i \cdot \underbrace{\left[1 - \frac{A_{VC,2}^{compl}}{A_{VC}^{compl}} \cdot \left(1 - 0.95 \cdot \sqrt{1 - \left(\overline{n_{fc,T}} \right)^2} \cdot \frac{y_{CG}}{t_{fc}+r_c} \right) \right]}_{\chi_{n,M-N}} \cdot \underbrace{\tau_y \cdot A_{VC}^{compl}}_{V_{y,Rk}^{CWP}} \tag{4-13}$$

B. Validation

All terms in Eq. (4-13) being known, the contribution $V_{y,Rk,compl}^{CWP}$ can be analytically predicted for every single numerical simulation. These results are given in Table 4-14 where they are compared to the $V_{y,Rk,num}^{CWP}$ values. These comparisons are conducted on the basis of the performance indicator E and the colour code defined in Table 3-1. It can be concluded from Table 4-14 that the proposed analytical model for the prediction of the plastic shear resistance of the CWP works well as it features a high level of accuracy for all the numerical simulations considered in the present parametric study.

N.B.: This good agreement between analytical and numerical results has been achieved by affecting a "0.95" reduction coefficient to the second term in Eqs. (4-12) and (4-13). This reduction coefficient is valid for the range of column web-to-flange thickness ratios considered in the present study (i.e. $0.55 - 0.62$, see Table 4-5), which includes 17.5% of the European IPE-profiles (total range: $0.55 \leq t_{wc}/t_{fc} \leq 0.80$), 40% of the European HE-profiles (total range: $0.52 \leq t_{wc}/t_{fc} \leq 0.78$) and 55% of the American W-profiles (total range: $0.53 \leq t_{wc}/t_{fc} \leq 0.91$). However, additional simulations would be required in order to validate this "0.95" reduction coefficient to the whole range of European IPE- and HE-profiles and American W-profiles, as it is likely that the τ stress distribution is influenced by the column web-to-flange thickness ratio t_{wc}/t_{fc}.

C. Discussion

Practically speaking, the derivation in Eq. (4-13) of the level of axial load $\overline{n_{fc,T}}$ in the column flanges is not easy as it depends on the M_{CT} (resp. M_{CB}) bending moment in the column, which continuously varies at each loading step of the numerical simulations. Therefore, it was decided to neglect the effect of the M_{CT} (resp. M_{CB}) bending moment in the column to facilitate the computation of the plastic shear resistance $V_{y,Rk,compl}^{CWP}$ of the CWP. This assumption seems reasonable as the $\sigma_{n,M}$ stresses coming from the M_{CT} (resp. M_{CB}) bending moment in the column are usually significantly lower than the $\sigma_{n,N}$ stresses coming from the N_{CT} (resp. N_{CB}) axial load in the column. Consequently, Eq. (4-11) can be simplified into Eq. (4-14) and the complex analytical model for the prediction of the contribution $V_{y,Rk,compl}^{CWP}$ of the CWP can be re-expressed as follows (see Eq. (4-15)-Eq. (4-18)):

$$n_{fc,T}^* = \frac{N_{fc,Ek}^*}{N_{pl,fc,T,Rk}} = \frac{N_c/2}{N_{pl,fc,T,Rk}} = \frac{\sigma_{n,N}}{f_y} \tag{4-14}$$

$$V_{y,Rk,compl}^{CWP} = \chi_i \cdot \chi_n \cdot V_{y,Rk}^{CWP} \tag{4-15}$$

Where:

$$\chi_i = \begin{cases} 0.95 & for\ exterior\ joints \\ 1.0 & for\ interior\ joints \end{cases} \tag{4-16}$$

$$\chi_n (= \chi_{n,N}) = \left[1 - \frac{A_{VC,2}^{compl}}{A_{VC}^{compl}} \cdot \left(1 - 0.90 \cdot \sqrt{1 - \left(n_{fc,T}^* \right)^2} \cdot \frac{y_{CG}}{t_{fc}+r_c} \right) \right] \tag{4-17}$$

$$V_{y,Rk}^{CWP} = A_{VC}^{compl} \cdot \tau_y \tag{4-18}$$

This second version of the complex analytical model for the prediction of the contribution $V_{y,Rk,compl}^{CWP}$ of the CWP has been validated against the 28 numerical results, similarly to the first version. This is done in Table 4-15, where it can be seen that this second version of the complex analytical model features a high level of accuracy for all the numerical simulations considered in the present parametric study. Therefore, this second version can be considered as valid and will be used as *the reference complex analytical model* for the prediction of the contribution $V_{y,Rk,compl}^{CWP}$ of the CWP in the rest of the present thesis. A graphical comparison between analytical and numerical results is also provided in APPENDIX C for every single numerical simulation (see the dark orange broken curves and the light orange continuous curves in Fig. C-1(c) to C-32(c), respectively).

N.B.: To obtain a good match between the analytical and numerical results, the "0.95" reduction coefficient in Eq. (4-12) has been replaced by a "0.90" reduction coefficient in Eq. (4-17). This small decrease of the reduction coefficient aims to account for the effect of the bending moment in the column on the plastic shear resistance $V_{y,Rk,compl}^{CWP}$ of the CWP, which is no longer accounted for in Eq. (4-17).

Table 4-14. Comparisons between $V_{y,Rk,compl}^{CWP(V1)}$ (1st version) and $V_{y,Rk,num}^{CWP}$.

Configuration	Category I (X="d", Y="/")			Category II (X="s", Y="/")		
	$V_{y,Rk,num}^{CWP}$ (kN)	$V_{y,Rk,compl}^{CWP(V1)}$ (kN)	E (%)	$V_{y,Rk,num}^{CWP}$ (kN)	$V_{y,Rk,compl}^{CWP(V1)}$ (kN)	E (%)
NR4-0-X-Y	256.3	262.2	2.30	251.9	249.8	-0.83
NR4-1-X-Y	258.8	260.0	0.46	253.7	248.4	-2.09
NR16-0-X-Y	684.4	701.6	2.51	657.1	668.0	1.66
NR16-1-X-Y	701.9	690.9	-1.57	668.6	662.4	-0.93
A-0-X-Y	268.5	267.3	-0.45	255.2	254.4	-0.31
A-1-X-Y	270.1	266.7	-1.26	261.1	254.0	-2.72
B-0-X-Y	851.2	873.4	2.61	/	/	/
B-1-X-Y	851.6	873.2	2.54	/	/	/
Configuration	Category III (X="d", Y="0.5N$_{pl}$")			Category IV (X="s", Y="0.5N$_{pl}$")		
	$V_{y,Rk,num}^{CWP}$ (kN)	$V_{y,Rk,compl}^{CWP(V1)}$ (kN)	E (%)	$V_{y,Rk,num}^{CWP}$ (kN)	$V_{y,Rk,compl}^{CWP(V1)}$ (kN)	E (%)
NR4-0-X-Y	244.1	250.2	2.50	233.4	236.3	1.24
NR4-1-X-Y	245.9	250.2	1.75	239.4	236.2	-1.34
NR16-0-X-Y	657.5	674.2	2.54	619.6	635.7	2.60
NR16-1-X-Y	672.6	674.2	0.24	638.1	634.7	-0.53
A-0-X-Y	252.8	250.2	-1.03	238.0	236.8	-0.50
A-1-X-Y	254.4	250.2	-1.65	245.7	236.8	-3.62
B-0-X-Y	804.0	824.7	2.57	/	/	/
B-1-X-Y	811.6	824.7	1.61	/	/	/

Table 4-15. Comparisons between $V_{y,Rk,compl}^{CWP(V2)}$ (2nd version) and $V_{y,Rk,num}^{CWP}$.

Configuration	Category I (X="d", Y="/")			Category II (X="s", Y="/")		
	$V_{y,Rk,num}^{CWP}$ (kN)	$V_{y,Rk,compl}^{CWP(V2)}$ (kN)	E (%)	$V_{y,Rk,num}^{CWP}$ (kN)	$V_{y,Rk,compl}^{CWP(V2)}$ (kN)	E (%)
NR4-0-X-Y	256.3	266.3	3.90	251.9	253.0	0.44
NR4-1-X-Y	258.8	266.3	2.90	253.7	253.0	-0.28
NR16-0-X-Y	684.4	703.9	2.85	657.1	668.7	1.77
NR16-1-X-Y	701.9	703.9	0.28	668.6	668.7	0.01
A-0-X-Y	268.5	266.3	-0.82	255.2	253.0	-0.86
A-1-X-Y	270.1	266.3	-1.41	261.1	253.0	-3.10
B-0-X-Y	851.2	866.2	1.76	/	/	/
B-1-X-Y	851.6	866.2	1.71	/	/	/
Configuration	Category III (X="d", Y="0.5N$_{pl}$")			Category IV (X="s", Y="0.5N$_{pl}$")		
	$V_{y,Rk,num}^{CWP}$ (kN)	$V_{y,Rk,compl}^{CWP(V2)}$ (kN)	E (%)	$V_{y,Rk,num}^{CWP}$ (kN)	$V_{y,Rk,compl}^{CWP(V2)}$ (kN)	E (%)
NR4-0-X-Y	244.1	246.2	0.86	233.4	233.9	0.21
NR4-1-X-Y	245.9	246.2	0.12	239.4	233.9	-2.30
NR16-0-X-Y	657.5	663.9	0.97	619.6	630.7	1.79
NR16-1-X-Y	672.6	663.9	-1.29	638.1	630.7	-1.16
A-0-X-Y	252.8	246.2	-2.61	238.0	233.9	-1.72
A-1-X-Y	254.4	246.2	-3.22	245.7	233.9	-4.80
B-0-X-Y	804.0	813.3	1.16	/	/	/
B-1-X-Y	811.6	813.3	0.21	/	/	/

4.3.1.2 Contribution of the SE

A. Description of the model

From the parametric study, it was concluded that, beyond the yielding of the CWP, extra shear forces are transferred to the SE until the development of a collapse mechanism, activated regardless the presence or otherwise of transverse column web stiffeners. Therefore, the collapse mechanisms have been studied for each joint configuration to quantify the contribution $\Delta V_{y,Rk,compl}^{SE}$ of the SE. For unstiffened joints, the collapse mechanism consists of the formation of four plastic hinges in the column flanges (see Table 4-1), thus leading to Eq. (4-21). For stiffened joints, two to four additional hinges are required in order for the collapse mechanism to develop (see Table 4-1). These additional plastic hinges are located either in the transverse column web stiffeners or in the beam(s) flanges, the plastic collapse mechanism actually developing being the one requiring the minimum energy, as stated by Eq. (4-22).

In Eq. (4-21) and Eq. (4-22), d_b^* is the depth of the PZ (assumed equal to the equivalent lever arm z_{eq} between the centres of tension and compression for a welded joint, see Eq. (2-5)); $M_{pl,fc,T,Rk}$, $M_{pl,fb,T,Rk}$ and $M_{pl,st,Rk}$ are the characteristic plastic bending moment resistances of a T-shaped column flange including the root fillets region, of a T-shaped beam flange including the root fillets region and of a rectangular transverse column web stiffener, respectively.

In addition, $M_{pl,fc,T,Rk}$, $M_{pl,fb,T,Rk}$ and $M_{pl,st,Rk}$ are reduced plastic bending moment resistances as the column flanges, the beam flanges and the transverse column web stiffeners also carry an axial load (see the equivalent truss model in Fig. B-5 and Fig. B-11 of APPENDIX C for exterior and interior joints, respectively). The vertical axial load $N_{fc,Ek}$ in the column flanges, at the level of the plastic hinges, can be computed through Eq. (4-7), where the expressions of M_{CT} (resp. M_{CB}) and N_{CT} (resp. N_{CB}) are given in Table B-1 and Table B-4 in APPENDIX B. Similarly, the horizontal axial load $N_{fb,Ek}$ (resp. $N_{st,Ek}$) in the beam flanges (resp. in the transverse column web stiffeners), at the level of the hinges, can be computed through Eq. (4-19), where the expressions of the beam bending moment M_{BL} (resp. M_{BR}) and the beam axial load N_{BL} (resp. N_{BR}) are provided in Table B-1 and Table B-4 in APPENDIX B.

These axial loads lead to a general decrease of the plastic bending moment resistances, as expressed through Eq. (4-20), where $\widehat{M}_{pl,fc,T,Rk}$, $\widehat{M}_{pl,fb,T,Rk}$ and $\widehat{M}_{pl,st,Rk}$ are the characteristic plastic bending moment resistances with no M-N interaction of a T-shaped column flange, of a T-shaped beam flange and of a rectangular stiffener, respectively and where $\Delta\chi_{n,M-N}$ is a reduction factor accounting for the M-N interaction, which can be deduced from the M-N interaction curves of the T-shaped column flanges, of the T-shaped beam flanges and of the rectangular stiffeners considered in the present study.

$$
N_{\substack{fb,Ek \\ st,Ek}} = \begin{cases} -\dfrac{M_{BL}}{d_b^*} - \dfrac{N_{BL}}{2} & TL\ corner \\[2mm] \dfrac{M_{BR}}{d_b^*} - \dfrac{N_{BR}}{2} & TR\ corner \\[2mm] \dfrac{M_{BL}}{d_b^*} - \dfrac{N_{BL}}{2} & BL\ corner \\[2mm] -\dfrac{M_{BR}}{d_b^*} - \dfrac{N_{BR}}{2} & BR\ corner \end{cases} \rightarrow \quad n_{\substack{fb,T \\ st}} = \dfrac{N_{\substack{fb,Ek \\ st,Ek}}}{N_{\substack{pl,fb,T,Rk \\ pl,st,Rk}}} \tag{4-19}
$$

$$
M_{\substack{pl,fc,T,Rk \\ pl,fb,T,Rk \\ pl,st,Rk}} = \Delta\chi_{n,M-N} \cdot \widehat{M}_{\substack{pl,fc,T,Rk \\ pl,fb,T,Rk \\ pl,st,Rk}} \tag{4-20}
$$

Table 4-16. List of all possible plastic collapse mechanisms for (un-)stiffened interior and exterior welded joints.

Unstiffened joints	Stiffened joints	
Interior joints — **1**	**2**	**3**
Exterior joints — **4**	**5**	**6**

$\Delta V_{y,Rk,compl}^{SE}$

$$4 \cdot \frac{M_{pl,fc,T,Rk}}{d_b^*} \qquad (4\text{-}21)$$

$$\begin{cases} 4 \cdot \dfrac{M_{pl,fc,T,Rk}}{d_b^*} + \min\left(4 \cdot \dfrac{M_{pl,st,Rk}}{d_b^*} \, ; \, 4 \cdot \dfrac{M_{pl,fb,T,Rk}}{d_b^*} \right) & \text{int. joints} \\[3ex] 4 \cdot \dfrac{M_{pl,fc,T,Rk}}{d_b^*} + \min\left(4 \cdot \dfrac{M_{pl,st,Rk}}{d_b^*} \, ; \, 2 \cdot \dfrac{M_{pl,fb,T,Rk}}{d_b^*} \right) & \text{ext. joints} \end{cases} \qquad (4\text{-}22)$$

All the formulae for the characterization of a rectangular (resp. T-shaped) plastic hinge in terms of geometric and mechanical properties are provided in APPENDIX D. Based on these formulae, it was possible to derive the axial strength, the plastic moment resistance and the M-N interaction curve of the different plastic hinges which are likely to develop for each of the 28 numerical simulations considered in the present study. These M-N interaction curves are presented in Table 4-17 and Table 4-18 for the eight numerical simulations performed with the model NR4.

Knowing the level of axial load $n_{fc,T}$ in the column flanges (i.e. $N_{fc,Ek}/N_{pl,fc,T,Rk}$, $N_{fc,Ek}$ being the equivalent axial load in the T-shaped column flange, see Eq. (4-7), and $N_{pl,fc,T,Rk}$ being the axial strength of this latter, see APPENDIX D.2), the level of axial load $n_{fb,T}$ in the beam flanges (i.e. $N_{fb,Ek}/N_{pl,fb,T,Rk}$, $N_{fb,Ek}$ being the equivalent axial load in the T-shaped beam flange, see Eq. (4-19), and $N_{pl,fb,T,Rk}$ being the axial strength of this latter, see APPENDIX D.2) and the level of axial load n_{st} in the stiffeners (i.e. $N_{st,Ek}/N_{pl,st,Rk}$, $N_{st,Ek}$ being the equivalent axial load in the rectangular stiffener, see Eq. (4-19), and $N_{pl,st,Rk}$ being the axial strength of this latter, see APPENDIX D.2), the reduction factor $\Delta\chi_{n,M-N}$ associated to each plastic hinge forming in the different simulations can be easily obtained from the M-N interaction curves, as shown in Table 4-17 and Table 4-18 hereafter. Consequently, the reduced plastic moment resistances of these different hinges can be obtained from Eq. (4-20).

B. Validation

Based on these values, the contribution $\Delta V_{y,Rk,compl}^{SE}$ associated to each of the 28 numerical simulations can be computed through Eq. (4-21) or Eq. (4-22). The results are given in Table 4-19 where the observed collapse mechanism is also reported.

C. Discussion

Practically speaking, the derivation of the reduction factor $\Delta\chi_{n,M-N}$ in Eq. (4-20), accounting for the M-N interaction in the column flanges, beam flanges and transverse column web stiffeners, is not easy, as it depends on the levels of axial load $n_{fc,T}$, $n_{fb,T}$ and n_{st} in these elements; and these levels of axial load $n_{fc,T}$, $n_{fb,T}$ and n_{st} continuously vary at each time step of the numerical simulations, together with the M_{CT} (resp. M_{CB}) and M_{BL} (resp. M_{BR}) bending moments in the column and in the beam(s).

Therefore, it was decided to neglect the effect of these bending moments to facilitate the derivation of the plastic shear resistance $\Delta V_{y,Rk,compl}^{SE}$ of the SE. This assumption seems reasonable as the axial load coming from the M_{CT} (resp. M_{CB}) bending moment in the column is usually significantly smaller than the axial strength $N_{pl,fc,T,Rk}$ of the column flanges and, similarly, the axial load coming from the M_{BR} (resp. M_{BL}) bending moment in the beam(s) is usually significantly smaller than the axial strength $N_{pl,fb,T,Rk}$ (resp. $N_{pl,st,Rk}$) of the beam flanges (resp. the transverse column web stiffeners). This can be observed in Table 4-17 where, in the absence of any axial load N_c and N_b in the column and in the beam(s), the reduction factor $\Delta\chi_{n,M-N}$ associated to the different plastic hinges oscillates around 0.90. Consequently, Eqs. (4-7), (4-19) and (4-20) can be simplified into Eqs. (4-23) to (4-26) as follows:

$$N_{fc,Ek}^* = \frac{N_c}{2} \quad \rightarrow \quad n_{fc,T}^* = \frac{N_{fc,Ek}^*}{N_{pl,fc,T,Rk}} \tag{4-23}$$

$$N_{\substack{fb,Ek \\ st,Ek}}^* = \frac{N_b}{2} = 0 \quad \rightarrow \quad n_{\substack{fb,T \\ st}}^* = 0 \tag{4-24}$$

$$M\begin{vmatrix} pl,fc,T,Rk \\ pl,fb,T,Rk \\ pl,st,Rk \end{vmatrix} = 0.95 \cdot \Delta\chi_n \cdot \hat{M}\begin{vmatrix} pl,fc,T,Rk \\ pl,fb,T,Rk \\ pl,st,Rk \end{vmatrix} \tag{4-25}$$

$$\Delta\chi_n(= \Delta\chi_{n,N}) = \left[1 - \left(n^*\begin{vmatrix} fc,T \\ fb,T \\ st \end{vmatrix}\right)^2\right] \tag{4-26}$$

From this new proposal (see Eqs. (4-23) to (4-26)), it can first be observed that a "0.95" reduction coefficient has been introduced in Eq. (4-25). This latter accounts for the effects of the column and beam(s) moments, which are no longer accounted for in Eqs. (4-23) and (4-24). In addition, the M-N interaction can always be neglected in the derivation of $M_{pl,fb,T,Rk}$ and $M_{pl,st,Rk}$ (i.e. $\Delta\chi_n = 1$) since the beams were assumed not to carry any axial load N_b in the scope of the present thesis. The same applies to $M_{pl,fc,T,Rk}$ in the absence of any axial load N_c in the column profile.

However, in the presence of a strong axial load N_c in the column profile, the M-N interaction is accounted for using the reduction coefficient $\Delta\chi_n$ (see Eq. (4-26)). For this latter, a simplified 2nd order expression is proposed. This simplified expression is plotted in Fig. 4-13 for the HEB160, HEB300 and HEB340 column profiles considered in the present study (see the black dotted curves) and it proves to provide a close but safe estimation of the actual M-N interaction curves.
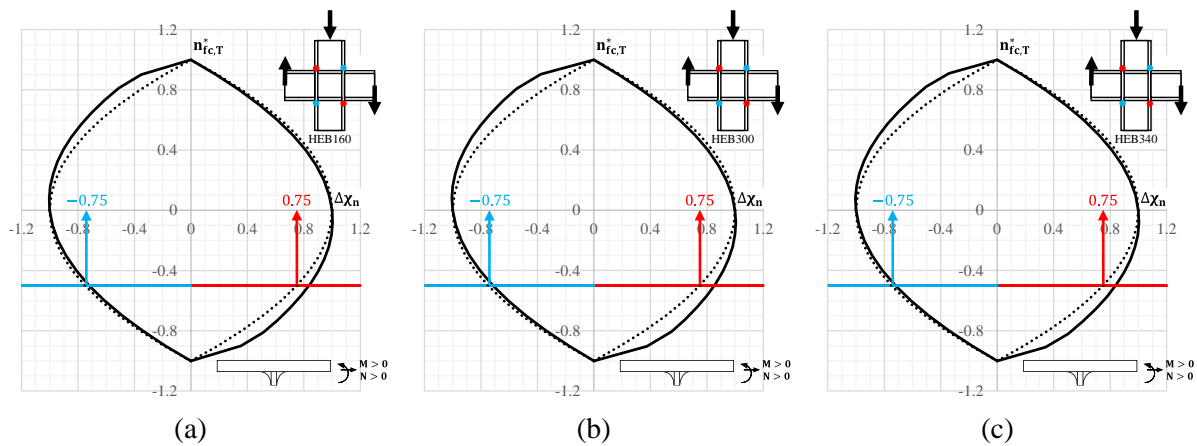
Fig. 4-13. Complex and simplified M-N interaction curves of a T-shaped column flange (see the black solid and dashed curves, respectively): (a) HEB160, (b) HEB300 and (c) HEB340.

This second version of the complex analytical model for the prediction of the contribution $\Delta V_{y,Rk,compl}^{SE}$ of the SE has been validated against the 28 analytical predictions of the first version. This is done in Table 4-20, using the performance indicator E and the colour code defined in Table 3-1. From Table 4-20, it can be observed that the second version of the analytical model features a high level of accuracy for 17 out of the 28 numerical results, a moderate level of accuracy for 8 out of the 28 results and a low level of accuracy for the remaining three results. The maximum difference between the two versions of the complex analytical model is limited to 15%.

Therefore, given that the contribution $\Delta V_{y,Rk,compl}^{SE}$ of the SE rarely exceeds $25\% - 30\%$ of the total plastic shear resistance $V_{y,Rk,compl}^{PZ}$ of the PZ, the differences between the first and second versions were assumed to have no significant influence on the final results. Consequently, the second version of the complex analytical model can be considered valid and will be used as *the reference complex analytical model* for the prediction of the contribution $\Delta V_{y,Rk,compl}^{SE}$ of the SE in the rest of the present thesis. A graphical comparison between this reference analytical model and the numerical results is provided in APPENDIX C for every single numerical simulation (see the dark green broken curves and the light green continuous curves in Fig. C-1(c) to Fig. C-32(c), respectively). From these figures, a rather good agreement can be observed between the analytical and numerical curves.

Table 4-17. M-N interaction curves for the non-axially loaded NR4 simulations.

Table 4-18. M-N interaction curves for the axially loaded NR4 simulations.

Table 4-19. Estimation of the contribution $\Delta V_{y,Rk,compl}^{SE(V1)}$ (1st version) for each individual numerical simulation.

Configuration	Category I (X="d", Y="/")		Category II (X="s", Y="/")	
	$\Delta V_{y,Rk,compl}^{SE(V1)}$ (kN)	Plastic mechanism*	$\Delta V_{y,Rk,compl}^{SE(V1)}$ (kN)	Plastic mechanism*
NR4-0-X-Y	37.0	1	37.6	4
NR4-1-X-Y	59.8	2	54.2	6
NR16-0-X-Y	109.9	1	110.5	4
NR16-1-X-Y	297.9	2	212.2	6
A-0-X-Y	66.3	1	67.0	4
A-1-X-Y	83.7	3	66.3	6
B-0-X-Y	228.2	1	/	/
B-1-X-Y	236.6	3	/	/
Configuration	Category III (X="d", Y="0.5N$_{pl}$")		Category IV (X="s", Y="0.5N$_{pl}$")	
	$\Delta V_{y,Rk,compl}^{SE(V1)}$ (kN)	Plastic mechanism*	$\Delta V_{y,Rk,compl}^{SE(V1)}$ (kN)	Plastic mechanism*
NR4-0-X-Y	25.3	1	24.6	4
NR4-1-X-Y	48.4	2	42.0	6
NR16-0-X-Y	79.8	1	72.9	4
NR16-1-X-Y	268.7	2	179.5	6
A-0-X-Y	45.6	1	48.4	4
A-1-X-Y	64.6	3	50.4	6
B-0-X-Y	158.3	1	/	/
B-1-X-Y	175.5	3	/	/
*See Table 4-16.				

Table 4-20. Comparisons between $\Delta V_{y,Rk,compl}^{SE(V1)}$ (1st version) and $\Delta V_{y,Rk,compl}^{SE(V2)}$ (2nd version).

Configuration	Category I (X="d", Y="/")			Category II (X="s", Y="/")		
	$\Delta V_{y,Rk,compl}^{SE(V1)}$ (kN)	$\Delta V_{y,Rk,compl}^{SE(V2)}$ (kN)	E $(\%)$	$\Delta V_{y,Rk,compl}^{SE(V1)}$ (kN)	$\Delta V_{y,Rk,compl}^{SE(V2)}$ (kN)	E $(\%)$
NR4-0-X-Y	37.0	39.5	6.76	37.6	39.5	5.05
NR4-1-X-Y	59.8	63.9	6.86	54.2	57.5	6.09
NR16-0-X-Y	109.9	109.9	0	110.5	109.9	-0.54
NR16-1-X-Y	297.9	302.8	1.64	212.2	217.7	2.59
A-0-X-Y	66.3	65.6	-1.06	67.0	65.6	-2.09
A-1-X-Y	83.7	86.0	2.75	66.3	75.8	14.33
B-0-X-Y	228.2	221.0	-3.16	/	/	/
B-1-X-Y	236.6	251.2	6.17	/	/	/
Configuration	Category III (X="d", Y="0.5N$_{pl}$")			Category IV (X="s", Y="0.5N$_{pl}$")		
	$\Delta V_{y,Rk,compl}^{SE(V1)}$ (kN)	$\Delta V_{y,Rk,compl}^{SE(V2)}$ (kN)	E $(\%)$	$\Delta V_{y,Rk,compl}^{SE(V1)}$ (kN)	$\Delta V_{y,Rk,compl}^{SE(V2)}$ (kN)	E $(\%)$
NR4-0-X-Y	25.3	24.6	-2.77	24.6	24.6	0
NR4-1-X-Y	48.4	49.0	1.24	42.0	42.7	1.67
NR16-0-X-Y	79.8	75.7	-5.14	72.9	75.7	3.84
NR16-1-X-Y	268.7	268.6	-0.04	179.5	183.5	2.23
A-0-X-Y	45.6	41.0	-10.09	48.4	41.0	-15.29
A-1-X-Y	64.6	61.3	-5.11	50.4	51.1	1.39
B-0-X-Y	158.3	142.6	-9.92	/	/	/
B-1-X-Y	175.5	172.6	-1.65	/	/	/

4.3.1.3 Validation

A. Validation against numerical results

i. In terms of $V - \gamma$ curves

Based on the results obtained from Sections 4.3.1.1 (see Table 4-15) and 4.3.1.2 (see Table 4-20), one can derive the total plastic shear resistance $V_{y,Rk,compl}^{PZ}$ of the PZ for each individual numerical simulation considered in the present parametric study, using Eq. (4-3). The results are reported in Table 4-21 where they are compared to the $V_{y,Rk,num}^{PZ}$ values, i.e. the numerical estimations of the plastic shear resistance of the PZ provided by the Abaqus© software. These latter have been extracted from the numerical $(V^{PZ} - \gamma)_{num}$ curves using the graphical method of Jaspart (presented in Section 3.2.2), i.e. the $V_{y,Rk,num}^{PZ}$ values are defined at the intersection between the y-axis and the line tangent to the residual post-plastic stiffness (see the red dotted lines in Figs. C-1(c) to C-32(c)). This residual post-plastic stiffness comes from the consideration in the Abaqus© software of the true stress-strain curve of the elastic, perfectly-plastic steel material, as described in Section 4.2.3.

The comparisons between the $V_{y,Rk,compl}^{PZ}$ analytical values and the $V_{y,Rk,num}^{PZ}$ numerical values were conducted on the basis of the performance indicator E and the colour code defined in Table 3-1. The following conclusions can be drawn from Table 4-21 regarding the performances of the complex analytical model:

- Generally speaking, the proposed complex analytical model seems to work well, as it features a high level of accuracy for 25 out of the 28 numerical simulations and a moderate to high level of accuracy for the remaining simulations;
- For the non-axially loaded joints (i.e. the categories I and II in Table 4-21), the relative errors E oscillate between -5 % and $+5$ %;
- For the axially loaded joints (i.e. the categories III and IV in Table 4-21), the model is a bit more conservative, almost all the relative errors E being negative.

These good performances from the complex analytical model are confirmed through graphical comparisons between the analytical and numerical results. These comparisons are provided in APPENDIX C for every single numerical simulation (see the dark blue broken curves and the light blue continuous curves in Figs. C-1(c) to C-32(c), respectively). From these figures, a good agreement can be observed between the analytical and numerical curves.

ii. In terms of $M - \Phi$ curves

Based on this new estimation of the plastic shear resistance of the PZ component, it was possible to re-evaluate the plastic resistance of the 32 joints considered in the present parametric study. This was done using the assembly procedure described in Eqs. (2-7) to (2-10). The results are presented in Table 4-22 for each numerical simulation in terms of the plastic bending moment resistance $M_{y,Rk,compl}^{j}$ and the expected plastic failure mode. From Table 4-22, it can be seen that 23 numerical simulations are characterized by a PZ plastic failure mode, while the nine remaining simulations are characterized by another plastic failure mode (either the CWC*/CWT for one of them or the CFB for eight of them).

Table 4-21. Comparisons between $V_{y,Rk,compl}^{PZ(V2)}$ (2nd version) and $V_{y,Rk,num}^{PZ}$.

Configuration	Category I (X="d", Y="/")			Category II (X="s", Y="/")		
	$V_{y,Rk,num}^{PZ}$ (kN)	$V_{y,Rk,compl}^{PZ(V2)}$ (kN)	E $(\%)$	$V_{y,Rk,num}^{PZ}$ (kN)	$V_{y,Rk,compl}^{PZ(V2)}$ (kN)	E $(\%)$
NR4-0-X-Y	293.0	303.8	3.69	280.0	290.5	3.75
NR4-1-X-Y	320.0	328.2	2.56	301.4	307.6	2.06
NR16-0-X-Y	800.0	808.3	1.04	756.0	773.1	2.26
NR16-1-X-Y	1,022.0	1,001.3	-2.03	886.7	875.5	-1.26
A-0-X-Y	330.0	328.7	-0.39	313.0	315.4	0.77
A-1-X-Y	352.0	348.0	-1.14	329.0	325.0	-1.22
B-0-X-Y	1,053.3	1,076.4	2.19	/	/	/
B-1-X-Y	1,076.0	1,104.9	2.69	/	/	/
Configuration	Category III (X="d", Y="0.5N_pl")			Category IV (X="s", Y="0.5N_pl")		
	$V_{y,Rk,num}^{PZ}$ (kN)	$V_{y,Rk,compl}^{PZ(V2)}$ (kN)	E $(\%)$	$V_{y,Rk,num}^{PZ}$ (kN)	$V_{y,Rk,compl}^{PZ(V2)}$ (kN)	E $(\%)$
NR4-0-X-Y	278.0	270.8	-2.59	260.0	258.5	-0.58
NR4-1-X-Y	301.3	295.2	-2.02	283.8	276.5	-2.57
NR16-0-X-Y	774.0	739.6	-4.44	703.3	706.4	0.44
NR16-1-X-Y	968.0	932.5	-3.67	847.5	814.2	-3.93
A-0-X-Y	308.6	287.1	-6.97	287.8	274.8	-4.52
A-1-X-Y	325.0	307.4	-5.42	307.1	285.0	-7.20
B-0-X-Y	983.3	955.8	-2.80	/	/	/
B-1-X-Y	1,005.0	985.8	-1.91	/	/	/

Table 4-22. Updated version of Table 4-6 based on the new complex analytical model for the PZ.

Configuration	Category I (X="d", Y="/")		Category II (X="s", Y="/")	
	$M_{y,Rk,compl}^{j}$ (kNm)	Plastic failure mode	$M_{y,Rk,compl}^{j}$ (kNm)	Plastic failure mode
NR4-0-X-Y	53.39	PZ	102.32	PZ
NR4-1-X-Y	57.65	PZ	108.64	PZ
NR16-0-X-Y	222.36	PZ	414.36	CWC^*/CWT
NR16-1-X-Y	275.06	PZ	486.65	PZ
A-0-X-Y	33.62	PZ	57.79	CFB
A-1-X-Y	35.68	PZ	57.79	CFB
B-0-X-Y	164.84	CFB	164.84	CFB
B-1-X-Y	164.84	CFB	164.84	CFB
Configuration	Category III (X="d", Y="0.5N_pl")		Category IV (X="s", Y="0.5N_pl")	
	$M_{y,Rk,compl}^{j}$ (kNm)	Plastic failure mode	$M_{y,Rk,compl}^{j}$ (kNm)	Plastic failure mode
NR4-0-X-Y	47.28	PZ	90.44	PZ
NR4-1-X-Y	51.54	PZ	96.75	PZ
NR16-0-X-Y	211.53	PZ	405.98	PZ
NR16-1-X-Y	266.70	PZ	467.92	PZ
A-0-X-Y	29.08	PZ	55.74	PZ
A-1-X-Y	31.14	PZ	57.70	PZ
B-0-X-Y	160.79	PZ	164.80	PZ
B-1-X-Y	164.84	CFB	164.84	CFB

These analytical predictions were graphically compared to the numerical $(M_B - \Phi)_{num}$ curves. The results are provided in APPENDIX C (see Fig. C-1(e) to Fig. C-32(e)), where several $M_B - \Phi$ curves are depicted:

- The analytical $(M^c - \phi^c)_{an}$ curves of the different activated components (where "c" stands for "CWC*", "CWT", "CFB" or "BFC"); the values of the $M^c_{y,Rk}$ associated to these components (excluding the PZ component) are given in Table C-1 to Table C-32 in APPENDIX C.
- The $(M^{PZ} - \gamma)_{an}$ curve of the new PZ component, which can be deduced from the $(V^{PZ} - \gamma)_{an}$ curve using Eq. (4-27) (resp. Eq. (4-28)) for exterior (resp. interior) joints. Eq. (4-27) (resp. Eq. (4-28)) has been obtained by isolating P in Eq. (B-8) (resp. Eq. (B-12)) and injecting this value in Eq. (B-20). It is a more complex version of Eq. (3-5).
- The $(M_B - \Phi)_{num}$ curve of each numerical simulation, which can be obtained through the procedure describes in APPENDIX B.2.
- The predicted $\left(M^j - \Phi\right)_{an}$ curve of the joint, which can be obtained as the minimum of the $(M^c - \phi^c)_{an}$ and $(M^{PZ} - \gamma)_{an}$ curves associated to the different activated components.

Comparisons between the analytical and the numerical curves show a very good agreement for the 23 numerical simulations characterized by a PZ plastic failure mode. The same conclusion applies to the numerical simulation characterized by a CWC*/CWT plastic failure mode. By contrast, for the remaining nine numerical simulations characterized by a CFB plastic failure mode, the prediction of the joint plastic bending resistance is much more conservative.

$$M^{PZ}_{Rk,compl} = 2 \cdot \frac{\cos\gamma}{\cos\gamma_1 \cdot \cos\gamma_2} \cdot d_b^* \cdot \frac{(L_c - d_b^*) \cdot \cos\gamma_2 + d_b^* \cdot \cos\gamma_1}{2 \cdot L_b \cdot L_c - 2 \cdot L_b \cdot d_b^* - d_c^* \cdot d_b^* + d_b^* \cdot (L_c - d_b^*) \cdot (\tan\gamma_2 + \tan\gamma_1)}$$
$$\cdot \left[V^{PZ}_{Rk,compl} - N_c \cdot \tan\gamma \cdot \frac{L_c - d_b^*}{(L_c - d_b^*) \cdot \cos\gamma_2 + d_b^* \cdot \cos\gamma_1}\right] \cdot L_b \cdot \cos\Phi \tag{4-27}$$

$$M^{PZ}_{Rk,compl} = \frac{\cos\gamma}{\cos\gamma_1 \cdot \cos\gamma_2} \cdot d_b^* \cdot \frac{(L_c - d_b^*) \cdot \cos\gamma_2 + d_b^* \cdot \cos\gamma_1}{2 \cdot L_b \cdot L_c - 2 \cdot L_b \cdot d_b^* - d_c^* \cdot d_b^*}$$
$$\cdot \left[V^{PZ}_{Rk,compl} - N_c \cdot \tan\gamma \cdot \frac{L_c - d_b^*}{(L_c - d_b^*) \cdot \cos\gamma_2 + d_b^* \cdot \cos\gamma_1}\right] \cdot L_b \cdot \cos\Phi \tag{4-28}$$

B. Validation against experimental results

As a second validation step, the performance of the new complex analytical model was assessed trough comparisons with the 12 experimental results on welded joints reported in Table 3-2. To this aim, the plastic shear resistance of the PZ was assessed analytically for each of the 12 test results, first in terms of $V_{y,Rk,compl}^{PZ}$ values. This was done applying Eqs. (4-3), (4-15), (4-21) and (4-22) and using the actual geometrical and mechanical properties given in Appendix A (see Fig. A-1(c),(d) to Fig. A-12(c),(d)) for the 12 relevant welded experimental results.

These $V_{y,Rk,compl}^{PZ}$ values were then assembled to obtain an analytical estimation of the plastic bending moment resistance $M_{y,Rk,compl}^{j}$ of the different welded joints considered in the present study. Since all of them exhibit a PZ plastic failure mode, Eq. (3-4) can be contemplated, where β and z_{eq} can be computed through Eqs. (3-3) and (2-5), respectively. The so-obtained $M_{y,Rk,compl}^{j}$ values are reported in Table 4-23 where they are compared to the experimental $M_{y,Rk,exp}^{j}$ values coming from Table 3-4. These comparisons are conducted using the performance indicator E and the colour code defined in Table 3-1. Graphical comparisons are also provided in Appendix A (see the red solid lines in Fig. A-1(e) to Fig. A-12(e)). For sake of completeness, the plastic collapse mechanism predicted by the model for each experimental result is also reported in Table 4-23.

These comparisons show that the new complex analytical model performs very well, as it displays a high level of accuracy for ten out of the twelve experimental results and a moderate level of accuracy for the two remaining experimental results. Moreover, it outperforms all other analytical models reported in Table 3-7 by providing a more coherent and physically founded estimation of the plastic shear resistance of the PZ.

Table 4-23. Comparisons between $M_{y,Rk,compl}^{j}$, $M_{y,Rk,simpl}^{j}$ and $M_{y,Rk,exp}^{j}$ for the 12 test results on welded joints reported in Table 3-2.

No.	Specimen	$M_{y,Rk,exp}^{j}$ (kNm)	$M_{y,Rk,compl}^{j}$ (kNm)	E (%)	$M_{y,Rk,simpl}^{j}$ (kNm)	E (%)	Plastic mechanism*
1	B1	868.4	842.2	-3.01	865.9	-0.28	5
2	NR2	58.8	58.9	0.24	57.7	-1.83	4
3	NR3	81.8	81.1	-0.81	79.2	-3.24	4
4	NR4	118.2	119.8	1.36	115.8	-2.04	4
5	NR7	158.1	166.3	5.22	164.2	3.86	4
6	BCC5-E	133.3	131.3	-1.52	123.8	-7.12	6
7	XU-W1	190.9	183.6	-3.81	170.1	-10.87	3
8	XU-CWP1	198.2	204.3	3.07	177.3	-10.54	3
9	E1.1	334.4	349.5	4.52	344.7	3.09	4
10	E1.2	328.2	349.5	6.49	344.7	5.05	4
11	CP-R-M	141.8	145.2	2.38	134.6	-5.11	1
12	No. 3	53.5	52.9	-1.19	52.6	-1.62	6
*See Table 4-16.							

4.3.2 Simplified analytical model

4.3.2.1 Contribution of the CWP

To facilitate the derivation of the contribution $V_{y,Rk,compl}^{CWP}$ of the CWP (see Eqs. (4-14) to (4-18)), it is proposed to replace the complex $\sigma_{n,M-N}$ and τ stress distributions presented in Fig. 4-11(b) and Fig. 4-12(b) respectively, by simpler ones, easier to integrate. These latter are given in Fig. 4-11(c) and Fig. 4-12(c) respectively. Regarding the $\sigma_{n,M-N}$ stress distribution, only the $\sigma_{n,N}$ stresses coming from the N_{CT} (resp. N_{CB}) axial load in the column, if any, are accounted for, as discussed in Section 4.3.1.1C. These latter are assumed to be uniformly distributed over the column flanges cross-sections (excluding the root fillets regions). Consequently, Eq. (4-14) expressing the level of axial load $n_{fc,T}^*$ in the column flanges can be replaced by Eq. (4-29), where $N_{pl,fc,Rk}$ is the axial strength of a rectangular column flange, excluding the root fillets region.

As regards the simplified τ stress distribution proposed in Fig. 4-12(b), it consists of a uniform distribution over the whole depth h_c of the column profile. In the presence of an axial load in the column, this uniform distribution is reduced over the area $A_{VC,2}^{simpl}$ to account for the $\tau - \sigma_{n,M-N}$ interaction in the column flanges. Consequently, the simplified analytical model for the prediction of the contribution $V_{y,Rk,simpl}^{CWP}$ of the CWP can be expressed through Eq. (4-29) to Eq. (4-33), A_{VC}^{simpl}, $A_{VC,1}^{simpl}$ and $A_{VC,2}^{simpl}$ being defined in Fig. 4-12(c):

$$n_{fc}^* = \frac{N_{fc,Ek}^*}{N_{pl,fc,Rk}} = \frac{N_c/2}{N_{pl,fc,Rk}} = \frac{\sigma_{n,N}}{f_y} \tag{4-29}$$

$$V_{y,Rk,simpl}^{CWP} = \chi_i \cdot \chi_n \cdot V_{y,Rk}^{CWP} \tag{4-30}$$

where:

$$\chi_i = \begin{cases} 0.95 & for\ exterior\ joints \\ 1.0 & for\ interior\ joints \end{cases} \tag{4-31}$$

$$\chi_n(= \chi_{n,N}) = \left[1 - \frac{A_{VC,2}^{simpl}}{A_{VC}^{simpl}} \cdot \left(1 - \sqrt{1 - \left(n_{fc}^*\right)^2}\right)\right] \tag{4-32}$$

$$V_{y,Rk}^{CWP} = A_{VC}^{simpl} \cdot \tau_y \tag{4-33}$$

In order to assess the validity of this new simplified model, the ratio $\hat{V}_{y,Rk,simpl}^{CWP}/\hat{V}_{y,Rk,compl}^{CWP}$ was plotted against the column flange thickness t_{fc} in Table 4-24 for all the American W-profiles and European HE- and IPE-profiles, where $\hat{V}_{y,Rk,simpl}^{CWP}$ (resp. $\hat{V}_{y,Rk,compl}^{CWP}$) is the simplified (resp. complex) formula for the prediction of the plastic shear resistance of the CWP with no stress interaction, i.e. χ_i and n_{fc}^* (resp. $n_{fc,T}^*$) are equal to respectively 1.0 and 0 in Eq. (4-31) and Eq. (4-32) (resp. Eq. (4-16) and Eq. (4-17)).

In Table 4-24, the W-, HE- and IPE-profiles which are relevant in the present study, i.e. those characterized by $0.55 \leq t_{wc}/t_{fc} \leq 0.62$, have been highlighted. In addition, a distinction is made between the profiles characterized by thin flanges, i.e. $t_{fc} \leq 40\ mm$, or thick flanges, i.e. $t_{fc} > 40\ mm$. The following observations can be made from Table 4-24:

- For all European profiles and for the American "thin flanges" W-profiles, the ratio $\hat{V}_{y,Rk,simpl}^{CWP}/\hat{V}_{y,Rk,compl}^{CWP}$ oscillates around 1.0. Therefore, $V_{y,Rk,simpl}^{CWP}$ can be used instead of $V_{y,Rk,compl}^{CWP}$.

- By contrast, for the American "thick flanges" W-profiles, the ratio $\hat{V}_{y,Rk,simpl}^{CWP}/\hat{V}_{y,Rk,compl}^{CWP}$ significantly diverges from 1.0 with increasing flange thickness. This observation is in line with the conclusion drawn in ([52], [57], [58]). Thus, it is suggested to keep the complex definition of $V_{y,Rk,compl}^{CWP}$ for this range of W-profiles.

Based on these conclusions, the simplified analytical model for the prediction of the plastic shear resistance $V_{y,Rk,simpl}^{CWP}$ of the CWP can be validated against the 28 numerical results, similarly to what was done with the complex analytical model. This is done in Table 4-25 where it can be seen that the simplified analytical model features a high level of accuracy for all the numerical simulations considered in the present study: the relative error E between the numerical results and the analytical values varies from -4.56% to 2.87%.

Table 4-24. Comparisons between $\hat{V}_{y,Rk,simpl}^{CWP}$ and $\hat{V}_{y,Rk,compl}^{CWP}$ for the relevant US W-profiles and EU HE- and IPE-profiles.
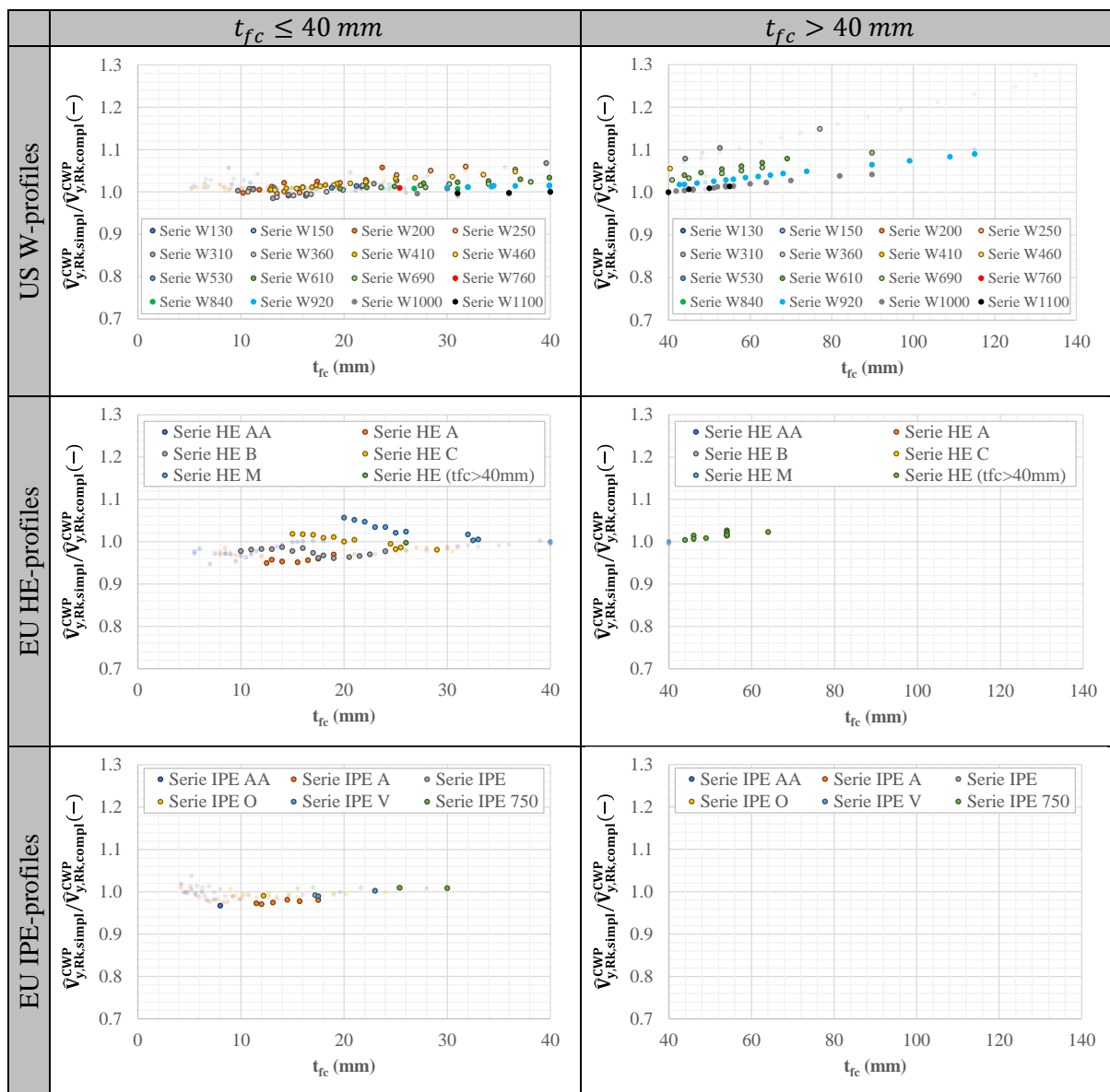
4.3.2.2 Contribution of the SE

Regarding the derivation of the contribution $\Delta V_{y,Rk,compl}^{SE}$ of the SE, two simplifications are proposed with respect to the complex analytical model presented in Eqs. (4-23) to (4-26). The first one consists in replacing, the plastic moment resistance of a T-shaped column flange (resp. beam flange), i.e. $M_{pl,fc,T,Rk}$ (resp. $M_{pl,fb,T,Rk}$) in Eq. (4-25), by the plastic moment resistance of a rectangular column flange (resp. beam flange), i.e. $M_{pl,fc,Rk}$ (resp. $M_{pl,fb,Rk}$). This is shown in Eq. (4-34). Secondly, the reduction factor $\Delta\chi_n$ in Eq. (4-26) has been modified accordingly (see Eq. (4-35)), where n_{fc}^* (resp. n_{fb}^*) is the level of axial load in the column (resp. beam) flanges, excluding the root fillets region (see Eqs. (4-36) to (4-37)).

$$
M\Big|_{\substack{pl,fc,Rk \\ pl,fb,Rk \\ pl,st,Rk}} = \Delta\chi_n \cdot \widehat{M}\Big|_{\substack{pl,fc,Rk \\ pl,fb,Rk \\ pl,st,Rk}}
\tag{4-34}
$$

Where:

$$
\Delta\chi_n\big(= \Delta\chi_{n,N}\big) = \left[1 - \left(n^*_{\substack{fc \\ fb \\ st}}\right)^2\right]
\tag{4-35}
$$

With:

$$
N_{fc,Ek}^* = \frac{N_c}{2} \quad \rightarrow \quad n_{fc}^* = \frac{N_{fc,Ek}^*}{N_{pl,fc,Rk}}
\tag{4-36}
$$

$$
N^*_{\substack{fb,Ek \\ st,Ek}} = \frac{N_b}{2} = 0 \quad \rightarrow \quad n^*_{\substack{fb \\ st}} = 0
\tag{4-37}
$$

These two simplifications tend to decrease (sometimes significantly) the contribution $\Delta V_{y,Rk,simpl}^{SE}$ with respect to the contribution $\Delta V_{y,Rk,compl}^{SE}$. This is shown in Table 4-26 where the relative error E between $\Delta V_{y,Rk,simpl}^{SE}$ and $\Delta V_{y,Rk,compl}^{SE}$ oscillates between -14.7% and -33.9%. Although the contribution of the SE rarely exceeds $25\% - 30\%$ of the total plastic shear resistance of the PZ, the simplified but conservative estimate $\Delta V_{y,Rk,simpl}^{SE}$ proposed in this Section 4.3.2.2 will lead to conservative predictions for the plastic shear resistance $V_{y,Rk,simpl}^{PZ}$ of the PZ. This will be demonstrated in the following Section 4.3.2.3.

Table 4-25. Comparisons between $V_{y,Rk,simpl}^{CWP}$ and $V_{y,Rk,num}^{CWP}$.

Configuration	Category I (X="d", Y="/")			Category II (X="s", Y="/")		
	$V_{y,Rk,num}^{CWP}$ (kN)	$V_{y,Rk,simpl}^{CWP}$ (kN)	E (%)	$V_{y,Rk,num}^{CWP}$ (kN)	$V_{y,Rk,simpl}^{CWP}$ (kN)	E (%)
NR4-0-X-Y	256.3	262.3	2.34	251.9	249.2	-1.07
NR4-1-X-Y	258.8	262.3	1.35	253.7	249.2	-1.77
NR16-0-X-Y	684.4	676.4	-1.17	657.1	642.5	-2.22
NR16-1-X-Y	701.9	676.4	-3.63	668.6	642.5	-3.90
A-0-X-Y	268.5	262.3	-2.31	255.2	249.2	-2.35
A-1-X-Y	270.1	262.3	-2.89	261.1	249.2	-4.56
B-0-X-Y	851.2	836.2	-1.76	/	/	/
B-1-X-Y	851.6	836.2	-1.81	/	/	/
Configuration	Category III (X="d", Y="0.5N_{pl}")			Category IV (X="s", Y="0.5N_{pl}")		
	$V_{y,Rk,num}^{CWP}$ (kN)	$V_{y,Rk,simpl}^{CWP}$ (kN)	E (%)	$V_{y,Rk,num}^{CWP}$ (kN)	$V_{y,Rk,simpl}^{CWP}$ (kN)	E (%)
NR4-0-X-Y	244.1	251.1	2.87	233.4	238.5	2.19
NR4-1-X-Y	245.9	251.1	2.11	239.4	238.5	-0.38
NR16-0-X-Y	657.5	658.1	0.09	619.6	625.2	0.90
NR16-1-X-Y	672.6	658.1	-2.16	638.1	625.2	-2.02
A-0-X-Y	252.8	251.1	-0.67	238.0	238.5	0.21
A-1-X-Y	254.4	251.1	-1.30	245.7	238.5	-2.93
B-0-X-Y	804.0	810.4	0.80	/	/	/
B-1-X-Y	811.6	810.4	-0.15	/	/	/

Table 4-26. Comparisons between $\Delta V_{y,Rk,simpl}^{SE}$ and $\Delta V_{y,Rk,compl}^{SE}$.

Configuration	Category I (X="d", Y="/")			Category II (X="s", Y="/")		
	$\Delta V_{y,Rk,compl}^{SE}$ (kN)	$\Delta V_{y,Rk,simpl}^{SE}$ (kN)	E (%)	$\Delta V_{y,Rk,compl}^{SE}$ (kN)	$\Delta V_{y,Rk,simpl}^{SE}$ (kN)	E (%)
NR4-0-X-Y	39.5	30.1	-23.8	39.5	30.1	-23.8
NR4-1-X-Y	63.9	53.7	-16.0	57.5	41.9	-27.1
NR16-0-X-Y	109.9	81.5	-25.8	109.9	81.5	-25.8
NR16-1-X-Y	302.8	258.4	-14.7	217.7	169.9	-22.0
A-0-X-Y	65.6	50.1	-23.6	65.6	50.1	-23.6
A-1-X-Y	85.9	63.5	-26.1	75.8	56.8	-25.1
B-0-X-Y	221.2	170.2	-23.06	/	/	/
B-1-X-Y	251.2	191.2	-23.9	/	/	/
Configuration	Category III (X="d", Y="0.5N_{pl}")			Category IV (X="s", Y="0.5N_{pl}")		
	$\Delta V_{y,Rk,compl}^{SE}$ (kN)	$\Delta V_{y,Rk,simpl}^{SE}$ (kN)	E (%)	$\Delta V_{y,Rk,compl}^{SE}$ (kN)	$\Delta V_{y,Rk,simpl}^{SE}$ (kN)	E (%)
NR4-0-X-Y	24.6	16.3	-33.7	24.6	16.3	-33.7
NR4-1-X-Y	49.0	39.9	-18.6	42.7	28.1	-34.2
NR16-0-X-Y	75.7	50.4	-33.4	75.7	50.4	-33.4
NR16-1-X-Y	268.6	227.3	-15.4	183.5	138.8	-24.4
A-0-X-Y	41.0	27.1	-33.9	41.0	27.1	-33.9
A-1-X-Y	61.3	40.5	-33.9	51.1	33.8	-33.9
B-0-X-Y	142.6	97.1	-31.9	/	/	/
B-1-X-Y	172.6	118.2	-31.5	/	/	/

4.3.2.3 Validation

A. Validation against numerical results

Based on the simplifications proposed in Section 4.3.2.1 (see Table 4-25) and Section 4.3.2.2 (see Table 4-26), one can derive the plastic shear resistance $V_{y,Rk,simpl}^{PZ}$ for the 28 numerical simulations considered in the present parametric study. The results are summarized in Table 4-27, where they are compared to the numerical values $V_{y,Rk,num}^{PZ}$ (coming from Table 4-21). These comparisons are conducted on the basis of the performance indicator E and the colour code defined in Table 3-1. The following conclusions can be drawn from Table 4-27 regarding the performances of the simplified analytical model:

- For non-axially loaded joints (i.e. categories I and II in Table 4-27), the proposed simplified model seems to work well, as it features a high level of accuracy for eight out of the 14 numerical simulations and a moderate level of accuracy for the six remaining simulations.
- For the axially loaded joints (i.e. categories III and IV in Table 4-27), as expected, the results are slightly more conservative, with four numerical results belonging to the high accuracy category, eight belonging to the moderate accuracy category and two belonging to the low accuracy category. The relative error E varies from -1.98% to -11.38%.
- In addition, it can be noticed that all the relative errors E are negative, which means that the simplified analytical model remains on the safe side.

Table 4-27. Comparisons between $V_{y,Rk,simpl}^{PZ}$ and $V_{y,Rk,num}^{PZ}$.

Configuration	Category I (X="d", Y="/")			Category II (X="s", Y="/")		
	$V_{y,Rk,num}^{PZ}$ (kN)	$V_{y,Rk,simpl}^{PZ}$ (kN)	E $(\%)$	$V_{y,Rk,num}^{PZ}$ (kN)	$V_{y,Rk,simpl}^{PZ}$ (kN)	E $(\%)$
NR4-0-X-Y	293.0	292.5	-0.18	280.0	279.4	-0.23
NR4-1-X-Y	320.0	316.1	-1.23	301.4	291.2	-3.40
NR16-0-X-Y	800.0	757.8	-5.27	756.0	724.0	-4.23
NR16-1-X-Y	1,022.0	934.7	-8.54	886.7	812.5	-8.37
A-0-X-Y	330.0	312.5	-5.31	313.0	299.4	-4.36
A-1-X-Y	352.0	325.9	-7.42	329.0	306.1	-6.97
B-0-X-Y	1,053.3	1,006.4	-4.45	/	/	/
B-1-X-Y	1,076.0	1,027.5	-4.51	/	/	/
Configuration	Category III (X="d", Y="0.5N$_{pl}$")			Category IV (X="s", Y="0.5N$_{pl}$")		
	$V_{y,Rk,num}^{PZ}$ (kN)	$V_{y,Rk,simpl}^{PZ}$ (kN)	E $(\%)$	$V_{y,Rk,num}^{PZ}$ (kN)	$V_{y,Rk,simpl}^{PZ}$ (kN)	E $(\%)$
NR4-0-X-Y	278.0	267.4	-3.81	260.0	254.9	-1.98
NR4-1-X-Y	301.3	291.0	-3.42	283.8	266.6	-6.04
NR16-0-X-Y	774.0	708.4	-8.47	703.3	675.5	-3.95
NR16-1-X-Y	968.0	885.3	-8.54	847.5	764.0	-9.85
A-0-X-Y	308.6	278.2	-9.84	287.8	265.7	-7.69
A-1-X-Y	325.0	291.6	-10.27	307.1	272.4	-11.31
B-0-X-Y	983.3	907.5	-7.71	/	/	/
B-1-X-Y	1,005.0	928.6	-7.60	/	/	/

B. Validation against experimental results

As a second validation step, the 12 experimental results on welded joints reported in Table 3-2 were also compared to the new simplified analytical model, to validate the good performances of the latter. To this aim, the plastic shear resistance of the PZ was assessed analytically for each of the 12 test results, first in terms of $V_{y,Rk,simpl}^{PZ}$ values. This was done applying the simplifications presented in Sections 4.3.2.1 and 4.3.2.2 and using the actual geometrical and mechanical properties given in Appendix A (see Fig. A-1(c),(d) to Fig. A-12(c),(d)) for the 12 relevant experimental results.

These $V_{y,Rk,simpl}^{PZ}$ values were then assembled to obtain an analytical estimation of the plastic bending moment resistance $M_{y,Rk,simpl}^{j}$ of the different welded joints, thereby allowing comparisons with the $M_{y,Rk,exp}^{j}$ experimental observations reported in Table 3-4. Since all the test results exhibit a PZ plastic failure mode, the simplified assembly formula given in Eq. (3-4) can be contemplated, β being the transformation parameter which is computed according to Eq. (3-3) and z_{eq} the equivalent lever arm obtained from Eq. (2-5). The so-derived 12 $M_{y,Rk,simpl}^{j}$ values are reported in Table 4-23, where they are compared to the experimental $M_{y,Rk,exp}^{j}$ values. These comparisons are conducted using the performance indicator E and the colour code defined in Table 3-1. Graphical comparisons are also provided in Appendix A (see the red solid lines in Fig. A-1(f) to Fig. A-12(f)).

These comparisons show that the model exhibits a high level of accuracy for seven of the experimental results, a moderate level of accuracy for three of them and a low level of accuracy for the remaining two. The model remains on the safe side for ten out of the 12 results, with all the relative errors E oscillating between −10.87% and +5.05%. These error levels can be seen as acceptable and are similar to the ones obtained from the comparisons with the numerical results (see Table 4-27).

Proposal for amendment of the prEN 1993-1-8:

N.B.: The final proposal for the improved PZ model, suggested for inclusion in the forthcoming prEN 1993-1-8, is summarized in Appendix F. It includes amendments of the current EN 1993-1-8 expressions for the initial stiffness and plastic resistance and a proposal for a ductility criterion.

For the prediction of the plastic shear resistance of the PZ in welded joints, it is proposed to replace the current EN 1993-1-8 expression given in Section 2.3.3.2 by the simplified analytical model developed in the present Section 4.3.2. This proposal is summarized in Appendix F.2. It is noteworthy that two minor simplifications were introduced to make the proposed expressions as simple as possible. Firstly, in the derivation of the V_{y,Rk,EU^*}^{CWP} contribution (see Eq. (F-2)), a 0.9 generic coefficient has been used to account for the $\tau - \sigma_i$ and $\tau - \sigma_n$ stress interactions in the CWP. This coefficient replaces the χ_i and χ_n reduction factors defined in Eqs. (4-31) and (4-32). Secondly, the $\Delta\chi_n$ reduction coefficient accounting in Eq. (4-34) for the M-N interaction in the column flanges has been neglected in the new proposal (i.e. it was set equal to 1.0 in Eq. (F-4)). This simplification is assumed to compensate for the non-consideration of the root fillets region in the derivation of $M_{pl,fc,Rd}$, $M_{pl,fb,Rd}$ and $M_{pl,st,Rd}$.

This new proposed formula, referred to as the EU* formula, has been validated against the 12 experimental results on welded joints reported in Table 3-2. The results are reported in Table 3-8, where they are compared to the experimental evidence on the one hand and to the EU and US predictions on the other hand, using the performance indicator E and the colour code defined in Table 3-1. Graphical comparisons are also provided in Appendix A.1 (see the red broken curves in Figs. A-1(f) to A-12(f)). These comparisons show that, despite being slightly conservative, the proposed EU* formula performs well, with a relative error E ranging from −18.44% to +4.99%. It clearly outperforms the current EU and US models shown in Section 3.3.2 to provide unsafe predictions.

4.4 CONCLUSIONS

In the present CHAPTER 4, a new sophisticated analytical model is proposed for the prediction of the plastic shear resistance of the PZ, in the case of welded beam-to-column joints under monotonic loading only. This model has been developed upon the deep understanding of the physical phenomena governing the plastic shear resistance of the PZ. This understanding has been gained through the analysis of the numerical results coming from an extensive parametric study carried out with the Abaqus© software. This parametric study investigated the influence of four main parameters on the plastic shear resistance of the PZ, namely: (i) the spread of yielding within the CWP, (ii) the type of plastic collapse mechanism which actually develops in the SE and (iii)-(iv) the $\tau - \sigma_i$ and $\tau - \sigma_{n,M-N}$ stress interactions. Another outcome from the parametric study is the proposal of a robust methodology for the extraction of the $(V - \gamma)_{num}$ curves associated to the CWP, SE and PZ. In all the 32 numerical simulations, a simplified elastic, perfectly-plastic material law was used in order to facilitate the derivation and the validation of the new analytical model. The main features of this new analytical model are summarized here below:

- this model accounts for both contributions $V_{y,Rk,compl}^{CWP}$ and $\Delta V_{y,Rk,compl}^{SE}$ of the CWP and the SE, separately;
- the contribution $V_{y,Rk,compl}^{CWP}$ of the CWP has been developed based on the analysis and the integration of the actual shear stress distribution in the CWP at yielding;
- the contribution $\Delta V_{y,Rk,compl}^{SE}$ of the SE has been derived based on the analysis of the collapse mechanism which actually develops within the SE;
- the $\tau - \sigma_i$ interaction has been taken into account in the contribution $V_{y,Rk,compl}^{CWP}$ only, through the use of a reduction factor χ_i. This interaction has to be accounted for in the case of exterior joint configurations only;
- the $\tau - \sigma_{n,M-N}$ interaction has been taken into account in both contributions $V_{y,Rk,compl}^{CWP}$ and $\Delta V_{y,Rk,compl}^{SE}$ through the use of two reduction factors, $\chi_{n,M-N}$ and $\Delta \chi_{n,M-N}$, eventhough it was observed that most of the axial load is carried by the column flanges. This interaction has to be accounted for in the presence of an axial load in the column only.

The so-developed analytical model has proven to work well through comparisons with numerical and experimental results characterized by a PZ plastic failure mode. This way, it outperforms the existing complex models introduced in CHAPTER 2. The author recommends the use of this complex model for scientific purposes. In addition, a simplified version of this model has also been proposed in view of its integration in the forthcoming prEN 1993-1-8 pre-normative document. Despite being more conservative, this simplified model shows good performance and outperforms the EU and US design criteria, currently prescribed in the EN 1993-1-8 and AISC normative documents, and which were shown to provide unsafe predictions in many cases.

It should be recalled that the range of validity for the model developed in the present CHAPTER 4 is so far limited to column profiles characterized by a web-to-flange thickness ratio $t_{wc}/t_{fc} \in [0.55 - 0.62]$, and to axial loads $N_c \leq 0.5 \cdot N_{pl,c}$, $N_{pl,c}$ being the axial capacity of the column profile. Based on the knowledge acquired in this CHAPTER 4, the following CHAPTER 5 tackles the problem of prediction of the full non-linear behaviour of the PZ up to failure, again in the case of welded joints only; the extension of the models to PZs in bolted joints being subsequently addressed in CHAPTER 6.

CHAPTER 5 Characterization of the panel zone full-range behaviour up to failure

5.1 INTRODUCTION

5.1.1 Objectives of the Chapter

CHAPTER 5 addresses *the problem of prediction of the deformation capacity of the sheared PZ*, which was identified in CHAPTER 3. More precisely, it focuses on the development and validation of a full-range constitutive model for the prediction of the full non-linear response of the PZ up to failure. This model will be built based on the knowledge acquired in CHAPTER 4.

5.1.2 Scope of the Chapter

The scope of this CHAPTER 5 is similar to CHAPTER 4 (see Section 4.1.2), i.e. exterior and interior welded joints, with beams of equal depth, under monotonic loading only. In this way, the shear force V_{Ek}^{PZ} acting on the PZ can be assumed constant over the whole depth d_b^* of the PZ, and is therefore easy to derive through Eq. (2-1). Moreover, the occurrence of any other failure mode in the connecting elements (i.e. bolts in tension, endplates in bending…) is avoided. The welded joints considered in this CHAPTER 5 also satisfy Eq. (2-39), thereby preventing the occurrence of the CWP shear buckling in the elastic range. The extension of the model to PZs in bolted joints will be addressed in CHAPTER 6.

The two joint configurations considered in the present CHAPTER 5 were already presented in Fig. 4-1 and Fig. 4-2 (see CHAPTER 4), but are recalled in Fig. 5-1 and Fig. 5-2, for sake of clarity. They are simply supported and the beams are loaded in such a way that the PZ becomes the governing component of the joint response. This is illustrated in the M-N-V diagrams in Fig. 5-1(b) and Fig. 5-2(b), where the PZ is subjected to significant shear. In addition, a vertical axial load N_c can be applied to the column profiles, with a magnitude of up to $0.5 \cdot N_{pl,c}$, $N_{pl,c}$ being the axial capacity of the column profile. By contrast, the beams are assumed to transfer no horizontal axial load N_b. For interior joints, the unbalanced bending moments in the beams are assumed to be equal (i.e. $|M_{BL}| = |M_{BR}|$). Finally, all the column profiles considered in the present study are characterized by a column web-to-flange thickness ratio oscillating between 0.55 and 0.62, which is the range of validity for all the developments presented in CHAPTER 4.
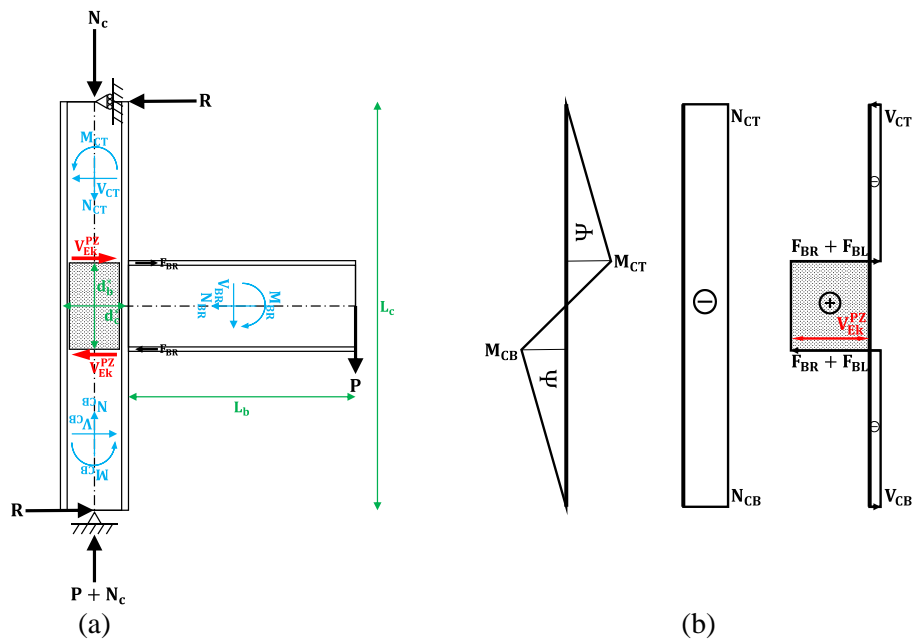
Fig. 5-1. Exterior welded joint: (a) loading conditions maximizing shear in the PZ and (b) resulting M-N-V diagrams in the column.
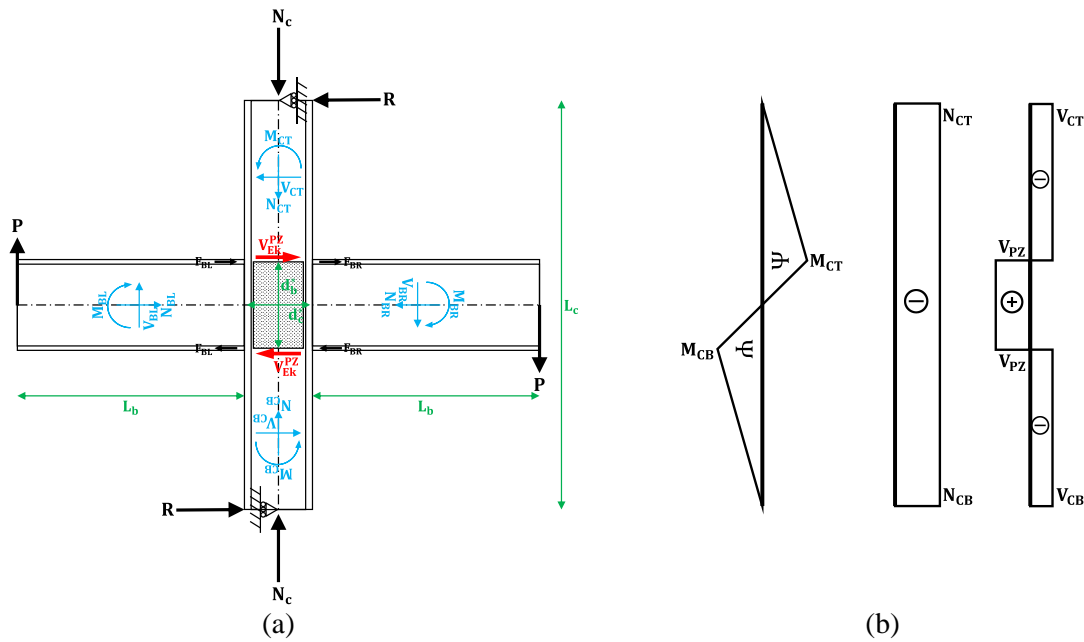
Fig. 5-2. Interior welded joint: (a) loading conditions maximizing shear in the PZ and (b) resulting M-N-V diagrams in the column.

5.1.3 Outline of the Chapter

To derive the new full-range constitutive model for the PZ, CHAPTER 5 has been organised as follows: (i) modification of the numerical models developed in CHAPTER 4 to simulate the full non-linear response of the PZ (see Section 5.2.2); (ii) development of an extensive campaign of numerical simulations, which will be used as validation tool for the analytical models (see Sections 5.2.3 and 5.2.4); (iii) development and validation of a complex analytical model against numerous numerical and experimental results (see Section 5.3.1); and (iv) simplification of this complex model in view of its possible integration in design codes (Section 5.3.2).

5.2 NUMERICAL PART

5.2.1 Introduction

The conclusions from CHAPTER 3 (see Section 3.4) highlighted that the scientific literature contains very few experimental results characterized by a PZ failure mode or at least a significant PZ deformation. This is a concern in view of the validation of the full-range constitutive models developed in the present CHAPTER 5.

Therefore, the main role of the FE analysis in the present study will be dedicated to the generation of a large number of FE results characterized by a PZ failure mode or a significant PZ deformation, with the aim of validating these full-range analytical models.

To this end, the numerical models developed in CHAPTER 4 (see Section 4.2.2 and Section 4.2.3) for the prediction of the plastic shear resistance of the PZ have been re-used and adapted to simulate the full non-linear response of the PZ. For sake of clarity, the main characteristics of these models are briefly recalled in Section 5.2.2.1 while the main changes to these original models are presented in Section 5.2.2.2. These changes include (i) introducing an initial shear imperfection in the web of the PZ, (ii) substituting the fictitious elastic, perfectly-plastic material law with the actual full material law and (iii) simulating the material damage and fracture.

5.2.2 FE modelling

5.2.2.1 Original FE models

The original FE models developed in CHAPTER 4 consist of four exterior welded joints, named NR4, NR16, A and B, respectively. The column and beam profiles are recalled in Table 5-1. For these profiles, the nominal geometric properties were used. The columns were simply supported (similarly to Fig. 5-1(a)) and had a length L_c of $4\ m$. The beams were welded at mid-height of the columns (the fillet welds were not modelled explicitly) and the length L_b of the beams was such that the distance between the beams end and the columns centreline was $1.5\ m$.

The Young's modulus and the Poisson's ratio were taken equal to $210{,}000\ MPa$ and 0.3, respectively. Furthermore, to facilitate the derivation of the plastic shear resistance of the PZ, all the members in CHAPTER 4 were assigned a fictitious elastic, perfectly-plastic material law, using the nominal yield strength f_y of the steel grade $S355$.

For all the models, the PZ region and the column supports were densely meshed, using fully-integrated eight-node brick elements (C3D8). However, to reduce the computation time, a coarser mesh made of eight-node brick elements with reduced integration (C3D8R) was adopted in all the other parts of the models. The root fillets were modelled using six-node triangular prisms with full integration (C3D6). Four finite elements were placed throughout the webs and flanges thicknesses.

Finally, the beams end section was properly restrained against out-of-plane displacement and a monotonic displacement history was imposed on the beams tip, using a general static analysis.

Table 5-1. Details of the numerical models used in the parametric study.

Model	Column profile	Beam profile	$t_{st}\ (mm)$	$N_c\ (kN)$	$t_{wc}/t_{fc}\ (-)$
NR4	HEB160	IPE330	12	1000	0.615
NR16	HEB300	HEB500	30	2500	0.579
A	HEB160	IPE200	10	1000	0.615
B	HEB340	IPE300	12	3000	0.558

5.2.2.2 Modifications of the FE models

A. *Initial geometric imperfection*

The first modification of the original models consists in introducing an equivalent geometric imperfection in the column web, following the procedure proposed in [123]. This equivalent imperfection is designed to cover the effect of both the geometrical imperfections and the residual stresses and it is shaped to correspond to the expected failure mode, namely the shear buckling of the CWP. This imperfection shape was obtained from the local buckling mode associated with the shear buckling of the CWP, obtained from a preliminary linear buckling analysis (LBA) performed on the "perfect" model. The magnitude of the initial imperfection was fixed to "$d_c/200$", d_c being the clear depth of the column cross-section (as recommended in [123]).

B. *Full-range material law and damage model*

Secondly, the material law was modified to account for both material strain-hardening and damage. In comparison with the models used in CHAPTER 4, the $S355$ steel grade was kept for all the members, but the fictitious elastic, perfectly-plastic material law was replaced by a simplified quad-linear model to represent the complete material response. Although the EN 1993-1-14 material model used in Section 4.2.2.1 was an option, it was decided to use a simpler one in the numerical simulations, known as the ECCS material model [124]. The main parameters of this model are given in Table 5-2. This model assumes the post-plastic strain ε_{pp} at the onset of strain-hardening equal to $10 \cdot \varepsilon_y$, the post-plastic modulus E_{pp} equal to $E/50$ and the strain at the onset of necking ε_n equal to 0.18. The material law which was reconstructed with this model is presented in Fig. 5-3(a) in terms of engineering stress-strain curve (see the black solid curve) and the main values of the parameters are given in Table 5-3. They were obtained, keeping the Young's modulus equal to 210,000 MPa and using the nominal values for the yield strength f_y and the ultimate strength f_u.

Table 5-2. Definition of the parameters used in the ECCS material model (engineering stress-strain curve).

| Parameters			Formula	Units
E	(Young's modulus)	=	210,000	(MPa)
σ_y	(yield strength)	=	f_y	(MPa)
ε_y	(yield strain)	=	$\dfrac{\sigma_y}{E}$	$(-)$
ΔE	(initial modulus increment)	=	$\dfrac{\sigma_{pp} - \sigma_y}{\varepsilon_{pp} - \varepsilon_y}$	(MPa)
σ_{pp}	(post-plastic strength)	=	f_y	(MPa)
ε_{pp}	(post-plastic strain)	=	$10 \cdot \varepsilon_y$	$(-)$
$\Delta\varepsilon_y$	(yield strain increment)	=	$\varepsilon_{pp} - \varepsilon_y$	$(-)$
$\Delta\sigma_y$	(yield strength increment)	=	$\sigma_{pp} - \sigma_y$	(MPa)
E_{pp}	(post-plastic modulus)	=	$\dfrac{E}{50}$	(MPa)
σ_u	(ultimate strength)	=	f_u	(MPa)
ε_u	(ultimate strain)	=	$\varepsilon_{pp} + \dfrac{f_u - f_y}{E_{pp}}$	$(-)$
ΔE_{pp}	(post-plastic modulus increment)	=	$\dfrac{\sigma_n - \sigma_u}{\varepsilon_n - \varepsilon_u}$	(MPa)
σ_n	(strength at the onset of necking)	=	f_u	(MPa)
ε_n	(strain at the onset of necking)	=	0.18	$(-)$
$\Delta\varepsilon_u$	(ultimate strain increment)	=	$\varepsilon_n - \varepsilon_u$	$(-)$
$\Delta\sigma_u$	(ultimate strength increment)	=	$\sigma_n - \sigma_u$	(MPa)
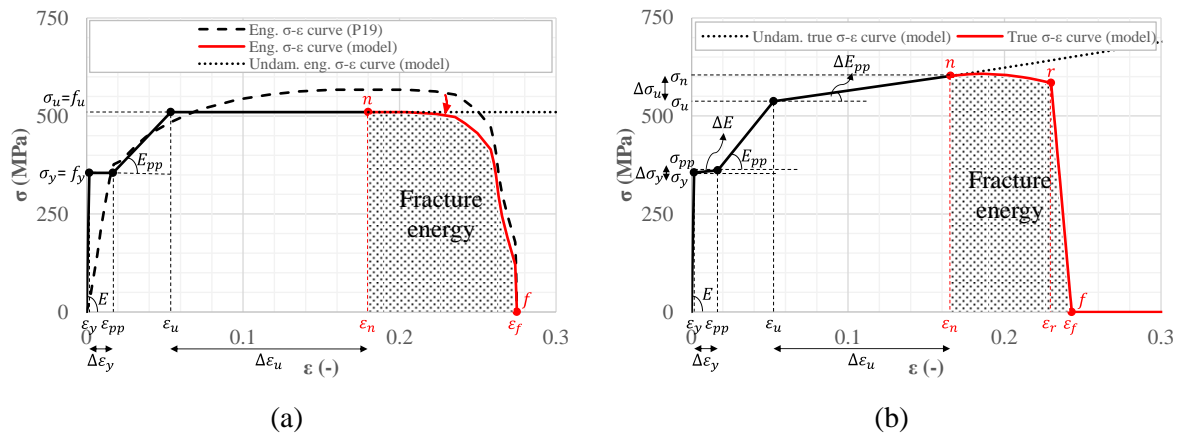
Fig. 5-3. Reconstructed material law (ECCS material model) used in the numerical simulations: (a) engineering stress-strain curve and (b) true stress-strain curve.

Table 5-3. Values of the parameters used in the fictitious material law defined in Fig. 5-3.

Parameters		Engineering stress-strain curve		True stress-strain curve		Units
E	(Young's modulus)	=	210,000	=	210,000	(MPa)
σ_y	(yield strength)	=	355	=	355	(MPa)
ε_y	(yield strain)	=	0.00169	=	0.00169	$(-)$
ΔE	(initial modulus increment)	=	0	=	358	(MPa)
σ_{pp}	(post-plastic strength)	=	355	=	361	(MPa)
ε_{pp}	(post-plastic strain)	=	0.0169	=	0.0168	$(-)$
$\Delta\varepsilon_y$	(yield strain increment)	=	0.0152	=	0.0151	$(-)$
$\Delta\sigma_y$	(yield strength increment)	=	0	=	6	(MPa)
E_{pp}	(post-plastic modulus)	=	4,200	=	4,950	(MPa)
σ_u	(ultimate strength)	=	510	=	537	(MPa)
ε_u	(ultimate strain)	=	0.054	=	0.0524	$(-)$
ΔE_{pp}	(post-plastic modulus increment)	=	0	=	569	(MPa)
σ_n	(strength at the onset of necking)	=	510	=	602	(MPa)
ε_n	(strain at the onset of necking)	=	0.18	=	0.166	$(-)$
$\Delta\varepsilon_u$	(ultimate strain increment)	=	0.126	=	0.1136	$(-)$
$\Delta\sigma_u$	(ultimate strength increment)	=	0	=	65	(MPa)
ε_r	(rupture strain)	=	/	=	/	$(-)$
ε_f	(fracture strain)	=	0.275	=	0.243	$(-)$

Regarding the softening part of the material behaviour, which is defined as the material response from the onset of necking ("n") up to the fracture ("f") of the material, it was derived based on a coupon test result taken from the scientific literature [125]. This coupon test, named P19, was performed at the University of Timisoara within the framework of an experimental campaign on T-stubs, and it is characterised by mechanical properties which are very close to the nominal ones, as depicted in Fig. 5-3(a) (see the black broken curve). Therefore, the softening part was extracted from the coupon test stress-strain curve and reattached to the quad-linear material model considered in the present study. This is illustrated in Fig. 5-3(a) (see the final red part of the curve).

This quad-linear hardening plus non-linear softening material law, defined in Fig. 5-3(a), was used as the reference material law for all the simulations carried out in the present CHAPTER 5. To comply with the Abaqus© formalism, the quad-linear part of the engineering stress-strain curve (see the black solid curve in Fig. 5-3(a)), describing the hardening behaviour of the material, was implemented in Abaqus© as an undamaged true stress-strain curve, using Eq. (4-1) and Eq. (4-2). This curve is reported in Fig. 5-3(b) (see the black dashed curve) and the main parameters are given in Table 5-3. By contrast, the non-linear softening part of the engineering stress-strain curve (see the red continuous curve in Fig. 5-3(b)), describing the material damage, was implemented in Abaqus© using the ductile damage model. This model is presented in Fig. 5-4 and requires the definition of a damage initiation criterion and a damage evolution law, developed hereafter (see Eqs. (5-1) and (5-2)).

$$\bar{\varepsilon}_0^{pl}(\eta) = \varepsilon_n^{pl}.\exp\left[-1.5\cdot\left(\eta-\frac{1}{3}\right)\right] \tag{5-1}$$

$$\sigma_i = (1-D_i)\cdot\bar{\sigma}_i \Rightarrow D_i = 1-\frac{\sigma_i}{\bar{\sigma}_i} \tag{5-2}$$

$$\text{with } \sigma_i = \begin{cases} \overline{\bar{\sigma}_i} & i \leq n \\ \underbrace{W\cdot(a\cdot\varepsilon_i+b)}_{linear\ law} + \underbrace{(1-W)\cdot(K\cdot[\varepsilon_i]^n)}_{power\ law} & i > n \end{cases} \tag{5-3}$$

$$\text{and } \begin{pmatrix} a \\ b \\ n \\ K \end{pmatrix} = \begin{pmatrix} \frac{\sigma_n}{a\cdot(1-n)} \\ \varepsilon_n \\ a/n^n \end{pmatrix} \tag{5-4}$$

$$\bar{u}_i^{pl} = L_E\cdot\left(\varepsilon_i^{pl}-\varepsilon_n^{pl}\right), \quad i \geq n \tag{5-5}$$
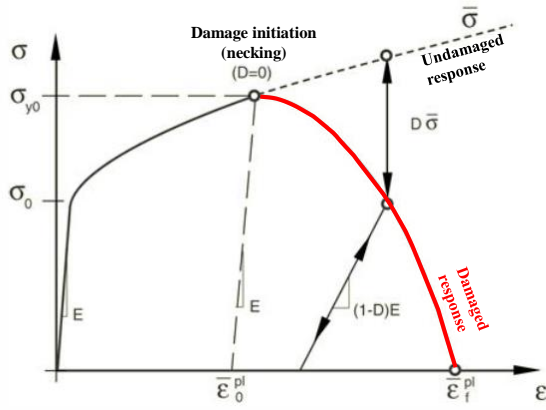
Fig. 5-4. Ductile damage model in Abaqus©.

The damage initiation criterion, defined by Eq. (5-1), assumes that the equivalent plastic strain at the onset of necking $\bar{\varepsilon}_0^{pl}$ ($D = 0$ in Fig. 5-4) is a function of the stress triaxiality η and the true plastic strain at the onset of necking ε_n^{pl} ($= \varepsilon_n - \varepsilon_y$). The damage initiation criterion used in the numerical simulations carried out in the present CHAPTER 5 is reported in Fig. 5-5(a).

The damage evolution law is defined through the damage variable D_i as the dimensionless difference between the undamaged and damaged plastic responses of the material (see Eq. (5-2) and Fig. 5-4). In Eq. (5-2), the formulation proposed by Yang et al. in [126] has been used for the description of the damaged material response. This expression consists of the combination of a linear and a power stress-strain law, as given in Eq. (5-3), where W is the weighting factor which needs to be calibrated, and the parameters a, b, n and K are given in Eq. (5-4).

The calibration of the weighting factor was conducted following an iterative energy-based approach, which consists in equalizing the fracture energy between the reference engineering and true stress-strain curves implemented in Abaqus©, as depicted in Fig. 5-3. The damage evolution law used in the numerical simulations carried out in the present CHAPTER 5 is reported in Fig. 5-5(b) as a function of the equivalent plastic displacement $\bar{u}_i^{pl}$, expressed in Eq. (5-5), L_E being the FE characteristic length.

The damage evolution law is dependent on the mesh size. Therefore, the equivalent plastic displacement $\bar{u}_i^{pl}$ has been normalized by L_E in Fig. 5-5(b). The critical damage variable D_{cr} is also reported in this Fig. 5-5(b). This variable is used to describe the point (i.e. the damage D_i) beyond which the material undergoes rupture ("r"), directly followed by fracture ("f") and has been calibrated using the same above-mentioned energy-based approach. Finally, to reduce the computation time, the damage was introduced in the PZ region only, where the highest plasticity is expected.
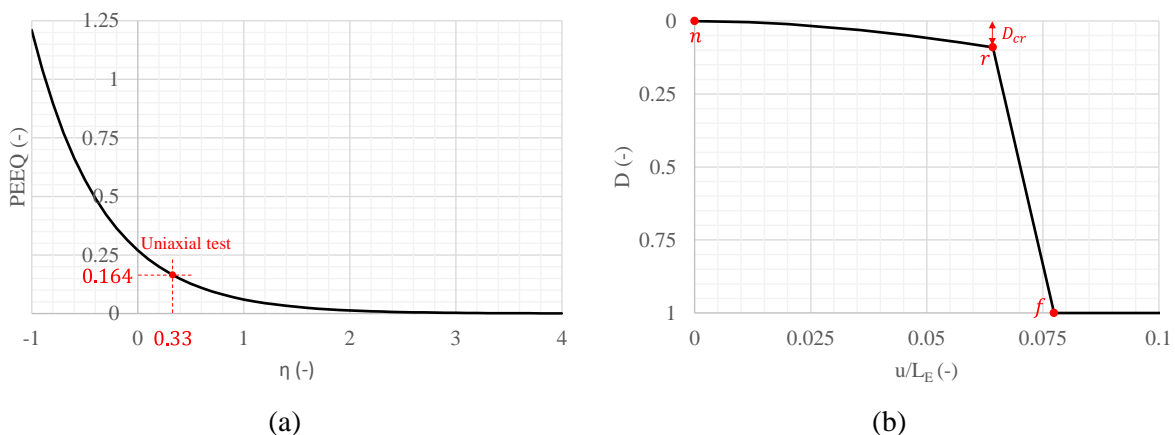

(a)

(b)

Fig. 5-5. Description of the ductile damage model parameters used in the present study: (a) damage initiation criterion and (b) damage evolution law.

5.2.3 Parametric study

The so-modified four numerical models were then used to perform a parametric study with the aim of generating a large number of FE results characterized by a PZ ultimate failure mode. Subsequently, these numerical results will be used for the validation of the full-range analytical models (see Section 1.1). The parametric study performed in the present CHAPTER 5 covers the same 32 joint configurations as in CHAPTER 4 (see Table 4-7). The results from the parametric study are discussed in the following Section 5.2.4.

5.2.4 FE results and discussion

The results from the parametric study are presented in Fig. 5-6 in terms of $(M_B - \Phi)_{num}$ curves (see the bolded black solid curves), M_B and Φ being defined in APPENDIX B.2. As a first step, the ultimate failure mode has been studied to identity the numerical simulations which are characterized by a PZ ultimate failure mode (see Section 5.2.4.1). Based on this analysis, it was possible to extract the ultimate bending moment resistance $M_{u,Rk,num}^j$ and rotation capacity $\Phi_{u,num}$ for every single numerical simulation, following a graphical procedure (see Section 5.2.4.2). These two parameters will be used in the following Section 5.3 for the validation of the full-range analytical model.

Again, similarly to Section 4.2.4, the procedure described here above will be illustrated for the eight numerical simulations carried out with the NR4 model only. The same procedure was also applied to each numerical simulation performed with the models NR16, A and B. However, for sake of clarity of the present manuscript, the figures are not presented in the present Section 5.2.4 (they may be found in APPENDIX C, see Fig. C-1(b) to Fig. C-32(b)). Only the final results related to these numerical simulations, i.e. $M_{u,Rk,num}^j$ and $\Phi_{u,num}$, will be reported in the present Section 5.2.4.

5.2.4.1 Study of the possible ultimate failure modes

To illustrate the possible ultimate failure modes which are likely to occur in the numerical simulations, eight pictures, coming from Abaqus©, are given in Fig. 5-7 in terms of equivalent plastic strain (PEEQ). These pictures correspond to the very last increment of the eight numerical simulations performed with the model NR4 (see the red squares in Fig. 5-6(a) to Fig. 5-6(h)). Based on the discussion held in Section 3.2.2.2, three main failure modes have been identified from the study of the numerical results, namely:

- The <u>global buckling</u> of the column (i.e. "GB_c") which was observed in the case of axially loaded exterior joints only (see Fig. 5-7(e) and Fig. 5-7(g)).
- The <u>local instability</u> of the sheared PZ (i.e. "LB_{PZ}"), of the CWC* (i.e. "LB_{CWC^*}") or of the BFC (i.e. "LB_{BFC}"). This failure mode can be observed in Fig. 5-7(b), (c), (d), (f) and (h).
- The <u>fracture of the material</u> (i.e. "MF") which was observed at two critical locations in the numerical simulations: (i) either at the beam-to-column interface, at the level of the roots of the fillet welds between the beam flanges and the column flange (see Fig. 5-7(a), (b), (e), (f), (g), (h)), or (ii) in the CWP, adjacent to the root radii of the column profile in the case of the shear buckling of the latter (see Fig. 5-7(c), (d)). Practically speaking, this failure mode only limits the deformation capacity of joints whose resistance is governed by a tensioned component (i.e. either the CWT or the CFB). By contrast, for joints whose resistance is governed by a local instability (i.e. the PZ, CWC* and BFC), the fracture of the material always occurs beyond this instability. The same observation was made for global instabilities.

Based on this analysis, the observed ultimate failure mode associated to each numerical simulation has been reported in Table 5-4.
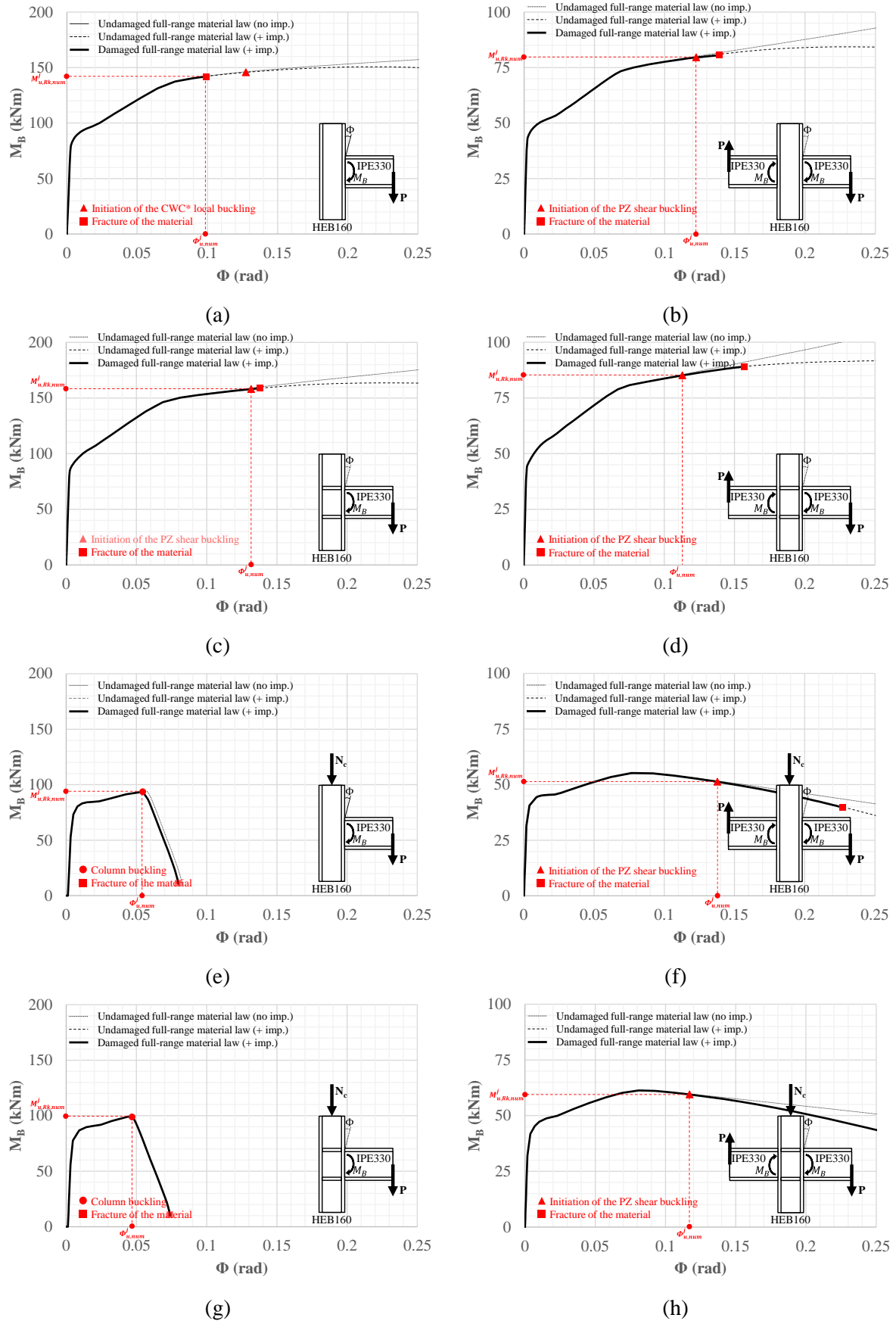
Fig. 5-6. Numerical results in terms of $(M_B - \Phi)_{num}$ curves: (a) simulation NR4-0-s-/, (b) simulation NR4-0-d-/, (c) simulation NR4-1-s-/, (d) simulation NR4-1-d-/, (e) simulation NR4-0-s-0.5N$_{pl}$, (f) simulation NR4-0-d-0.5N$_{pl}$, (g) simulation NR4-1-s-0.5N$_{pl}$ and (h) simulation NR4-1-d-0.5N$_{pl}$.
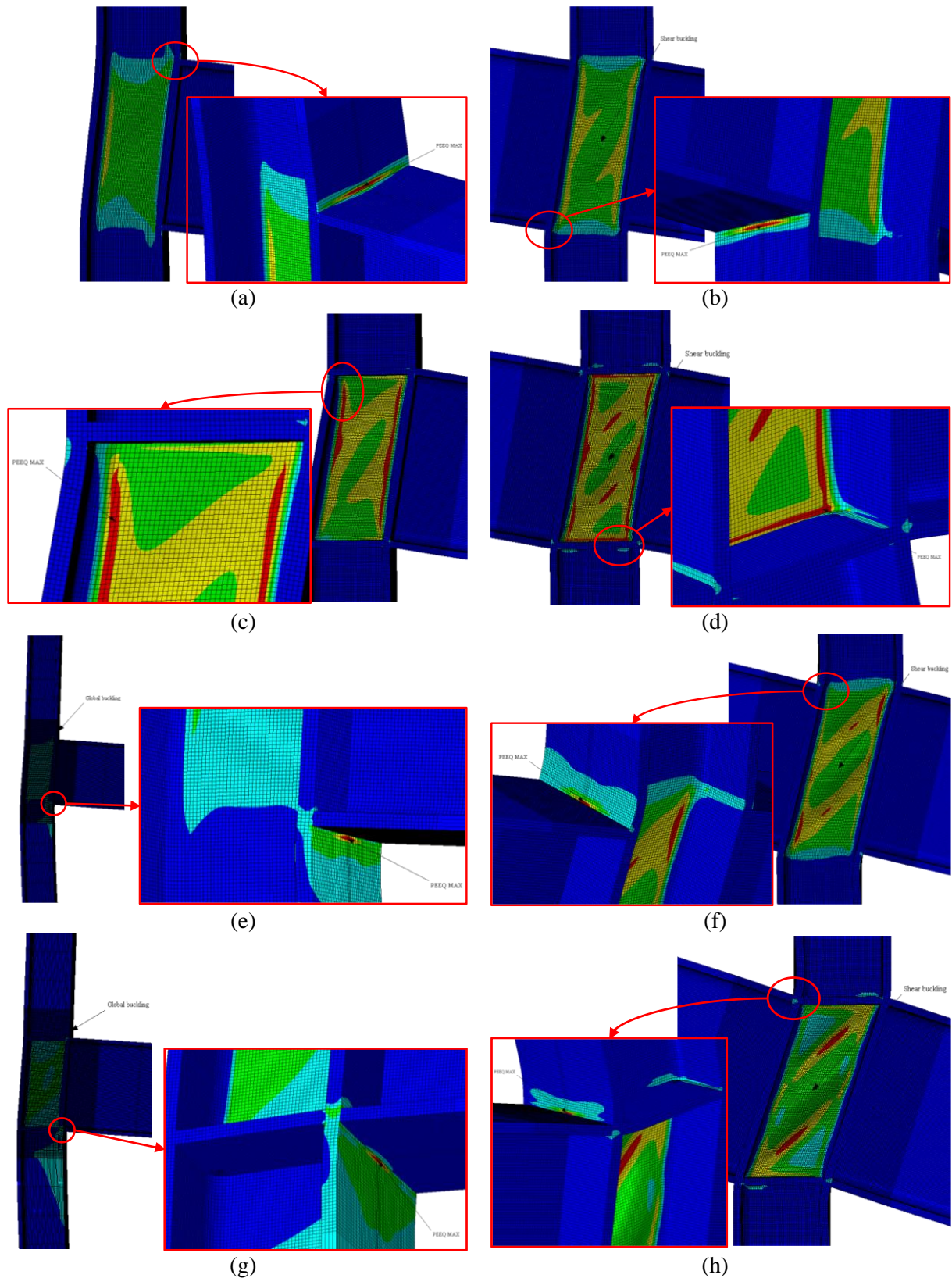
Fig. 5-7. Study of the ultimate failure mode: (a) simulation NR4-0-s-/, (b) simulation NR4-0-d-/, (c) simulation NR4-1-s-/, (d) simulation NR4-1-d-/, (e) simulation NR4-0-s-0.5N_{pl}, (f) simulation NR4-0-d-0.5N_{pl}, (g) simulation NR4-1-s-0.5N_{pl} and (h) simulation NR4-1-d-0.5N_{pl}.

Table 5-4. Description of the observed ultimate bending resistance $M_{u,Rk,num}^{j}$, ultimate rotation capacity $\Phi_{u,num}$ and ultimate failure mode for each individual numerical simulation of the parametric study.

Configuration	Category I (X="d", Y="/")			Category II (X="s", Y="/")		
	$M_{u,Rk,num}^{j}$ (kNm)	$\Phi_{u,num}$ (rad)	Ultimate. failure mode	$M_{u,Rk,num}^{j}$ (kNm)	$\Phi_{u,num}$ (rad)	Ultimate failure mode
NR4-0-X-Y	79.56	0.1225	LB_{PZ}	141.96	0.0990	MF
NR4-1-X-Y	85.09	0.1129	LB_{PZ}	158.02	0.1317	LB_{PZ}
NR16-0-X-Y	320.88	0.0758	LB_{PZ}	583.53	0.0909	LB_{CWC*}
NR16-1-X-Y	416.16	0.1043	LB_{PZ}	709.72	0.1083	LB_{PZ}
A-0-X-Y	52.98	0.1574	LB_{PZ}	90.42	0.1446	MF
A-1-X-Y	55.31	0.1414	LB_{PZ}	96.55	0.1474	MF
B-0-X-Y	237.93	0.1096	LB_{PZ}	346.63	0.1724	MF
B-1-X-Y	254.46	0.1375	LB_{PZ}	352.46	0.1580	MF
Configuration	Category III (X="d", Y="0.5N$_{pl}$")			Category IV (X="s", Y="0.5N$_{pl}$")		
	$M_{u,Rk,num}^{j}$ (kNm)	$\Phi_{u,num}$ (rad)	Ultimate. failure mode	$M_{u,Rk,num}^{j}$ (kNm)	$\Phi_{u,num}$ (rad)	Ultimate. failure mode
NR4-0-X-Y	51.31	0.1379	LB_{PZ}	93.62	0.0545	GB_{c}
NR4-1-X-Y	59.47	0.1172	LB_{PZ}	98.85	0.0469	GB_{c}
NR16-0-X-Y	251.53	0.0681	LB_{PZ}	450.42	0.0882	LB_{CWC*}
NR16-1-X-Y	328.82	0.0986	LB_{PZ}	522.94	0.1202	LB_{PZ}
A-0-X-Y	34.65	0.1430	LB_{PZ}	62.46	0.1122	GB_{c}
A-1-X-Y	38.85	0.1281	LB_{PZ}	68.51	0.1531	LB_{PZ}
B-0-X-Y	177.39	0.0679	LB_{PZ}	292.46	0.1195	MF
B-1-X-Y	185.58	0.0639	LB_{PZ}	324.97	0.1359	MF

5.2.4.2 Extraction of the ultimate bending moment resistance $M_{u,Rk,num}^{j}$ and rotation capacity $\Phi_{u,num}$

Table 5-4 also provides the ultimate bending resistance $M_{u,Rk,num}^{j}$ and the ultimate rotation capacity $\Phi_{u,num}$. These performance parameters were extracted from the numerical $(M_B - \Phi)_{num}$ curves of each numerical simulation, following a graphical procedure. This procedure is illustrated in Fig. 5-6 for the eight numerical simulations performed with the model NR4. From Fig. 5-6, it can be seen that each numerical simulation was run three times with three different material laws to facilitate the extraction of $M_{u,Rk,num}^{j}$ and $\Phi_{u,num}$, which led to three different $(M_B - \Phi)_{num}$ curves for each numerical simulation. These three $(M_B - \Phi)_{num}$ curves can be described as follows:

- The dashed curves were obtained, assuming an undamaged full-range material law and no initial geometric imperfection.
  ➔ These curves only allow the identification of the global column buckling, if any. These points are identified with red circles in Fig. 5-6(a) to Fig. 5-6(h).
- The broken curves were obtained, assuming an undamaged full-range material law with an initial geometric imperfection.
  ➔ The rotation at which these curves begin to diverge from the dashed curves defines the initiation of the local buckling. Practically speaking, these rotations are not easy to extract graphically. However, an estimation of these latter is provided in Fig. 5-6(a) to Fig. 5-6(h), see the red triangles.

- The bolded solid curves were obtained, assuming now a damaged full-range material law with an initial geometric imperfection.
  ➔ The final point of these curves defines the fracture of the material. These points are identified with red squares in Fig. 5-6(a) to Fig. 5-6(h).

Based on these three curve families, it was possible to identify the actual ultimate failure mode, i.e. the first failure mode to occur among the three above-mentioned failure modes, and to extract the values of $M_{u,Rk,num}^{j}$ and $\Phi_{u,num}$. These values are reported in Table 5-4.

5.2.4.3 Conclusion of the parametric study

From Table 5-4, it can be seen that only 20 of the 32 numerical simulations are characterized by a PZ ultimate failure mode. These numerical simulations are highlighted in light blue in Table 5-4. They consist of all the 16 numerical simulations performed on interior joints but only four numerical simulations performed on the exterior joints.

Regarding the ultimate failure mode of the 12 remaining numerical simulations performed on exterior joints, it consists of: (i) the local buckling of the CWC* (i.e. LB_{CWC^*}) for two of them; (ii) the global instability of the column (i.e. GB_c) for three of them; or (iii) the material fracture due to the failure of a tensile component (i.e. MF) for seven of them.

At the end, only the 20 numerical simulations characterized by a PZ ultimate failure mode (i.e. LB_{PZ}) will be kept in the present CHAPTER 5 for the prediction of the deformation capacity of the PZ component. The 12 remaining ones are less interesting and will be abandoned.

For some numerical simulations among the 20 selected ones, it can be observed that the ultimate failure mode occurs in the final descending branch of the $(M_B - \Phi)_{num}$ curve, beyond the observed maximum bending moment $M_{B,max}$ at the beam-to-column interface. This is the case for some of the axially loaded joints such as the NR4-0-d-0.5N$_{pl}$ simulation in Fig. 5-6(f) or the NR4-1-d-0.5N$_{pl}$ simulation in Fig. 5-6(h). In theory, beyond $M_{B,max}$, any increase of the applied load P (and hence of the bending moment M_B) should lead to the buckling of the column. However, since the numerical simulations were performed based on a displacement-controlled approach rather than a load-controlled approach, the vertical displacement at the beam(s) tip can be increased while reducing the bending moment M_B in the beam.

This can be explained, referring to Eq. (B-8) and Eq. (B-12) in APPENDIX B.1. In these equations, the equivalent shear force $V_{Ek,num}^{PZ}$ acting on the PZ comes from two contributions, i.e. a first contribution from the applied load P and a second contribution from the applied axial load N_c. For increasing PZ shear deformations, this latter becomes more and more significant with respect to the contribution from the applied load P. Therefore, it becomes possible to increase the shear force $V_{Ek,num}^{PZ}$ acting on the PZ (and thus the shear deformation γ of the PZ and consequently the vertical displacement v at the beam(s) tip), while reducing the load P acting at the beam(s) tip. This is what happens in Fig. 5-6(f) and Fig. 5-6(h).

5.3 ANALYTICAL PART

5.3.1 Complex analytical model

5.3.1.1 Description of the model

Based on the conclusions made in the previous CHAPTER 4 (and especially in Section 4.2.4), it is now clearly established that the behaviour of the PZ can always be divided into the contributions of the CWP and the SE. Moreover, these contributions can be assumed to behave independently. Therefore, similarly to the analytical model developed in CHAPTER 4 for the plastic resistance, the contributions of the CWP and the SE can be modelled separately and superimposed through Eqs. (2-14) and (2-15), to get the full-range model up to failure of the whole PZ, as shown in Fig. 5-8.

For the contribution of the CWP, a uniform shear stress distribution over the whole depth d_b^* of the CWP is assumed. Consequently, the analytical model for the prediction of the full-range behaviour of the CWP exhibits the same quad-linear shape as the ECCS material model used in the numerical simulations (see the black solid curve in Fig. 5-3(b)). This model is presented in Fig. 5-8(a) and it is divided into four main "zones", which are named as follows: (i) the initial elastic range, (ii) the plastic range, (iii) the post-plastic range and, eventually, (iv) the flowed range. The main parameters of this model are given in Table 5-5 and they will be described in detail in Section 5.3.1.2.

For the contribution of the SE, we know that it consists of the minimum required number of plastic hinges in order for a plastic collapse mechanism to develop. The behaviour of a plastic hinge is known to be highly non-linear. However, in civil engineering, it is commonly accepted to replace this highly non-linear behaviour by a simplified elastic, perfectly-plastic one, disregarding the strain-hardening effects of the material ([127], [128]). This kind of model is used, for instance, within the framework of a plastic analysis of a framed structure. In the present thesis, the strain-hardening of the material has been accounted for, assuming a linear hardening law until failure. The resulting full-range bilinear model is presented in Fig. 5-8(b). The main parameters of this model are given in Table 5-6 for the particular case of an unstiffened joint and they will be described in detail in Section 5.3.1.3.

Table 5-5. Parameters of the original and modified full-range models of the CWP.

Original full-range model of the CWP			Modified full-range model of the CWP		
γ_y^{CWP}	$=$	$\dfrac{V_y^{CWP}}{K_y^{CWP}}$	$C_y^{CWP} \cdot \gamma_y^{CWP}$	$=$	$\dfrac{C_y^{CWP} \cdot V_y^{CWP}}{K_y^{CWP}}$
K_y^{CWP}	$=$	$\dfrac{K_{y,sh}^{CWP} \cdot K_{y,b}^{CWP}}{K_{y,sh}^{CWP} + K_{y,b}^{CWP}}$	K_y^{CWP}	$=$	$\dfrac{K_{y,sh}^{CWP} \cdot K_{y,b}^{CWP}}{K_{y,sh}^{CWP} + K_{y,b}^{CWP}}$
V_y^{CWP}	$=$	$\chi_i \cdot \chi_n \cdot A_{VC}^{compl} \cdot \tau_y$	$C_y^{CWP} \cdot V_y^{CWP}$	$=$	$C_y^{CWP} \cdot \chi_i \cdot \chi_n \cdot A_{VC}^{compl} \cdot \tau_y$
γ_{pp}^{CWP}	$=$	$\gamma_y^{CWP} + \dfrac{\Delta V_y^{CWP}}{\Delta K_y^{CWP}}$	γ_{pp}^{CWP}	$=$	$\gamma_y^{CWP} + \dfrac{\Delta V_y^{CWP}}{\Delta K_y^{CWP}}$
ΔK_y^{CWP}	$=$	$\dfrac{\Delta E}{3} \cdot A_{VC}^{simpl}$	$\Delta K_{y,mod}^{CWP}$	$=$	$\dfrac{\Delta V_{y,mod}^{CWP}}{\Delta \gamma_{y,mod}^{CWP}}$
V_{pp}^{CWP}	$=$	$\chi_i \cdot \chi_n \cdot A_{VC}^{compl} \cdot \tau_{pp}$	$\Delta C_y^{CWP} \cdot V_{pp}^{CWP}$	$=$	$\Delta C_y^{CWP} \cdot \chi_i \cdot \chi_n \cdot A_{VC}^{compl} \cdot \tau_{pp}$
$\Delta \gamma_y^{CWP}$	$=$	$\gamma_{pp}^{CWP} - \gamma_y^{CWP}$	$\Delta \gamma_{y,mod}^{CWP}$	$=$	$\gamma_{pp}^{CWP} - C_y^{CWP} \cdot \gamma_y^{CWP}$
ΔV_y^{CWP}	$=$	$V_{pp}^{CWP} - V_y^{CWP}$	$\Delta V_{y,mod}^{CWP}$	$=$	$\Delta C_y^{CWP} \cdot V_{pp}^{CWP} - C_y^{CWP} \cdot V_y^{CWP}$
γ_u^{CWP}	$=$	$\gamma_{pp}^{CWP} + \dfrac{V_u^{CWP} - V_{pp}^{CWP}}{K_{pp}^{CWP}}$	$\gamma_{u,mod}^{CWP}$	$=$	$\gamma_{pp}^{CWP} + \dfrac{V_u^{CWP} - V_{pp,mod}^{CWP}}{K_{pp}^{CWP}}$
K_{pp}^{CWP}	$=$	$\dfrac{E_{pp}}{3} \cdot A_{VC}^{simpl}$	K_{pp}^{CWP}	$=$	$\dfrac{E_{pp}}{3} \cdot A_{VC}^{simpl}$
V_u^{CWP}	$=$	$\chi_i \cdot \chi_n \cdot A_{VC}^{compl} \cdot \tau_u$	V_u^{CWP}	$=$	$\chi_i \cdot \chi_n \cdot A_{VC}^{compl} \cdot \tau_u$
γ_n^{CWP}	$=$	$\gamma_u^{CWP} + \dfrac{\Delta V_u^{CWP}}{\Delta K_{pp}^{CWP}}$	$\gamma_{n,mod}^{CWP}$	$=$	$\gamma_{u,mod}^{CWP} + \dfrac{\Delta V_u^{CWP}}{\Delta K_{pp}^{CWP}}$
ΔK_{pp}^{CWP}	$=$	$\dfrac{\Delta E_{pp}}{3} \cdot A_{VC}^{simpl}$	ΔK_{pp}^{CWP}	$=$	$\dfrac{\Delta E_{pp}}{3} \cdot A_{VC}^{simpl}$
V_n^{CWP}	$=$	$\chi_i \cdot \chi_n \cdot A_{VC}^{compl} \cdot \tau_n$	V_n^{CWP}	$=$	$\chi_i \cdot \chi_n \cdot A_{VC}^{compl} \cdot \tau_n$
$\Delta \gamma_u^{CWP}$	$=$	$\gamma_n^{CWP} - \gamma_u^{CWP}$	$\Delta \gamma_{u,mod}^{CWP}$	$=$	$\gamma_{n,mod}^{CWP} - \gamma_{u,mod}^{CWP}$
ΔV_u^{CWP}	$=$	$V_n^{CWP} - V_u^{CWP}$	ΔV_u^{CWP}	$=$	$V_n^{CWP} - V_u^{CWP}$

Table 5-6. Parameters of the original and modified full-range models of the SE (unstiffened joints).

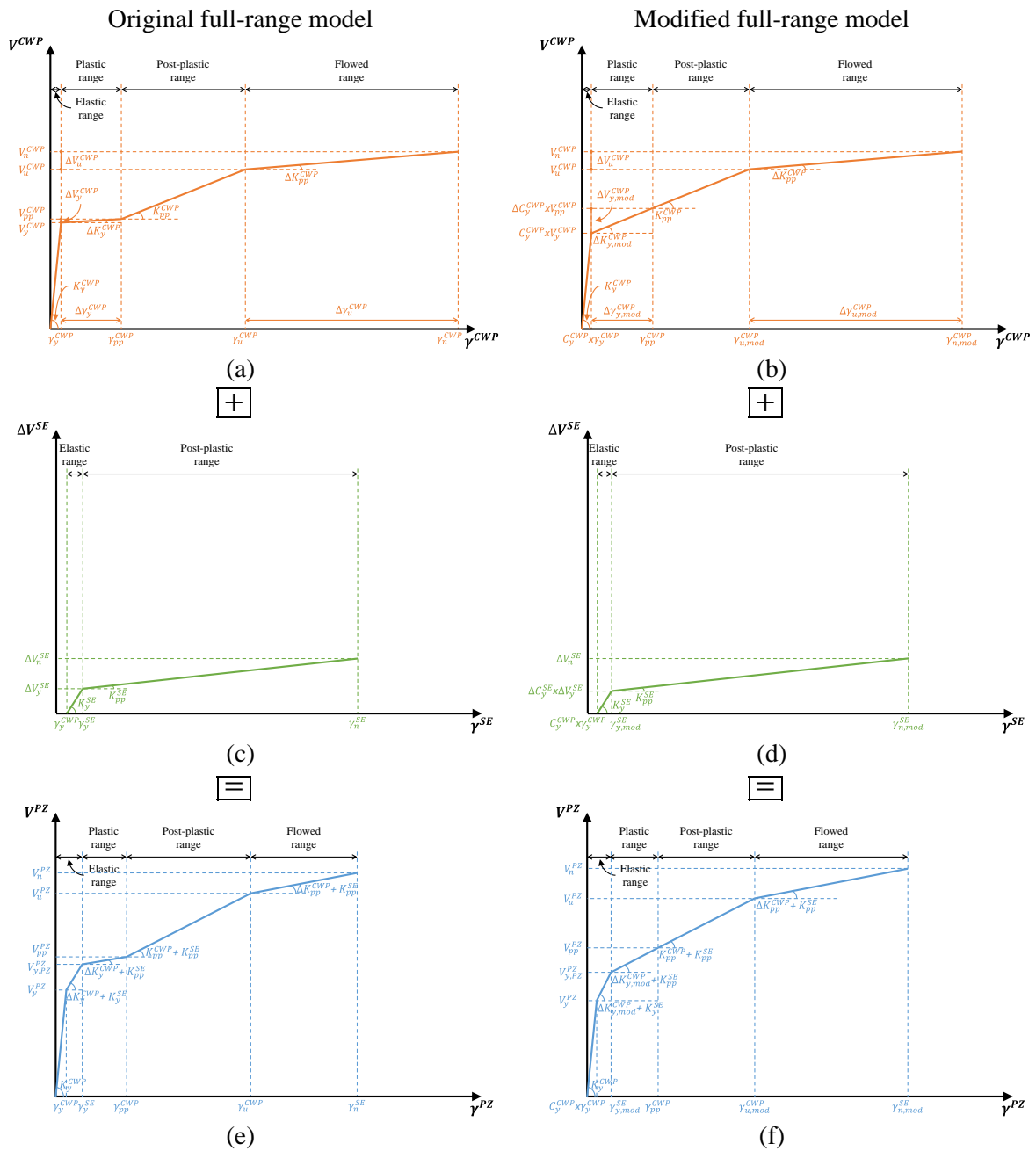| Original full-range model of the SE			Modified full-range model of the SE		
γ_y^{CWP}	$=$	$\dfrac{V_y^{CWP}}{K_y^{CWP}}$	$C_y^{CWP} \cdot \gamma_y^{CWP} =$		$\dfrac{C_y^{CWP} \cdot V_y^{CWP}}{K_y^{CWP}}$
γ_y^{SE}	$=$	$\gamma_y^{CWP} + \dfrac{\Delta V_y^{SE}}{K_y^{SE}}$	$\gamma_{y,mod}^{SE}$	$=$	$C_y^{CWP} \cdot \gamma_y^{CWP} + \dfrac{\Delta C_y^{SE} \cdot \Delta V_y^{SE}}{K_y^{SE}}$
K_y^{SE}	$=$	$\dfrac{1}{\eta} \cdot \left[4 \cdot \dfrac{E \cdot I_{fc,T}}{L_{fc,T} \cdot d_b^*} \right]$	K_y^{SE}	$=$	$\dfrac{1}{\eta} \cdot \left[4 \cdot \dfrac{E \cdot I_{fc,T}}{L_{fc,T} \cdot d_b^*} \right]$
ΔV_y^{SE}	$=$	$4 \cdot \dfrac{M_{pl,fc,T,Rk}}{d_b^*}$	$\Delta C_y^{SE} \cdot \Delta V_y^{SE} =$		$4 \cdot \Delta C_y^{SE} \cdot \dfrac{M_{pl,fc,T,Rk}}{d_b^*}$
γ_n^{SE}	$=$	$\gamma_y^{SE} + \dfrac{\Delta V_n^{SE} - \Delta V_y^{SE}}{K_{pp}^{SE}}$	$\gamma_{n,mod}^{SE}$	$=$	$\gamma_{y,mod}^{SE} + \dfrac{\Delta V_n^{SE} - \Delta C_y^{SE} \cdot \Delta V_y^{SE}}{K_{pp}^{SE}}$
K_{pp}^{SE}	$=$	$\dfrac{1}{\eta} \cdot \left[4 \cdot \dfrac{E_{pp} \cdot I_{fc,T}}{L_{fc,T} \cdot d_b^*} \right]$	K_{pp}^{SE}	$=$	$\dfrac{1}{\eta} \cdot \left[4 \cdot \dfrac{E_{pp} \cdot I_{fc,T}}{L_{fc,T} \cdot d_b^*} \right]$
ΔV_n^{SE}	$=$	$4 \cdot \dfrac{M_{n,fc,T,Rk}}{d_b^*}$	ΔV_n^{SE}	$=$	$4 \cdot \dfrac{M_{n,fc,T,Rk}}{d_b^*}$

Fig. 5-8. Description of the original and modified full-range constitutive models of the PZ: (a)-(b) contribution of the CWP, (c)-(d) contribution of the SE and (e)-(f) sum of the two.

5.3.1.2 Contribution of the CWP

A. *Characterization of the CWP resistance*

i. In the absence of shear buckling

As already mentioned in Section 5.1.2, the scope of the present CHAPTER 5 meets the EN 1993-1-8 requirements in terms of the CWP slenderness (see Eq. (2-39)). This means that the risk of shear buckling of the CWP in the elastic range is prevented. If the CWP is rather stocky, no instability occurs in the post-elastic ranges either and the shear resistance of the CWP is governed by material necking and fracture. The proposed quad-linear model for the prediction of the full-range behaviour of the CWP, presented in Fig. 5-8(a), exhibits four main values of resistance, namely:

- V_y^{CWP} (i.e. $V^{CWP}(\gamma_y^{CWP})$ or $V_{y,Rk,compl}^{CWP}$): the plastic shear resistance of the CWP;

- V_{pp}^{CWP} (i.e. $V^{CWP}(\gamma_{pp}^{CWP})$ or $V_{pp,Rk,compl}^{CWP}$): the post-plastic shear resistance of the CWP;

- V_u^{CWP} (i.e. $V^{CWP}(\gamma_u^{CWP})$ or $V_{u,Rk,compl}^{CWP}$): the ultimate shear resistance of the CWP;

- V_n^{CWP} (i.e. $V^{CWP}(\gamma_n^{CWP})$ or $V_{n,Rk,compl}^{CWP}$): the shear resistance of the CWP at necking.

Knowing the expression for the prediction of the plastic shear resistance $V_{y,Rk,compl}^{CWP}$ of the CWP (see Eqs. (4-14) to (4-18) in CHAPTER 4), a good estimation of the three other values may be simply obtained by substituting, in these Eqs. (4-14) to (4-18), the yield strength of the material (σ_y) by either the post-plastic strength of the material (σ_{pp}), the ultimate strength of the material (σ_u) or the strength of the material at the onset of necking (σ_n). These values of the material strength can be easily extracted from the material true stress-strain curve, given in Fig. 5-3(b). They are reported in Table 5-3 for the $S355$ steel material considered in the numerical simulations. The expressions of $V_{y,Rk,compl}^{CWP}$, $V_{pp,Rk,compl}^{CWP}$, $V_{u,Rk,compl}^{CWP}$ and $V_{n,Rk,compl}^{CWP}$ are reported in Table 5-5.

ii. In the presence of shear buckling

However, for an increasing CWP slenderness, the ultimate shear resistance of the CWP is not governed by the material necking and fracture anymore, but by the shear buckling of the CWP. This buckling can occur either in the flowed range, or even in the post-plastic range of the quad-linear model depicted in Fig. 5-8(a). To evaluate the shear buckling resistance of the CWP, it was referred to the procedure developed by Cerfontaine in [129]. This procedure is based on the approach proposed in the Part 1-5 of Eurocode 3 (i.e. EN 1993-1-5, [130]) dedicated to the design of steel plates. It was originally developed in [129] for slender build-up sections, whose shear buckling occurs in the elastic range.

As a first step, this procedure has been particularised to the elastic range of the quad-linear model presented in Fig. 5-8(a), even though we know there is no risk of instability in this particular range. Then, the procedure was extended to the post-elastic ranges where the shear buckling is likely to govern the resistance of the CWP.

According to [129], Eq. (4-15) characterizing the plastic shear resistance of the CWP should be re-expressed through Eq. (5-6) to account for the potential risk of shear buckling:

$$V_{y,Rk,compl}^{CWP} = \min\left(\chi_i \cdot \chi_n \cdot \underbrace{A_{VC}^{compl} \cdot \tau_y}_{V_{y,Rk}^{CWP}} ; \chi_i \cdot \chi_n \cdot \overbrace{A_{VC}^{compl} \cdot \rho_y \cdot \tau_y}^{V_{y,Rk,buck}^{CWP}} \right) \qquad (5\text{-}6)$$

All the parameters but ρ_y in Eq. (5-6) were defined in Section 4.3.1.1. Thus they are not recalled here for sake of clarity of the present manuscript. The parameter ρ_y is a reduction factor accounting for the possible shear buckling of the CWP and which can be defined through Eq. (5-7):

$$\rho_y = \begin{cases} 1.0 & if\ \overline{\lambda_w} \leq 0.83 \\ \dfrac{0.83}{\overline{\lambda_w}} & if\ 0.83 \leq \overline{\lambda_w} < 1.08 \\ \dfrac{1.37}{0.7 + \overline{\lambda_w}} & if\ 1.08 < \overline{\lambda_w} \end{cases} \tag{5-7}$$

In Eq. (5-7), $\overline{\lambda_w}$ is the slenderness factor of the CWP and it can be evaluated through Eq. (5-8) as the square root of the ratio between the shear yield strength τ_y and the shear critical stress τ_{cr} of the plate:

$$\overline{\lambda_w} = \sqrt{\dfrac{\tau_y}{\tau_{cr}}} \tag{5-8}$$

Regarding the shear critical stress τ_{cr}, it can be evaluated through Eq. (5-9):

$$\tau_{cr} = k_\tau \cdot \sigma_E \tag{5-9}$$

In Eq. (5-9), σ_E is the Euler critical stress of the plate (see Eq. (5-10)) and k_τ is the buckling coefficient related to the plate and which depends on the geometry, loading and boundary conditions of the plate.

For CWPs of depth "b" and width "a", such as those presented in Fig. 5-9(a) and (b), this buckling coefficient can be expressed as an interpolation between the value $k_{\tau,clamped}$ (see Eq. (5-12)) referring to the case where the CWP is assumed to be fully clamped along its edges and the value $k_{\tau,pinned}$ (see Eq. (5-13)) referring to the case where the CWP is assumed to be simply supported along the edges.

The weighted factor r is given by Eq. (5-14), where b_i, L_i and t_i are the dimensions of the plates located around the CWP, see Fig. 5-9(a) and (b). The minimum given by the four plates is safely considered, or 1.0 if smaller. The value $r = 1$ corresponds to a fully clamped CWP while $r = 0$ corresponds to a simply supported CWP.

$$\sigma_E = \dfrac{\pi^2 \cdot E}{12 \cdot (1 - v^2)} \cdot \left(\dfrac{t_{wc}}{a}\right)^2 \tag{5-10}$$

$$k_\tau = r \cdot k_{\tau,clamped} + (1 - r) \cdot k_{\tau,pinned} \tag{5-11}$$

$$k_{\tau,clamped} = \begin{cases} 8.98 + 5.6 \cdot \left(\dfrac{a}{b}\right)^2 & when\ \dfrac{a}{b} \leq 1 \\ 5.6 + 8.98 \cdot \left(\dfrac{a}{b}\right)^2 & when\ \dfrac{a}{b} > 1 \end{cases} \tag{5-12}$$

$$k_{\tau,pinned} = \begin{cases} 5.34 + 4.0 \cdot \left(\dfrac{a}{b}\right)^2 & when\ \dfrac{a}{b} \leq 1 \\ 4.0 + 5.34 \cdot \left(\dfrac{a}{b}\right)^2 & when\ \dfrac{a}{b} > 1 \end{cases} \tag{5-13}$$

$$r = \min_{i=1\rightarrow 4} \left(\dfrac{1}{3} \cdot \dfrac{b_i \cdot t_i^3 \cdot (1 - v)}{L_i \cdot t_{wc}^3}; 1.0\right) \tag{5-14}$$

(a)   (b)
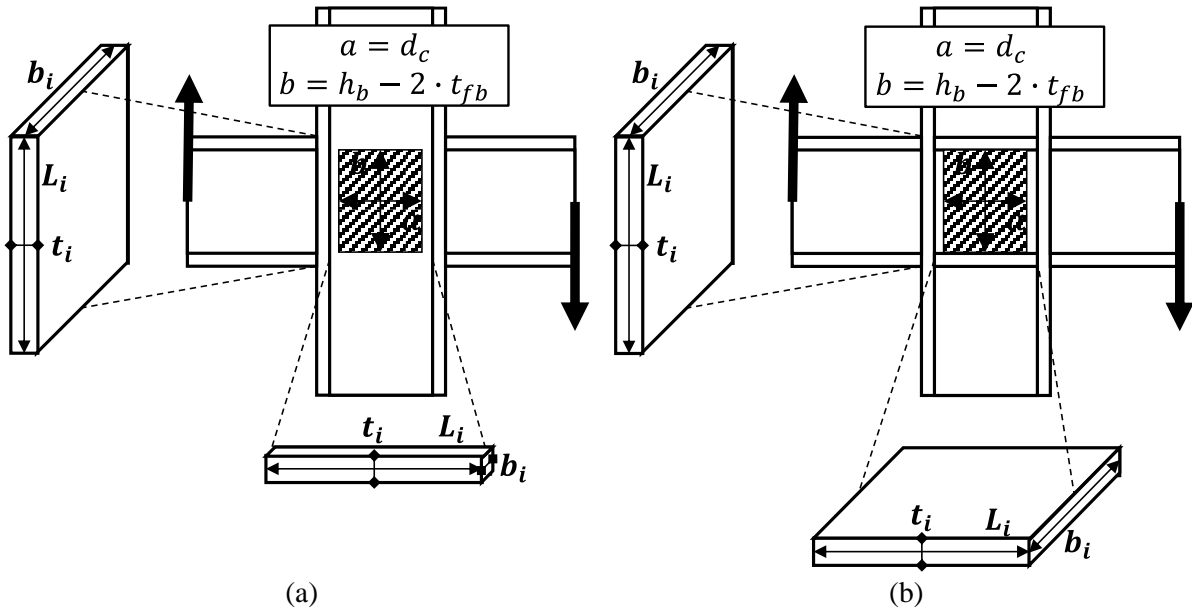
Fig. 5-9. Dimensions of the CWP and the surrounding plates: (a) unstiffened joints and (b) stiffened joints.

For the CWPs considered in the present study, it is known that the reduction factor ρ_y defined through Eq. (5-7) will always be equal to 1.0 since all the CWPs satisfy Eq. (2-39). Therefore, there is no risk of shear buckling in the elastic range.

The procedure described hereabove has been extended to the post-elastic ranges, and especially to the post-plastic and flowed ranges of the quad-linear model (see Table 5-7). To this aim, a small trick has been used, consisting in isolating the post-plastic (resp. flowed) branch of the model from the rest of the model through the use of a local $\sigma' - \varepsilon'$ axis system. The risk of shear buckling can then be studied in this local $\sigma' - \varepsilon'$ axis system, following the same procedure as for the first elastic branch but with the parameters τ_u' and E_{pp} (resp. τ_n' and ΔE_{pp}) of the post-plastic (resp. flowed) range instead of the parameters τ_y and E of the elastic range. Moreover, the boundaries are assumed to remain elastic.

Based on this procedure, the reduction factor ρ_u' (resp. ρ_n') can be computed. If it is equal to 1.0, there is no risk of shear buckling in the studied range and the ultimate (resp. necking) shear strength τ_u (resp. τ_n) of the material can be used to compute the ultimate (resp. necking) shear resistance $V_{u,Rk,compl}^{CWP}$ (resp. $V_{n,Rk,compl}^{CWP}$) of the CWP. If it is lower than 1.0, there is a risk of shear buckling in the studied range, and therefore, a reduced ultimate (resp. necking) shear strength τ_u^* (resp. τ_n^*) has so to be used to compute the ultimate (resp. necking) shear resistance $V_{u,Rk,compl}^{CWP}$ (resp. $V_{n,Rk,compl}^{CWP}$) of the CWP. At the end, the final shear resistance $V_{f,Rk,compl}^{CWP}$ of the CWP can be computed through Eq. (5-15).

$$V_{f,Rk,compl}^{CWP} = \begin{cases} V_{u,Rk,compl}^{CWP} & if\ \rho_u' < 1 \\ V_{n,Rk,compl}^{CWP} & if\ \rho_u' = 1 \end{cases} \tag{5-15}$$

Table 5-7. Computation of the shear resistances $V_{u,Rk,compl}^{CWP}$ and $V_{n,Rk,compl}^{CWP}$ of the CWP taking into account the potential risk of shear buckling.

Post-plastic range	Flowed range
$$\overline{\lambda_w} = \sqrt{\frac{\tau_u{'}}{\tau_{cr}}}$$	$$\overline{\lambda_w} = \sqrt{\frac{\tau_n{'}}{\tau_{cr}}}$$
$$\tau_u' = \frac{\sigma_u'}{\sqrt{3}} = \frac{\sigma_u - \sigma_{pp}}{\sqrt{3}}$$	$$\tau_n' = \frac{\sigma_n'}{\sqrt{3}} = \frac{\Delta\sigma_u}{\sqrt{3}} = \frac{\sigma_n - \sigma_u}{\sqrt{3}}$$
$$\tau_{cr} = k_\tau \cdot \sigma_E$$	
$$\sigma_E = \frac{\pi^2 \cdot E_{pp}}{12 \cdot (1 - v^2)} \cdot \left(\frac{t_{wc}}{a}\right)^2$$	$$\sigma_E = \frac{\pi^2 \cdot \Delta E_{pp}}{12 \cdot (1 - v^2)} \cdot \left(\frac{t_{wc}}{a}\right)^2$$
$$k_\tau = r \cdot k_{\tau,clamped} + (1 - r) \cdot k_{\tau,pinned}$$	
$$k_{\tau,clamped} = \begin{cases} 8.98 + 5.6 \cdot \left(\frac{a}{b}\right)^2 & when\ \frac{a}{b} \le 1 \\ 5.6 + 8.98 \cdot \left(\frac{a}{b}\right)^2 & when\ \frac{a}{b} > 1 \end{cases}$$	
$$k_{\tau,pinned} = \begin{cases} 5.34 + 4.0 \cdot \left(\frac{a}{b}\right)^2 & when\ \frac{a}{b} \le 1 \\ 4.0 + 5.34 \cdot \left(\frac{a}{b}\right)^2 & when\ \frac{a}{b} > 1 \end{cases}$$	
$$r = \min_{i=1 \to 4} \left(\frac{1}{3} \cdot \frac{b_i \cdot t_i^3 \cdot (1 - v)}{L_i \cdot t_{wc}^3}; 1.0\right)$$	
$$\rho_u' = \begin{cases} 1 & if\ \overline{\lambda_w} \le 0.83 \\ \dfrac{0.83}{\overline{\lambda_w}} & if\ 0.83 \le \overline{\lambda_w} < 1.08 \\ \dfrac{1.37}{0.7 + \overline{\lambda_w}} & if\ 1.08 < \overline{\lambda_w} \end{cases}$$	$$\rho_n' = \begin{cases} 1 & if\ \overline{\lambda_w} \le 0.83 \\ \dfrac{0.83}{\overline{\lambda_w}} & if\ 0.83 \le \overline{\lambda_w} < 1.08 \\ \dfrac{1.37}{0.7 + \overline{\lambda_w}} & if\ 1.08 < \overline{\lambda_w} \end{cases}$$
$$V_{u,Rk,compl}^{CWP} = \chi_i \cdot \chi_n \cdot \underbrace{A_{VC}^{compl} \cdot \tau_u}_{V_{u,Rk}^{CWP}}$$ $$\le \chi_i \cdot \chi_n \cdot \underbrace{A_{VC}^{compl} \cdot \tau_u^*}_{V_{u,Rk,buck}^{CWP}}$$ With $\tau_u^* = \rho_u' \cdot \tau_u' + \tau_{pp}$	$$V_{n,Rk,compl}^{CWP} = \chi_i \cdot \chi_n \cdot \underbrace{A_{VC}^{compl} \cdot \tau_n}_{V_{n,Rk}^{CWP}}$$ $$\le \chi_i \cdot \chi_n \cdot \underbrace{A_{VC}^{compl} \cdot \tau_n^*}_{V_{n,Rk,buck}^{CWP}}$$ With $\tau_n^* = \rho_n' \cdot \tau_n' + \tau_u$

B. Characterization of the CWP deformation capacity

i. Elastic range

The elastic behaviour of the PZ was extensively described in Section 3.3.1.1, which was dedicated to the review of the complex analytical models coming from the scientific literature. As a reminder, it was shown from this Section 3.3.1.1 (see Fig. 2-8) that the PZ undergoes shear and bending deformations in the elastic range, before yielding initiates in the CWP. The characterization of these two deformation modes, which are assumed to work in series, yields an estimation of the initial elastic stiffness of the PZ, see Eq. (2-21). This complex expression will be used in the present Section 5.3.1.2 for the description of the CWP elastic behaviour. It is recalled in Eq. (5-16) for sake of clarity of the present manuscript, where $K_{y,sh}^{CWP}$ and $K_{y,b}^{CWP}$ are the shear and bending elastic stiffnesses of the CWP, which are given through Eqs. (5-17) and (5-18), respectively. Knowing the elastic stiffness K_y^{CWP}, the yield shear deformation γ_y^{CWP} of the CWP can be computed through Eq. (5-19):

$$K_y^{CWP} = \left(\frac{1}{K_{y,b}^{CWP}} + \frac{1}{K_{y,sh}^{CWP}} \right)^{-1} = \frac{K_{y,sh}^{CWP} \cdot K_{y,b}^{CWP}}{K_{y,sh}^{CWP} + K_{y,b}^{CWP}} \tag{5-16}$$

$$K_{y,b}^{CWP} = \frac{12 \cdot E \cdot I_c}{d_b^{*\,2}} \tag{5-17}$$

$$K_{y,sh}^{CWP} = G \cdot A_{VC}^{simpl} \tag{5-18}$$

$$\gamma_y^{CWP} = \frac{V_{y,Rk,compl}^{CWP}}{K_y^{CWP}} \tag{5-19}$$

ii. Post-elastic ranges

After the shear yielding of the CWP, the PZ begins to behave as a system made of two independent components, namely the CWP and the SE. Most of the shear effect is carried by the CWP whose shear stiffness is significantly larger than that of the SE. By contrast, most of the bending effect is carried by the SE whose bending stiffness is significantly larger than that of the CWP. Based on this observation, the three stiffnesses, namely ΔK_y^{CWP}, K_{pp}^{CWP} and ΔK_{pp}^{CWP}, characterizing the post-elastic behaviour of the CWP, can be defined through Eqs. (5-20) to (5-22), where ΔG, G_{pp} and ΔG_{pp} are the shear moduli associated to the plastic, post-plastic and flowed ranges, respectively. These formulae were summarized in previous Table 5-5.

$$\Delta K_y^{CWP} = \Delta G \cdot A_{VC}^{simpl} = \frac{\Delta E}{3} \cdot A_{VC}^{simpl} \tag{5-20}$$

$$K_{pp}^{CWP} = G_{pp} \cdot A_{VC}^{simpl} = \frac{E_{pp}}{3} \cdot A_{VC}^{simpl} \tag{5-21}$$

$$\Delta K_{pp}^{CWP} = \Delta G_{pp} \cdot A_{VC}^{simpl} = \frac{\Delta E_{pp}}{3} \cdot A_{VC}^{simpl} \tag{5-22}$$

Based on these values, the post-plastic shear deformation of the CWP (i.e. γ_{pp}^{CWP}), the ultimate shear deformation of the CWP (i.e. γ_u^{CWP}) and the shear deformation of the CWP at necking (i.e. γ_n^{CWP}) can be defined through Eqs. (5-23) to (5-25). Again, these formulae were summarized in previous Table 5-5.

$$\gamma_{pp}^{CWP} = \gamma_y^{CWP} + \frac{V_{pp,Rk,compl}^{CWP} - V_{y,Rk,compl}^{CWP}}{\Delta K_y^{CWP}} \qquad (5\text{-}23)$$

$$\gamma_u^{CWP} = \gamma_{pp}^{CWP} + \frac{V_{u,Rk,compl}^{CWP} - V_{pp,Rk,compl}^{CWP}}{K_{pp}^{CWP}} \qquad (5\text{-}24)$$

$$\gamma_n^{CWP} = \gamma_u^{CWP} + \frac{V_{n,Rk,compl}^{CWP} - V_{u,Rk,compl}^{CWP}}{\Delta K_{pp}^{CWP}} \qquad (5\text{-}25)$$

iii. Final deformation capacity

At the end, the final shear deformation γ_f^{CWP} of the CWP can be computed through Eq. (5-26):

$$\gamma_f^{CWP} = \begin{cases} \gamma_u^{CWP} & if \; \rho_u' < 1 \\ \gamma_n^{CWP} & if \; \rho_u' = 1 \end{cases} \qquad (5\text{-}26)$$

C. Validation

All the parameters in Table 5-5 being known, the full-range behaviour of the CWP can be analytically predicted for the 20 numerical simulations characterized by PZ ultimate failure mode. Based on the comparisons between the analytical and numerical results, the full-range model of the CWP that was presented in Fig. 5-8(a) has been slightly modified to better fit the numerical results. The modified model is presented in Fig. 5-8(b) and all the parameters of the model are given in previous Table 5-5. In this model, two new coefficients have been introduced, namely C_y^{CWP} and ΔC_y^{CWP}. These coefficients are fitting parameters which take into account that the shear stress distribution is not perfectly uniform over the CWP (i.e. yielding and strain-hardening do not initiate uniformly over the CWP). These coefficients have been calibrated to the numerical results. From this calibration, it was considered that $C_y^{CWP} = 0.9$ and $\Delta C_y^{CWP} = 1.1$ are reasonable values.

A graphical comparison between the numerical results and the modified analytical model is provided in APPENDIX C (see the light orange solid curves and the dark orange broken curves in Fig. C-1(d) to Fig. C-32(d), respectively) for the 32 numerical simulations performed in the present parametric study. The parameters of the analytical $(V^{CWP} - \gamma)_{an}$ curves are given in Table C-1 to Table C-32 in APPENDIX C. Furthermore, the geometric 2nd order effects were accounted for, based on the results provided in APPENDIX E, but were shown not to play any role for the contribution of the SE. As for the numerical $(V^{CWP} - \gamma)_{num}$ curves, they were derived based on the procedure presented in APPENDIX B.1.

From this comparison, a good agreement can be observed between the numerical curves and the analytical model, especially in the 20 numerical simulations characterized by PZ ultimate failure mode. For these latter, the final shear resistance $V_{f,Rk,compl}^{CWP}$ and shear deformation γ_f^{CWP} of the CWP have been computed, using Eqs. (5-15) and (5-26). The results are reported in Table 5-8, together with the predicted failure mode (i.e. either the shear buckling of the CWP, LB_{PZ}, or the fracture of the material, MF). For all of them, it turns out that the shear resistance of the CWP is governed by the shear buckling of the latter, rather than the fracture of the material. However, for the simulations performed with the models NR4 and A, the shear buckling occurs in the flowed range, which leads to significant shear deformations γ_f^{CWP}. By contrast, for the simulations carried out with the NR16 and B models, the shear buckling occurs in the post-plastic range, which leads to significantly lower shear deformation capacities, as shown in Table 5-8.

5.3.1.3 Contribution of the SE

A. Characterization of the SE resistance

The proposed bilinear model for the prediction of the full-range behaviour of the SE, presented in Fig. 5-8(c), exhibits two main values of resistance, namely:

- ΔV_y^{SE} (i.e. $\Delta V^{SE}(\gamma_y^{SE})$ or $\Delta V_{y,Rk,compl}^{SE}$): the plastic shear resistance of the SE;

- ΔV_n^{SE} (i.e. $\Delta V^{SE}(\gamma_n^{SE})$ or $\Delta V_{n,Rk,compl}^{SE}$): the shear resistance of the SE at necking.

The plastic shear resistance $\Delta V_{y,Rk,compl}^{SE}$ of the SE was studied in CHAPTER 4 (see Section 4.3.1.2). It can be computed based on the analysis of the possible plastic collapse mechanisms given in Table 4-16, where $M_{pl,fc,T,Rk}$, $M_{pl,fb,T,Rk}$ and $M_{pl,st,Rk}$ are the reduced plastic moment resistances of a T-shaped column flange including the root fillets region, of a T-shaped beam flange including the root fillets region and of a rectangular transverse column web stiffener, see Eqs. (4-23) to (4-26).

Knowing the plastic collapse mechanism actually developing, a good estimation of $\Delta V_{n,Rk,compl}^{SE}$ can be simply obtained by substituting the yield strength σ_y of the material by the strength of the material at necking, i.e. σ_n, in Table 4-16 and Eqs. (4-23) to (4-26). This value can be easily extracted from the material true stress-strain curve given in Fig. 5-3(b). It is reported in Table 5-3 for the $S355$ steel material considered in the numerical simulations. The expression of $\Delta V_{n,Rk,compl}^{SE}$ is reported in Table 5-6 in the particular case of an unstiffened joint only. The shear resistance of the SE is thus always governed by the fracture of the material.

B. Characterization of the SE deformation capacity

In the model in Fig. 5-8(c), the deformability of the SE is assumed to arise from the deformability of the hinges only. As a reminder (see Table 4-16), depending on the type of joint configuration, three types of hinges are likely to develop in the SE, namely four main hinges in the column flanges, and two to four additional hinges in the beam flanges or in the transverse column web stiffeners.

In the model, it is assumed that all these hinges yield simultaneously and instantaneously for a given shear deformation γ_y^{SE}. Therefore, the initial stiffness K_y^{SE} can be expressed through Eq. (5-27), where a disctinction is made between the unstiffened joints, the stiffened interior joints and the stiffened exterior ones:

$$K_y^{SE} = \frac{1}{\eta} \cdot \frac{\Delta V_{y,Rk,compl}^{SE}}{\gamma_y^{SE}} = \begin{cases} \frac{1}{\eta} \cdot \left[4 \cdot \dfrac{E \cdot I_{fc,T}}{L_{h,fc,T} \cdot d_b^*} \right] & \text{unstiffened joints} \\[3mm] \frac{1}{\eta} \cdot \left[4 \cdot \dfrac{E \cdot I_{fc,T}}{L_{h,fc,T} \cdot d_b^*} + \min\left(4 \cdot \dfrac{E \cdot I_{fb,T}}{L_{h,fb,T} \cdot d_b^*} ; 4 \cdot \dfrac{E \cdot I_{st}}{L_{h,st} \cdot d_b^*} \right) \right] & \text{stiffened int. joints} \\[3mm] \frac{1}{\eta} \cdot \left[4 \cdot \dfrac{E \cdot I_{fc,T}}{L_{h,fc,T} \cdot d_b^*} + \min\left(2 \cdot \dfrac{E \cdot I_{fb,T}}{L_{h,fb,T} \cdot d_b^*} ; 4 \cdot \dfrac{E \cdot I_{st}}{L_{h,st} \cdot d_b^*} \right) \right] & \text{stiffened ext. joints} \end{cases} \quad (5\text{-}27)$$

In Eq. (5-27), $I_{fc,T}$, I_{st} and I_{st} are the second moments of area of a T-shaped column flange, of a T-shaped beam flange and of a rectangular stiffener, respectively, and $L_{h,fc,T}$, $L_{h,fb,T}$ and $L_{h,st}$ are the equivalent lengths of the hinges. The analytical expressions for computing these two geometric properties are given in APPENDIX D.1 (see Eqs. (D-7) and (D-10) for a T-shaped flange and Eqs. (D-8) and (D-11) for a rectangular one). In addition, the parameter η in Eq. (5-27) is a stiffness modification coefficient which accounts for the actual non-linear behaviour of the hinges and for the fact that not all the hinges will actually form simultaneously. This coefficient has been set at 3.0, following the EN 1993-1-8 approach.

Consequently, the yield shear distortion γ_y^{SE} of the SE can easily be deduced from Eq. (5-27), as expressed through Eq. (5-28). The post-plastic stiffness K_{pp}^{SE} is then simply obtained by substituting, in Eq. (5-27), the Young's modulus E by the post-plastic modulus E_{pp}, leading to Eq. (5-29), where a distinction is made again between the unstiffened joints, the stiffened interior joints and the stiffened exterior ones. In the post-elastic range, the parameter η can be taken equal to 1.0. Based on these values, the shear deformation of the SE at necking can be defined through Eq. (5-30). For sake of clarity, the parameters K_y^{SE}, γ_y^{SE}, K_{pp}^{SE} and γ_{pp}^{SE} were reported in Table 5-6 for unstiffened joints only.

$$\gamma_y^{SE} = \frac{1}{\eta} \cdot \frac{\Delta V_{y,Rk,compl}^{SE}}{K_y^{SE}} \tag{5-28}$$

$$K_{pp}^{SE} = \begin{cases} \frac{1}{\eta} \cdot \left[4 \cdot \frac{E_{pp} \cdot I_{fc,T}}{L_{h,fc,T} \cdot d_b^*} \right] & \text{unstiffened joints} \\ \frac{1}{\eta} \cdot \left[4 \cdot \frac{E_{pp} \cdot I_{fc,T}}{L_{h,fc,T} \cdot d_b^*} + \min\left(4 \cdot \frac{E_{pp} \cdot I_{fb,T}}{L_{h,fb,T} \cdot d_b^*}; 4 \cdot \frac{E_{pp} \cdot I_{st}}{L_{h,st} \cdot d_b^*} \right) \right] & \text{stiffened int. joints} \\ \frac{1}{\eta} \cdot \left[4 \cdot \frac{E_{pp} \cdot I_{fc,T}}{L_{h,fc,T} \cdot d_b^*} + \min\left(2 \cdot \frac{E_{pp} \cdot I_{fb,T}}{L_{h,fb,T} \cdot d_b^*}; 4 \cdot \frac{E_{pp} \cdot I_{st}}{L_{h,st} \cdot d_b^*} \right) \right] & \text{stiffened ext. joints} \end{cases} \tag{5-29}$$

$$\gamma_n^{SE} = \gamma_y^{SE} + \frac{\Delta V_{n,Rk,compl}^{SE} - \Delta V_{y,Rk,compl}^{SE}}{K_{pp}^{SE}} \tag{5-30}$$

C. Validation

All the parameters in Table 5-6 being known, the full-range behaviour of the SE can be analytically predicted for the 20 numerical simulations characterized by PZ ultimate failure mode. Based on the comparisons between the analytical and numerical results, the full-range model of the SE presented in Fig. 5-8(c) has been slightly modified to better fit the numerical results. The modified model is presented in Fig. 5-8(d) and all the parameters of the model are given in Table 5-6. In this model, a new coefficient has been introduced, namely ΔC_y^{SE}. Similarly to the CWP, this coefficient is a fitting parameter and accounts for the actual stress distribution within the plastic hinges (i.e. not all the fibres in the hinge start yielding at the same time). This coefficient has been calibrated to the numerical results: from this calibration, it has been considered that $\Delta C_y^{SE} = 0.9$ is reasonable.

A graphical comparison between the numerical results and the modified analytical model is provided in APPENDIX C (see the light green solid curves and the dark green broken curves in Figs. C-1(d) to C-32(d), respectively) for the 32 numerical simulations performed within the framework of the numerical study. The parameters of the analytical $(\Delta V^{SE} - \gamma)_{an}$ curves are given in Tables C-1 to C-32 in APPENDIX C. Furthermore, the geometric 2nd order effects were accounted for, using a $1/\cos\gamma$ factor, see APPENDIX E. As for the numerical $(\Delta V^{SE} - \gamma)_{num}$ curves, they were derived based on the procedure presented in APPENDIX B.1.

From this comparison, a good agreement can be observed between the numerical curve and the analytical model, especially for the 20 numerical simulations characterized by PZ ultimate failure mode. For these latter, the final shear resistance $\Delta V_{f,Rk,compl}^{SE}$ and the final shear distortion γ_f^{SE} of the SE have been computed through Eqs. (5-31) and (5-32). The results are reported in Table 5-9, together with the predicted ultimate failure mode (i.e. the fracture of the material, MF).

$$\Delta V_{f,Rk,compl}^{SE} = \Delta V_{n,Rk,compl}^{SE} \tag{5-31}$$

$$\gamma_f^{SE} = \gamma_n^{SE} \tag{5-32}$$

Table 5-8. Description of the final shear resistance $V_{f,Rk,compl}^{CWP}$, final shear deformation $\gamma_{f,compl}^{CWP}$ and ultimate failure mode of the CWP for the 20 numerical simulations characterized by a PZ failure mode.

Configuration	Category I (X="d", Y="/")			Category II (X="s", Y="/")		
	$V_{f,Rk,compl}^{CWP}$ (kN)	$\gamma_{f,compl}^{CWP}$ (rad)	Ult. fail. mode	$V_{f,Rk,compl}^{CWP}$ (kN)	$\gamma_{f,compl}^{CWP}$ (rad)	Ult. fail. mode
NR4-0-X-Y	434.27	0.2116	LB_{PZ}	/	/	/
NR4-1-X-Y	436.81	0.2221	LB_{PZ}	414.97	0.2110	LB_{PZ}
NR16-0-X-Y	977.18	0.0680	LB_{PZ}	/	/	/
NR16-1-X-Y	1023.05	0.0764	LB_{PZ}	971.90	0.0726	LB_{PZ}
A-0-X-Y	435.55	0.2166	LB_{PZ}	/	/	/
A-1-X-Y	439.05	0.2310	LB_{PZ}	/	/	/
B-0-X-Y	1220.95	0.0702	LB_{PZ}	/	/	/
B-1-X-Y	1241.54	0.0733	LB_{PZ}	/	/	/
Configuration	Category III (X="d", Y="0.5N$_{pl}$")			Category IV (X="s", Y="0.5N$_{pl}$")		
	$V_{f,Rk,compl}^{CWP}$ (kN)	$\gamma_{f,compl}^{CWP}$ (rad)	Ult. fail. mode	$V_{f,Rk,compl}^{CWP}$ (kN)	$\gamma_{f,compl}^{CWP}$ (rad)	Ult. fail. mode
NR4-0-X-Y	423.69	0.2262	LB_{PZ}	/	/	/
NR4-1-X-Y	426.18	0.2364	LB_{PZ}	/	/	/
NR16-0-X-Y	954.18	0.0735	LB_{PZ}	/	/	/
NR16-1-X-Y	998.96	0.0817	LB_{PZ}	949.01	0.0776	LB_{PZ}
A-0-X-Y	424.94	0.2311	LB_{PZ}	/	/	/
A-1-X-Y	428.37	0.2452	LB_{PZ}	406.95	0.2329	LB_{PZ}
B-0-X-Y	1190.31	0.0762	LB_{PZ}	/	/	/
B-1-X-Y	1210.38	0.0792	LB_{PZ}	/	/	/

Table 5-9. Description of the final shear resistance $\Delta V_{n,Rk,compl}^{SE}$, final shear deformation $\gamma_{n,compl}^{SE}$ and ultimate failure mode of the SE for the 20 numerical simulations characterized by a PZ failure mode.

Configuration	Category I (X="d", Y="/")			Category II (X="s", Y="/")		
	$\Delta V_{f,Rk,compl}^{SE}$ (kN)	$\gamma_{f,compl}^{SE}$ (rad)	Ult. fail. mode	$\Delta V_{f,Rk,compl}^{SE}$ (kN)	$\gamma_{f,compl}^{SE}$ (rad)	Ult. fail. mode
NR4-0-X-Y	67.56	0.1369	MF	/	/	/
NR4-1-X-Y	108.94	0.1084	MF	98.37	0.1306	MF
NR16-0-X-Y	187.91	0.1278	MF	/	/	/
NR16-1-X-Y	519.82	0.1558	MF	372.61	0.1365	MF
A-0-X-Y	112.36	0.1367	MF	/	/	/
A-1-X-Y	147.04	0.1334	MF	/	/	/
B-0-X-Y	378.36	0.1344	MF	/	/	/
B-1-X-Y	429.58	0.1332	MF	/	/	/
Configuration	Category III (X="d", Y="0.5N$_{pl}$")			Category IV (X="s", Y="0.5N$_{pl}$")		
	$\Delta V_{f,Rk,compl}^{SE}$ (kN)	$\gamma_{f,compl}^{SE}$ (rad)	Ult. fail. mode	$\Delta V_{f,Rk,compl}^{SE}$ (kN)	$\gamma_{f,compl}^{SE}$ (rad)	Ult. fail. mode
NR4-0-X-Y	58.84	0.1512	MF	/	/	/
NR4-1-X-Y	100.21	0.1153	MF	/	/	/
NR16-0-X-Y	167.81	0.1388	MF	/	/	/
NR16-1-X-Y	497.60	0.1344	MF	352.53	0.1424	MF
A-0-X-Y	97.86	0.1509	MF	/	/	/
A-1-X-Y	132.55	0.1440	MF	115.20	0.1468	MF
B-0-X-Y	332.36	0.1477	MF	/	/	/
B-1-X-Y	383.63	0.1448	MF	/	/	/

5.3.1.4 Validation

A. Validation against numerical results

i. In terms of $(V - \gamma)$ curves

Based on the results obtained from Section 5.3.1.2 and Section 5.3.1.3, one can derive the full-range constitutive model of the PZ component for the 20 numerical simulations characterized by a PZ ultimate failure mode, using Eqs. (2-14) and (2-15). The resulting analytical $(V^{PZ} - \gamma)_{an}$ curves are reported in APPENDIX C (see the dark blue broken curves in Fig. C-1(d) to Fig. C-32(d), which integrate the geometric 2nd order effects, derived in APPENDIX E) where they are compared to the numerical $(V^{PZ} - \gamma)_{num}$ curves (see the dark blue solid curves in Fig. C-1(d) to Fig. C-32(d), V^{PZ} and γ being defined in APPENDIX B.1). These graphical comparisons between the analytical and numerical results show a fairly good agreement for the 20 numerical simulations characterized by a PZ ultimate failure mode.

Regarding the ultimate failure mode predicted by the analytical model, it is obtained as the minimum between the ultimate failure mode of the CWP (see Table 5-8) and the ultimate failure mode of the SE (see Table 5-9). The values of the predicted ultimate failure mode, final shear resistance $V^{PZ}_{f,Rk,compl}$ and final shear deformation $\gamma^{PZ}_{f,compl}$ are reported in Table 5-10, Table 5-11 and Table 5-12 where they are compared to the observed ones coming from the numerical simulations. These comparisons are conducted on the basis of the performance indicator E and the colour code defined in Table 3-1. Based on the analysis of the results in Table 5-10, Table 5-11 and Table 5-12, the analytical results can be classified into two main categories, according to the predicted level of shear buckling:

- When the predicted shear buckling of the CWP occurs in the <u>post-plastic range</u> (see Eq. (5-15)), this latter governs the ultimate resistance of the PZ. This is observed in the numerical simulations performed with the NR16 and B models. In this case, the analytical model accurately predicts the actual ultimate failure mode observed in the numerical simulations, see Table 5-10. The level of resistance at failure is also rather well predicted, as the model features a high level of accuracy for three numerical simulations and a moderate level of accuracy for the seven remaining simulations, see Table 5-11. Regarding the prediction of the deformation capacity, the model is less efficient as it underestimates, sometimes significantly, the actual shear deformation capacity $\gamma^{PZ}_{f,num}$ of the PZ, see Table 5-12. This is due to the fact that, for some numerical simulations, the shear buckling of the CWP is predicted in the post-plastic range while it actually occurs in the flowed range. Given the small stiffness of the flowed range with respect to the post-plastic range, this small difference of shear resistance can lead to a significant scatter in terms of shear deformation.
- When the predicted shear buckling of the CWP occurs in the <u>flowed range</u> (see Eq. (5-15)), the PZ ultimate failure mode is governed by the fracture of the material in the SE, rather than the shear buckling of the CWP. This is observed for the numerical simulations performed with the NR4 and A models. In this case, the analytical model mispredicts the actual ultimate failure mode observed in the numerical simulations, see Table 5-10. However, the model shows good performances in terms of both the prediction of the final shear resistance of the PZ (see Table 5-11), and the prediction of the shear deformation capacity of the PZ (see Table 5-12). For the former, the model features a high level of accuracy for five numerical simulations and a moderate level of accuracy for the five other ones. For the latter, the model features a low level of accuracy for three numerical simulations only, with a maximum relative error of 20%.

At the end, the complex analytical model developed in the present Section 5.3.1 turns out to provide a fairly good, but sometimes conservative, estimation of the full-range behaviour of the PZ up to failure.

Table 5-10. Comparisons between the predicted and observed ultimate failure modes for the 20 numerical simulations characterized by a PZ ultimate failure mode.

Configuration	Category I (X="d", Y="/")		Category II (X="s", Y="/")	
	Observation	Prediction	Observation	Prediction
NR4-0-X-Y	LB_{PZ}	MF	/	/
NR4-1-X-Y	LB_{PZ}	MF	LB_{PZ}	MF
NR16-0-X-Y	LB_{PZ}	LB_{PZ}	/	/
NR16-1-X-Y	LB_{PZ}	LB_{PZ}	LB_{PZ}	LB_{PZ}
A-0-X-Y	LB_{PZ}	MF	/	/
A-1-X-Y	LB_{PZ}	MF	/	/
B-0-X-Y	LB_{PZ}	LB_{PZ}	/	/
B-1-X-Y	LB_{PZ}	LB_{PZ}	/	/
Configuration	Category III (X="d", Y="0.5N_pl")		Category IV (X="s", Y="0.5N_pl")	
	Observation	Prediction	Observation	Prediction
NR4-0-X-Y	LB_{PZ}	MF	/	/
NR4-1-X-Y	LB_{PZ}	MF	/	/
NR16-0-X-Y	LB_{PZ}	LB_{PZ}	/	/
NR16-1-X-Y	LB_{PZ}	LB_{PZ}	LB_{PZ}	LB_{PZ}
A-0-X-Y	LB_{PZ}	MF	/	/
A-1-X-Y	LB_{PZ}	MF	LB_{PZ}	MF
B-0-X-Y	LB_{PZ}	LB_{PZ}	/	/
B-1-X-Y	LB_{PZ}	LB_{PZ}	/	/

Table 5-11. Comparisons between $V_{f,Rk,compl}^{PZ}$ and $V_{f,Rk,num}^{PZ}$ for the 20 numerical simulations characterized by a PZ ultimate failure mode.

Configuration	Category I (X="d", Y="/")			Category II (X="s", Y="/")		
	$V_{f,Rk,num}^{PZ}$ (kN)	$V_{f,Rk,compl}^{PZ}$ (kN)	E (%)	$V_{f,Rk,num}^{PZ}$ (kN)	$V_{f,Rk,compl}^{PZ}$ (kN)	E (%)
NR4-0-X-Y	459.6	483.7	5.25	/	/	/
NR4-1-X-Y	490.8	518.2	5.58	464.9	493.8	6.23
NR16-0-X-Y	1,179.1	1,118.8	-5.12	/	/	/
NR16-1-X-Y	1,535.8	1,402.7	-8.66	1,338.4	1,252.5	-6.41
A-0-X-Y	530.7	528.5	-0.41	/	/	/
A-1-X-Y	552.4	562.4	1.80	/	/	/
B-0-X-Y	1,510.7	1,504.2	-0.43	/	/	/
B-1-X-Y	1,622.2	1,569.0	-3.28	/	/	/
Configuration	Category III (X="d", Y="0.5N_pl")			Category IV (X="s", Y="0.5N_pl")		
	$V_{f,Rk,num}^{PZ}$ (kN)	$V_{f,Rk,compl}^{PZ}$ (kN)	E (%)	$V_{f,Rk,num}^{PZ}$ (kN)	$V_{f,Rk,compl}^{PZ}$ (kN)	E (%)
NR4-0-X-Y	441.3	464.3	5.21	/	/	/
NR4-1-X-Y	467.3	497.0	6.36	/	/	/
NR16-0-X-Y	1,103.1	1,071.4	-2.87	/	/	/
NR16-1-X-Y	1,473.2	1,385.7	-5.93	1,286.3	1,208.4	-6.06
A-0-X-Y	498.2	503.4	1.03	/	/	/
A-1-X-Y	524.7	536.4	2.22	490.0	501.3	2.30
B-0-X-Y	1,334.0	1,416.7	6.20	/	/	/
B-1-X-Y	1,373.2	1,482.5	7.96	/	/	/

Table 5-12. Comparisons between $\gamma^{PZ}_{f,compl}$ and $\gamma^{PZ}_{f,num}$ for the 20 numerical simulations characterized by a PZ ultimate failure mode.

Configuration	Category I (X="d", Y="/")			Category II (X="s", Y="/")		
	$\gamma^{PZ}_{f,num}$ (rad)	$\gamma^{PZ}_{f,compl}$ (rad)	E $(\%)$	$\gamma^{PZ}_{f,num}$ (rad)	$\gamma^{PZ}_{f,compl}$ (rad)	E $(\%)$
NR4-0-X-Y	0.1369	0.1369	0.00	/	/	/
NR4-1-X-Y	0.1265	0.1084	-14.31	0.1443	0.1306	-9.49
NR16-0-X-Y	0.0887	0.0680	-23.34	/	/	/
NR16-1-X-Y	0.1215	0.0764	-37.12	0.1236	0.0726	-41.26
A-0-X-Y	0.1715	0.1366	-20.35	/	/	/
A-1-X-Y	0.1535	0.1334	-13.09	/	/	/
B-0-X-Y	0.1198	0.0702	-41.40	/	/	/
B-1-X-Y	0.1453	0.0733	-49.55	/	/	/
Configuration	Category III (X="d", Y="0.5N$_{pl}$")			Category IV (X="s", Y="0.5N$_{pl}$")		
	$\gamma^{PZ}_{f,num}$ (rad)	$\gamma^{PZ}_{f,compl}$ (rad)	E $(\%)$	$\gamma^{PZ}_{f,num}$ (rad)	$\gamma^{PZ}_{f,compl}$ (rad)	E $(\%)$
NR4-0-X-Y	0.1453	0.1512	4.06	/	/	/
NR4-1-X-Y	0.1215	0.1153	-5.10	/	/	/
NR16-0-X-Y	0.0787	0.0735	-6.61	/	/	/
NR16-1-X-Y	0.1144	0.0817	-28.58	0.1279	0.0776	-39.33
A-0-X-Y	0.1531	0.1509	-1.44	/	/	/
A-1-X-Y	0.1377	0.1440	4.58	0.1489	0.1468	-1.41
B-0-X-Y	0.0741	0.0762	2.83	/	/	/
B-1-X-Y	0.0698	0.0792	13.47	/	/	/

ii. In terms of $(M - \Phi)$ curves

Based on this new model for the prediction of the PZ behaviour up to failure, one can assess the ability of the "extended" component method to predict the full $\left(M^j - \Phi\right)_{num}$ curves of the 32 joints considered in the present parametric study. These curves can be obtained from the assembly of the deformation curves of each individual active component in the joint, following the exact same procedure as the one presented in Section 3.3.1.2. This procedure is briefly recalled here below.

As a first step, the $(V^{PZ} - \gamma)_{an}$ curves derived in the previous section are translated into $(M^{PZ} - \gamma)_{an}$ curves using Eqs. (4-27) and (4-28). These equations, which are more general versions of Eq. (3-5), have been obtained by isolating P in Eqs. (B-8) and (B-12) and injecting this value in Eq. (B-20). The so-obtained $(M^{PZ} - \gamma)_{an}$ curves are depicted in Appendix C (see the dark blue solid curves in Figs. C-1(f) to C-32(f)) for the 32 numerical simulations considered in the parametric study.

Secondly, the $(F^c - \Delta^c)_{an}$ curves (subscript "c" standing for CWC*, CWT, CFB or BFC) can be analytically derived for all the other active components, using: (i) the analytical expressions provided in Table 2-2 for the description of the component elasto-plastic behaviour and (ii) the procedure suggested by Jaspart (see Section 2.2.3.2) for the description of the component post-plastic behaviour up to failure. The main parameters of these $(F^c - \Delta^c)_{an}$ curves are given in Appendix C (see Tables C-1 to C-32) for each numerical simulation. These curves were then transformed into $(M^c - \phi^c)_{an}$ curves, by applying Eq. (3-5). The so-obtained $(M^c - \phi^c)_{an}$ curves are depicted in Appendix C for each numerical simulation (see Figs. C-1(f) to C-32(f), where the solid green, pink, purple and blue curves are associated to the CWC*, CWT, CFB and BFC components, respectively). The main parameters of these $(M^c - \phi^c)_{an}$ curves are reported in Tables C-1 to C-32. It is noteworthy that: (i) the resistance of the BFC was limited to the plastic resistance to account for the risk of local buckling, as explained in Section 3.3.1.2, and (ii) the characterization of the CWC* was carried out following the procedure developed in [21].

The component $(M^{PZ} - \gamma)_{an}$ and $(M^c - \phi^c)_{an}$ deformation curves were eventually assembled to obtain the overall joint $\left(M^j - \Phi\right)_{an}$ curves. These curves are depicted in Appendix C (see the bolded red solid curves in Figs. C-1(f) to C-32(f)) for the 32 numerical simulations, where they are compared to the numerical $\left(M^j - \Phi\right)_{num}$ curves which can be obtained from the procedure described in Appendix B.2.

To facilitate the comparisons between the numerical results and the analytical predictions, the predicted ultimate failure mode, ultimate bending moment resistance $M^j_{u,Rk,compl}$ and ultimate rotation capacity $\Phi_{u,compl}$ are reported in Table 5-13 to Table 5-15 for each numerical simulation, where they are compared to the numerical ones. These comparisons are conducted on the basis of the performance indicator E and the colour code defined in Table 3-1. The following observations can be made from Table 5-13 to Table 5-15 and Figs. C-1(f) to C-32(f) in Appendix C:

- For 18 of the 32 numerical simulations, the model predicts a PZ ultimate failure mode, see Table 5-13. For these simulations, both $M^j_{u,Rk,num}$ and $\Phi_{u,num}$ values are predicted with a fairly reasonable level of accuracy (see the discussion here above). The observed failure mode is also correctly predicted for all 18 numerical simulations, which gives confidence in the full-range PZ model developed in the present CHAPTER 5.
- For six numerical simulations, the analytical model predicts a CFB ultimate failure mode, see Table 5-13. For these simulations, the ultimate bending moment resistance $M^j_{u,Rk,num}$ and the ultimate rotation capacity $\Phi_{u,num}$ are significantly underestimated by the analytical model, as shown in Table 5-14 and Table 5-15, respectively. The observed failure mode is also mispredicted for one numerical simulation (namely the B-0-d-/ simulation, see Table 5-13).

From the author's point of view, these discrepancies arise from two main causes: (i) the consideration of the engineering material properties (instead of the true ones) for the computation of $M_{u,Rk,compl}^{j}$ and (ii) the non-consideration of the CFB deformability in the derivation of $\Phi_{u,compl}$ (the latter being accounted for in the deformation of the beam), whereas it is actually included in the numerical $\left(M^{j} - \Phi\right)_{num}$ curves (since the procedure described in Appendix B.2 does not allow to differentiate the CFB deformability from the total rotation ϕ of the connection). Addressing these two issues would most likely bring the analytical and numerical $\left(M^{j} - \Phi\right)$ curves closer to each other and change the predicted ultimate failure mode in the simulation B-0-d-/ from CFB to PZ, the latter being the one observed in the numerical simulation.

- For five numerical simulations, the model predicts a CWC* ultimate failure mode, see Table 5-13. For these simulations, the ultimate bending moment resistance $M_{u,Rk,num}^{j}$ and the ultimate rotation capacity $\Phi_{u,num}$ are significantly underestimated by the model, as shown in Table 5-14 and Table 5-15, respectively. The observed failure mode is also mispredicted for four of the five numerical simulations, see Table 5-13. According to the author, these discrepancies arise from the non-consideration, in the numerical simulations, of an equivalent geometric imperfection associated to the potential local buckling of the CWC* component. Indeed, the initial geometric imperfection is known to influence significantly the CWC* buckling resistance and, consequently, the ultimate deformation capacity of the CWC*. Introducing such geometric imperfection in the models would most likely reduce both $M_{u,Rk,num}^{j}$ and $\Phi_{u,num}$ numerical values, thus bringing the analytical predictions closer to the numerical results.

- For the last three numerical simulations (i.e. the NR4-0-s-0.5Npl, NR4-0-d-0.5Npl and A-0-s-0.5Npl simulations), the governing failure mode is the global buckling of the column, see Table 5-13. This failure mode bypasses the failure of the joint, which makes these numerical results irrelevant in the present study.

Table 5-13. Comparisons between the predicted and observed ultimate failure modes in the numerical simulations.

Configuration	Category I (X="d", Y="/")		Category II (X="s", Y="/")	
	Observation	Prediction	Observation	Prediction
NR4-0-X-Y	LB_{PZ}	PZ	MF	CWC^{*}
NR4-1-X-Y	LB_{PZ}	PZ	LB_{PZ}	PZ
NR16-0-X-Y	LB_{PZ}	PZ	$LB_{CWC^{*}}$	CWC^{*}
NR16-1-X-Y	LB_{PZ}	PZ	LB_{PZ}	PZ
A-0-X-Y	LB_{PZ}	PZ	MF	CWC^{*}
A-1-X-Y	LB_{PZ}	PZ	MF	CFB
B-0-X-Y	LB_{PZ}	CWC^{*}	MF	CFB
B-1-X-Y	LB_{PZ}	CFB	MF	CFB
Configuration	Category III (X="d", Y="0.5N_{pl}")		Category IV (X="s", Y="0.5N_{pl}")	
	Observation	Prediction	Observation	Prediction
NR4-0-X-Y	LB_{PZ}	PZ	GB_{c}	/
NR4-1-X-Y	LB_{PZ}	PZ	GB_{c}	/
NR16-0-X-Y	LB_{PZ}	PZ	$LB_{CWC^{*}}$	CWC^{*}
NR16-1-X-Y	LB_{PZ}	PZ	LB_{PZ}	PZ
A-0-X-Y	LB_{PZ}	PZ	GB_{c}	/
A-1-X-Y	LB_{PZ}	PZ	LB_{PZ}	PZ
B-0-X-Y	LB_{PZ}	PZ	MF	CFB
B-1-X-Y	LB_{PZ}	PZ	MF	CFB

Table 5-14. Comparisons between $M_{u,Rk,compl}^{j}$ and $M_{u,Rk,num}^{j}$.

Configuration	Category I (X="d", Y="/")			Category II (X="s", Y="/")		
	$M_{u,Rk,num}^{j}$ (kNm)	$M_{u,Rk,compl}^{j}$ (kNm)	E (%)	$M_{u,Rk,num}^{j}$ (kNm)	$M_{u,Rk,compl}^{j}$ (kNm)	E (%)
NR4-0-X-Y	79.6	83.1	4.40	142.0	130.4	-8.17
NR4-1-X-Y	85.1	88.9	4.47	158.0	167.9	6.27
NR16-0-X-Y	320.9	298.3	-7.04	583.5	414.4	-28.98
NR16-1-X-Y	416.2	379.6	-8.79	709.7	676.4	-4.69
A-0-X-Y	53.0	52.3	-1.32	90.4	79.2	-12.39
A-1-X-Y	55.3	55.9	1.08	96.5	83.0	-13.99
B-0-X-Y	237.9	218.3	-8.24	346.6	236.8	-31.68
B-1-X-Y	254.5	236.8	-6.95	352.5	236.8	-32.82
Configuration	Category III (X="d", Y="0.5N$_{pl}$")			Category IV (X="s", Y="0.5N$_{pl}$")		
	$M_{u,Rk,num}^{j}$ (kNm)	$M_{u,Rk,compl}^{j}$ (kNm)	E (%)	$M_{u,Rk,num}^{j}$ (kNm)	$M_{u,Rk,compl}^{j}$ (kNm)	E (%)
NR4-0-X-Y	51.3	54.8	6.82	93.6	/	/
NR4-1-X-Y	59.5	66.1	11.09	98.8	/	/
NR16-0-X-Y	251.5	236.4	-6.00	450.4	414.4	-7.99
NR16-1-X-Y	328.8	312.0	-5.11	522.9	546.8	4.57
A-0-X-Y	34.6	36.1	4.34	62.5	/	/
A-1-X-Y	38.8	39.6	2.06	68.5	71.7	4.67
B-0-X-Y	177.4	187.9	5.92	292.5	236.8	-19.04
B-1-X-Y	185.6	190.5	2.64	325.0	236.8	-27.14

Table 5-15. Comparisons between $\Phi_{u,compl}$ and $\Phi_{u,num}$.

Configuration	Category I (X="d", Y="/")			Category II (X="s", Y="/")		
	$\Phi_{u,num}$ (rad)	$\Phi_{u,compl}$ (rad)	E (%)	$\Phi_{u,num}$ (rad)	$\Phi_{u,compl}$ (rad)	E (%)
NR4-0-X-Y	0.1225	0.1310	6.94	0.0990	0.0607	-38.69
NR4-1-X-Y	0.1129	0.0989	-12.40	0.1317	0.1172	-11.01
NR16-0-X-Y	0.0758	0.0677	-10.69	0.0909	0.0183	-79.87
NR16-1-X-Y	0.1043	0.0749	-28.19	0.1083	0.0715	-33.98
A-0-X-Y	0.1574	0.1311	-16.71	0.1446	0.0555	-61.62
A-1-X-Y	0.1414	0.1235	-12.66	0.1474	0.0422	-71.37
B-0-X-Y	0.1096	0.0604	-44.89	0.1724	0.0096	-94.43
B-1-X-Y	0.1375	0.0602	-56.22	0.1580	0.0023	-98.54
Configuration	Category III (X="d", Y="0.5N$_{pl}$")			Category IV (X="s", Y="0.5N$_{pl}$")		
	$\Phi_{u,num}$ (rad)	$\Phi_{u,compl}$ (rad)	E (%)	$\Phi_{u,num}$ (rad)	$\Phi_{u,compl}$ (rad)	E (%)
NR4-0-X-Y	0.1379	0.1460	5.87	0.0545	/	/
NR4-1-X-Y	0.1172	0.1098	-6.31	0.0469	/	/
NR16-0-X-Y	0.0681	0.0663	-2.64	0.0882	0.0485	-45.01
NR16-1-X-Y	0.0986	0.0716	-27.38	0.1202	0.0753	-37.35
A-0-X-Y	0.1430	0.1360	-4.90	0.1122	/	/
A-1-X-Y	0.1281	0.1377	7.49	0.1531	0.1432	-6.47
B-0-X-Y	0.0679	0.0804	18.41	0.1195	0.0115	-90.38
B-1-X-Y	0.0639	0.0698	9.23	0.1359	0.0046	-96.62

B. *Validation against experimental results*

As a second validation step, the performances of the new full-range analytical model were assessed through comparisons with the 12 experimental results on welded joints reported in Table 3-2. Among them, four tests (namely the tests NR2, NR3, NR4 and NR7) were excluded from the study since the strain-hardening and ultimate material properties are not available. The comparisons were conducted on the basis of the experimental $(M^j - \Phi)_{exp}$ curves of the joints. Therefore, the component method was applied, similarly to what was done in Section 3.3.1.2 where the performances of the Jaspart model were evaluated against the same experimental results. This procedure firstly requires the characterization of the PZ component in terms of its $(M^{PZ} - \gamma)_{an}$ deformation curve and the characterization of the other active components in terms of their $(M^c - \phi^c)_{an}$ deformation curves. As a second step, these $(M^{PZ} - \gamma)_{an}$ and $(M^c - \phi^c)_{an}$ curves need to be assembled to get the overall $(M^j - \Phi)_{an}$ curve of the joint. The latter can eventually be compared to the experimental $(M^j - \Phi)_{exp}$ curve for each of the eight relevant experimental results on welded joints.

Defining an adequate material model for the characterization of the material laws is a preliminary step to the characterization of the components' behaviour. The PZ full-range model developed in the present CHAPTER 5 requires quad-linear material laws as input. So far, two types of quad-linear material models have been contemplated in the present thesis, namely: (i) the sophisticated EN 1993-1-14 model in CHAPTER 4 (see Section 4.2.2) and (ii) the simpler ECCS model in the present CHAPTER 5 (see Section 5.2.2). These two material models will be considered and compared in the present study, the goal being to investigate the influence of the material modelling on the accuracy of the predictions at the component level.

Particular attention will be paid to three test results, namely tests BCC5-E, E1.1 and E1.2, for which the coupon test results are available for the columns and beams' webs and flanges. These results are presented in Fig. 5-10 in terms of engineering stress-strain curves (see the black dashed curves in Fig. 5-10), thereby allowing the investigation of the performances of the ECCS and EN 1993-1-14 material models. The engineering stress-stress curves, reconstructed with the two material models, are also plotted in Fig. 5-10 (see the blue and orange solid curves, obtained with the ECCS and EN 1993-1-14 model, respectively). Comparisons with the experimental curves show that the more advanced EN 1993-1-14 material model performs better than the simpler ECCS one, even though it sometimes underestimates the actual deformation capacity of the steel material.

Based on these two material models, two analytical $(M^j - \Phi)_{an}$ curves can be derived for each relevant experimental result. The graphical comparisons with the experimental $(M^j - \Phi)_{exp}$ curves are provided in Appendix A (see Figs. A-1(h) to A-12(h)), where several curves are depicted:

- the $(M^c - \phi^c)_{an}$ curves of the CFB and BFC components, plus the CWC* and CWT components, when relevant (see the purple, sky-blue, green and pink solid curves in Figs. A-1(h) to A-12(h), respectively);
- the $(M^{PZ} - \gamma)_{an}$ curves of the PZ component, obtained with the ECCS and En 1993-1-14 material models (see the blue solid and dashed curves in Figs. A-1(h) to A-12(h), respectively);
- the $(M^j - \Phi)_{an}$ curves of the joints, obtained from the assembly of the different components' moment-rotation curves (see the bolded red solid and dashed curves in Figs. A-1(h) to A-12(h), the former being derived with the ECCS material model and the latter with the EN 1993-1-14 one);
- the experimental $(M^j - \Phi)_{exp}$ curves associated to each relevant experimental result (see the black solid and dashed curves in Figs. A-1(h) to A-12(h)).
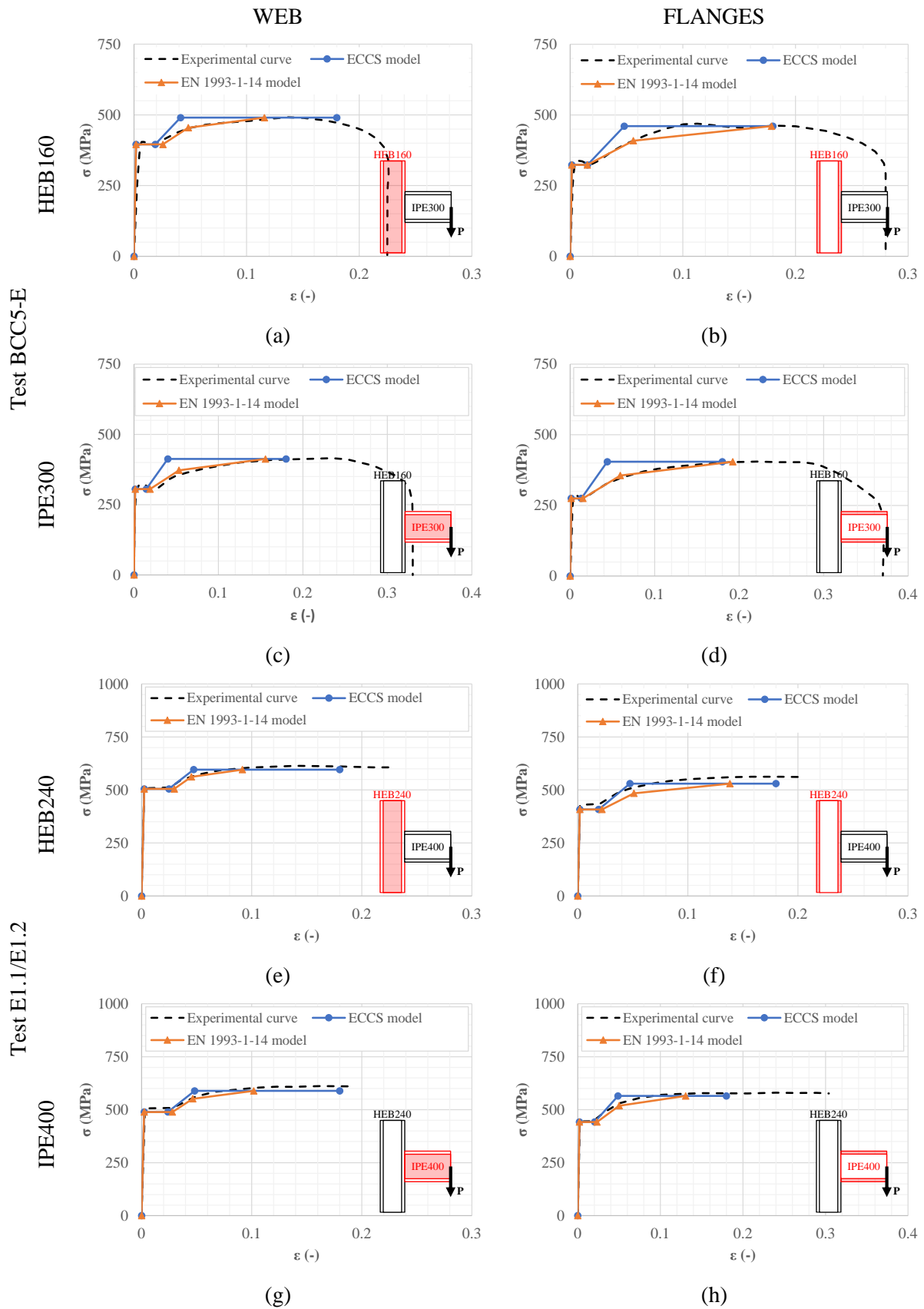
Fig. 5-10. Comparisons between the coupon test results and the ECCS and EN 1993-1-14 models for the test results BCC5-E and E1.1: (a) HEB160 column web, (b) HEB160 column flanges, (c) IPE300 beam web, (d) IPE300 beam flanges, (e) HEB240 column web, (f) HEB240 column flanges, (g) IPE400 beam web and (h) IPE400 beam flanges.

The following conclusions can be drawn from the visual comparisons between the analytical and experimental results in Figs. A-1(h) to A-12(h), see Appendix A:

- For the test B1, a really good agreement is observed between the experimental $\left(M^j - \Phi\right)_{exp}$ curve and the analytical $\left(M^j - \Phi\right)_{an}$ prediction when the ECCS material model is used (see the blue solid curve in Fig. A-1(h)). This suggests that the PZ behaviour is accurately predicted with the new proposed analytical model. By contrast, when the EN 1993-1-14 material model is used, significant discrepancies are observed after the initiation of strain-hardening. These observations suggest that the EN 1993-1-14 material model poorly predicts the material post-plastic modulus E_{pp} for this specific test.

  As regards the ultimate failure mode, it is correctly yet conservatively predicted. This conservative result arises from the computation of the ultimate resistance of the BFC, which uses the yield material properties instead of the ultimate ones to account for the possible risk of local buckling. More accurate predictions would be possible when a formula accounting for that risk becomes available in the code.

- For the test BCC5-E, it can be observed that the PZ behaviour is rather well predicted when the ECCS material model is used even though the deformation capacity is slightly underestimated (see the blue solid curve in Fig. A-6(h)). By contrast, the analytical curve obtained with the EN 1993-1-14 material model is more consistent in terms of deformation capacity, but underestimates the actual PZ deformation curve. These results may look contradictory as the analysis of the coupon tests in Fig. 5-10(a)-(d) shows more reliable predictions with the EN 1993-1-14 material model. An explanation for these unexpected conservative predictions may come from the derivation of the β parameter, which was used to transform the $(V^{PZ} - \gamma)_{an}$ curve into an $(M^{PZ} - \gamma)_{an}$ curve. This parameter, which can be derived from Eq. (3-3), accounts for the shear effect in the column. The BCC5-E test setup being statically undetermined (see Fig. A-6(a)), an assumption was made for the distribution of the bending moment in the column (i.e. $b = 0.25$ in Eq. (3-3)), thereby allowing the derivation of β. Consequently, the model imprecision may be attributed to this assumption.

  As regards the ultimate failure mode, it is significantly underestimated by the model. This is due to the misprediction of the actual ultimate failure mode. Indeed, the model predicts a CFB failure mode whereas the experimental test was stopped due to the initiation of local buckling in the BFC. From the author's point of view, this misprediction arises from the computation of the CFB ultimate resistance which uses the engineering material properties instead of the true ones, thereby leading to the underestimation of the actual CFB ultimate resistance.

- For the tests XU-W1 and XU-CWP1, it can be seen from Figs. A-7(h) and A-8(h) in Appendix A that the model works well, especially when the ECCS material model is used for the characterization of the material laws.

  However, the model fails in predicting the actual failure mode, i.e. the fracture of the welds at the beam-to-column interface. This is because this failure mode is beyond the scope of the present thesis which assumes the welds to be fully resistant (i.e. no brittle failure in the welds, see Section 5.1.2).

- For the tests E1.1 and E1.2 (see Figs. A-9(h) and A-10(h) in Appendix A), it can be seen that the model works pretty well too, regardless of which material model is used. This is easily understandable given that both ECCS and EN 1993-1-14 models show very similar results in terms of prediction of the material laws in Fig. 5-10(e)-(f).

The actual failure mode (i.e. the local buckling of the CWC*) is also very well captured by the model, what gives confidence in the new procedure developed in ([21], [22]) for the characterization of the CWC* behaviour up to failure.

- For the <u>test CP-R-M</u>, it can be seen from Fig. A-11(h) in Appendix A that the model predicts very well the elasto-plastic behaviour of the joint, regardless of which material model is used. However, once strain-hardening initiates, the two predictions of the PZ behaviour, obtained with the ECCS and EN 1993-1-14 models, start diverging quite significantly from each other. The same observation was made for the test B1, but, here, none of the two predictions succeeds in accurately capturing the actual post-plastic behaviour of the joint. The former overestimates the post-plastic stiffness, thus leading to the underestimation of the ultimate deformation capacity; and the reverse applies for the latter.

  This observation emphasizes the importance of a very careful modelling of the material laws, especially the post-plastic ranges of the latter.

- For the <u>test No. 3</u>, shear buckling occurred in the PZ, somewhere in between the rotations $\Phi = 0.05$ and $\Phi = 0.15$ (see Fig. A-12(h) in Appendix A), but the exact rotation at which the shear buckling initiated in the PZ was not specified in [117]. The push over test was carried on beyond the PZ shear buckling but, it was stopped before fracture occurs in the material, due to the attainment of the test setup limitations. Based on these observations, it can be concluded from Fig. A-12(h) in Appendix A that the model predicts very well the PZ behaviour up to the shear buckling of the PZ (highlighted with the blue triangles in Fig. A-12(h)). The analytical prediction obtained with the EN 1993-1-14 material model outperforms a little bit the one derived with the ECCS material model.

  Assuming that the shear buckling of the PZ is allowed, the post-buckling behaviour of the PZ is very well predicted too (see the final dotted part of the blue curves in Fig. A-12(h)). With the EN 1993-1-14 material model, the actual deformation capacity of the PZ can be captured, whereas the deformation capacity is limited by the fracture of the material in the SE (highlighted with a blue square in Fig. A-12(h)) with the ECCS material model.

Based on these comparisons, it can be concluded that the new complex analytical model, which was developed in the present Section 5.3.1, shows rather good performances in terms of prediction of the PZ behaviour up to failure. However, an important outcome from this study is the high sensitivity of the model to the specimen material laws used as inputs in the model. Significant attention must thus be paid to the modelling of the material laws.

5.3.2 Simplified analytical model

5.3.2.1 Introduction

From the author's point of view, the derivation of a simplified analytical model for the prediction of the PZ full-range behaviour is of moderate interest. In fact, when it comes to the prediction of the joint ductility, sophisticated numerical tools will be used thereby allowing the integration of more accurate complex full-range analytical models, such as the one derived in the previous Section 5.3.1.

However, there is a clear need for improved analytical expressions for the prediction of the PZ initial stiffness $K_{y,simpl}^{PZ}$, plastic shear resistance $V_{y,Rk,simpl}^{PZ}$ and deformation capacity $\gamma_{f,simpl}^{PZ}$. Indeed, it was shown in Section 3.3.1.1 that the current EN 1993-1-8 formulae, taken from the Jaspart model (see Table Table 2-6), significantly overestimates the actual PZ initial stiffness and plastic resistance in many cases. In addition, a simplified criterion for the prediction of the deformation capacity $\gamma_{f,simpl}^{PZ}$ of the PZ is also required, as it was shown in Section 2.2.3.1 that almost no information is provided in the EN 1993-1-8 as regards the deformation capacity of the individual components, thus preventing any ductility prediction at the joint level. The prediction of the plastic shear resistance has already been addressed in Section 4.3.2. The following Sections 5.3.2.2 and 5.3.2.3 focus on the two remaining parameters, namely the elastic stiffness and ultimate deformation capacity, respectively.

5.3.2.2 Elastic stiffness $K_{y,simpl}^{PZ}$

As regards the initial stiffness, the complex analytical expression, given in Eq. (5-16), has been simplified by neglecting the bending deformation mode, thus leading to Eq. (5-33), where G is the shear modulus and A_{VC}^{simpl} the simplified shear area given in Fig. 4-12:

$$K_{y,simpl}^{PZ} = K_{y,simpl}^{CWP} = K_{y,sh}^{CWP} = G \cdot A_{VC}^{simpl} \tag{5-33}$$

Both complex (see Eq. (5-16)) and simplified (see Eq. (5-33)) analytical expressions have been applied to the 16 non-axially loaded numerical simulations considered in the parametric study (see Section 5.2.3). The results are reported in Table 5-16, where they are compared to the numerical values $K_{y,num}^{PZ}$ coming from the numerical simulations. These comparisons are conducted on the basis of the performance indicator E and the colour code defined in Table 3-1. From Table 5-16, it can be concluded that the simplified analytical model performs very well, with a relative error E ranging from -10.22% to $+9.62\%$ while the complex analytical model is a bit more conservative, the relative error E ranging from -19.22% to $+3.38\%$.

As a second validation step, Eqs. (5-16) and (5-33) were also applied to the six relevant experimental results on welded joints reported in Table 3-6. The results are summarized in Table 5-17 in terms of the $S_{ini,compl}^{j}$ and $S_{ini,simpl}^{j}$ values, the latter being obtained by applying Eqs. (3-1) and (3-2). The comparisons with the $S_{ini,exp}^{j}$ values, coming from Table 3-4, are conducted again on the basis of the performance indicator E and the colour code defined in Table 3-1. From these comparisons, a fairly good agreement can be observed between the analytical predictions $S_{ini,compl}^{j}$ and $S_{ini,simpl}^{j}$ and the experimental observations $S_{ini,exp}^{j}$ for the three tests results on interior joints (namely tests XU-W1, XU-CWP1 and CP-R-M). By contrast, significant discrepancies are observed for the three test results on single-sided joints (namely tests B1, BCC5-E and No. 3). Potential reasons that may explain these dispersions were given in Section 3.3.1.1. For the tests B1 and BCCE, the assumption of fixed supports, which was made for the derivation of the β parameter can be pointed out, while for the test No. 3, this scatter may be attributed to the faulty recording of the initial test data.

Proposal for amendment of the prEN 1993-1-8:

N.B.: The final proposal for the improved PZ model, suggested for inclusion in the forthcoming prEN 1993-1-8, is summarized in Appendix F. It includes amendments of the current EN 1993-1-8 expressions for the initial stiffness and plastic resistance and a proposal for a ductility criterion.

For the prediction of the initial stiffness of the PZ component, it is proposed to replace the current EN 1993-1-8 expression, taken from the Jaspart model (see Table Table 2-6), by the simplified expression proposed in Eq. (5-33). The main difference between the two expressions is the effective shear area which is used, namely A_{VC}^{compl} in the former and A_{VC}^{simpl} in the latter. It is also suggested to use this new expression for both stiffened and unstiffened joints. The complete proposal is summarized in Appendix F.1 and has been proven to perform well against numerical and experimental results. From a consistency point of view, it should also be mentioned that this new proposal for the initial stiffness is in line with the new proposal made for the prediction of the plastic shear resistance of the PZ, where the use of A_{VC}^{simpl} is also recommended.

Table 5-16. Comparisons between $K_{y,compl}^{PZ}$, $K_{y,simpl}^{PZ}$ and $K_{y,num}^{PZ}$.

| Configuration | Category I (X="d", Y="/") | | | | |
	$K_{y,num}^{PZ}$ (kN)	$K_{y,compl}^{PZ}$ (kN)	E (%)	$K_{y,simpl}^{PZ}$ (kN)	E (%)
NR4-0-X-Y	109,669.6	88,589.8	-19.22	103,384.6	-5.73
NR4-1-X-Y	108,633.9	88,589.8	-18.45	103,384.6	-4.83
NR16-0-X-Y	291,050.3	243,718.1	-16.26	266,538.5	-8.42
NR16-1-X-Y	296,883.2	243,718.1	-17.91	266,538.5	-10.22
A-0-X-Y	94,314.1	97,498.3	3.38	103,384.6	9.62
A-1-X-Y	99,467.8	97,498.3	-1.98	103,384.6	3.94
B-0-X-Y	362,316.6	319,984.5	-11.68	329,538.5	-9.05
B-1-X-Y	341,971.9	319,984.5	-6.43	329,538.5	-3.64
Configuration	Category II (X="s", Y="/")				
	$K_{y,num}^{PZ}$ (kN)	$K_{y,compl}^{PZ}$ (kN)	E (%)	$K_{y,simpl}^{PZ}$ (kN)	E (%)
NR4-0-X-Y	108,575.7	88,589.8	-18.41	103,384.6	-4.78
NR4-1-X-Y	107,211.9	88,589.8	-17.37	103,384.6	-3.57
NR16-0-X-Y	286,532.3	243,718.1	-14.94	266,538.5	-6.98
NR16-1-X-Y	287,108.4	243,718.1	-15.11	266,538.5	-7.16
A-0-X-Y	108,757.5	97,498.3	-10.35	103,384.6	-4.94
A-1-X-Y	106,057.3	97,498.3	-8.07	103,384.6	-2.52
B-0-X-Y	344,220.9	319,984.5	-7.04	329,538.5	-4.27
B-1-X-Y	339,720.6	319,984.5	-5.81	329,538.5	-3.00

Table 5-17. Comparisons between $S_{ini,compl}^{j}$, $S_{ini,simpl}^{j}$ and $S_{ini,exp}^{j}$ for the six relevant welded tests coming from Table 3-2.

No.	Specimen	$S_{ini,exp}^{j}$ (kNm/rad)	$S_{ini,compl}^{j}$ (kNm/rad)	E (%)	$S_{ini,simpl}^{j}$ (kNm/rad)	E (%)
1	B1	363,636.4	495,927.5	36.38	548,500.4	50.84
6	BCC5-E	23,325.0	35,594.7	52.60	40,499.1	73.63
7	XU-W1	59,429.0	56,118.8	-5.57	59,160.8	-0.45
8	XU-CWP1	62,939.0	63,476.8	0.85	67,654.8	7.49
11	CP-R-M	51,166.7	52,023.4	1.67	54,660.7	6.83
12	No. 3	7,068.2	19,917.9	181.80	20,207.2	185.89

5.3.2.3 Ultimate deformation capacity $\gamma_{f,simpl}^{PZ}$

Practically speaking, it was observed in Section 5.2 that the failure of the PZ, most of the time, occurs in the flowed range. It is due either to the fracture of the material in the SE, or to the shear buckling of the CWP. However, the flowed range is characterized by a very small stiffness. This makes it difficult to define a reliable (i.e. safe) ductility criterion in this range as any small overestimation of the shear resistance could cause significant overestimation of the shear deformation capacity. Consequently, the author suggests the use of γ_u^{CWP}, i.e. the ultimate shear deformation of the CWP at the end of the post-plastic range (see the left column in Table 5-5 and Fig. 5-8(a)), as a safe but simple criterion for the prediction of the PZ shear deformation capacity $\gamma_{f,simpl}^{PZ}$.

Based on the assumption that was made in Section 5.3.1.2 of a quad-linear model for the CWP behaviour, the ultimate shear deformation γ_u^{CWP} of the CWP can be derived step by step, by computing first the elastic and post-plastic shear deformations γ_y^{CWP} and γ_{pp}^{CWP} of the CWP. The general expressions of the latter are given in Table 5-5, yet they are recalled in Eq. (5-34) and Eq. (5-35) respectively, where they are further developed. Based on Eq. (5-34) and Eq. (5-35), a general expression can be obtained for γ_u^{CWP}, see Eq. (5-36), which can be used as a general criterion for the prediction of the shear deformation capacity $\gamma_{f,simpl}^{PZ}$ of the PZ. In Eqs. (5-34) to (5-36), V_y^{CWP}, V_{pp}^{CWP} and V_u^{CWP} were derived using the simplified expressions given in Eqs. (4-29) to (4-33), and assuming χ_i and χ_n equal to 1.0; K_y^{CWP} was derived using the simplified expression given in Eq. (5-33); and ΔE and E_{pp} were obtained from Table 5-3. Furthermore, the engineering and true strains are assumed to be small enough (i.e. significantly smaller than 1.0) in such a way that they can be used indistinctly from each other, as expressed through Eq. (5-37).

$$\gamma_y^{CWP} \quad = \frac{V_y^{CWP}}{K_y^{CWP}} = \frac{A_{VC}^{simpl} \cdot \tau_y}{G \cdot A_{VC}^{simpl}} = \frac{\sigma_y}{\sqrt{3} \cdot G} \tag{5-34}$$

$$\gamma_{pp}^{CWP} \quad = \gamma_y^{CWP} + \frac{V_{pp}^{CWP} - V_y^{CWP}}{\frac{\Delta E}{3} \cdot A_{VC}^{simpl}} = \gamma_y^{CWP} + \frac{A_{VC}^{simpl} \cdot \tau_{pp} - A_{VC}^{simpl} \cdot \tau_y}{\frac{\Delta E}{3} \cdot A_{VC}^{simpl}} = \gamma_y^{CWP} + 3 \cdot \frac{\sigma_{pp} - \sigma_y}{\sqrt{3}} \cdot \frac{1}{\Delta E}$$

$$= \gamma_y^{CWP} + 3 \cdot \frac{\sigma_{pp} - \sigma_y}{\sqrt{3}} \cdot \frac{\varepsilon_{pp} - \varepsilon_y}{\sigma_{pp} - \sigma_y} \approx \gamma_y^{CWP} + \frac{3}{\sqrt{3}} \cdot \left(\varepsilon_{pp}^{eng} - \varepsilon_y^{eng}\right) \tag{5-35}$$

$$\gamma_u^{CWP} \quad = \gamma_{pp}^{CWP} + \frac{V_u^{CWP} - V_{pp}^{CWP}}{K_{pp}^{CWP}} = \gamma_{pp}^{CWP} + \frac{A_{VC}^{simpl} \cdot \tau_u - A_{VC}^{simpl} \cdot \tau_{pp}}{\frac{E_{pp}}{3} \cdot A_{VC}^{simpl}} = \gamma_{pp}^{CWP} + 3 \cdot \frac{\sigma_u - \sigma_{pp}}{\sqrt{3}} \cdot \frac{1}{E_{pp}}$$

$$= \gamma_{pp}^{CWP} + 3 \cdot \frac{\sigma_u - \sigma_{pp}}{\sqrt{3}} \cdot \frac{\varepsilon_u - \varepsilon_{pp}}{\sigma_u - \sigma_{pp}} = \gamma_{pp}^{CWP} + \frac{3}{\sqrt{3}} \cdot \left(\varepsilon_u - \varepsilon_{pp}\right) \approx \gamma_y^{CWP} + \frac{3}{\sqrt{3}} \cdot \left(\varepsilon_u^{eng} - \varepsilon_y^{eng}\right) \tag{5-36}$$

with:

$$\begin{vmatrix} \varepsilon_y = \ln\left(1 + \varepsilon_y^{eng}\right) \approx \varepsilon_y^{eng} & with\ \varepsilon_y^{eng} \ll 1 \\ \varepsilon_{pp} = \ln\left(1 + \varepsilon_{pp}^{eng}\right) \approx \varepsilon_{pp}^{eng} & with\ \varepsilon_{pp}^{eng} \ll 1 \\ \varepsilon_u = \ln\left(1 + \varepsilon_u^{eng}\right) \approx \varepsilon_u^{eng} & with\ \varepsilon_u^{eng} \ll 1 \end{vmatrix} \tag{5-37}$$

Eqs. (5-34) to (5-36) are functions of the parameters (i.e. G, σ_y, ε_y^{eng}, ε_{pp}^{eng} and ε_u^{eng}) of the material stress-strain curve of the CWP. Among them, the different strain levels ε_y^{eng}, ε_{pp}^{eng} and ε_u^{eng} are hardly ever known from the coupon tests. This is problematic as it makes the use of Eq. (5-36) less straightforward and subsequently less attractive as a simple criterion for the prediction of the PZ shear deformation capacity. Therefore, these different strain levels have been estimated, using the two material models which have been contemplated in the present thesis for the characterization of the material laws, namely: (i) the sophisticated EN 1993-1-14 model in CHAPTER 4 (see Table 4-3 in Section 4.2.2) and (ii) the simpler ECCS model in the present CHAPTER 5 (see Table 5-2 in Section

5.2.2). Introducing the expressions provided in Table 4-3 and Table 5-2 into Eqs. (5-34) to (5-36) and simplifying yields the simplified expressions for γ_y^{CWP}, γ_{pp}^{CWP} and γ_u^{CWP} given in Eqs. (5-38) to (5-40), where f_y, f_u, G and ν are the material yield strength, ultimate strength, shear modulus and Poisson's ratio which can be easily obtained from a standard coupon test:

$$\gamma_y^{CWP} = \frac{f_y}{\sqrt{3} \cdot G} \quad \begin{vmatrix} EN\ 1993\text{-}1\text{-}14\ model \\ ECCS\ model \end{vmatrix} \tag{5-38}$$

$$\gamma_{pp}^{CWP} = \begin{cases} \gamma_y^{CWP} \cdot \left[-0.15 + 0.3 \cdot \frac{G}{f_u} \cdot \left(1 - 0.55 \cdot \frac{f_u}{f_y} \right) \right] & EN\ 1993\text{-}1\text{-}14\ model \\ \gamma_y^{CWP} \cdot \left[1 + \frac{27}{2 \cdot (1+\nu)} \right] \approx 11 \cdot \gamma_y^{CWP} & ECCS\ model \end{cases} \tag{5-39}$$

$$\gamma_u^{CWP} = \begin{cases} \gamma_y^{CWP} \cdot \left[-0.15 - 0.225 \cdot \frac{G}{f_u} \cdot \left(1 - 1.45 \cdot \frac{f_u}{f_y} \right) \right] & EN\ 1993\text{-}1\text{-}14\ model \\ \gamma_y^{CWP} \cdot \left[-46.3 + 57.7 \cdot \frac{f_u}{f_y} \right] & ECCS\ model \end{cases} \tag{5-40}$$

$$= \gamma_{f,simpl}^{PZ}$$

These two simplified criteria given in Eq. (5-40) have been applied to the 20 numerical results given in Table 5-4, which are characterized by a PZ ultimate failure mode. The values obtained based on the ECCS and EN 1993-1-14 models are reported in Table 5-18 and Table 5-19 respectively and they appear to be very close to each other. In these tables, they are compared to the numerical $\gamma_{f,num}^{PZ}$ values coming from the numerical simulations. These comparisons are conducted using the performance indicator defined in Table 3-1. However, a different colour code has been used with respect to the one defined in Table 3-1: the negative relative errors E are highlighted in light blue while the positive ones are highlighted in dark blue. The comparisons show that the simplified criteria provide conservative estimations of the actual ultimate deformation capacity of the PZ in most of the cases (i.e. for 16 numerical results out of 20). For these simulations, the relative error varies from -18.83% up to -45.86% (resp. -14.72% up to -43.12%) with the criterion based on the ECCS (resp. EN 1993-1-14) material model, which gives a significant safety margin. For the four remaining simulations, the simplified criterion based on the ECCS (resp. EN 1993-1-14) material model overestimates the actual deformation capacity of the PZ by up to 39.77% (resp. 33.03%). This is because the shear buckling of the CWP occurs in the post-plastic range, rather than the flowed range. Strictly speaking, the shear buckling of the CWP does not correspond to the actual failure of the PZ as additional deformation capacity is available until the fracture of the material occurs in the SE. The study of the Fig. C-10(d), C-14(d), C-30(d) and C-32(d) in Appendix C for the four relevant numerical simulations shows that the fracture of the material actually occurs for shear deformation levels significantly larger than $0.100\ rad$. Thus, the proposed simplified criteria remain valid, keeping in mind also that this level of shear deformation is in reality almost never met in a joint, since other less ductile components will fail earlier, at much lower deformation levels.

> **Proposal for amendment of the prEN 1993-1-8:**
>
> *N.B.: The final proposal for the improved PZ model, suggested for inclusion in the forthcoming prEN 1993-1-8, is summarized in Appendix F. It includes amendments of the current EN 1993-1-8 expressions for the initial stiffness and plastic resistance and a proposal for a ductility criterion.*
>
> For the prediction of the deformation capacity of the PZ component, the author suggests the introduction, in the pre-normative prEN 1993-1-8 document, of the simplified criterion given in Eq. (5-40). For sake of consistency with EN 1993-1-14, it is recommended to use the criterion which was derived based on the EN 1993-1-14 material model instead of the one based on the ECCS material model, even though both of them yield very similar results. The complete summary of the proposal may be found in Appendix F.3.

Table 5-18. Comparisons between $\gamma_{f,simpl}^{PZ}$ (derived based on the ECCS material model) and $\gamma_{f,num}^{PZ}$ for the 20 numerical simulations characterized by a PZ ultimate failure model.

Configuration	Category I (X="d", Y="/")			Category II (X="s", Y="/")		
	$\gamma_{f,num}^{PZ}$ (rad)	$\gamma_{f,simpl}^{PZ}$ (rad)	E (%)	$\gamma_{f,num}^{PZ}$ (rad)	$\gamma_{f,simpl}^{PZ}$ (rad)	E (%)
NR4-0-X-Y	0.1369		-32.17	/		/
NR4-1-X-Y	0.1265		-26.59	0.1443		-35.65
NR16-0-X-Y	0.0887		4.69	/		/
NR16-1-X-Y	0.1215	0.0929	-23.57	0.1236	0.0929	-24.87
A-0-X-Y	0.1715		-45.86	/		/
A-1-X-Y	0.1535		-39.51	/		/
B-0-X-Y	0.1198		-22.49	/		/
B-1-X-Y	0.1453		-36.09	/		/
Configuration	Category III (X="d", Y="0.5N$_{pl}$")			Category IV (X="s", Y="0.5N$_{pl}$")		
	$\gamma_{f,num}^{PZ}$ (rad)	$\gamma_{f,simpl}^{PZ}$ (rad)	E (%)	$\gamma_{f,num}^{PZ}$ (rad)	$\gamma_{f,simpl}^{PZ}$ (rad)	E (%)
NR4-0-X-Y	0.1453		-36.09	/		/
NR4-1-X-Y	0.1215		-23.57	/		/
NR16-0-X-Y	0.0787		17.99	/		/
NR16-1-X-Y	0.1144	0.0929	-18.83	0.1279	0.0929	-27.40
A-0-X-Y	0.1531		-39.35	/		/
A-1-X-Y	0.1377		-32.57	0.1489		-37.64
B-0-X-Y	0.0741		25.31	/		/
B-1-X-Y	0.0698		33.03	/		/

Table 5-19. Comparisons between $\gamma_{f,simpl}^{PZ}$ (derived based on the EN 1993-1-14 material model) and $\gamma_{f,num}^{PZ}$ for the 20 numerical simulations characterized by a PZ ultimate failure model.

Configuration	Category I (X="d", Y="/")			Category II (X="s", Y="/")		
	$\gamma_{f,num}^{PZ}$ (rad)	$\gamma_{f,simpl}^{PZ}$ (rad)	E (%)	$\gamma_{f,num}^{PZ}$ (rad)	$\gamma_{f,simpl}^{PZ}$ (rad)	E (%)
NR4-0-X-Y	0.1369		-28.74	/		/
NR4-1-X-Y	0.1265		-22.88	0.1443		-32.39
NR16-0-X-Y	0.0887		9.98	/		/
NR16-1-X-Y	0.1215	0.0976	-19.71	0.1236	0.0976	-21.07
A-0-X-Y	0.1715		-43.12	/		/
A-1-X-Y	0.1535		-36.45	/		/
B-0-X-Y	0.1198		-18.57	/		/
B-1-X-Y	0.1453		-32.86	/		/
Configuration	Category III (X="d", Y="0.5N$_{pl}$")			Category IV (X="s", Y="0.5N$_{pl}$")		
	$\gamma_{f,num}^{PZ}$ (rad)	$\gamma_{f,simpl}^{PZ}$ (rad)	E (%)	$\gamma_{f,num}^{PZ}$ (rad)	$\gamma_{f,simpl}^{PZ}$ (rad)	E (%)
NR4-0-X-Y	0.1453		-32.86	/		/
NR4-1-X-Y	0.1215		-19.71	/		/
NR16-0-X-Y	0.0787		23.96	/		/
NR16-1-X-Y	0.1144	0.0976	-14.72	0.1279	0.0976	-23.72
A-0-X-Y	0.1531		-36.28	/		/
A-1-X-Y	0.1377		-29.15	0.1489		-34.48
B-0-X-Y	0.0741		31.66	/		/
B-1-X-Y	0.0698		39.77	/		/

5.4 CONCLUSIONS

In the present CHAPTER 5, a new constitutive model is proposed for the prediction of the full non-linear behaviour of the PZ up to failure, in the case of welded beam-to-column joints under monotonic loading only. This model has been developed upon the deep understanding of the physical phenomena governing the deformability and the failure of the PZ. This understanding has been gained through the careful analysis of the relevant numerical results coming from an extensive parametric study carried out with the Abaqus© software. In these simulations, a simplified quad-linear material law was used in order to facilitate the derivation and the validation of the new analytical model. The main features of this model can be summarized as follows:

- it exhibits a multi-linear shape, resulting from the superposition of the quad-linear and bilinear contributions of the CWP and the SE, which are assumed to behave independently from each other;
- it requires a simplified quad-linear material model as input, which needs first to be translated into a true stress-strain curve;
- the contribution of the CWP is based on the integration of the actual shear stress distribution in the CWP at four different stress levels and neglects the bending deformation mode with respect to the shear deformation one;
- the contribution of the SE describes the collapse mechanism which actually develops within the SE, integrates the effect of strain-hardening and assumes that all the deformability of the SE is concentrated in the hinges;
- the model accounts for the risk of shear buckling in the CWP and material fracture in the SE, the ultimate failure mode of the PZ being the minimum of the two;
- finally, it accounts for the geometrical second order effects through the use of a $1/\cos\gamma$ factor, affecting the contribution of the SE only.

The so-developed analytical model has proven to work well through comparisons with numerical and experimental results. This way, it outperforms the Jaspart model introduced in CHAPTER 2, by providing a more consistent estimation of the PZ behaviour up to failure. However, an important outcome from these comparisons is the high sensitivity of the model to the material laws used as inputs, showing that reliable material models are the prerequisite for accurately estimating the components' complete behaviour. Notwithstanding that, two simplified criteria for the prediction of the PZ elastic stiffness and deformation capacity were deduced from the complex model and proposed for integration in the forthcoming prEN 1993-1-8 pre-normative document.

It should be recalled that the range of validity for the constitutive model developed in the present CHAPTER 5 is so far limited to PZs in welded joints and to column profiles characterized by a web-to-flange thickness ratio $t_{wc}/t_{fc} \in [0.55 - 0.62]$. The maximum axial load N_c applied to the column is also limited to $0.5 \cdot N_{pl,c}$, $N_{pl,c}$ being the axial capacity of the column profile. Based on these limitations, the following CHAPTER 6 will be dedicated to the extension of the model to PZs in bolted joints.

CHAPTER 6 Extension to bolted joints

6.1 INTRODUCTION

6.1.1 Objectives of the Chapter

The issue regarding the prediction of the plastic shear resistance of the PZ, identified in CHAPTER 3, was investigated in CHAPTER 4, leading to the proposal of a new analytical formula. This preliminary step was necessary in the perspective of predicting the complete behaviour of the PZ up to failure, a problem that was subsequently addressed in CHAPTER 5. It is noteworthy that CHAPTER 4 and CHAPTER 5 focused on PZs in welded joints only. This is because the welded joints are the simplest joints: they involve a limited number of active components and exhibit only one single subpanel, which makes the derivation, through Eq. (2-1), of the equivalent shear force V_{Ek}^{PZ} acting on the PZ relatively straightforward. Consequently, the range of validity of the models developed in these two Chapters is so far limited to welded joints only. In this context, the present CHAPTER 6 precisely aims at filling this gap by extending the field of application of these models to PZs in bolted joints.

6.1.2 Scope of the Chapter

By dealing with bolted joints instead of welded ones, the scope of the present CHAPTER 6 has obviously been slightly modified with respect to CHAPTER 4 (see Section 4.1.2) and CHAPTER 5 (see Section 5.1.2). In particular, the present CHAPTER 6 focuses on bolted joints with extended endplate connections only. Extension of the models to other typologies of bolted connections (for instance bolted connections with angle flange cleats), even though being rather straightforward, is a perspective of the present thesis.

Apart from this change at the level of the connection, it was not intended to further enlarge the domain of application of the models developed in CHAPTER 4 and CHAPTER 5. Consequently, all the other assumptions that were made in these Chapters remain valid in the present CHAPTER 6. From a practical point of view, this means that the study will be limited to joints under monotonic loading only, focusing on two types of joint configurations, namely exterior joints and interior joints with beams of equal depth.

These two joint configurations are illustrated in Fig. 6-1(a) and Fig. 6-2(a), respectively, in the particular case where two bolt-rows are active in tension. For the exterior (resp. interior) joint, three (resp. six) load-introduction connection rows are contemplated on the height of the PZ, which is thus divided into two (resp. five) subpanels. Both exterior and interior beam-to-column sub-assemblies are simply supported and the beams are loaded in such a way that the PZ becomes the governing component of the joint response. This is illustrated in the M-N-V diagrams in Fig. 6-1(b) (resp. Fig. 6-2(b)), where the lower subpanel (resp. the central subpanel) is subjected to significant shear. In addition, a vertical axial load N_c can be applied to the column profiles, with a magnitude of up to $0.5 \cdot N_{pl,c}$, $N_{pl,c}$ being the axial capacity of the column profile. By contrast, the beams are assumed to transfer no horizontal axial load N_b, while the unbalanced bending moments, in the case of interior joints, are assumed to be equal (i.e. $|M_{BL}| = |M_{BR}|$). Finally, all the column profiles considered in the present study are characterized by a column web-to-flange thickness ratio t_{wc}/t_{fc} oscillating between 0.55 and 0.62, which is the range of validity of the analytical models developed in CHAPTER 4 and CHAPTER 5.

6.1.3 Outline of the Chapter

In order to extend the analytical models developed in CHAPTER 4 and CHAPTER 5 to PZs in bolted joints, the present CHAPTER 6 has been divided into two parts:

- The first part (see Section 6.2) addresses the prediction of the plastic shear resistance of the PZ. Section 6.2.2 highlights the modifications to be accounted for at the component and assembly levels due to the presence of a bolted connection before the complex and simplified analytical models developed in CHAPTER 4 are validated against experimental results, using the so-modified component method (see Sections 6.2.3.1 and 6.2.3.2, respectively).

- The second part (see Section 6.3) addresses the prediction of the deformation capacity of the PZ. For this part, the use of the generalised mechanical model introduced in Section 2.2.3.2 is required. However, the use of the latter in the large deformation field is not yet fully satisfactory for several reasons which are given in Section 6.3.1.2. Consequently, Section 6.3.2 provides preliminary results only which were obtained through comparisons with experimental results carefully selected from the database of bolted joints given in Table 3-3.
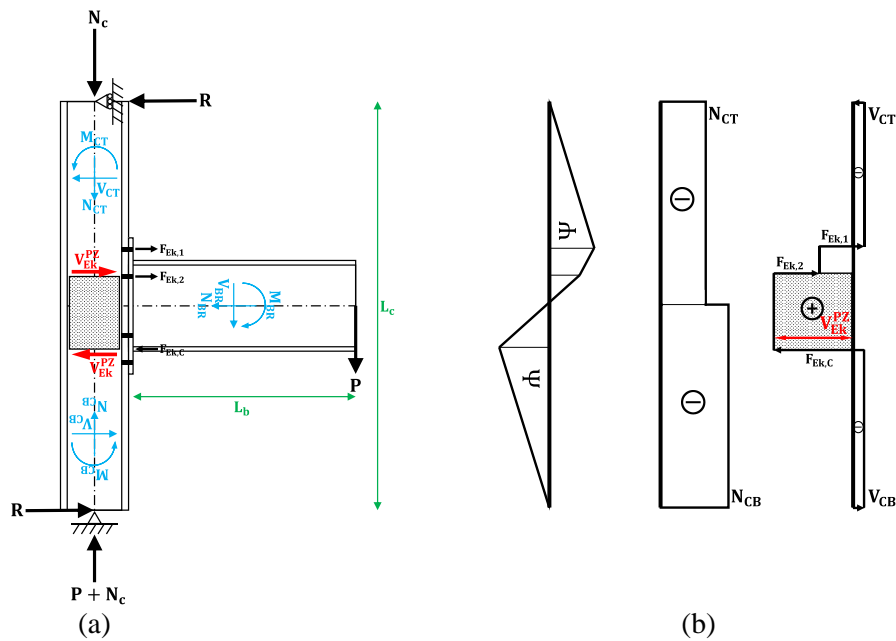

Fig. 6-1. Exterior bolted joint: (a) loading conditions maximizing shear in the PZ and (b) resulting M-N-V diagrams in the column.
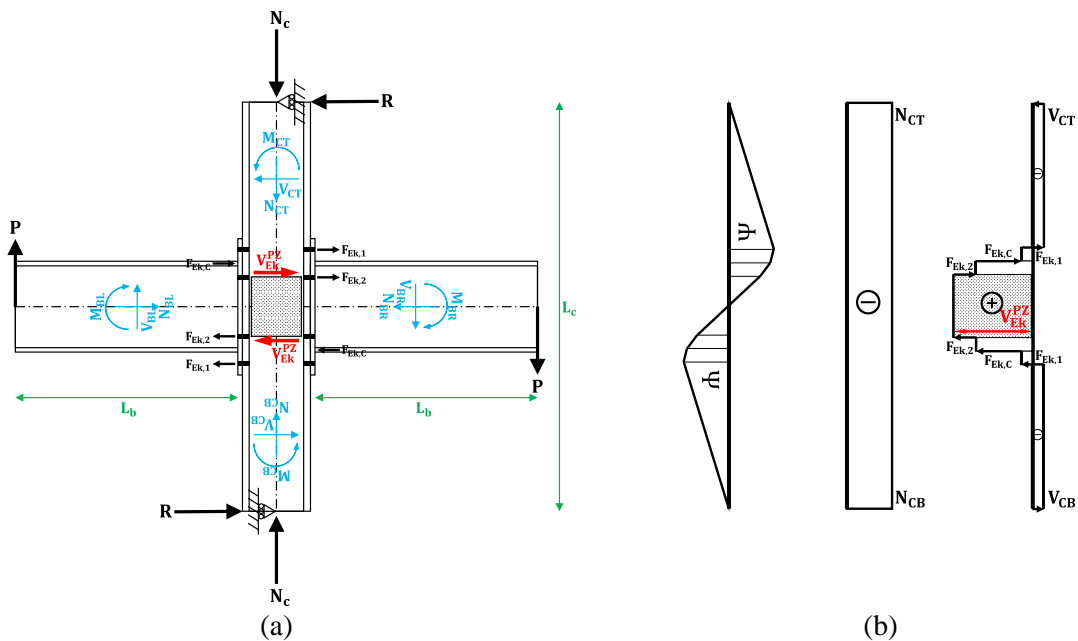

Fig. 6-2. Interior bolted joint: (a) loading conditions maximizing shear in the PZ and (b) resulting M-N-V diagrams in the column.

6.2 CHARACTERIZATION OF THE PANEL ZONE PLASTIC RESISTANCE

6.2.1 Original approach in welded joints

6.2.1.1 Description

Up to now, the plastic shear resistance of the PZ has been characterized using the EN 1993-1-8 expression given in Table 2-2. However, the latter was proven to provide unsafe estimations of the resistance in some cases. Therefore, a new formula was developed in CHAPTER 4, based on the understanding of the physical phenomena governing the plastic shear resistance of the PZ. This understanding was gained through the careful analysis of the FE results coming from an extensive parametric study on welded joints. The new suggested formula accounts for both contributions $V_{y,Rk,compl}^{CWP}$ and $\Delta V_{y,Rk,compl}^{SE}$ of the CWP and SE separately, regardless the presence or otherwise of transverse column web stiffeners. The former is derived assuming a uniform shear stress distribution over the height d_b^* of the unique subpanel (see Eqs. (4-14) to (4-18)). The latter is obtained based on the study of the plastic collapse mechanisms which may develop in the SE framing around the unique CWP, see Table 4-16.

Based on this new formula, the characterization of the joint resistance can eventually be contemplated, following the procedure given in Section 2.2.2.4.

6.2.1.2 Limitations

For welded joints, such as the ones depicted in Fig. 4-1(a) and Fig. 4-2(a), only two load-introduction rows are contemplated over the height of the PZ, which is thus divided into one single subpanel (this is also true for bolted joints with only one bolt-row in tension). This makes the derivation of the lever arm z_{eq} straightforward, as given by Eq. (2-5). The shear force V_{Ek}^{PZ} acting on the PZ can be obtained through Eq. (2-1) and is constant over the entire height of the PZ (i.e. of the single subpanel), as depicted in Fig. 4-1(b) and Fig. 4-2(b). It can eventually be compared to the plastic shear resistance $V_{y,Rk}^{PZ}$ of the PZ.

For bolted joints, such as the ones depicted in Fig. 6-1(a) and Fig. 6-2(a), multiple load-introduction bolt-rows are contemplated over the height of the CWP, the latter being thus divided into several subpanels. This makes the definition of the lever arm much more challenging. EN 1993-1-8 recommends deriving a unique equivalent lever arm z_{eq} through a stiffness calculation, as given by Eq. (2-5). Consequently, this leads to the definition, through Eq. (2-1), of a unique equivalent shear force V_{Ek}^{PZ} acting on the PZ, which can eventually be compared to the plastic shear resistance $V_{y,Rk}^{PZ}$ of the PZ.

However, this definition of a unique equivalent shear force V_{Ek}^{PZ} does not appropriately reflect the actual distribution of shear forces along the PZ height. As shown in Fig. 6-1(b) and Fig. 6-2(b), V_{Ek}^{PZ} actually varies along the height of the PZ according to the loads introduced by the connection rows. This limitation was already raised in Section 2.2.3.2, and will be addressed in the following Section 6.2.2 through slight adjustments of the EN 1993-1-8 procedure at the component characterization and assembly levels.

6.2.2 Modifications of the approach for bolted joints

6.2.2.1 Component characterization

At the component characterization level, the proposed adjustments affect the web panel components, namely the sheared PZ and the load-introduction CWC* and CWT components.

A. PZ

As regards the PZ, Eq. (4-3) can be kept for the characterization of the PZ plastic resistance. However, the contribution $\Delta V_{y,Rk,compl}^{SE}$ needs to be re-evaluated to more faithfully depict the plastic collapse mechanism actually developing in the SE. Therefore, the collapse mechanisms have been studied for the particular cases of (un-)stiffened interior and exterior joints with one, two or three bolt-rows active in tension (see Table 6-1, Table 6-2 and Table 6-3, respectively). These tables show that the activated height of the CWP, and thus the governing plastic collapse mechanism in the SE, varies with the number of activated bolt-rows in the connection. As such, three main situations may be contemplated, starting from the top row and working down:

- If the PZ is weak with respect to the connection, it fails before the 1st connection bolt-row reaches its plastic resistance $F_{y,Rk,1}$. In this case, the height of the activated subpanel is h_1 (see Table 6-1), which is the lever arm to be used for the computation of the contribution $\Delta V_{y,Rk,compl}^{SE}$ of the SE. For unstiffened joints, the plastic collapse mechanism consists of the formation of four plastic hinges in the column flanges (see Table 6-1), thus leading to Eq. (6-3). For stiffened joints, three to four additional hinges are located either in the transverse column web stiffeners or in the beam(s) flange(s), the plastic collapse mechanism actually developing being the one requiring the minimum energy, as stated by Eq. (6-4). It is also noteworthy that, when the endplate extends below the compressed beam(s) flange(s), one additional hinge needs to be accounted for in the endplate, see Eqs. (6-3) and (6-4).
- If the PZ has an intermediate strength with respect to the connection, r connection bolt-rows can be activated in the latter before the PZ actually fails, r ranging from 2 to n, and n being the number of bolt-rows above the centre of compression of the connection. In this case, the height of the activated subpanel is h_r (see Table 6-2 and Table 6-3, for $r = 2$ and $r = 3$, respectively), which is the lever arm to be used for the computation of the contribution $\Delta V_{y,Rk,compl}^{SE}$ of the SE. Again, for unstiffened joints, the plastic collapse mechanism consists in the formation of four plastic hinges in the column flanges (see Table 6-2 and Table 6-3), thus leading to Eqs. (6-5) and (6-7). However, for stiffened joints, only one or two additional hinges are required in the stiffeners or the beam(s) flange(s) in contrast with the weak PZ. This is expressed through Eqs. (6-6) and (6-8) for $r = 2$ and $r = 3$, respectively. Eqs. (6-5) to (6-8) also account for the additional plastic hinge which develops in the endplate when the latter extends below the compressed beam flange.
- If the PZ is strong with respect to the connection, the latter yields entirely (i.e. each of the n connection bolt-rows reaches its own plastic resistance $F_{y,Rk,r}$) before the plastic resistance of the PZ is reached (i.e. in both the CWP and SE). This case is not relevant in the present study as the PZ is not activated.

In Eqs. (6-3) to (6-8), h_r is the height of the activated subpanel, where r is the number of activated bolt-rows among the n bolt-rows located above the centre of compression of the connection; $M_{pl,fc,T,Rk}$, $M_{pl,fb,T,Rk}$, $M_{pl,st,Rk}$ and $M_{pl,ep,Rk}$ are the characteristic plastic bending moment resistances of a T-shaped column flange including the root fillets region, of a T-shaped beam flange including the root fillets region, of a rectangular transverse column web stiffener and of a rectangular endplate, respectively. They were defined in Section 4.3.1.2, see Eq. (4-25).

B. CWC*/CWT

As regards the CWC*/CWT components, the adjustment of the formulae given in [21] and Table 2-2 for the prediction of the plastic resistance concerns the stress interaction factor ω. This reduction factor accounts for the $\tau - \sigma_i$ stress interaction in the CWP (see Fig. 2-2), where τ is the shear stress coming from the equivalent shear force V_{Ek}^{PZ} acting on the PZ and σ_i is the horizontal normal stress coming from the couple of tensile and compressive load-introduction forces F_{BR}. The expression of ω is given in Table 2-2 and relies on the transformation parameter β, for which EN 1993-1-8 assumes one singular value between 0 and 2.0 for the whole joint, according to the type of joint configuration, i.e. either exterior or interior.

Although this assumption is valid for joints with two load-introduction rows (such as welded joints or bolted joints with only one bolt-row active in tension), it is not the case for bolted joints with multiple load-introduction bolt-rows anymore, where it varies from one load-introduction row to another, at least theoretically, from 0 to ∞. Consequently, it is suggested to re-evaluate the reduction factor ω_r through Eq. (6-1) for each of the n load-introduction rows, where $b_{eff,cwc}$ is the effective width given in Table 2-2, A_{VC}^{compl} is the effective shear area defined in Fig. 4-12, t_{wc} is the column web thickness and β_r is the value of the transformation parameter which is computed at the level of the rth load-introduction row through Eq. (6-2), as the ratio between the local shear force $V_{Ek,r}^{PZ}$ and the local load-introduction force $F_{Ek,r}$ (see Fig. 6-1(b) and Fig. 6-2(b)):

$$\omega_r = \frac{1}{\sqrt{1 + 1.3 \cdot \beta_r^2 \cdot \left[\dfrac{b_{eff,cwc} \cdot t_{wc}}{A_{VC}^{compl}}\right]^2}} \tag{6-1}$$

$$\beta_r = \left|\frac{V_{Ek,r}^{PZ}}{F_{Ek,r}}\right| \tag{6-2}$$

From a theoretical point of view, the derivation of the β_r values is an iterative process as it relies on the distribution of the shear forces along the height of the CWP and the latter cannot be derived before the resistance of each connection bolt-row is known. To overcome this problem, a simplified approach can be contemplated consisting in assuming that the sheared PZ is inactive (i.e. $\beta_r = 0$, strong PZ-weak connection approach).

Based on this assumption, the plastic bending moment resistance $M_{y,Rk}^{con}$ of the connection can be derived, applying Eqs. (2-7) to (2-11). Subsequently, the so-obtained distribution of forces in the connection rows can be used to deduce the actual distribution of shear forces along the height of the CWP, thereby allowing the derivation, through Eq. (6-2), of the local β_r values associated to each load-introduction bolt-row. The ω_r values can eventually be computed for each load introduction CWC*/CWT component, using Eq. (6-1).

Table 6-1. List of all possible plastic collapse mechanisms for (un-)stiffened interior and exterior bolted joints ($r = 1$, one bolt-row active in tension).

$$\Delta V_{y,Rk,compl}^{SE} \begin{cases} 4 \cdot \dfrac{M_{pl,fc,T,Rk}}{h_1} + 2 \cdot \dfrac{M_{pl,ep,Rk}}{h_1} & \text{int. joints} \\[2ex] 4 \cdot \dfrac{M_{pl,fc,T,Rk}}{h_1} + 1 \cdot \dfrac{M_{pl,ep,Rk}}{h_1} & \text{ext. joints} \end{cases} \quad (6\text{-}3)$$

$$\begin{cases} 4 \cdot \dfrac{M_{pl,fc,T,Rk}}{h_1} + 2 \cdot \dfrac{M_{pl,ep,Rk}}{h_1} + \min\left(4 \cdot \dfrac{M_{pl,st,Rk}}{h_1} ; 2 \cdot \dfrac{M_{pl,st,Rk}}{h_1} + 2 \cdot \dfrac{M_{pl,fb,T,Rk}}{h_1} \right) & \text{int. joints} \\[2ex] 4 \cdot \dfrac{M_{pl,fc,T,Rk}}{h_1} + 1 \cdot \dfrac{M_{pl,ep,Rk}}{h_1} + \min\left(4 \cdot \dfrac{M_{pl,st,Rk}}{h_1} ; 2 \cdot \dfrac{M_{pl,st,Rk}}{h_1} + 1 \cdot \dfrac{M_{pl,fb,T,Rk}}{h_1} \right) & \text{ext. joints} \end{cases} \quad (6\text{-}4)$$

Table 6-2. List of all possible plastic collapse mechanisms for (un-)stiffened interior and exterior bolted joints ($r = 2$, two bolt-rows active in tension).

$$\Delta V_{y,Rk,compl}^{SE}
\begin{cases}
4 \cdot \dfrac{M_{pl,fc,T,Rk}}{h_2} + 2 \cdot \dfrac{M_{pl,ep,Rk}}{h_2} & \text{int. joints} \\[2ex]
4 \cdot \dfrac{M_{pl,fc,T,Rk}}{h_2} + 1 \cdot \dfrac{M_{pl,ep,Rk}}{h_2} & \text{ext. joints}
\end{cases}
\qquad (6\text{-}5)$$

$$\begin{cases}
4 \cdot \dfrac{M_{pl,fc,T,Rk}}{h_2} + 2 \cdot \dfrac{M_{pl,ep,Rk}}{h_2} + \min\left(2 \cdot \dfrac{M_{pl,st,Rk}}{h_2}; 2 \cdot \dfrac{M_{pl,fb,T,Rk}}{h_2}\right) & \text{int. joints} \\[2ex]
4 \cdot \dfrac{M_{pl,fc,T,Rk}}{h_2} + 1 \cdot \dfrac{M_{pl,ep,Rk}}{h_2} + \min\left(2 \cdot \dfrac{M_{pl,st,Rk}}{h_2}; 1 \cdot \dfrac{M_{pl,fb,T,Rk}}{h_2}\right) & \text{ext. joints}
\end{cases}
\qquad (6\text{-}6)$$

Table 6-3. List of all possible plastic collapse mechanisms for (un-)stiffened interior and exterior bolted joints ($r = 3$, three bolt-rows active in tension).

	Unstiffened joints	Stiffened joints	
Interior joints	/	/	/
Exterior joints	4C	5C	6C
$\Delta V_{y,Rk,compl}^{SE}$	$\begin{cases} / & \text{int. joints} \\ 4 \cdot \dfrac{M_{pl,fc,T,Rk}}{h_3} + 1 \cdot \dfrac{M_{pl,ep,Rk}}{h_3} & \text{ext. joints} \end{cases}$ (6-7)	$\begin{cases} / & \text{int. joints} \\ 4 \cdot \dfrac{M_{pl,fc,T,Rk}}{h_3} + 1 \cdot \dfrac{M_{pl,ep,Rk}}{h_3} + \min\left(2 \cdot \dfrac{M_{pl,st,Rk}}{h_3} ; 1 \cdot \dfrac{M_{pl,fb,T,Rk}}{h_3} \right) & \text{ext. joints} \end{cases}$ (6-8)	

6.2.2.2 Component assembly

In order to account for these new expressions for the characterization of the PZ component, the current EN 1993-1-8 assembly procedure needs to be slightly modified. As a reminder, this procedure was exemplified in Section 2.2.2.4 (see Eqs. (2-7) to (2-11)) for the particular case of an unstiffened exterior bolted joint with only two bolt-rows in tension, such as the one depicted in Fig. 2-5. In fact, most of the joints reported in Table 3-3 exhibit only two active bolt-rows. Therefore, for sake of consistency, the modifications brought to the assembly procedure will be illustrated for the same joint configuration as the one given in Fig. 2-5.

For the computation of the plastic bending moment resistance $M_{y,Rk}^{j}$ of the joint, Eq. (2-7) is still valid, and is replicated in Eq. (6-9) for sake of clarity:

$$M_{y,Rk}^{j} = \sum_{r=1}^{2} F_{y,Rk,r} \cdot h_r \tag{6-9}$$

where $F_{y,Rk,r}$ is the plastic resistance of the rth bolt-row in tension and is given in Eq. (6-10) for $r = 1$ and $r = 2$, respectively:

$$F_{y,Rk,r} = \begin{cases} \min\left(F_{y,Rk,r}^{CWT}; F_{y,Rk,r}^{CFB}; F_{y,Rk,r}^{EPB}; F_{y,Rk,r}^{BT}; \dfrac{V_{y,Rk,compl,r}^{PZ}}{\beta}; F_{y,Rk,C} \right) & r = 1 \\ \min\left(F_{y,Rk,r}^{CWT}; F_{y,Rk,r}^{CFB}; F_{y,Rk,r}^{EPB}; F_{y,Rk,r}^{BT}; F_{y,Rk,r}^{BWT}; \dfrac{V_{y,Rk,compl,r}^{PZ}}{\beta} - F_{y,Rk,r-1}; F_{y,Rk,C} - F_{y,Rk,r-1} \right) & r = 2 \end{cases} \tag{6-10}$$

with $F_{y,Rk,C}$ the plastic resistance of the bolt-row in compression:

$$F_{y,Rk,C} = \min\left(F_{y,Rk}^{CWC^*}; F_{y,Rk}^{BFC} \right) \tag{6-11}$$

and $V_{y,Rk,compl,r}^{PZ}$ the plastic shear resistance of the subpanel associated to the rth bolt-row:

$$V_{y,Rk,compl,r}^{PZ} = V_{y,Rk,compl}^{CWP} + \Delta V_{y,Rk,compl,r}^{PZ} \tag{6-12}$$

For the derivation, in Eqs. (2-8) and (2-10), of the plastic resistance $F_{y,Rk,r}^{c}$ of the CWC*/CWT components, it can be referred to Section 6.2.2.1, while for the derivation the plastic resistance $F_{y,Rk,r}^{c}$ of the other active components (i.e. CFB, EPB, BT, BWT, BFC), it can be referred to Table 2-2. In Eq. (6-12), the plastic shear resistance $V_{y,Rk,compl}^{CWP}$ of the CWP can be computed through Eqs. (4-14) to (4-18), while the contribution $\Delta V_{y,Rk,compl}^{SE}$ of the SE can be obtained from Table 6-1 to Table 6-3 according to the number r of activated bolt-rows.

Finally, Eq. (2-11) remains valid for the consideration of the possible group effects that may develop around several adjacent bolt-rows in the plate components.

6.2.3 Validation

6.2.3.1 Complex analytical model

The modifications made to the component method at the component characterization and assembly levels should allow for more accurate predictions of the plastic bending moment resistance $M_{y,Rk}^j$ of bolted joints characterized by a PZ plastic failure mode. This was confirmed by applying Eqs. (6-9) to (6-12) to the 14 bolted experimental results reported in Table 3-3. The so-obtained $M_{y,Rk,compl}^j$ values of the plastic bending moment resistance are reported in Table 6-4, where they are compared to the $M_{y,Rk,exp}^j$ values coming from Table 3-5. These comparisons are conducted using the performance indicator E and the colour code defined in Table 3-1. Graphical comparisons are also provided in Appendix A (see the red solid lines in Figs. A-13(e) to A-26(e)). For sake of completeness, the plastic collapse mechanism predicted by the model for each experimental result is also reported in Table 6-4.

From the comparisons in Table 6-4, a high level of accuracy can be observed for nine out of the 13 predictions, while the remaining four predictions moderately to significantly overestimate the actual plastic shear resistance of the PZ. For the last test, i.e. test J3.1, there is no prediction available since the governing plastic failure mode turns out to be the CWC* instead of the sheared PZ.

The moderately to poorly accurate results all consist of stiffened exterior joints. From the author's point of view, these overestimations may arise from the non-consideration of the M-N interaction in the computation of the resistance $M_{pl,fb,T,Rk}$ of the plastic hinge forming in the compressed beam flange (see the plastic collapse mechanisms No. 6A, 6B and 6C in Table 6-1, Table 6-2 and Table 6-3, respectively). Indeed, this beam flange carries a significant axial load coming from the M_{BR} bending moment in the beam. This explanation seems reasonable for the moderately accurate results but is not sufficient to explain the poorly accurate result. The author considers that these significant discrepancies observed in the test E2-TB-E-M may be attributed to the faulty post-processing of the data recorded during the test.

It can be concluded that the complex analytical model developed in CHAPTER 4 (see Section 4.3.1) in the context of welded joints works relatively well in the context of bolted joints too, provided that it is used with the updated assembly procedure presented in Section 6.2.2.

Table 6-4. Comparisons between $M_{y,Rk,compl}^j$, $M_{y,Rk,simpl}^j$ and $M_{y,Rk,exp}^j$ for the 14 bolted test results reported in Table 3-3.

No.	Specimen	$M_{y,Rk,exp}^j$ (kNm)	$M_{y,Rk,compl}^j$ (kNm)	E (%)	$M_{y,Rk,simpl}^j$ (kNm)	E (%)	Plastic mechanism*
1	01	58.8	59.9	1.82	58.1	-1.21	4B
2	04	55.9	55.4	-0.96	56.9	1.79	4B
3	07	59.0	60.6	2.69	58.1	-1.46	4B
4	010	94.4	96.2	1.95	91.4	-3.14	4B
5	J1.1	333.8	359.2	7.60	331.7	-0.62	6B
6	J2.1	325.3	356.3	9.51	331.2	1.82	6B
7	J3.1	381.5	CWC*	CWC*	390.3	2.29	6B
8	J4.1	266.2	285.3	7.17	260.7	-2.05	6B
9	E1-TB-E-M	338.1	347.5	2.77	328.0	-2.97	6B
10	E1-XW-P-C1	282.4	291.8	3.31	274.1	-2.95	3B
11	E2-TB-E-M	530.6	648.8	22.28	610.9	15.13	6B
12	E2-XW-P-C2	533.3	552.3	3.57	530.3	-0.57	3B
13	E3-TB-E-C2	1,230.3	1,289.5	4.81	1,243.6	1.08	NA
14	E3-XW-P-C2	938.1	981.1	4.58	952.7	1.56	NA

*See Table 6-1, Table 6-2 and Table 6-3.

6.2.3.2 Simplified analytical model

In a second stage, for sake of consistency, the ability of the simplified PZ model developed in CHAPTER 4 (see Section 4.3.2) in predicting the plastic shear resistance of the 14 test results on bolted joints reported in Table 3-3 was also investigated. This was done by applying the same updated EN 1993-1-8 procedure as the one used hereabove for the complex analytical model, i.e. Eqs. (6-9) to (6-12). However, the contribution $V_{y,Rk,simpl}^{CWP}$ of the CWP was derived using the simplified expressions given in Eqs. (4-29) to (4-33). As regards the derivation of the contribution $\Delta V_{y,Rk,simpl}^{SE}$, it was still referred to the different plastic collapse mechanisms defined in Table 6-1 to Table 6-3, but taking into account the simplifying assumptions introduced in Section 4.3.2.2.

The so-obtained predictions are given in Table 6-4 for the 14 bolted test results, where they are compared to the $M_{y,Rk,exp}^{j}$ values coming from Table 3-5. These comparisons are conducted using the performance indicator E and the colour code defined in Table 3-1. Graphical comparisons are also provided in Appendix A (see the red solid lines in Figs. A-13(f) to A-26(f)).

From these comparisons, it can be observed that the model performs really well (i.e. high level of accuracy) for 13 out of the 14 experimental results, the test E2-TB-E-M being the only exception as it provides a significant overestimation of the plastic resistance (i.e. low level of accuracy). The same observation was made with the complex analytical model as well as with the EN 1993-1-8 and AISC models in Table 3-9. According to the author, these discrepancies may be attributed to the faulty post-processing of the data recorded during the test.

> **Proposal for amendment of the prEN 1993-1-8:**
>
> *N.B.: The final proposal for the improved PZ model, suggested for inclusion in the forthcoming prEN 1993-1-8, is summarized in Appendix F. It includes amendments of the current EN 1993-1-8 expressions for the initial stiffness and plastic resistance and a proposal for a ductility criterion.*
>
> For the prediction of the plastic shear resistance of the PZ in bolted joints, it is proposed to consider the simplified analytical model developed in Section 4.3.2 together with the modifications presented in Section 6.2.2. This proposal is summarized in Appendix F.2. It is noteworthy that three minor additional simplifications were introduced to make the proposed expressions as simple as possible. Firstly, in the derivation of the V_{y,Rk,EU^*}^{CWP} contribution (see Eq. (F-2)), a generic coefficient equal to 0.9 is used to account for the $\tau - \sigma_i$ and $\tau - \sigma_n$ stress interactions in the CWP. This coefficient replaces the χ_i and χ_n reduction factors defined in Eqs. (4-31) and (4-32). Secondly, the $\Delta\chi_n$ reduction coefficient which accounts for the M-N interaction in the column flanges in Eq. (4-34) has been neglected in the new proposal (i.e. it was set equal to 1.0 in Eq. (F-4)). This simplification is assumed to compensate for the non-consideration of the root fillets region in the derivation of $M_{pl,fc,Rd}$. Finally, for stiffened joints, it was decided to consider only the plastic collapse mechanisms No. 2A, 2B, 5A, 5B and 5C, for sake of simplicity, and to neglect, in these plastic collapse mechanisms, the plastic hinge(s) forming in the endplate(s).
>
> The validation of this new proposed formula against the 14 test results on bolted joints is conducted in Table 3-9, using the performance indicator E and the colour code defined in Table 3-1. Graphical comparisons are also provided in Appendix A.2 (see the red broken curves in Figs. A-13(f) to A-26(f)). These comparisons show that the model performs well, with all the relative errors E (but one) being negative and ranging from -9.85% to $+9.15\%$. This clearly highlights the safe character of the new proposed EU* model in contrast with the current EU and US design provisions, also reported in Table 3-9.

6.3 CHARACTERIZATION OF THE PANEL ZONE BEHAVIOUR UP TO FAILURE

6.3.1 Validation procedure for bolted joints

6.3.1.1 Description

In CHAPTER 5 (see Section 5.3.1), a new analytical model has been developed for the prediction of the full non-linear behaviour of the PZ up to failure. The validation of this model was performed against experimental and numerical results on welded joints only, such as the exterior and interior joints depicted in Fig. 5-1(a) and Fig. 5-2(a). The reason for considering only welded joints was twofold, as described in Section 3.1.2: (i) firstly, welded joints are characterized by one single sub-panel, as shown in Fig. 5-1(a) and Fig. 5-2(a), which makes the derivation of the equivalent shear force V_{Ek}^{PZ} acting on the PZ relatively straightforward; (ii) secondly, these joints exhibit a limited number of active components in addition to the sheared PZ, thus leading to a simple assembly procedure, as highlighted in Fig. 2-4. All in all, welded joints turn out to be very simple joints, hence particularly suitable for the validation of the new constitutive model for the prediction of the PZ full-range behaviour.

Based on these considerations, the present Section 6.3.1 addresses the extension of this analytical model to the case of bolted joints, such as the ones presented in Fig. 6-1(a) and Fig. 6-2(a). However, this task turns out to be much less straightforward, given the complexity of the bolted joints with respect to welded joints, as described in Section 3.1.2: (i) firstly, the shear force is no longer constant along the height of the PZ, but instead varies according to the loads introduced by the connection rows, thus dividing the PZ into a series of subpanels, as depicted in Fig. 6-1(a) and Fig. 6-2(a); (ii) secondly, bolted joints exhibit a much larger number of active components, which contribute to the joint deformability, therefore making the assembly procedure significantly more challenging, as shown in Fig. 2-5.

Consequently, the use of the generalized mechanical model introduced in Section 2.2.3.2 is required for the assembly procedure. This model is shown in Fig. 2-5(c) for the specific case of an unstiffened exterior bolted joint with only two bolt-rows in tension. It consists of a series of extensional springs, which are interconnected by infinitely rigid pinned-end elements. Each spring corresponds to an individual basic component which is active in the joint and is assigned the force-displacement curve of this component in order to simulate its behaviour. Additional fully rigid-plastic springs are also used to account for the group effects which could develop around several adjacent bolt-rows in the plate components, as depicted in Fig. 2-5(c). Such a mechanical model can be easily built within a FE software, and progressively loaded in order to simulate the joint's rotational response up to failure. Furthermore, such model allows tracking the "yield" sequence (i.e. the spread of plasticity among the components) up to the failure of the joint.

This new generalised mechanical model has been used to validate the full-range PZ constitutive model, developed in the Section 5.3.1 of CHAPTER 5, on bolted joints. The general validation procedure is described hereafter and includes the six following steps:

1) Selecting a test result which is characterized by a significant PZ shear deformation. Such tests can be found in the database given in Table 3-3.

2) Building the mechanical model associated to the selected test result within a FE software. In the present thesis, the homemade FINELG© software [131] has been used.

3) Deriving the full-range $F^c - \Delta^c$ curve associated to each individual basic component, using the actual geometrical and mechanical properties of the joint:

   (i)   For the characterization of the full-range behaviour of the different subpanels, it is referred to the new analytical model presented in Fig. 5-8(b) and to the analytical expressions given in Table 5-5.

   (ii) For the characterization of the full-range behaviour of the connection components, it is referred to Section 2.2.3.1, where the use of a trilinear relationship is suggested. Such trilinear model is illustrated by a blue dashed curve in Fig. 2-6. The parameters of this trilinear model can be obtained from [21] for the CWC* component and from Table 2-2, Eq. (2-12) and Eq. (2-13) for the other connection components.

   (iii) For the characterization of the group effects, the rigid-plastic elements are assigned a plastic strength equal to the group resistance. This value can be obtained from the EN 1993-1-8 expressions provided in Table 2-2.

4) Assigning these constitutive $F^c - \Delta^c$ relationship to each individual spring element.

5) Running the numerical model by progressively increasing the applied loads until the failure of the joint is reached. The numerical $\left(M^j - \Phi\right)_{num}$ curve can eventually be extracted from the numerical simulation and compared to the $\left(M^j - \Phi\right)_{exp}$ experimental one.

6) Conclusions can be drawn from these comparisons, regarding the performances of the PZ constitutive model, and more largely, of the generalized mechanical model used to simulate the joint's rotational response.

In the forthcoming Section 6.3.2, this validation procedure will be applied to three bolted experimental results (i.e. tests 01, 04 and 07) coming from Table 3-3. Before that, some limitations in the validation procedure are to be highlighted in the following Section 6.3.1.2.

6.3.1.2 Limitations and perspectives

A. Modelling of the PZ

The generalized mechanical model, as it is presented in Fig. 2-5(c), allows accounting for the contribution of the CWP associated to the different subpanels. However, it is not general enough to account for the different collapse mechanisms (see Table 6-1 to Table 6-3) which are susceptible to develop in the SE. As a consequence, a small trick needs to be performed. It consists in analytically predicting the actual plastic collapse mechanism which develops in the SE, through the use of the modified component method presented in Section 6.2.2. This is done in Section 6.2.3 (see Table 6-4) for the 14 experimental results on bolted joints reported in Table 3-3. Based on these results, the activated subpanels (i.e. those falling within the lever arm of the actual collapse mechanism) are known and can be assigned the contribution of the SE in addition to that of the CWP.

Although this approach should perform rather well, it is not convenient to use. Therefore, the author suggests decoupling the contributions of the CWP and the SE in a future version of the mechanical model. To do so, new elements should be added to the mechanical model, such as rotational springs in the corners of the different subpanels, or additional extensional springs crossing the different subpanels, to simulate the contribution of the SE.

B. Modelling of the connection components

For the BFC component, it was already mentioned in Section 3.3.1.2 that the risk of local buckling is not covered yet by the formula provided in EN 1993-1-8. Therefore, the author suggests that a study is conducted for the BFC component, similar to the one reported in [21] for the CWC* component. Meanwhile, for the validation procedure (see the following Section 6.3.2), test results characterized by stocky BFCs will be selected so that this component does not play any role in the simulations (i.e. it is not activated). This being, the strength of the rigid-plastic spring simulating this component will be taken equal to the theoretical ultimate resistance that the BFC would exhibit in the absence of local buckling.

As regards the characterization of the plate components (i.e. CFB and EPB), which can be modelled through the T-stub approach, the simplified procedure provided in Section 2.2.3.1 is known to be significantly conservative in terms of the prediction of the ultimate resistance and deformation capacity, especially when the components exhibit a ductile ultimate failure mode (i.e. mode 1 or 2). This underestimation issue, which has already been discussed in the introduction (see WP1B in Fig. 1-2), is related to the development of beneficial membrane effects in the plates when the latter starts deforming. The topic is currently being investigated within the CMM research team in the framework of another PhD thesis and the first results are expected soon. In the meantime, for the validation procedure (see the following Section 6.3.2), it will be assumed that these components can deform freely after they reach their ultimate resistance (i.e. assumption of a yield plateau).

In the characterization of the CWC*/CWT components, a new expression has been suggested for the ω reduction factor, accounting for the $\tau - \sigma_i$ stress interaction, see Eq. (6-1). This expression relies on local values of the β parameter which have to be computed at each bolt-row and updated at each iteration step in the simulation. The currently available mechanical model does not allow to do so though.

C. Modelling of the group effects

As regards the group effects in the plate components, they are modelled by means of rigid-plastic extensional springs, which can be seen as fuse elements: once the force transferred through the spring reaches the group plastic resistance, the fuse element is tripped. Although this modelling works well for the prediction of the group plastic resistance, it does not allow the prediction of either the group ultimate resistance or the deformation capacity since it ignores all the strain-hardening effects in the group. Consequently, the author suggests a more refined modelling for the group effects in a future version of the mechanical model.

For the validation procedure (see the following Section 6.3.2), this issue can be easily overcome. Indeed, all the test results investigated in Section 6.2.3 exhibit a PZ plastic failure mode, which means that the group effects are not activated at yielding. Nonetheless, they can still govern the joint ultimate resistance. Therefore, the strength of the rigid-plastic extensional springs simulating these group effects will be taken equal to the group ultimate resistance instead of the plastic one.

6.3.2 Preliminary results and discussion

Given the numerous limitations and perspectives of improvement of the new generalised mechanical model, highlighted in the previous Section 6.3.1.2, the validation procedure described in Section 6.3.1.1 will be applied to three test results only, namely the tests 01, 04 and 07 performed at the University of Liège (see Table 3-3). All these tests consist of the same pushover test performed on an unstiffened exterior subassembly made of an HEB160 column and an IPE200 beam, as depicted in Fig. 6-3(a). The only difference between the tests is the level of axial load which is applied to the column, namely $0.2 \cdot N_{pl,c}$ for the test 01, $0.45 \cdot N_{pl,c}$ for the test 04, and no axial load for the test 07,

$N_{pl,c}$ being the axial capacity of the column profile. All actual geometrical and mechanical properties are reported in Appendix A.2 (see the Fig. A-13(c) to A-15(c) and A-13(d) to A-15(d), respectively). The experimentally observed plastic and ultimate failure modes consist of the yielding of the sheared PZ and the local buckling of the CWC* in all three cases, respectively.

The mechanical model associated with these three tests is depicted in Fig. 6-3(b). It is noteworthy that the 3rd bolt-row can be considered inactive since it is located very close to the compression centre, thereby simplifying the final mechanical model. As a preliminary step, it is necessary to select a material model to reconstruct the material laws; this step is necessary in view of the subsequent characterization of the active components. For the tests considered in this preliminary study, both ECCS and EN 1993-1-14 material models provided very similar results. However, only the results obtained with the simple ECCS model will be presented in this manuscript, for sake of clarity. The full-range analytical $(F^c - \Delta^c)_{an}$ curves obtained with this model for each individual basic component active in the joint are depicted in Fig. 6-3 while the main parameters of the curves are reported in Table 6-5 to Table 6-7 for the components in tension, compression and shear, respectively.

As regards more specifically the behaviour of the PZ, which is the component of interest in the present thesis, two types of analytical models have been contemplated, namely the author model (so called Corman model), i.e. the complex analytical model developed in the present thesis in CHAPTER 5 (see Table 5-5 and Table 5-6 in Section 5.3.1), and the Jaspart model presented in CHAPTER 2 (see Table 2-6 in Section 2.3.2). The main parameters of the analytical $(V^{CWP} - \gamma)_{an}$ and $(\Delta V^{SE} - \gamma)_{an}$ curves obtained with these two models for the tests 01, 04 and 07 are reported in Table 6-7. These curves can eventually be superimposed through Eqs. (2-14) and (2-15), in order to get the analytical $(V^{PZ} - \gamma)_{an}$ curves of the whole PZ. It is noteworthy that the parameters of the $(\Delta V^{SE} - \gamma)_{an}$ curves in the Corman model given in Table 6-7 were obtained knowing a priori (see Table 6-4) the actual plastic collapse mechanism which develops in the SE. Before being assigned to the different shear springs in the mechanical model, these analytical $(V^{PZ} - \gamma)_{an}$ curves need to be transformed into $(F_r^{PZ} - \Delta_r^{PZ})_{an}$ force-displacement curves, where F_r^{PZ} and Δ_r^{PZ} designate the axial force and resultant elongation of the rth shear spring. This is done by means of Eqs. (6-13) and (6-14), where z_r is the height of the rth subpanel:

$$F_r^{PZ} = \begin{cases} V^{CWP} & \text{disactivated subpanel} \\ V^{PZ} & \text{activated subpanel} \end{cases} \tag{6-13}$$

$$\Delta_r^{PZ} = \gamma \cdot z_r \tag{6-14}$$

Knowing the $(F^c - \Delta^c)_{an}$ curves of the different individual basic components which are active in the joint, the mechanical model depicted in Fig. 6-3(b) can be built in the FINELG© FE software and loaded progressively up to the joint's failure. The so-obtained numerical $(M_B - \Phi)_{num}$ curves are depicted in Fig. 6-4(a) to Fig. 6-4(c) (see the red solid and dashed curves obtained with the Corman and the Jaspart PZ models respectively) for the tests 01, 04 and 07 respectively, where they are compared to the experimental $(M_B - \Phi)_{exp}$ curves (see the black solid curves in Fig. 6-4(a) to Fig. 6-4(c)).

From a macroscopic point of view, it can be observed that the mechanical model numerically implemented in the FINELG© software performs very well as it is able to accurately mimic the experimental $(M_B - \Phi)_{exp}$ curves for the three test results. The ultimate bending moment resistance $M_{u,Rk,exp}^j$ and the ultimate rotation capacity $\Phi_{u,exp}$ are well predicted for tests 01 and 07, while they are slightly overestimated for test 04. These good results are obtained regardless the constitutive model which is used for the modelling of the different subpanels, i.e. either the Corman model or the Jaspart one. This is not surprising given that the $(F^c - \Delta^c)_{an}$ curves obtained with these two constitutive models for the lower subpanel which is the one being activated are very close to each

other, as depicted in Fig. 6-3. However, it is noteworthy that, for these three test results, the good results obtained with the Jaspart model most probably arise from the compensation of errors in the characterisation of the CWP and SE contributions: (i) on the one hand, the model neglects the contribution of the SE when the joint is unstiffened, whereas this contribution does actually exist in the joint and does participate to the joint resistance; (ii) on the other hand, the model overestimates the effective shear area A_{VC}, as already highlighted in Section 3.3.1.1, thus leading to the overestimation of the actual contribution of the CWP. The Corman model, on the contrary, was developed in CHAPTER 5 upon the deep understanding of the physical phenomena governing the behavior of the PZ, and was proven to provide a coherent and reliable estimation of the PZ behaviour up to failure. This gives confidence in the good results obtained in Fig. 6-4(a) to Fig. 6-4(c), with the Corman model.

At a microscopic level, the FINELG© FE software also allows to track the "yield" sequence (i.e. the spread of plasticity among the components) up to the joint's failure. The relevant values of this sequence are reported on the $(M_B - \Phi)_{num}$ curves in Fig. 6-4(a) to Fig. 6-4(c) for the three test results.

The first component which starts to yield is the lower subpanel directly followed by the CFB in the 1st bolt-row. This load level corresponds to the plastic bending moment resistance $M_{y,Rk}^{j}$ of the joint.

After that, the 1st bolt-row quickly reaches its ultimate resistance with the failure of the EPB. In theory, this load level corresponds to the maximum bending moment which can be transferred by the joint. However, it was emphasized in the previous Section 6.3.1.2 that for the plate components failing in mode 1 or mode 2, the actual ultimate resistance is significantly larger than the one predicted by the model. This is due to the development of beneficial 2nd order effects within the deformed plate. Consequently, the 1st bolt-row will be assumed to deform freely after it reaches its ultimate resistance (assumption of yield plateau).

At the end, the ultimate failure mode predicted by the model is the local buckling of the CWC* component (i.e. LB_{CWC^*}), which is similar to the one observed experimentally. Under this ultimate load level, the upper subpanel turns out to remain in the elastic field, while the lower one deforms significantly as it undergoes, in the test 01, a maximum shear deformation $\gamma \approx 0.075 \, rad$ (resp. elongation $\Delta^{PZ} \approx 11.5 \, mm$) for a load level $V^{PZ} \approx 410 \, kN$. When the Jaspart model is used instead of the Corman one for the characterization of the PZ behaviour, it is even observed that the PZ ultimate failure mode bypasses the CWC* one.

Given the good results which are obtained in terms of the global rotational response of the joint, and the significant contribution of the PZ to the latter, it can be concluded from this preliminary study that the complex analytical model developed in CHAPTER 5 in the context of welded joints is also valid for the prediction of the PZ behaviour up to failure in bolted joints. However, this conclusion will have to be confirmed on a larger number of experimental results when a more sophisticated mechanical model for the assembly procedure becomes available.
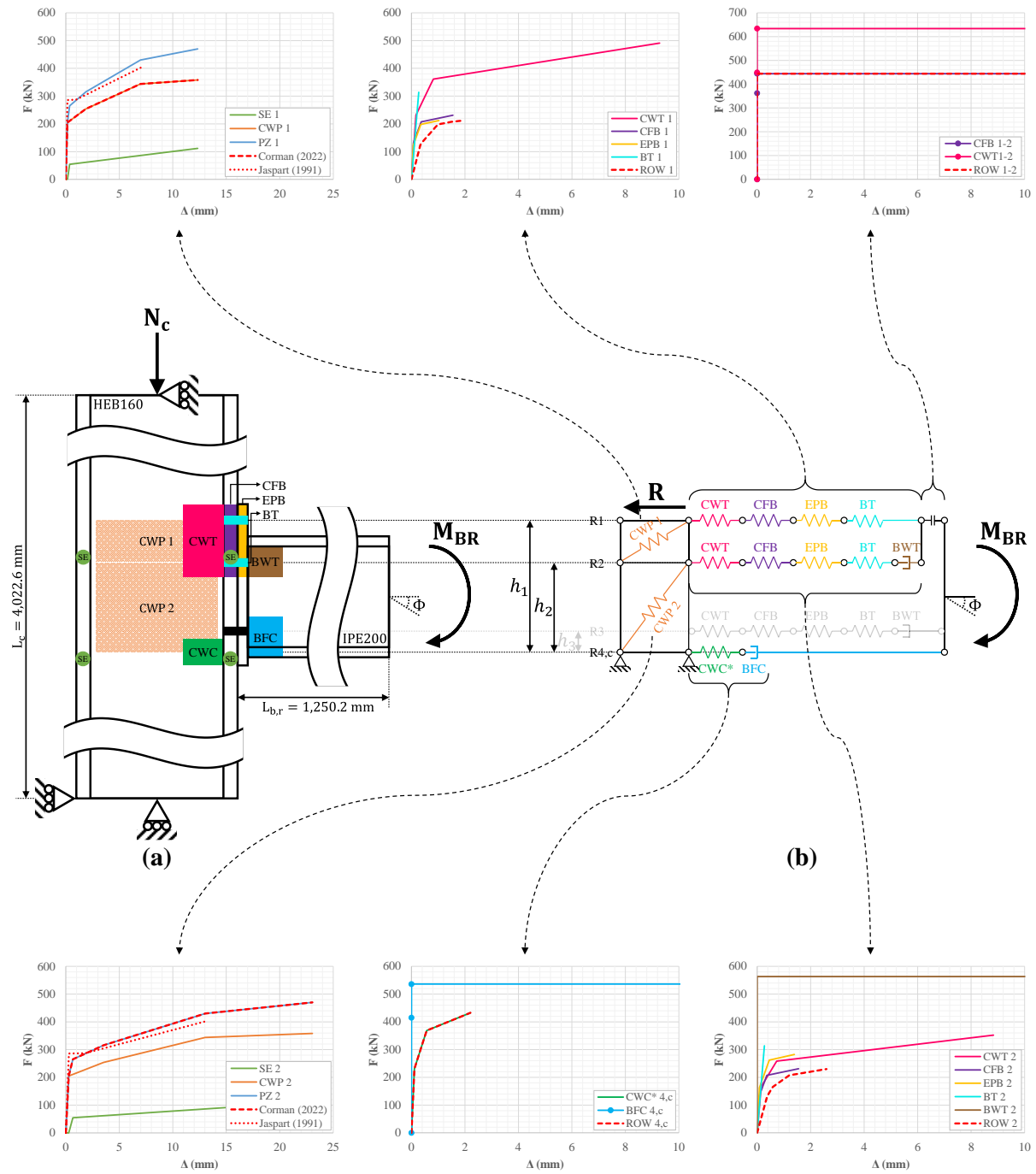
Fig. 6-3. Test 01: (a) component identification and (b) generalised mechanical model.

Table 6-5. Characterization of the components in tension for the experimental tests 01, 04 and 07.

ROWS	Components				
$r = 1$	$c = CWT$	$c = CFB$	$c = EPB$	$c = BT$	$c = BWT$
$k_{ini,r}^{c}\ (mm)$	6.64	8.70	8.81	5.55	-
$F_{y,Rk,r}^{c}\ (kN)$	347.5	197.4	184.6	282.6	-
$k_{pp,r}^{c}\ (mm)$	0.08	0.13	0.18	5.55	-
$F_{u,Rk,r}^{c}\ (kN)$	490.8	230.9	212.0	314.0	
$r = 2$	$c = CWT$	$c = CFB$	$c = EPB$	$c = BT$	$c = BWT$
$k_{ini,r}^{c}\ (mm)$	5.28	8.70	8.97	5.55	∞
$F_{y,Rk,r}^{c}\ (kN)$	249.4	197.4	244.7	282.6	437.9
$k_{pp,r}^{c}\ (mm)$	0.06	0.13	0.18	5.55	∞
$F_{u,Rk,r}^{c}\ (kN)$	352.2	230.9	282.6	314.0	563.1
$r = 1 - 2$	$c = CWT$	$c = CFB$	$c = EPB$	$c = BT$	$c = BWT$
$k_{ini,r}^{c}\ (mm)$	∞	∞	-	-	-
$F_{y,Rk,r}^{c}\ (kN)$	448.8	362.0	-	-	-
$k_{pp,r}^{c}\ (mm)$	∞	∞	-	-	-
$F_{u,Rk,r}^{c}\ (kN)$	633.8	444.2	-	-	-

Table 6-6. Characterization of the components in compression for the experimental tests 01, 04 and 07.

ROWS	Components				
$r = 4, c$	$c = CWC^{*}$	$c = BFC$	/	/	/
$k_{ini,r}^{c}\ (mm)$	10.00	∞			
$F_{y,Rk,r}^{c}\ (kN)$	346.3	414.9	/	/	/
$k_{pp,r}^{c}\ (mm)$	0.19	∞			
$F_{u,Rk,r}^{c}\ (kN)$	432.8	536.1			

Table 6-7. Characterization of the components in shear for the experimental tests 01, 04 and 07.

| Corman (2022)							
CWP	Test 01	Test 04	Test 07	SE	Test 01	Test 04	Test 07
$K_{y}^{CWP}\ (kN)$	109,819.9	109,801.2	109,805.3	$K_{y}^{SE}\ (kN)$	21,510.0	21,207.2	21,273.2
$V_{y,mod}^{CWP}\ (kN)$	205.0	194.3	206.9	$\Delta V_{y,mod}^{SE}\ (kN)$	54.4	38.6	56.8
$\Delta K_{y,mod}^{CWP}\ (kN)$	2,254.3	2,083.4	2,346.3	-	-	-	-
$V_{pp,mod}^{CWP}\ (kN)$	253.9	241.0	256.1	-	-	-	-
$K_{pp}^{CWP}\ (kN)$	1,413.5	1,413.5	1,413.5	$K_{pp}^{SE}\ (kN)$	383.5	378.1	379.3
$V_{u}^{CWP}\ (kN)$	343.8	336.9	217.2	-	-	-	-
$\Delta K_{pp}^{CWP}\ (kN)$	217.2	217.2	217.2	-	-	-	-
$V_{n}^{CWP}\ (kN)$	371.4	365.3	372.1	$\Delta V_{n}^{SE}\ (kN)$	111.8	100.4	112.1
$\gamma_{f,mod}^{CWP}\ (rad)$	0.2142	0.2228	0.2119	$\gamma_{f,mod}^{SE}\ (rad)$	0.1541	0.1670	0.1504
Jaspart (1991)							
CWP	Test 01	Test 04	Test 07	SE	Test 01	Test 04	Test 07
$K_{y}^{CWP}\ (kN)$		149,421.7		$K_{y}^{SE}\ (kN)$		0	
$V_{y}^{CWP}\ (kN)$		286.1		$\Delta V_{y}^{SE}\ (kN)$		0	
$\gamma_{y}^{PZ}\ (rad)$		0.0120		$\gamma_{y}^{PZ}\ (rad)$		0.0120	
$K_{pp}^{CWP}\ (kN)$		1,539.3		$K_{pp}^{SE}\ (kN)$		0	
$V_{u}^{CWP}\ (kN)$		404.1		$\Delta V_{u}^{SE}\ (kN)$		0	
$\gamma_{u}^{PZ}\ (rad)$		0.0887		$\gamma_{u}^{PZ}\ (rad)$		0.0887	

(a)

(b)

(c)
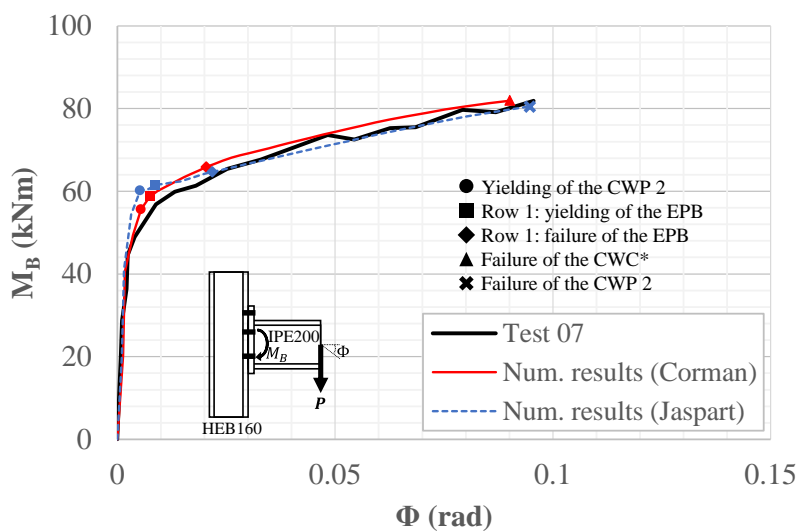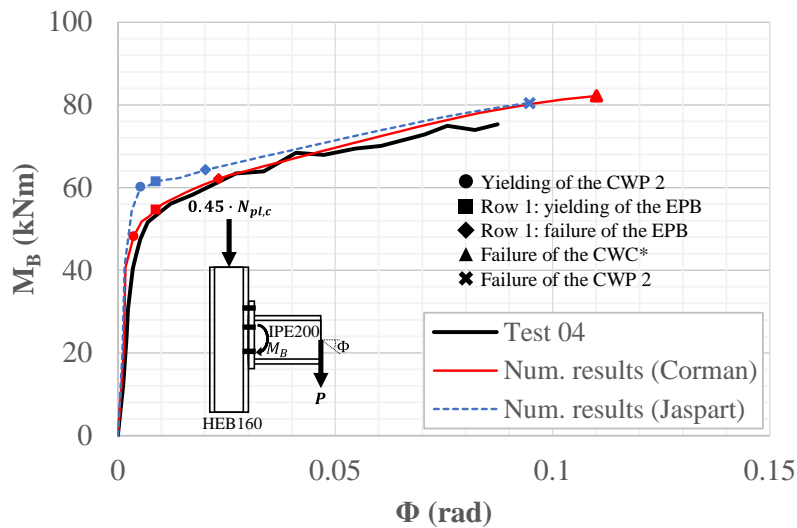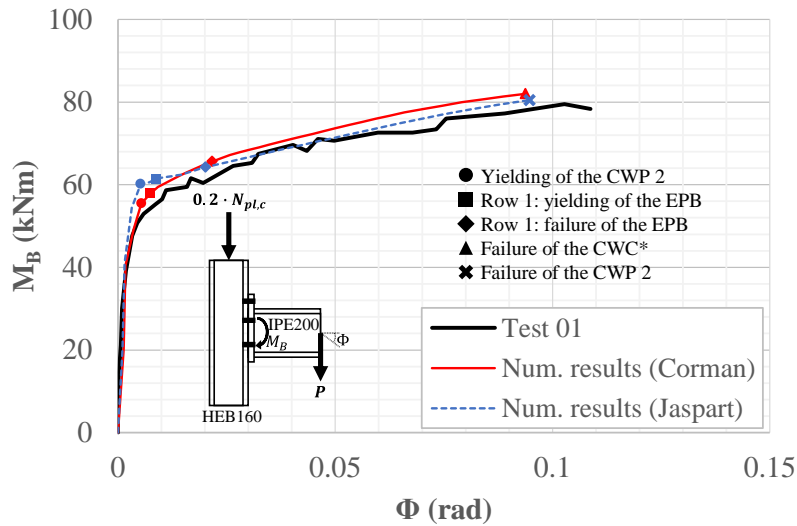
Fig. 6-4. Comparisons between the $\left(M^j - \Phi\right)_{exp}$ and $\left(M^j - \Phi\right)_{num}$ curves: (a) test 01, (b) test 04 and (c) test 07.

6.4 CONCLUSIONS

In the present CHAPTER 6, the new PZ analytical models developed in CHAPTER 4 and CHAPTER 5 in the case of welded joints, have been extended to PZs in bolted connections.

The prediction of the PZ plastic shear resistance has been considered first. As a first outcome, it was suggested that the complex formula developed in CHAPTER 4 could be kept as it is, with a small adjustment to the contribution of the SE, so that it more faithfully depicts the plastic collapse mechanism which actually develops in the SE. This modified formula has been validated against experimental results characterized by a PZ plastic failure mode. Before that, the assembly procedure in the current component method was slightly revised in order to better account for the actual distribution of the shear forces over the height of the PZ. This is a second outcome of the study.

Using this updated component method, the comparisons with the experimental results showed a reasonable agreement, highlighting the good performance of the complex analytical formula for the prediction of the PZ plastic shear resistance in bolted joints. In addition, a simplified version of this expression has also been proposed in view of its integration in the forthcoming prEN 1993-1-8 pre-normative document. Despite being more conservative, this simplified formula shows good performance and outperforms current EU and US design criteria, currently prescribed in the EN 1993-1-8 and AISC normative documents, and which were shown previously (see CHAPTER 3) to provide unsafe predictions in many cases.

As a second step, the prediction of the PZ full-range behaviour up to failure has been addressed. The complex analytical model developed in CHAPTER 5 has been validated through comparisons against experimental results on bolted joints characterized by a significant PZ shear deformation. This was achieved using the generalized mechanical model currently being developed within the CMM research team (see WP2 in Fig. 1-2). This mechanical model was built within a FE software for three carefully selected experimental tests. Promising preliminary results were obtained, showing a very good agreement between the experimental and numerical curves. From these results, a number of limitations in the mechanical model have been identified though, preventing the validation process to be conducted against a larger range of experimental results. Among them, it is recommended that the contributions of the CWP and the SE are decoupled in a future version of the mechanical model.

It should be recalled that the range of validity for the constitutive model developed in the present CHAPTER 6 is so far limited to column profiles characterized by a web-to-flange thickness ratio $t_{wc}/t_{fc} \in [0.55 - 0.62]$ and to axial loads $N_c \leq 0.5 \cdot N_{pl,c}$, $N_{pl,c}$ being the axial capacity of the column profile.

CHAPTER 7 Conclusions

7.1 SUMMARY AND GENERAL CONCLUSIONS

The present thesis is the first outcome of a larger research project conducted at the University of Liège and which aims at extending the component method towards the large deformation field, and under complex loading conditions (impact, fire, explosion, earthquake…). The contribution of the present thesis to this research project takes place at the component characterization level, as it focuses on the prediction of the full non-linear behaviour up to failure of the sheared PZ under monotonic loading conditions.

In this context, CHAPTER 2 provided an extensive literature review of past research works dedicated to the study of the behaviour of the PZ. Particular attention was paid to the available analytical models for the prediction of the PZ behaviour. The main observation was that all these models expressed the behaviour of the PZ as the sum of two independent contributions, namely that of the CWP and that of the SE, which can be modelled separately before being superimposed. However, different assumptions were made by the different authors for the modelling of these two contributions. Two sets of summary tables emerged from this study: the first one includes ten of the most referenced sophisticated models for the prediction of the PZ full-range behaviour (see Table 2-5 to Table 2-7); the second one includes four simplified design criteria for the prediction of the PZ plastic resistance, coming from various international standards (see Table 2-8 and Table 2-9). These tables use the same formalism for all the models in order to facilitate their comparison. From these comparisons, it was observed that only the Jaspart model among the ten sophisticated models provided analytical expressions to capture the full non-linear behaviour of the PZ up to failure. All the other models were limited to the yielding of the PZ only.

Based on this review, each analytical model's ability to accurately predict the PZ behaviour was investigated in CHAPTER 3 through comparisons with relevant experimental evidence. Two databases were compiled for that purpose, including respectively 12 experimental results on welded joints and 14 experimental results on bolted joints, carefully selected from the scientific literature. These tests all exhibited a PZ plastic failure mode and significant PZ shear deformations. They were processed in order to extract the main performance parameters of the joint's moment-rotation curve (i.e. initial rotational stiffness, plastic bending moment resistance, post-plastic rotational stiffness, ultimate bending moment resistance and ultimate rotation capacity), thereby allowing comparisons with the analytical models. From these comparisons, it was first observed that none of the complex analytical models was able to consistently capture the plastic shear resistance of the PZ. This observation also applied to the simplified EU and US design criteria for which unsafe predictions were obtained in many cases. Furthermore, the Jaspart model was not able to consistently predict the PZ deformation capacity up to failure either. These observations highlighted the need for a more sophisticated constitutive model for the PZ, built upon the deep understanding of the complex phenomena governing the behaviour of this component, and starting with the accurate estimation of its plastic shear resistance.

The prediction of the PZ plastic shear resistance was addressed in CHAPTER 4, focusing on welded joints only. This preliminary step was absolutely necessary to be able to subsequently characterize the complete deformation curve of the PZ up to failure. The scope was purposely limited to PZs in welded joints because this type of joint is much simpler to deal with than bolted ones: they are characterized by one single subpanel and involve a limited number of active components in addition to the sheared PZ. These two aspects made tests on welded joints particularly suitable for the development and validation of analytical models since they are the closest to tests on isolated PZs.

The numerical approach was used in order to identify the main parameters governing the plastic resistance of the PZ and to quantify their respective influences. A FE model was first built using the Abaqus© software and validated against two well-documented experimental results, coming from the scientific literature. Once validated, the numerical model was used to perform an extensive parametric study made of 32 numerical simulations. For all these simulations, a simplified elastic, perfectly-plastic material law was used in order to facilitate the derivation of the plastic shear resistance of the PZ. A robust methodology was also proposed for the extraction, from the numerical simulations, of the $(V - \gamma)_{num}$ curves associated to the PZ, CWP and SE. At the end, four main conclusions were drawn from the parametric study, regarding the spread of yielding across the PZ, the type of plastic collapse mechanism which actually develops in the SE and the influence of the $\tau - \sigma_i$ and $\tau - \sigma_{n,M-N}$ stress interactions.

Based on these conclusions, the two contributions of the CWP and SE were evaluated separately and then superimposed in order to obtain a new analytical expression for the prediction of the PZ plastic shear resistance. This new expression showed a great performance when compared to numerical and experimental results, thereby outperforming the available complex analytical models reviewed in CHAPTER 2, by providing a more consistent and physically-founded estimation of the PZ plastic shear resistance. It was recommended for scientific purposes only and was used as the basis for the development of a new full-range analytical model for the prediction of the PZ behaviour up to failure. In addition, this complex expression was also simplified in view of its integration in the forthcoming prEN 1993-1-8 pre-normative document. This simplified expression showed a reasonable but conservative performance, and outperformed the current EU and US design criteria, prescribed in the EN 1993-1-8 and AISC normative documents, and which were shown in CHAPTER 3 to provide unsafe prediction in many cases.

After proposing new analytical expressions for the prediction of the PZ plastic shear resistance, the scope of the study was extended to the prediction of the full non-linear response up to failure of PZs in welded joints. The first challenge in this study was the simulation of a large number of FE results, characterized by a PZ ultimate failure mode, as it was pointed out that very few experimental results collected in CHAPTER 3 exhibited such ultimate failure mode. To this aim, the parametric study conducted in CHAPTER 4 was relaunched but the simplified elastic, perfectly-plastic material law was then replaced by a more sophisticated quad-linear material law which accounts for material strain-hardening and damage. The results of the parametric study were carefully studied, revealing a PZ ultimate failure mode for 20 of the 32 numerical simulations, which were subsequently used for the validation of the analytical model.

This full-range analytical model was built from the knowledge acquired in previous CHAPTER 4 and consists of the superposition of the quad-linear and bilinear contributions of the CWP and the SE, respectively. The former was obtained by assuming a uniform shear stress distribution up to the shear buckling of the CWP, thus following the quad-linear material law; the latter was obtained by studying the collapse mechanism which actually develops in the SE and accounting for the material strain-hardening up to fracture. Both contributions were derived using the true stresses of the material. Furthermore, the geometrical second order effects, which develop in the large deformation field, were integrated within the model through the use of a $1/\cos\gamma$ coefficient affecting the contribution of the SE only, γ being the shear deformation of the PZ.

Quantitative comparisons with the 20 relevant numerical results showed that the model was able to capture the observed ultimate resistance and ultimate deformation capacity of the PZ with reasonable accuracy. For the comparisons with the experimental results, two quad-linear material models were contemplated, namely the simplified ECCS model and the more sophisticated EN 1993-1-14 model. Qualitative comparisons between the experimental and analytical results highlighted the high sensitivity of the model to the material laws used as inputs, leading to the conclusion that reliable

material models are the prerequisite for accurate predictions at the component level. Nonetheless, the model remained more performant than the Jaspart one, providing a more consistent estimation of the PZ behaviour up to failure. Two simplified criteria for the prediction of the PZ elastic stiffness and deformation capacity were derived from this new complex full-range model and proposed for integration in the forthcoming prEN 1993-1-8 pre-normative document. The first one was shown to outperform the current EN 1993-1-8 expression and to be fully consistent with the new proposal made in the prEN 1993-1-8 for the prediction of the plastic shear resistance of the PZ. The second one fills a gap in the EN 1993-1-8 normative document where no criterion is currently available for the prediction of the PZ deformation capacity.

Based on the new analytical models developed in CHAPTER 4 and CHAPTER 5 and extensively validated in the case of welded joints, the final step consisted in extending these models to PZs in bolted joints. This goal was partially achieved in CHAPTER 6, following a two-step procedure. The prediction of the plastic shear resistance of the PZ was considered first, before addressing the prediction of the PZ full-range behaviour up to failure.

For the former, the new expression developed in CHAPTER 4 was slightly adjusted in such a way that the contribution of the SE more faithfully depicts the actual plastic collapse mechanism which develops in the SE. The validation of this new formula against experimental results required also a minor revision of the current EN 1993-1-8 assembly procedure, in order to better account for the actual distribution of the shear forces over the height of the PZ. The comparisons with the 14 experimental results on bolted joints characterized by a PZ plastic failure mode highlighted the rather good performances of the updated complex analytical expression for the prediction of the PZ plastic shear resistance. In addition, this complex analytical formula was simplified in view of its integration in the forthcoming prEN 1993-1-8 pre-normative document. This expression showed reasonable (but conservative) performances when compared to the 14 experimental results on bolted joints. Notwithstanding that, it outperformed the current EU and US design criteria, currently prescribed in the EN 1993-1-8 and AISC normative documents, which were shown in CHAPTER 3 to be unsafe in many cases.

As a second step, the model for the prediction of the PZ full-range behaviour was validated against experimental results on bolted joints characterized by a significant PZ shear deformation. This step required the use of the generalized mechanical model currently being developed within the CMM research team, to take into account the different sources of deformability within the joint. In its current state, this mechanical model integrates the group effects, accounts for the actual distribution of the shear forces along the height of the PZ and was proven to accurately predict the joint's plastic bending moment resistance through comparisons with experimental and analytical results ([23], [24]). However, a number of limitations were identified in the present thesis, which prevent the straightforward extension of this mechanical model to the prediction of the joint's rotation capacity. Consequently, the model was used for a limited number of carefully selected experimental results only, for which promising preliminary results were obtained in terms of the prediction of the joint's rotation capacity, and thus of the PZ deformation capacity. Given the limitations of the mechanical model that were highlighted in this thesis, an extensive validation of the PZ constitutive model against a wide range of experimental results could not be achieved though and, therefore, constitutes a perspective of the present thesis.

7.2 MAIN CONTRIBUTIONS OF THE THESIS

The present thesis is, to the author's knowledge, the first comprehensive study dedicated to the characterization of the full non-linear behaviour of the PZ up to failure. The main contributions of this research work can be grouped into three main categories, namely experimental, numerical and analytical, and summarized as follows:

Experimental contributions

1. Two large databases have been built and consist of 12 experimental results on welded joints and 14 experimental results on bolted joints, respectively (see Appendix A.1 and Appendix A.2). These experimental results have been carefully selected from the scientific literature, and they all exhibit a PZ plastic failure mode and a significant PZ shear deformation. The available data are reported in a systematic manner for each test and consist of: (i) the test setup (see Fig. A-1(a) to Fig. A-26(a)); (ii) the available moment-rotation curve(s) of the joint, together with the main performance parameters (see Fig. A-1(b) to Fig. A-26(b)), the moment M_B being taken at the beam-to-column interface, and the rotation being either the shear distortion γ of the PZ or the total rotation Φ of the joint when the former is not available; (iii) the actual geometrical properties, when available – if not, the nominal ones are reported (see Fig. A-1(c) to Fig. A-26(c), respectively); (iv) the actual material properties (see Fig. A-13(d) to Fig. A-26(d), respectively). These experimental results can be re-used for the validation of further numerical and analytical models.

Numerical contributions

2. Two sophisticated FE models of two welded beam-to-column subassemblies, namely models NR4 and NR16, have been built within the Abaqus© environment and calibrated on experimental results in order to validate the numerical tool.

3. Practical procedures have been developed for the characterization of the PZ behaviour from FE results. These procedures allow for the extraction of the $(V - \gamma)_{num}$ deformation curves of the PZ, the CWP and the SE, and for the extraction of the joint's $\left(M^j - \Phi\right)_{num}$ moment-rotation curve, from the numerical simulations. These procedures are provided in Appendix B.

4. Two extensive parametric studies have been conducted with the validated numerical models. They both consist of 32 numerical simulations, which were performed with four different beam-to-column subassemblies (i.e. the models NR4, NR16, A and B) covering eight different joint configurations. For the first parametric study, a simplified elastic, perfectly-plastic material law has been used while in the second one, a more sophisticated quad-linear material law accounting for material strain-hardening and damage has been employed. The results from both parametric studies are extensively described in Appendix C where they can be easily re-used.

Analytical contributions

5. Two sets of summary tables have been prepared, which contain respectively ten of the most referenced analytical models for the prediction of the PZ behaviour (see Table 2-5 to Table 2-7) and four design criteria for the prediction of the plastic shear resistance of the PZ, coming from various international standards (see Table 2-8 and Table 2-9). These tables use the same formalism to present the models so that they facilitate their comparison.

6. A new complex analytical expression for the prediction of the PZ plastic shear resistance has been developed and extensively validated against experimental and numerical results for both welded and bolted joints (see CHAPTER 4 and Section 6.2 in CHAPTER 6, respectively). This model depicts the physical phenomena governing the yielding of the PZ more faithfully, and it is now available for the scientific community. The use of this model is recommended for scientific purposes.

7. A new constitutive model characterizing the full non-linear behaviour of the PZ up to failure has been developed and extensively validated against experimental and numerical results in the case of welded joints, while it still requires further validation in the case of bolted joints (see CHAPTER 5 and Section 6.3 in CHAPTER 6, respectively). This model depicts the physical phenomena governing the deformability and the failure of the PZ more faithfully, and it is now available for the scientific community.

8. A new set of simplified design criteria has been developed and validated against experimental and numerical results. This set includes analytical expressions for the prediction of the PZ initial stiffness, plastic resistance and deformation capacity. It has been proposed for introduction in the forthcoming prEN 1993-1-8 pre-normative document. A complete summary of the proposal is available to the reader in Appendix F.

7.3 LIMITATIONS AND PERSPECTIVES

The work presented in this doctoral thesis successfully addressed the overall objective of providing a new constitutive model for the PZ, capable of predicting the full non-linear response of this component up to failure, under monotonic loading conditions. Along the way, some assumptions were made though, which are recalled here below. The relaxation of these assumptions requires additional fundamental research efforts which constitute perspectives of the present work:

1. Firstly, the scope of the model was purposely limited to two widely used joint configurations, namely exterior joints on the one hand, and interior joints with beams of equal depth, subjected to equal but unbalanced bending moments on the other hand. The extension of the model to other joint configurations, for instance interior joints with beams of unequal depth and/or subjected to unequal and unbalanced bending moments, requires additional numerical and analytical developments.

2. Secondly, the model was validated for a given range of HE, IPE and W column profiles, characterized by a web-to-flange thickness ratio $t_{wc}/t_{fc} \in [0.55; 0.62]$. This range includes 17.5% of the IPE-profiles, 40% of the HE-profiles and 55% of the W-profiles. The validation of the model against the whole range of IPE, HE and W profiles of course requires additional numerical simulations to be performed.

3. Then, the model does not explicitly account for the presence of a supplementary web plate. This parameter should be easy to integrate into the model, but the approach still needs to be validated against numerical and/or experimental results.

4. After that, the model has been developed in the context of monotonic loading conditions. Now the way is paved, it could be extended to more complex loading conditions (impact, fire, explosion, earthquake…).

5. Furthermore, the model can take into account the effect of an axial load N_c in the column, with a magnitude up to $0.5 \cdot N_{pl,c}$, $N_{pl,c}$ being the axial capacity of the column profile. This load level is assumed to be representative of the maximum axial load that a column may encounter in a typical steel frame structure. While this assumption seems valid under classical monotonic loading conditions, it may no longer be true in the context of an exceptional loading. Therefore, the model should also be validated for stronger axial loads N_c in the column.

6. Finally, the model does not take into account the effect of an axial load N_b in the beam(s), since this load is assumed to be negligible with respect to the beam bending moment, under classical monotonic loading conditions. However, this assumption is no longer valid in the context of a column loss scenario, in robustness applications, where the beams are subjected to strong axial loads N_b. Therefore, the model should be further developed to accommodate the effect of these axial loads coming from the beams.

The integration of this new constitutive model in the generalized mechanical model that is being developed within the CMM research team also raised some other limitations, at both component and assembly levels. They are recalled here below:

Component level

7. For the characterization of the BFC component, the risk of local buckling (i.e. LB_{BFC}) is not covered yet by the formula provided in EN 1993-1-8. However, the present thesis showed that this ultimate failure mode actually governs the joint's ultimate resistance in many cases, and often by-passes the PZ ultimate failure mode. Consequently, it is suggested that a study is conducted for the BFC, similar to the one reported in [21] for the CWC* component.

8. As regards the characterization of the plate components (i.e. CFB and EPB), the current formulae for the prediction of the ultimate resistance and deformation capacity are known to be far too conservative, especially when a ductile ultimate failure mode (i.e. mode 1 or 2) is occuring. This leads to simulations that stop far too early when these components are activated at ultimate state. The PhD thesis that has just been initiated within the CMM research team (see WP1B in Fig. 1-1) should fix this issue and provide more sophisticated formulae to accurately predict the full-range behaviour up to failure of these components.

Assembly level

9. In the characterization of the CWC*/CWT components, a new expression has been suggested for the ω reduction factor, accounting for the $\tau - \sigma_i$ stress interaction. This expression relies on local values of the β parameter which have to be computed at each bolt-row and updated at each iteration step in the simulation. The generalized mechanical model which is currently available does not allow to do so though.

10. As for the modeling of the PZ, the generalized mechanical model accounts for the contribution of the CWP correctly, but it is not broad-based enough to account for the different collapse mechanisms which are susceptible to develop in the SE. In a future version of the model, the author suggests decoupling the contributions of the CWP and SE, which means developing additional elements capable of simulating the contribution of the SE. Once this future version is available, a thorough validation of the PZ constitutive model can eventually be achieved against a large number of bolted experimental results, this step being missing in the present thesis.

11. Finally, the model is currently using rigid-plastic extensional springs to account for the group effects that may develop in the plate components. However, this modeling does not allow to predict the group ultimate resistance since it ignores the strain-hardening effect in the group. Consequently, the author suggests a more refined modelling of the group effects in a future version of the mechanical model.

7.4 LIST OF PUBLICATIONS

Sheared panel zone

1. A. Corman, J.-P. Jaspart, and J.-F. Demonceau, "Resistance of the beam-to-column component *column web panel in shear,*" *Steel Construction*, vol. 12, no. 3, pp. 222-230, 2019. DOI
   doi: https://doi.org/10.1002/stco.201900020

2. A. Corman, J.-P. Jaspart, and J.-F. Demonceau, "Resistance of the beam-to-column component *column web panel in shear* – numerical and analytical investigations,*" *ce/papers*, vol. 3, no. 3-4, pp. 325-330, 2019.
   doi: https://doi.org/10.1002/cepa.1061

3. A. Corman, J.-F. Demonceau, and J.-P. Jaspart, "Analytical model for the prediction of the plastic shear resistance of the panel zone in welded joints,*" *ce/papers*, vol. 4, no. 2-4, pp. 995-1005, 2021.
   doi: https://doi.org/10.1002/cepa.1389

4. A. Corman, J.-F. Demonceau, and J.-P. Jaspart, "Characterization of the panel zone shear behaviour in steel beam-to-column joints,*" *Steel Construction*, vol. 15, 2022.
   doi: https://doi.org/10.1002/stco.202100052

5. A. Corman, J.-F. Demonceau, and J.-P. Jaspart, "Analytical model for the panel zone resistance in welded steel beam-to-column joints,*" *Journal of Constructional Steel Research*, vol. 189, no. 107099, 2022.
   doi: https://doi.org/10.1016/j.jcsr.2021.107099

Column web in compression

6. J.-P. Jaspart, A. Corman, and J.-F. Demonceau, "Mechanical Properties of the Component 'Column Web in Compression' in Steel Beam-to-column Joints," *ce/papers*, vol. 5, no. 4, pp. 242–250, 2022.
   doi: https://doi.org/10.1002/cepa.1752

7. J. P. Jaspart, A. Corman, and J. F. Demonceau, "Characterization of unstiffened column webs in transverse compression in steel beam-to-column joints," *Thin-Walled Structures*, vol. 180, no. 109848, 2022.
   doi: https://doi.org/10.1016/j.tws.2022.109848

Assembly procedure

8. J.-P. Jaspart, A. Corman, and J.-F. Demonceau, "Ductility assessment of structural steel and composite joints," in *SDSS 2019 - International Colloquium on Stability and Ductility of Steel Structures*, 2019.
   doi: https://doi.org/10.1201/9780429320248

9. T. Golea, A. Corman, J. Mathieu, Y. Duchêne, J.-P. Jaspart, and J.-F. Demonceau, "An innovative mechanical model for steel and steel-concrete composite joints (under review),*" *Engineering Structures*, 2022.

Bibliography

[1] European Committee for Standardization (CEN), "EN 1993-1-8, Eurocode 3: Design of steel structures - Part 1-8: Design of joints," Brussels, Belgium, 2005.

[2] European Committee for Standardization (CEN), "EN 1990, Eurocode - Basis of structural design," Brussels, Belgium, 2002.

[3] European Committee for Standardization (CEN), "EN 1991-1-7, Eurocode 1 - Actions on structures - Part 1-7: General actions - Accidental actions," Brussels, Belgium, 2006.

[4] L. Simões da Silva, "Towards a consistent design approach for steel joints under generalized loading," *J. Constr. Steel Res.*, vol. 64, no. 9, pp. 1059–1075, 2008, doi: 10.1016/j.jcsr.2008.02.017.

[5] C. Haremza, A. Santiago, J. F. Demonceau, J. P. Jaspart, and L. S. Da Silva, "Composite joints under M-N at elevated temperatures," *J. Constr. Steel Res.*, vol. 124, pp. 173–186, 2016, doi: 10.1016/j.jcsr.2016.05.012.

[6] C. Liu, K. H. Tan, and T. C. Fung, "Component-based steel beam-column connections modelling for dynamic progressive collapse analysis," *J. Constr. Steel Res.*, vol. 107, pp. 24–36, 2015, doi: 10.1016/j.jcsr.2015.01.001.

[7] M. D'Aniello, R. Tartaglia, S. Costanzo, and R. Landolfo, "Seismic design of extended stiffened end-plate joints in the framework of Eurocodes," *J. Constr. Steel Res.*, vol. 128, pp. 512–527, 2017, doi: 10.1016/j.jcsr.2016.09.017.

[8] S. Oliveira, R. Costa, A. Shahbazian, C. Rebelo, Y. Harada, and L. S. da Silva, "Component-based method for quasi-static cyclic behaviour of steel joints," *J. Constr. Steel Res.*, vol. 181, no. 106551, 2021, doi: 10.1016/j.jcsr.2021.106551.

[9] L. Simões Da Silva and A. G. Coelho, "Ductility model for steel connections," *J. Constr. Steel Res.*, vol. 57, no. 1, pp. 45–70, 2001, doi: 10.1016/S0143-974X(00)00009-2.

[10] L. Simões Da Silva, A. Santiago, and P. Vila Real, "Post-limit stiffness and ductility of end-plate beam-to-column steel joints," *Comput. Struct.*, vol. 80, no. 5–6, pp. 515–531, 2002, doi: 10.1016/S0045-7949(02)00014-7.

[11] S. Yan and K. J. R. Rasmussen, "Generalised Component Method-based finite element analysis of steel frames," *J. Constr. Steel Res.*, vol. 187, 2021, doi: 10.1016/j.jcsr.2021.106949.

[12] W. Wan, S. Yan, H. Zhang, and K. J. R. Rasmussen, "A generalised component method for bolted angle connections," *J. Constr. Steel Res.*, vol. 198, no. 107530, 2022, doi: 10.1016/j.jcsr.2022.107530.

[13] A. M. Coelho Girão, "Characterization of the Ductility of Bolted End Plate Beam-To-Column Steel Connections (PhD thesis)," University of Coimbra, Coimbra (Portugal), 2004.

[14] D. Beg, E. Zupančič, and I. Vayas, "On the rotation capacity of moment connections," *J. Constr. Steel Res.*, vol. 60, no. 3–5, pp. 601–620, 2004, doi: 10.1016/S0143-974X(03)00132-9.

[15] A. M. Girão Coelho, L. S. Da Silva, and F. S. K. Bijlaard, "Ductility analysis of bolted extended end plate beam-to-column connections in the framework of the component method," *Steel Compos. Struct.*, vol. 6, no. 1, pp. 33–53, 2006, doi: 10.12989/scs.2006.6.1.033.

[16] A. A. Del Savio, D. A. Nethercot, P. C. G. S. Vellasco, S. A. L. Andrade, and L. F. Martha, "Generalised component-based model for beam-to-column connections including axial versus moment interaction," *J. Constr. Steel Res.*, vol. 65, no. 8–9, pp. 1876–1895, 2009, doi: 10.1016/j.jcsr.2009.02.011.

[17] C. Zhu, K. J. R. Rasmussen, and S. Yan, "Generalised component model for structural steel joints," *J. Constr. Steel Res.*, vol. 153, pp. 330–342, 2019, doi: 10.1016/j.jcsr.2018.10.026.

[18] K. J. R. Rasmussen, X. Zhao, S. Yan, L. Dai, C. Zhu, and L. Jiang, "Recent developments of the Component Method," *Ce/Papers*, vol. 3, no. 3–4, pp. 313–323, 2019, doi: 10.1002/cepa.1060.

[19] S. Yan, K. J. R. Rasmussen, L. L. Jiang, C. Zhu, and H. Zhang, "Experimental evaluation of the full-range behaviour of steel beam-to-column connections," *Adv. Steel Constr.*, vol. 16, no. 1, pp. 77–84, 2020, doi: 10.18057/IJASC.2020.16.1.9.

[20] S. Yan, L. Jiang, K. Rasmussen, and H. Zhang, "Full-Range Behavior of Top-and-Seat Angle Connections," *J. Struct. Eng.*, vol. 147, no. 1, pp. 1–20, 2021, doi: 10.1061/(asce)st.1943-541x.0002893.

[21] J. P. Jaspart, A. Corman, and J. F. Demonceau, "Characterization of unstiffened column webs in transverse compression in steel beam-to-column joints," *Thin-Walled Struct.*, vol. 180, no. 109848, 2022, doi: 10.1016/j.tws.2022.109848.

[22] J.-P. Jaspart, A. Corman, and J.-F. Demonceau, "Mechanical Properties of the Component 'Column Web in Compression' in Steel Beam-to-column Joints," *ce/papers*, vol. 5, no. 4, pp. 242–250, 2022, doi: https://doi.org/10.1002/cepa.1752.

[23] T. Golea, A. Corman, J. Mathieu, J. Demonceau, and J.-P. Jaspart, "An innovative mechanical model to characterise structural joints (unpublished)," *Work. Connect. IX*, 2020.

[24] T. Golea, A. Corman, J. Mathieu, Y. Duchêne, J.-P. Jaspart, and J.-F. Demonceau, "An innovative mechanical model for steel and steel-concrete composite joints (under review)," *Eng. Struct.*, 2022.

[25] Simulia, "ABAQUS User's Manual (Version 6.14)." Dassault Systèmes Simulia Corp., 2014, [Online]. Available: http://130.149.89.49:2080/v6.14/.

[26] J.-P. Jaspart and K. Weynand, *Design of Joints in Steel and Composite Structures*. Weinheim, Germany: Wiley-VCH Verlag GmbH & Co. KGaA, 2016.

[27] R. Maquoi and J. P. Jaspart, "Load-Introduction Resistance of Column Webs in Strong Axis Beam-to-Column Joints," in *Contact Loading and Local Effects in Thin-walled Plated and Shell Structures*, 1992, pp. 204–211.

[28] J.-P. Jaspart, "Study of the semi-rigid behaviour of beam-to-column joints and of its influence on the stability and strength of steel building frames (PhD thesis, in French)," University of Liège, Liège (Belgium), 1991. doi: http://hdl.handle.net/2268/30426.

[29] J.-P. Jaspart and R. Maquoi, "Prediction of the Semi-Rigid and Partial-Strength Properties of Structural Joints," in *SSRS Annual Task Group Technical Session and Meeting*, 1994, pp. 177–191, doi: http://hdl.handle.net/2268/30582.

[30] J.-P. Jaspart, A. Corman, and J.-F. Demonceau, "Ductility assessment of structural steel and composite joints," 2019, doi: https://doi.org/10.1201/9780429320248.

[31] C. Faella, V. Piluso, and G. Rizzano, *Structural steel semirigid connections : theory, design and software*. Boca Raton, FL: CRC Press [Chemical Rubber Company], 2000.

[32] U. Kuhlmann and F. Kühnemund, "Rotation capacity of steel joints: verification procedure and component tests.," in *Proceedings of the NATO Advanced Research Workshop: The paramount role of joints into the reliable response of structures*, 2000, pp. 363–372.

[33] F. Kühnemund, "Verification of the rotation capacity of joints in steel structures (PhD thesis, in German)," University of Stuttgart, Stuttgart (Germany), 2003. doi: 10.1002/stab.200302270.

[34]   V. Piluso, C. Faella, and G. Rizzano, "Ultimate Behavior of Bolted T-Stubs. I: Theoretical Model," *J. Struct. Eng.*, vol. 127, no. 6, pp. 686–693, 2001, doi: 10.1061/(asce)0733-9445(2001)127:6(694).

[35]   V. Piluso, C. Faella, and G. Rizzano, "Ultimate Behavior of Bolted T-Stubs. II: Model Validation," *J. Struct. Eng.*, vol. 127, no. 6, pp. 694–704, 2001, doi: 10.1061/(asce)0733-9445(2001)127:6(694).

[36]   A. C. Faralli, M. Latour, P. J. Tan, G. Rizzano, and P. Wrobel, "Experimental investigation and modelling of T-stubs undergoing large displacements," *J. Constr. Steel Res.*, vol. 180, no. 106580, 2021, doi: 10.1016/j.jcsr.2021.106580.

[37]   A. B. Francavilla, M. Latour, and G. Rizzano, "Ultimate behaviour of bolted T-stubs under large displacements: A mechanical model," *J. Constr. Steel Res.*, vol. 195, no. 107355, 2022, doi: 10.1016/j.jcsr.2022.107355.

[38]   A. Corman, J.-F. Demonceau, and J.-P. Jaspart, "Analytical model for the panel zone resistance in welded steel beam-to-column joints," *J. Constr. Steel Res.*, vol. 189, p. 107099, 2022, doi: https://doi.org/10.1016/j.jcsr.2021.107099.

[39]   A. Corman, J.-P. Jaspart, and J.-F. Demonceau, "Resistance of the beam-to-column component "column web panel in shear"," *Steel Constr.*, vol. 12, no. 3, 2019, doi: 10.1002/stco.201900020.

[40]   E. P. Popov and R. M. Stephen, "Cyclic loading of full- size steel connections," 1972.

[41]   E. P. Popov, "Seismic moment connections for moment-resisting steel frames," Berkley (California), 1983. doi: 10.1016/0143-974X(88)90030-2.

[42]   G. C. Driscoll and J. W. Peters, "A study of the behaviour of beam-to-column connections.," Bethlehem (Pennsylvania), 1968.

[43]   L. Van Zuilen, D. J. Fielding, and G. C. Driscoll, "Proposal for Test of Full Size Beam-To-Column Connection Subjected to Moment. Shear, and High Axial Loads," Bethlehem (Pennsylvania), 1968.

[44]   H. Krawinkler, V. V. Bertero, and E. P. Popov, "Behaviour of Steel Beam- Column Subassemblages Under Cyclic Loading," Berkley (California), 1970.

[45]   L.-W. Lu, R. G. Slutter, and S. J. Lee, "Ductility and Fracture of Joints with Panel Zone Deformation," 1985, doi: 10.1061/ciegag.0001084.

[46]   E. P. Popov, M. Eeri, R. A. Navin, J. J. C. Louie, and R. M. Stephen, "Cyclic behaviour of large beam-column assemblies," *Earthq. Spectra*, vol. 1, no. 2, pp. 203–238, 1985.

[47]   A. Matsuo, Y. Nakamura, R. W. Salib, Y. Mukudai, and T. Takamatsu, "Evaluation of the maximum strength of H-shaped steel beam-to-column connections," in *Earthquake Engineering, Tenth World Conference*, 1992, pp. 2873–2878.

[48]   M. D. Engelhardt and A. S. Husain, "Cyclic-Loading Performance of Welded Flange-Bolted Web Connections," *J. Struct. Eng.*, vol. 119, no. 12, pp. 3537–3550, 1993.

[49]   E. Mele, *Moment resisting welded connections: An extensive review of design practice and experimental research in usa, japan and europe*, vol. 6, no. 1. 2002.

[50]   J. S. Huang, D. J. Fielding, and J. S. Huang, "Shear in steel beam-to-column connections," *Weld. Res. Suppl.*, pp. 313–326, 1971.

[51]   H. Krawinkler, V. V Bertero, E. P. Popov, B. University of California, and E. E. R. Center., "Inelastic behavior of steel beam-to-column subassemblages," Berkeley, 1971. [Online]. Available: http://nisee.berkeley.edu/elibrary/Text/1000429.

[52]   H. Krawinkler, "Shear in Beam-Column Joints in Seismic Design of Steel Frames," *Eng. J.*, vol. 15, pp. 88–91, 1978, [Online]. Available: https://www.aisc.org/Shear-in-Beam-Column-Joints-in-Seismic-Design-of-Steel-Frames.

[53]   L.-W. Lu, S.-J. Wang, and S.-J. Lee, "Cyclic behaviour of steel and composite joints with panel zone deformation," in *Proceedings of 9th World Conference on Earthquake Engineering, Tokyo-Kyoto, Japan*, 1988, pp. 701–706.

[54]   B. Kato, W. F. Chen, and M. Nakao, "Effects of joint-panel shear deformation on frames," *J. Constr. Steel Res.*, vol. 10, no. C, pp. 269–320, 1988, doi: 10.1016/0143-974X(88)90033-8.

[55]   A. Matsuo, Y. Nakamura, and R. W. Salib, "Seismic behavior in steel structures of weak connections," in *IABSE Reports*, 1995, pp. 1435–1440.

[56]   S. El-Tawil, E. Vidarsson, T. Mikesell, and S. K. Kunnath, "INELASTIC BEHAVIOR AND DESIGN OF STEEL PANEL ZONES By," *J. Struct. Eng.*, vol. 125, no. 2, pp. 183–193, 1999.

[57]   K. D. Kim and M. D. Engelhardt, *Monotonic and cyclic loading models for panel zones in steel moment frames*, vol. 58, no. 5–8. 2002.

[58]   A. Skiadopoulos, A. Elkady, and D. G. Lignos, "Proposed Panel Zone Model for Seismic Design of Steel Moment-Resisting Frames," *J. Struct. Eng.*, vol. 147, no. 4, p. 04021006, 2021, doi: 10.1061/(asce)st.1943-541x.0002935.

[59]   E. M. Lui and W. F. Chen, "FRAME ANALYSIS WITH PANEL ZONE DEFORMATION," *Int. J. Solids Struct.*, vol. 22, no. 12, pp. 1599–1627, 1986.

[60]   H. Krawinkler and S. Mohasseb, "Effects of panel zone deformations on seismic response," *J. Constr. Steel Res.*, vol. 8, no. C, pp. 233–250, 1987, doi: 10.1016/0143-974X(87)90060-5.

[61]   J. Y. R. Liew and W. F. Chen, "Analysis and Design of Steel Frames Considering Panel Joint Deformations," *J. Struct. Eng.*, vol. 121, no. 10, pp. 1531–1540, 1995, doi: 10.1061/(asce)0733-9445(1995)121:10(1531).

[62]   S. P. Schneider and A. Amidi, "Seismic Behavior of Steel Frames with Deformable Panel Zones," *J. Struct. Eng.*, vol. 124, no. 1, pp. 35–42, 1998, doi: 10.1061/(asce)0733-9445(1998)124:1(35).

[63]   J. M. Castro, A. Y. Elghazouli, and B. A. Izzuddin, "Modelling of the panel zone in steel and composite moment frames," *Eng. Struct.*, vol. 27, no. 1, pp. 129–144, 2005, doi: 10.1016/j.engstruct.2004.09.008.

[64]   J. M. Castro, F. J. Dávila-Arbona, and A. Y. Elghazouli, "Seismic design approaches for panel zones in steel moment frames," *J. Earthq. Eng.*, vol. 12, no. SUPPL. 1, pp. 34–51, 2008, doi: 10.1080/13632460801922712.

[65]   I. Mansouri and H. Saffari, "New mathematical modeling of steel panel zone with thin to thick column flanges," *Asian J. Civ. Eng.*, vol. 16, no. 4, pp. 451–466, 2015.

[66]   E. Bayo, J. Gracia, B. Gil, and R. Goñi, "An efficient cruciform element to model semirigid composite connections for frame analysis," *J. Constr. Steel Res.*, vol. 72, pp. 97–104, 2012, doi: 10.1016/j.jcsr.2011.11.006.

[67]   K. C. Tsai, S. Wu, and E. P. Popov, "Experimental Performance of Seismic Steel Beam-Column Moment Joints," *J. Struct. Eng.*, vol. 121, no. 6, pp. 925–931, 1995.

[68]   E. P. Popov and M. Blondet, "Bahavior of large steel beam-column connections," in *Eleventh World Conference on Earthquake Engineering*, 1996, p. Paper No. 166.

[69]   B. Stojadinovic, C. G. Subhash, K.-H. Lee, A. G. Margarian, and J.-H. Choi, "PARAMETRIC TESTS ON UNREINFORCED STEEL MOMENT CONNECTIONS," *J. Struct. Eng.*, vol.

126, no. 1, pp. 40–49, 2000.

[70]   K. C. Lin, K. C. Tsai, S. L. Kong, and S. H. Hsien, "Effects of Panel Zone Deformations On Cyclic Performance of Welded Moment Connections," 2000.

[71]   D. Lee, S. C. Cotton, J. F. Hajjar, R. J. Dexter, and Y. Ye, "Cyclic behavior of steel moment-resisting connections reinforced by alternative column stiffener details I. Connection performance and continuity plate detailing," *Eng. J.*, vol. 42, no. 4, pp. 189–213, 2005.

[72]   C. H. Lee and J. H. Kim, "Effects of panel zone strength on cyclic performance of reduced beam section steel moment connections," *Proc. Int. Colloq. Stab. Ductility Steel Struct. SDSS 2006*, no. December 2005, pp. 943–950, 2006.

[73]   D. W. Kim, C. Blaney, and C. M. Uang, "Panel zone deformation capacity as affected by weld fracture at column kinking location," *Eng. J.*, vol. 52, no. 1, pp. 27–46, 2015.

[74]   E. A. Sumner and T. M. Murray, "Behavior of Extended End-Plate Moment Connections Subject to Cyclic Loading," *J. Struct. Eng.*, vol. 128, no. 4, pp. 501–508, 2002, doi: 10.1061/(asce)0733-9445(2002)128:4(501).

[75]   B. M. Nakashima and Y. Maruoka, "Tests of welded beam-column subassemblies. I: Global behavior," *J. Struct. Eng.*, vol. 124, no. 11, pp. 1236–1244, 1998.

[76]   H. Namba, M. Tabuchi, and T. Tanaka, "Evaluation for Restoring Force Characteristic of Joint Panels with Various Cross Sections (in Japanese)," *Steel Constr. Eng.*, vol. 11, no. 42, 2004.

[77]   F. Rahiminia, "Effects of Joint Panel Shear Deformation on Elasto-Plastic Behavior of Steel Beam-to-Column Connections," 2010, pp. 1–5, doi: 10.13140/RG.2.1.3106.9602.

[78]   F. Rahiminia and H. Namba, "Joint panel shear yielding in steel moment," 2012.

[79]   F. Rahiminia and H. Namba, "Joint panel in steel moment connections, Part 1: Experimental tests results," *J. Constr. Steel Res.*, vol. 89, pp. 272–283, 2013, doi: 10.1016/j.jcsr.2013.07.002.

[80]   F. Rahiminia, "Effect of Joint Panel Shear Deformation on Elasto-Plastic Behavior of Steel Beam-to-Column Connections (PhD thesis)," University of Kobe, Kobe (Japan), 2013.

[81]   L. Calado, C. A. Castiglioni, and C. Bernuzzi, "Seismic Behaviour of Welded Beam-to-Column Joints: Experimental and Numerical Analysis," in *Fourth International Workshop on Connections in Steel Structures*, 2000, pp. 243–256.

[82]   L. Calado, "Design of Connections," in *Seismic Resistant Steel Structures*, 2000, pp. 349–399.

[83]   E. Mele, L. Calado, and A. De Luca, "Experimental Investigation on European Welded Connections," *J. Struct. Eng.*, vol. 129, no. 10, pp. 1301–1311, 2003, doi: 10.1061/(ASCE)0733-9445(2003)129:10(1301).

[84]   D. Dubina, A. Ciutina, and A. Stratan, "Cyclic Tests of Double-Sided Beam-to-Column Joints," *J. Struct. Eng.*, vol. 127, no. 2, pp. 129–136, 2001.

[85]   A. L. Ciutina and D. Dubina, "Seismic behaviour of steel beam-to-column joints with column web stiffening," *Steel Compos. Struct.*, vol. 6, no. 6, pp. 493–512, 2006, doi: 10.12989/scs.2006.6.6.493.

[86]   P. Nogueiro, "Dynamic Behaviour of Steel Connections (PhD thesis, in Portugese)," University of Coimbra, Coimbra (Portugal), 2009.

[87]   SAC Venture, "FEMA-350, Recommended Seismic Design Criteria for New Steel Moment-Frame Buildings," 2000.

[88]   AISC, "ANSI/AISC 360-16, Specification for Structural Steel Buildings," Chicago (Illinois), 2016.

[89] European Committee for Standardization (CEN), "EN 1998-1, Eurocode 8: Design of structures for earthquake resistance - Part 1: General rules, seismic actions and rules for buildings," Brussels, Belgium, 2004.

[90] The Architectural Institute of Japan, "AIJ, Recommendation for Design of Connections in Steel Structures (In Japanese)," Tokyo (Japan), 2012.

[91] China Architecture & Building, "GB 50017-2017, Standard for Design of Steel Structures (in Chinese)," Beijing (China), 2018.

[92] J. Jin and S. El-Tawil, "Evaluation of FEMA-350 Seismic Provisions for Steel Panel Zones," *J. Struct. Eng.*, vol. 131, no. 2, pp. 250–258, 2005, doi: 10.1061/(asce)0733-9445(2005)131:2(250).

[93] F. J. Dávila-Arbona, J. M. Castro, and A. Y. Elghazouli, "Review of panel zone design approaches for steel moment frames," 2008.

[94] G. Brandonisio, A. De Luca, and E. Mele, "Shear strength of panel zone in beam-to-column connections," *J. Constr. Steel Res.*, vol. 71, pp. 129–142, 2012, doi: 10.1016/j.jcsr.2011.11.004.

[95] M. Tuna and C. Topkaya, "Panel zone deformation demands in steel moment resisting frames," *J. Constr. Steel Res.*, vol. 110, pp. 65–75, 2015, doi: 10.1016/j.jcsr.2015.02.017.

[96] H. Augusto, "Characterization of the behaviour of partial-strength joints under cyclic and seismic loading conditions (PhD thesis)," University of Coimbra, Coimbra (Portugal), 2017.

[97] F. Iannone, M. Latour, V. Piluso, and G. Rizzano, *Experimental analysis of bolted steel beam-to-column connections: Component identification*, vol. 15, no. 2. 2011.

[98] RFCS, "Project EQUALJOINTS-PLUS under the Grant Agreement n°754048."

[99] P. Zoetemeijer, "The influence of normal, bending and shear stresses on the ultimate compression force exerted laterally to European rolled sections," Stevin laboratory of Steel Structures (The Nederlands), 1975.

[100] H. Klein, "Characterization of the elasto-plastic moment-rotation curve of unstiffened welded joints for the calculation of steel frame structures with HEB columns (PhD thesis, in German)," University of Innsbruck, Innsbruck (Austria), 1985.

[101] C. Braun, "Study of the moment-rotation behaviour of unstiffened welded joints under shear force loading (PhD thesis, in German)," University of Innsbruck, Innsbruck (Austria), 1987.

[102] C. Humer, "Study of the moment-rotation behaviour of unstiffened joints with end-plate connections (PhD thesis, in German)," University of Innsbruck, Innsbruck (Austria), 1987.

[103] F. Tschemmernegg and C. Humer, "The design of structural steel frames under consideration of the nonlinear behaviour of joints," *J. Constr. Steel Res.*, vol. 11, no. 2, pp. 73–103, 1988, doi: 10.1016/0143-974X(88)90045-4.

[104] F. Frey and W. Atamaz Sibai, "Numerical simulation of the behaviour up to collapse of two welded unstiffened one-side flange connections," in *Connections and the Behaviour, Strength and Design of Steel Structures*, 1987, pp. 85–92.

[105] W. Atamaz Sibai and J.-P. Jaspart, "Study of the full-range behaviour up to failure of welded joints (in French)," Liège (Belgium), 1989.

[106] J.-P. Jaspart, "Shear and load-introduction deformability and strength of column web panels in strong axis beam-to-column joints," Liège (Belgium), 1990.

[107] J.-P. Jaspart, "Recent advances in the field of steel joints; column bases and further

configurations for beam-to-column joints and beam splices (Professorship thesis)," University of Liège, Liège (Belgium), 1997. doi: http://hdl.handle.net/2268/30425.

[108]   A. M. Girão Coelho, F. S. K. Bijlaard, and M. H. Kolstein, "Numerical modelling of high strength steel column web shear panel behaviour," in *Proceedings of the Eurosteel Conference*, 2008, pp. 1125–1136.

[109]   A. M. Girão Coelho, F. S. K. Bijlaard, and M. H. Kolstein, "Behaviour of high strength steel web shear panels," Delft (The Nederlands), 2008.

[110]   A. M. Girão Coelho, F. S. K. Bijlaard, and H. Kolstein, "Experimental behaviour of high-strength steel web shear panels," *Eng. Struct.*, vol. 31, no. 7, pp. 1543–1555, 2009, doi: 10.1016/j.engstruct.2009.02.023.

[111]   A. M. Girão Coelho and F. S. K. Bijlaard, "Moment-resisting joints in HSS - code improvement proposals," *Steel Constr. - Des. Res.*, vol. 11, no. 4, pp. 294–305, 2018.

[112]   S. Jordão, L. Simões Da Silva, and R. Simões, "Behaviour of welded beam-to-column joints with beams of unequal depth," *J. Constr. Steel Res.*, vol. 91, pp. 42–59, 2013, doi: 10.1016/j.jcsr.2013.07.023.

[113]   S. Jordão, "Behaviour of internal welded joints with beams of different depths and high strength steel (PhD thesis, in Portuguese)," University of Coimbra, Coimbra (Portugal), 2008.

[114]   G. Brandonisio, A. De Luca, and E. Mele, "Shear instability of panel zone in beam-to-column connections," *J. Constr. Steel Res.*, vol. 67, no. 5, pp. 891–903, 2011, doi: 10.1016/j.jcsr.2010.11.019.

[115]   A. Skiadopoulos and D. G. Lignos, "Development of Inelastic Panel Zone Database," *J. Struct. Eng.*, vol. 147, no. 4, pp. 1–14, 2021, doi: 10.1061/(asce)st.1943-541x.0002957.

[116]   H. Augusto, L. Simões da Silva, C. Rebelo, and J. M. Castro, "Characterization of web panel components in double-extended bolted end-plate steel joints," *J. Constr. Steel Res.*, vol. 133, pp. 310–333, 2017, doi: 10.1016/j.jcsr.2017.01.021.

[117]   Z. Fasoulakis, H. Pasternak, I. Vayas, and Z. Li, "Stützen-Riegel-Knoten ohne und mit geklebter CFK-Verstärkung – Versuche und numerische Simulationen," *Bauingenieur*, vol. 96, no. 06, pp. 201–211, 2021, doi: 10.37544/0005.

[118]   M. Elflah, M. Theofanous, S. Dirar, and H. Yuan, "Behaviour of stainless steel beam-to-column joints — Part 1: Experimental investigation," *J. Constr. Steel Res.*, vol. 152, pp. 183–193, 2019, doi: 10.1016/j.jcsr.2018.02.040.

[119]   European Convention for Constructional Steelwork (ECCS), "Recommended testing procedure for assessing the behaviour of structural steel elements under cyclic loads, Technical Committee 1, TWG 1.3 — Seismic Design," Brussels, Belgium, 1986.

[120]   P. Zanon and R. Zandonini, "Experimental analysis of end plate connections," in *ProceedingState of the ArtWorkshop on Connections and the Behaviour of Strength and Design of Steel Structuress of a State-of-the-Art Workshop on Connections and the Behaviour, Strength and Design of Steel Structures*, 1988, pp. 41–51.

[121]   K. Weynand, "Safety and economic feasibility studies for the application of semi-rigid connections in steel construction - contribution to the further development of modern design codes (PhD thesis, in German)," University of Aachen, Aachen (Germany), 1997.

[122]   G. Brandonisio, "The column web panel in welded beam-to-column joints (Msc thesis, in Italian)," University of Naples, Naples (Italy), 2004.

[123]   European Committee for Standardization (CEN), "EN 1993-1-14, Eurocode 3: Design of steel structures — Part 1-14: Design assisted by finite element analysis," Brussels, Belgium, 2021.

[124] X. Yun and L. Gardner, "Stress-strain curves for hot-rolled steels," *J. Constr. Steel Res.*, vol. 133, no. June, pp. 36–46, 2017, doi: 10.1016/j.jcsr.2017.01.024.

[125] I. Marginean, "Robustness of moment steel frames under column loss scenarios (PhD thesis)," University of Timisoara, Timisoara (Romania), 2017.

[126] F. Yang, M. Veljkovic, and Y. Liu, "Ductile damage model calibration for high-strength structural steels," *Constr. Build. Mater.*, vol. 263, no. 120632, Dec. 2020, doi: 10.1016/j.conbuildmat.2020.120632.

[127] V. L. Hoang and H. Nguyen Dang, "Second-order plastic-hinge analysis of 3-D steel frames including strain hardening effects," *Eng. Struct.*, vol. 30, no. 12, pp. 3505–3512, 2008, doi: 10.1016/j.engstruct.2008.05.013.

[128] V.-L. Hoang, H. Nguyen Dang, J.-P. Jaspart, and J.-F. Demonceau, "An overview of the plastic-hinge analysis of 3D steel frames," *Asia Pacific J. Comput. Eng.*, vol. 2, no. 1, 2015, doi: 10.1186/s40540-015-0016-9.

[129] F. Cerfontaine, "Study of the M-N interaction in bolted joints (PhD thesis, in French)," University of Liège, Liège (Belgium), 2004.

[130] European Committee for Standardization (CEN), "EN 1993-1-5, Eurocode 3: Design of steel structures - Part 1-5: Plated structural elements," Brussels, Belgium, 2003.

[131] "FINELG User's Manual." Greisch Design Office, Liège (Belgium), 2019.